# PEM fuel cells: Analytical modelling and experimental validation

Thesis Submitted to AcSIR for the Award of
the Degree of
**DOCTOR OF PHILOSOPHY**
In Engineering Sciences


By
**Aniket U. Thosar**
Reg. No. 20EE14A26052

Under the guidance of
**Dr. Chetan J. Gadgil and Dr. Ashish K. Lele**

Chemical Engineering and Process Development Division
**CSIR-National Chemical Laboratory, Pune**

राष्ट्रीय रासायनिक प्रयोगशाला
(वैज्ञानिक तथा औद्योगिक अनुसंधान परिषद)
डॉ. होमी भाभा मार्ग पुणे - 411 008. भारत
NATIONAL CHEMICAL LABORATORY
(Council of Scientific & Industrial Research)
Dr. Homi Bhabha Road, Pune - 411 008. India.

## Certificate

This is to certify that the work incorporated in this Ph.D. thesis entitled "PEM fuel cells: Analytical modelling and experimental validation" submitted by Mr. Aniket Thosar to Academy of Scientific and Innovative Research (AcSIR) in fulfillment of the requirements for the award of the Degree of Philosophy in Engineering Sciences, embodies original research work under our supervision. We further certify that this work has not been submitted to any other University or Institution in part or full for the award of any degree or diploma. Research material obtained from other sources has been duly acknowledged in the thesis. Any text, illustration, table etc., used in the thesis from other sources, have been duly cited and acknowledged.

It is also certified that this work done by the student, under my supervision, is plagiarism free.

| Aniket Thosar | Dr. Chetan J. Gadgil | Dr. Ashish K. Lele |
|---|---|---|
| (Student) | (Supervisor) | (Co-Supervisor) |

Communication Channels
☎ +91-20-5893300
+91-20-5893315-18
+91-20-5893400* (DID)
FAX +91-20-5893619
WEBSITE www.ncl-india.org

# Declaration by the Candidate

I hereby declare that the thesis entitled **"PEM fuel cells: Analytical modelling and experimental validation"** submitted by me for the Degree of Doctor of Philosophy to Academy of Scientific & Innovative Research (AcSIR) is the record of work carried out by me at Polymer Sciences & Engineering Division (PSE), CSIR- National Chemical Laboratory, Pune - 411008, India, under the supervision of Dr. Chetan Gadgil and Dr. Ashish Lele. The work is original and has not formed the basis for the award of any degree, diploma, associateship and fellowship titles in this or any other university or other institute of higher learning. I further declare that the material obtained from other resources has been duly acknowledged in the thesis.

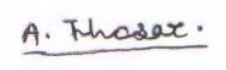

Aniket Thosar
AcSIR ID: 20EE14A26052

April 2019

Chemical Engineering and Process Development division
CSIR-National Chemical Laboratory
Dr. Homi Bhabha Road, Pashan
Pune – 411008
Maharashtra, India

# Synopsis

## Introduction

Recently, policy makers of India (NITI Aayog) has decided to generate 175 GW of power from renewables by 2022, which is roughly 32-36% of the total electricity generation in India [1]. Remarkably, the cost of renewable energy (Rs/kW-hr) has also started approaching the cost of conventional electricity (from coal/ fossil fuels) [2, 3]. Thus, the renewable energy generation in synergy with energy storage technologies can drive humanity towards 'energy sustainability' and therefore is going to disrupt the energy business in near future. While electrochemical storage of renewable energy using battery technology is the most popular, chemical storage (eg: $H_2$) of renewable energy using photo-electrochemical or thermochemical pathways is getting large attention in recent years. The chemical energy of $H_2$ can then be converted into electricity using 'fuel cells' as and when required. Fuel cells find multitude applications in transportation, stationary power-backup, strategic and industrial sectors because of their high efficiency, low/nil end-to-end emissions depending on the source of hydrogen, low noise, low vibrations, small footprint, compatibility of various fuels and complimentary opportunities with batteries. Of all the various types of fuel cells, Proton Exchange Membrane Fuel Cells (PEMFC) are the most popular, especially in the 1-100 kW power generation range. The present doctoral thesis focuses on Proton Exchange Membrane Fuel Cells (PEMFC) and attempts to provide a comprehensive analytical model of the complex physico-chemical processes that occur inside the device during power generation operation.

PEMFC technology has great potential in transportation sector, particularly for heavy-duty vehicles (trucks, trailers (Toyota), forklifts (amazon), military vehicles (GM) etc.) wherein non-sustainable fossil fuel based internal combustion-based energy conversion can be competitively replaced with PEMFC technology. PEMFCs also have enormous opportunities in stationary power back-up applications such as replacement of the ubiquitous diesel generator sets on telecom towers. However, current high capital cost of PEMFC is a major hurdle in deep penetration of PEMFC technology in these markets. Maximizing the power output of a PEMFC using appropriate

scientific innovations is one of the approaches to bring the capital cost down; the other being scaling up of manufacturing processes and taking advantage of economy of scale. Scientific innovations can be accelerated if correlations between the various design, operating and material parameters of a PEMFC device with its current-potential relationship (polarization curve) is rationalized. **The highlight of the work presented in this thesis is the derivation of a comprehensive physics-based analytical equation of the polarization curve which is valid over the entire range of current density** and provides the important correlations stated above. The model is also experimentally validated in the present work.

## Statement of Problem and Objectives

While extensive modelling and simulation efforts have been made in the recent past towards establishing correlations between all the physicochemical processes involved in an operational PEMFC to its performance, there are important lacunae which have remained unaddressed. These are:

i) Analytical solutions to the governing equations of one-dimensional model of the cathode catalyst layer (CCL) of a PEMFC for all possible regimes of CCL operation, especially in the current density regime that is relevant to actual operational conditions.

ii) Two-dimensional analytical framework incorporating convection of reactant gases along the axis of the flow channel and simultaneous diffusion through GDL in the transverse direction coupled with consumption in the CCL for its various operating regimes.

iii) Experimental validation of the developed analytical model.

Thus, in this thesis, we have aimed to derive a comprehensive *PEM fuel cell equation* i.e., an analytical equation of the polarization curve of PEM fuel cells which is valid over entire range of current density. The specific research objectives of the thesis are:

***Research objectives:***

1. To derive generalized analytical solution to one dimensional model of the CCL incorporating the microstructural details of the CCL in the regime of simultaneous oxygen and proton transport limited reaction kinetics and therefore derive a comprehensive analytical current-potential relationship that relates all the CCL parameters to the power output of a PEMFC.

2. To incorporate the laminar flow of reactant gas along the axis of the flow channel, transverse gas diffusion along the depth of the flow channel and gas diffusion layer (GDL) and consumption in the CCL as dictated by the regime of operation.
3. To design and implement experimental methodologies to determine oxygen diffusion coefficient in the different domains of PEMFC.
4. To validate the predictions of analytical model with real-time experimental results.

## Key findings of the research work

A detailed analytical modelling of PEMFC supported by numerical simulations invoked in this work has provided the following key results [4-6]:-

**1) A comprehensive understanding of *all* the possible regimes of CCL operation**

This work provides generalized solution to the governing equations of 1-D macro-homogeneous (MH) model of the CCL. The derived analytical equations of the polarization curve in our study not only capture the limiting cases i.e. poor oxygen transport but ideal proton transport and poor proton transport but ideal oxygen transport but also captures a regime wherein neither oxygen transport nor proton transport can be neglected. While MH model describes the simultaneous reaction and protons and oxygen in the CCL, it doesn't incorporate an additional resistance to oxygen transport in the ionomer phase of the CCL. The flooded agglomerate (FA) model captures the essential microstructural features of the CCL in a phenomenological sense and can be regarded as a correction to the MH model and is solved in this work.

**2) *The PEM fuel cell equation***

We develop a two-dimensional framework that incorporates laminar flow along the axis of the flow channel and transverse oxygen diffusion along the channel depth and gas diffusion layer (GDL). The FA corrected MH model dictates the oxygen consumption source at the CCL-GDL boundary. Analytical solution to this 2-D problem leads to the '*The PEM fuel cell equation*'. This current-potential relationship relates all the material, operating and geometric parameters involved in an operational PEMFC with its power output and valid over entire range of current density i.e. zero to limiting current.

**3) Development of physics-based experimental methodologies to determine the regime of CCL operation and to estimate oxygen diffusion coefficient in the different domains of PEMFC (CCL and GDL) and experimental validation of *The PEM fuel cell equation***

We elucidate an experimental methodology to determine the regime of CCL operation which comprised of comparing experimental scaling laws with the scaling laws derived from the theory and provided a systematic approach to estimate the effective oxygen diffusion coefficient in the catalyst layer. This work also establishes a methodology to estimate the oxygen diffusion coefficient in the gas diffusion layer based on the limiting cases of our isothermal two-dimensional model of PEMFC. These transport parameters are then used for model predictions. Finally, we show that the analytical polarization curve predicted using these parameters shows excellent match with the experimental and numerically simulated polarization curves over the entire range of current density.

The significance of this work is that the analytical model relates the performance of a PEMFC to all the operating and geometric parameters as well as the average transport and kinetic properties of the materials used in its different components, without the need for computationally expensive numerical simulations. The model can provide useful insights for enhancing the performance of PEMFC in different regimes of current density and therefore can be used as a design tool to maximize the power output of a PEMFC and can help in reducing its capital cost.

**References**

1) Report of the expert group on 175 GW RE by 2022, National Institution for Transforming India, (NITI Aayog), New Delhi.
2) Solar tariffs once again hit all-time low of Rs 2.44 a unit at SECI auction, Kaavya Chandrasekaran, The Economic Times, 3rd July, 2018.
3) Wind power prices crash to ₹2.43/unit in Gujarat auction, M. Ramesh, The Hindu, 21st December 2017.
4) A. U. Thosar and A. K. Lele, Analytical solutions of an isothermal two-dimensional model of a cathode flow channel in a proton exchange membrane fuel cell, Chemical Engineering Science 190 (2018) 333–344.

5) A. U. Thosar and A. K. Lele, Analytical solutions of an isothermal two-dimensional model of a cathode flow channel in transport limited operational regimes of a proton exchange membrane fuel cell, Chemical Engineering Science 196 (2019) 166–175.
6) A. U. Thosar, H. Agarwal, Govarthan S. and A. K. Lele, Comprehensive analytical model for polarization curve of a PEM fuel cell and experimental validation, Chemical Engineering Science 206 (2019) 96–117 (Editor's Choice Article).

# Acknowledgement

This thesis is an output of last four and half years of my work at National Chemical Laboratory (NCL, Pune) and I take this opportunity to extend my sincere gratitude to all those who made these four and half years of my life memorable forever.

First and foremost, I would like to thank my research co-supervisor Dr. Ashish Lele for his constant support and guidance. There were times in my PhD when I had a feeling that I am going nowhere and extremely confused and his constant support and faith in me was really the motivation to pursue the research. The brain-storming discussions with him in J-103, PSE office as well as over phone were the best times in my PhD. I sincerely wish to have such brain-storming sessions continued occasionally in future as well :). The casual discussions over coffee/tea/lunch/dinner (of course sponsored by Lele sir) were also stimulating. His training has helped me learn how to simplify a very complicated looking problem. I will always remember his response on one of our derivations that 'Nature always admires simplicity; it is just that we should have faith'. I would also like to thank my supervisor, 'Dr. Chetan Gadgil' for stimulating discussions on various topics ranging from bioinformatics to career building. I also thank him for being patient with my administrative hiccups.

Besides my advisors, I would like to thank the rest of my doctoral advisory committee (DAC): Dr. K. Sreekumar, Dr. Amol Kulkarni, Dr Ulhas Kharul and Dr. Pradeep Kumar, for their insightful comments and encouragement. I would also like to thank Prof. J. B. Joshi for his constant support and for his extremely valuable comments/ suggestions.

My sincere thanks to coursework instructors: Dr. Guruswamy, Dr. Rajnish Kumar, Dr. Amol Kulkarni, Dr. Chetan Gadgil, Dr. Pankaj Doshi, Dr. Vivek Ranade, Dr. Sarika Bhattacharya, Dr. K. Sreekumar, Dr. P. A. Joy and Dr. BLV Prasad. I really enjoyed the regular lectures, tests, homework assignments and really learnt core Chemical Engineering from these masters.

I am extremely thankful to Dr. S D Bhat, Dr. Vishal, Harshal, Govarthan, Nagraju and Karthika from CSIR-CECRI, Chennai unit for their help in experimentation. I would really like to thank Harshal for his support in every way during my stay at CSIR-CECRI.

I would like to thank the Macro-Meet team (Dr. Guruswamy, Karthika, Ramnedra, Emmanuel, Anup, Gunvant, Ram, Prashant) and NCL-Technology and Entrepreneurship Club team (Dr. Premnath, Dr. Smita, Pravin, Karthika, Ramendra, Emmanuel, Vishwanath, Meenakshi) for the great time. The time spent at these two activities has really helped me shaping my overall personality and soft-skills. I would also like to thank Aakash, Dr. Anuya and Dr. Anees for initiating the activity, 'Research Discussion Forum (RDF)'. I enjoyed the regular presentations, lecture series as well as brain-storming sessions at RDF.

I would like to thank my NCL-mates Ramendra, Ajinkya and Harshal (although he is from CECRI, I count him as my NCL-mate only) for everything. They witnessed and lived all ups and downs during my PhD along with me. The mentally tiring nature of PhD became super-easy because of these guys. I would also like to thank all my fuel cell lab-mates from D-103, Pritish, Sachin, Hari, Ajinkya, Ruhi, Pradeep, Abhishek, Dhiraj, Shivani. I am also thankful to my room-mates, Dr. Vishal (221, old hostel), Aakash (121, HOR-4) and Prashant (121, HOR-4) for patiently handling my laziness in day-to-day activities :).

I also find myself fortunate to have brain-storming discussions with fuel cell teams from KPIT technologies (Mr. Deepesh Gujrathi, Mr. Bhushan Velis, Mr. Manmath Kharade), Reliance Industries Ltd. (Dr. Anurag Pandey, Mr. Sarathi L) and Thermax Ltd. (Mr. Siddharth Limaye).

Lastly but most importantly, I am sincerely thankful to my parents for their support, love and affection and to all my school and college teachers for guiding me to choose a correct path in life.

Aniket Thosar
April, 2019.

# Table of Contents

# List of figures

# List of Tables

# Nomenclature

## Symbols

| | |
|---|---|
| $A_c$ | Tafel slope, (V) |
| $C$ | Local oxygen concentration ($mol/m^3$) |
| $C_{in}$ | Inlet gas concentration, ($mol/m^3$) |
| $C_{CCL-GDL}$ | Local oxygen concentration at the CCL-GDL interface at any point '$x$' along the channel length, ($mol/m^3$) |
| $C_{Ch-GDL}$ | Local oxygen concentration at the channel-GDL interface at any point '$x$' along the channel length, ($mol/m^3$) |
| $D$ | Oxygen diffusion coefficient in channel, ($m^2/s$) |
| $D_{agg}$ | Effective oxygen diffusion coefficient inside the agglomerate, ($m^2/s$) |
| $D_{CCL}$ | Effective oxygen diffusion coefficient inside the CCL, ($m^2/s$) |
| $D_{GDL}$ | Effective oxygen diffusion coefficient inside the GDL, ($m^2/s$) |
| $E$ | Effectiveness factor |
| $E_{eq}$ | Equilibrium voltage ($V$) |
| $F$ | Faraday's constant, ($C/mol$) |
| $2h$ | Channel height, ($m$) |

| | |
|---|---|
| $i_{o,c}A$ | Volumetric exchange current density, $(A/m^3)$ |
| $j$ | Local current density in the CCL, $(A/m^2)$ |
| $J$ | Local current density at any point '$x$' along the channel length, $(A/m^2)$ |
| $J_{crit,(H+)transport}$ | Current density above which proton transport across the CCL becomes rate limiting $(A/m^2)$ |
| $J_{crit,(O2)transport}$ | Current density above which oxygen transport across the CCL becomes rate limiting $(A/m^2)$ |
| $J_{crit,(O2)\ transport\ in\ CCL\ and\ agglomerate}$ | Current density above which oxygen transport inside the agglomerate becomes rate limiting $(A/m^2)$ |
| $J_{1-D}$ | Current density as given by one dimensional framework, $(A/m^2)$ |
| $J_{flow}$ | Inlet oxygen flow rate driven limiting current density, $(A/m^2)$ |
| $J_{GDL}$ | Oxygen diffusion inside GDL driven limiting current density, $(A/m^2)$ |
| $J_{diff,ch}$ | Oxygen diffusion along the depth of the channel driven limiting current density, $(A/m^2)$ |
| $J_{total}$ | Total area averaged current density of a PEMFC $(A/m^2)$ |
| $L$ | Channel length, $(m)$ |
| $l_{GDL}$ | Thickness of GDL, $(m)$ |
| $l_t$ | Thickness of CCL, $(m)$ |
| $l_{membrane}$ | Thickness of membrane $(m)$ |
| $M_T$ | Thiele modulus |
| $R_{agg}$ | Agglomerate radius $(m)$ |
| $u$ | Local velocity, $(m/s)$ |

| | |
|---|---|
| $U_{mean}$ | Mean velocity at the channel inlet |
| $V_{cell}$ | Operating cell voltage ($V$) |
| $w_{channel}$ | Width of channel ($m$) |
| $w_{rib}$ | Width of ribs ($m$) |
| $x$ | Co-ordinate along the channel, ($m$) |
| $y$ | Co-ordinate along the channel depth, ($m$) |

## Greek Letters

| | |
|---|---|
| $\alpha$ | Dimensionless current density, $\frac{J_{1-D}}{J_{GDL}}$ |
| $\beta$ | Dimensionless current density, $\frac{J_{1-D}}{J_{flow}}$ |
| $\xi$ | Dimensionless current density, $\frac{J_{1-D}}{J_{diff,ch}}$ |
| $\sigma$ | Proton conductivity of CCL ($S/cm$) |
| $\sigma_{membrane}$ | Proton conductivity of membrane ($S/cm$) |
| $\sigma_{GDL,tp}$ | Through-plane electrical conductivity of GDL ($S/cm$) |
| $\sigma_{GDL,ip}$ | In-plane electrical conductivity of GDL ($S/cm$) |
| $\varepsilon_{CCL}$ | CCL porosity |
| $\varepsilon_{GDL}$ | GDL porosity |
| $\eta$ | Local overpotential in the CCL ($V$) |
| $\eta_o$ | Total overpotential ($V$) |
| $\eta_{o,CCL}$ | Total cathodic overpotential ($V$) |
| $\eta_{o,iR-free,CCL}$ | Cathodic iR-free overpotential ($V$) |
| $\eta_{ohmic}$ | Overpotential due to total ohmic resistance ($V$) |
| $\varphi$ | Ratio of flow area to the total area, $\frac{w_{channel}}{w_{channel}+w_{rib}}$ |

## Abbreviations

| | |
|---|---|
| PEMFC | Proton Exchange Membrane Fuel Cell |
| PEM | Proton Exchange Membrane |
| ORR | Oxygen Reduction Reaction |
| HOR | Hydrogen Oxidation Reaction |
| CCL | Cathode Catalyst Layer |
| ACL | Anode Catalyst Layer |
| GDL | Gas Diffusion Layer |
| MPL | Microporous Layer |
| MHM | Macro-homogeneous model of the CCL |
| FAM | Flooded Agglomerate model of the CCL |

# Chapter 1

## Introduction to PEMFC technology

'Energy affordability, accessibility and sustainability' are going to be essential aspects of the society of 21st century [1]. This has driven a large part of scientific community to invest their efforts in the pursuit of 'sustainable energy generation, storage and transmission' [2]. It is remarkable that the scale of operation has already helped in bringing down the cost of renewable energy generation (solar and wind energy) closer to conventional (coal or fossil fuel based) electricity cost [3-4]. However, the inherent constraints on 24x7x365 continuous availability of renewable energy sources establishes the need for large scale energy storage. Chemical storage of renewable energy into hydrogen using electrochemical, photo-electrochemical or thermochemical pathways is attracting large attention in recent years [5-7]. 'Fuel cells' then convert the chemical energy of hydrogen into electricity as and when required. This thesis, in particular focuses on proton exchange membrane fuel cell (PEMFC) which is the most widely used fuel cell type because of its mild operating conditions (near room temperature and atmospheric pressure operation).

PEMFCs are already introduced in the following markets:-

1) Stationary back-up power

Being second largest consumer of diesel in the country (excess of 500,000 cell towers), telecom industry in India consumes about 2.5 billion litres of diesel annually for DG sets used as a back-up power for cell towers. This leads to 6.6 MMT of $CO_2$ emission and also results in a revenue loss of about INR 3600 Crore annually [8]. Therefore, DG set as a back-power for

the telecom industry is turning out to be an unattractive option economically as well as environmentally. The telecom regulatory authority of India has already indicated a need to shift from DG-set based back-power to the greener options [9]. PEMFC technology with its compelling attributes such as high efficiency, low end-to-end emissions depending on the source of hydrogen, low noise, low vibrations, small footprint, compatibility of various fuels and complimentary opportunities with batteries is proving to be one of the best alternatives to DG-sets. The exciting recent economic analysis of conversion of renewable power into hydrogen suggests that the hydrogen cost will reach 2.5 $/kg by 2030 i.e. equivalent of diesel cost (based on energy equivalence) [10]. Therefore, the replacement of DG with PEMFC is economically possible if the capital cost of PEMFC system becomes comparable with the DG-set. Furthermore, given that there are in excess of 500,000 towers in India, a significant fraction of which require backup power in excess of 8 hours, therefore the replacement of diesel-based back-up power generators for telecom towers with PEMFC system can be expected to be a huge market and a significant business opportunity. PEMFC systems have already been deployed by telecom companies in India [11-12].

2) Automotive sector

The leading companies in the automotive sectors have already introduced their Fuel Cell Vehicles (cars) in the market for example, Mirai- Toyota, Clarity- Honda, Nexo- Hyundai and F cell- Mercedez. PEMFCs are thought to be better than battery electric vehicles for heavy-duty transportation such as trucks, trailers, railway and ships. Toyota (Project Portal), Nikola Motor and Hyundai are introducing their heavy-duty truck proto-type in the market [13-15]. Longer time of operation and fast refueling of hydrogen tanks have attracted Walmart and Amazon to replace their conventional forklifts with PEMFC powered forklifts [16]. GM

defence has introduced its fuel cell based military grade based truck to move equipment and supplies around the battlefield more efficiently and safely [17].

Although as mentioned above, PEMFCs can cater to huge markets in the automotive sector as well as stationary applications, higher capital cost brings a hurdle in deep penetration of PEMFC technology in cost sensitive such as India markets. Therefore, it raises an important question: what innovations are required to be implemented immediately to bring down the capital cost of the PEMFC technology? Since the fuel cell stack is a large contributor to the overall cost of PEMFC system, therefore it becomes important to assess the contributions of the various factors influencing the PEMFC to increase its performance and thereby lower initial capital costs.

Before we begin approaching this problem, we provide a brief account on the construction and working principle of PEMFC and key components involved.

### 1.1) PEMFC: Construction and working principle

When the positive and negative electrodes of a fuel cell on which counter-balancing spontaneous oxidation and reduction reactions occur are electrically connected in terms of providing a path for ions (electrolyte), it causes a flow of electrons through an external load thus producing the power to drive the load. Thus, in a PEM fuel cell, hydrogen oxidation reaction (HOR) takes place on the anode and the oxidized hydrogen ions i.e. protons migrate through a polymer electrolyte membrane to the cathode whereas the electrons are dragged through an external circuit to the cathode where they combine with oxygen to produce water and heat. The reaction on the cathode is called the oxygen reduction reaction (ORR). The electrochemical reactions in an operational PEM fuel cell are:

$2H_2 \rightarrow 4H^+ + 4e^-$ (HOR on anode side)

$4H^+ + 4e^- + O_2 \rightarrow 2H_2O$ (ORR on Cathode side)

Figure 1.1 shows a schematic of a typical PEM fuel cell and illustrates different components such as flow field plate (FP), gas diffusion layer (GDL), catalyst layer and proton exchange membrane or polymer electrolyte membrane (PEM). As shown in the schematic, a single cell is arranged in series to build a fuel cell stack.

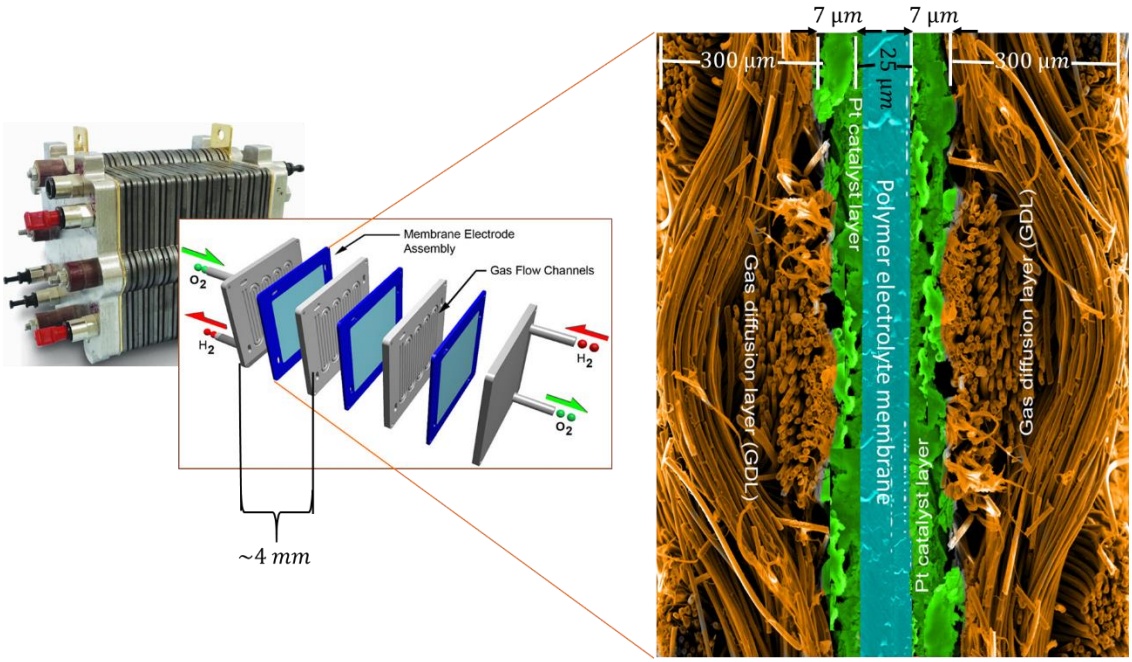


**Fig. 1.1** Fuel cell assembly and different components (image credits: [18-20])

We now elaborate on different components of a PEMFC:

- Flow field plate

The channels on the flow field plate allow the flow of reactant gases ensure their supply to the catalyst layer. The ribs on the flow field plate allow electrical contact with the GDL. The flow field plate can either be monopolar wherein one side of the plate is engraved with the channels (typically first and last cell of the stack) or bipolar, with channels on both sides. A monopolar plate can serve as either anode or cathode plate, whereas a bipolar plate serves as anode on one side and cathode on the other. Therefore, flow field plate should be electrically conducting and impermeable to reactant gases. Usually, flow field plates are graphite based

[21]. However, metallic bipolar plates coated with a thin layer of anti-corrosive agents are becoming more popular [22]. Figure 1.2 shows the typical flow field plates.

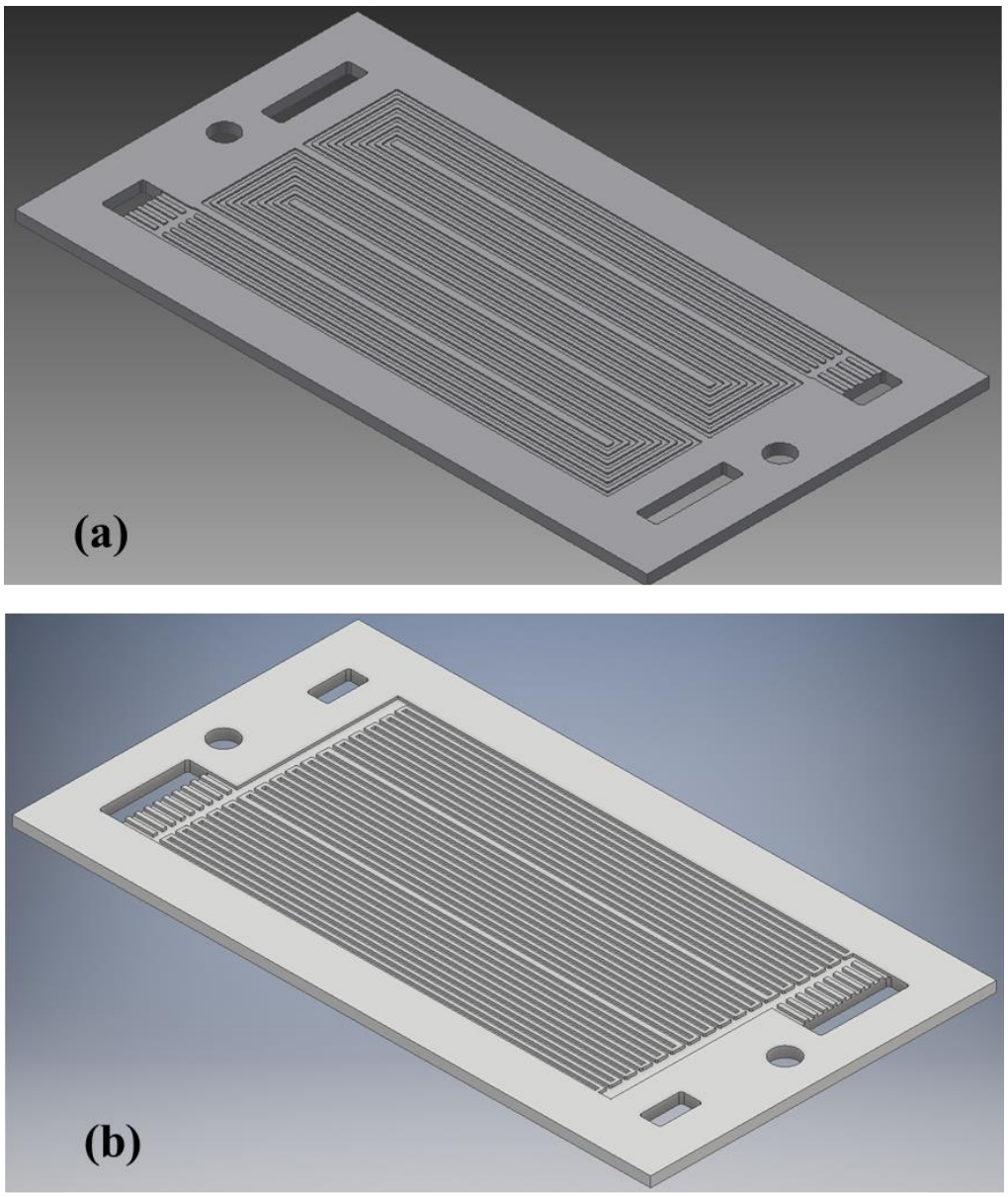


**Fig. 1.2** Schematic of flow field plate, a) Serpentine flow field plate, b) Interdigitated type flow field plate

- Gas diffusion layer

As mentioned above, although reactant gases are available in the channels, the area above the ribs is deficient of reactant gases. A gas diffusion layer (GDL), which is a porous layer sandwiched between the flow field plate and the catalyst layer, enables the reactant gases to

diffuse uniformly over the entire active area. Also, it allows electrons to be transported between the catalyst layer and the flow field plates at either electrodes. GDL is typically composed of nonwoven carbon fibres or woven carbon cloth which is electrically conducting as well as porous. The GDLs are coated with fluoropolymers to render them hydrophobic. This allows for easy removal of water formed during the reaction [23]. Figure 1.3 illustrates the gas diffusion layer and zoomed view (SEM image) along the thickness [24-25].

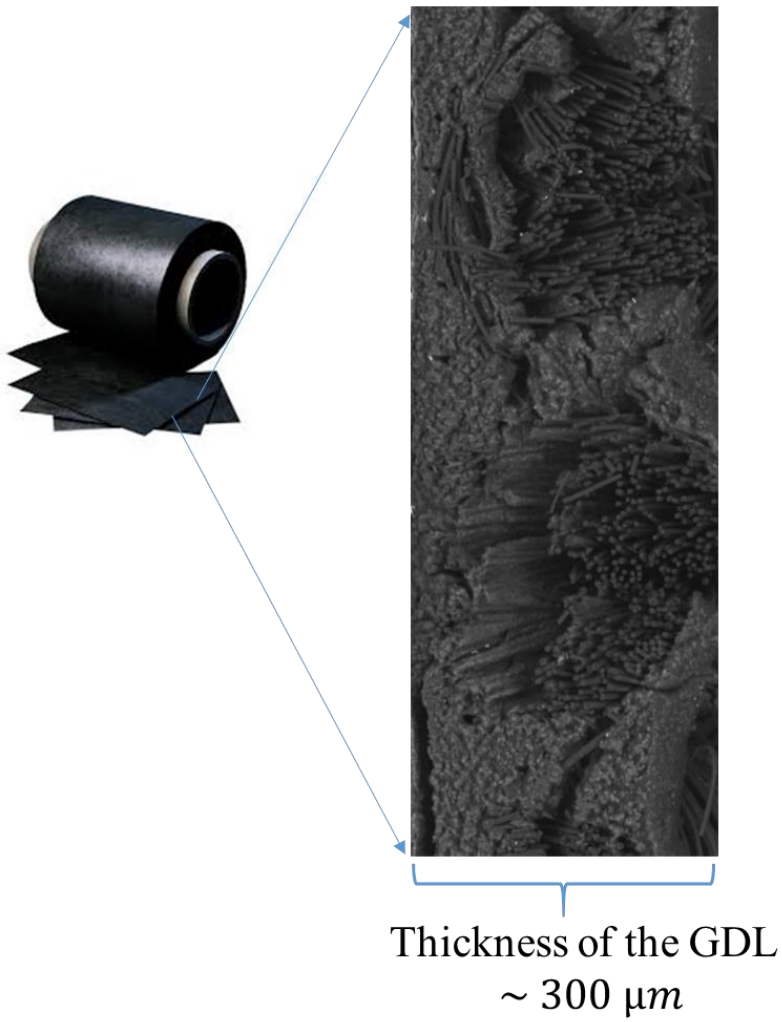


**Fig. 1.3** Typical gas diffusion layer and zoomed view along the thickness (image credits: [24-25])

- Catalyst layer

A catalyst layer (CL) consists of a network of supported catalyst nanoparticles (usually Pt/C) that are coated with an ionomer phase (usually nafion). Typically, 3-5 nm platinum particles

are supported on ~50-80 nm carbon particles. The ionomer in the catalyst layer ensures a connected path for protons, while the voids between the carbon particles allow the transport of reactant gases from the GDL-CL interface to CL-membrane interface. Figure 1.4 depicts the catalyst layer and zoomed TEM image of the catalyst particles.

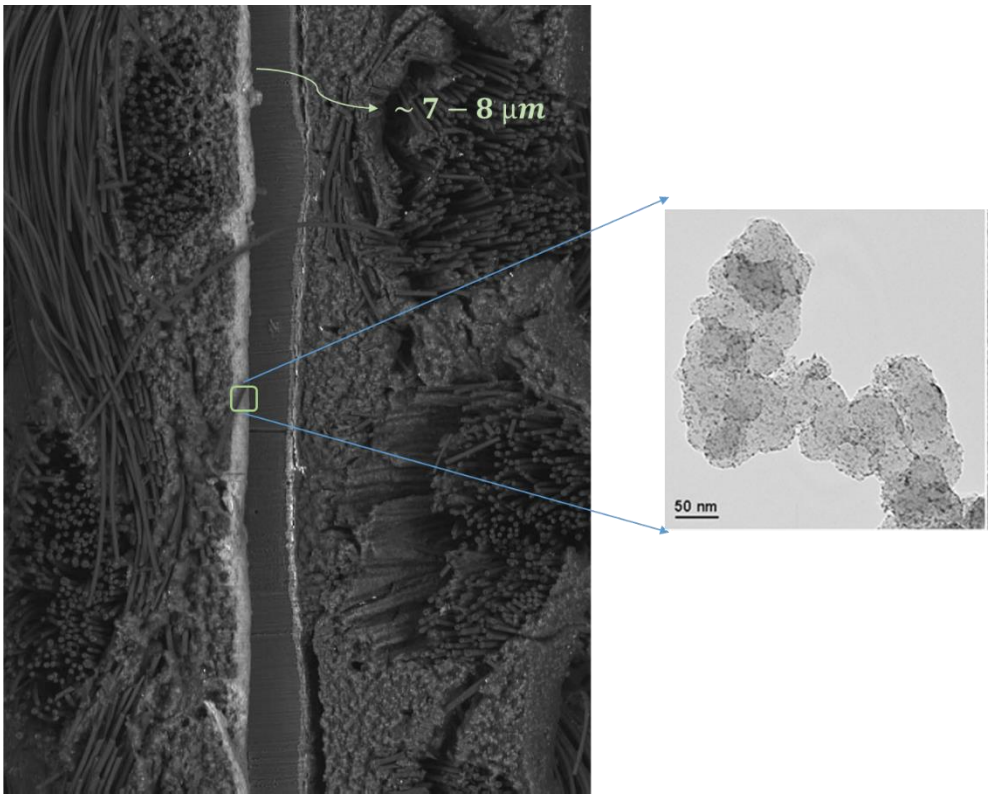


**Fig. 1.4** Typical cathode catalyst layer and zoomed view illustrating Pt/C catalyst particles (image credits: [25-26])

- Polymer electrolyte membrane

Polymer electrolyte membrane or proton exchange membrane (PEM) separates anode compartment (flow field, GDL and anode catalyst layer) and cathode compartment (flow field, GDL and cathode catalyst layer). It is semipermeable in nature and allows only protons to pass through while restricting the reactant gases and electrons to permeate from anode to cathode or vice-a-versa. 'Nafion membrane' is a typical PEM used widely and requires enough hydration to allow transport of protons from anode to cathode [27]. Therefore, PEMFC is operated with humidified reactant gases i.e. the relative humidity of entering reactant gases is near 100%.

Structurally, Nafion consists of a hydrophobic teflon backbone and hydrophilic side-chains ($SO_3$ groups). When hydrated, the hydrophilic side chains form nano-domains wherein protons either get molecularly transported across the percolated nano-domains or the rotation and re-orientation of water molecules allow the hopping mechanism for proton transport. Figure 1.5 depicts the nafion-microstructure and the proton transport mechanism [28-29].

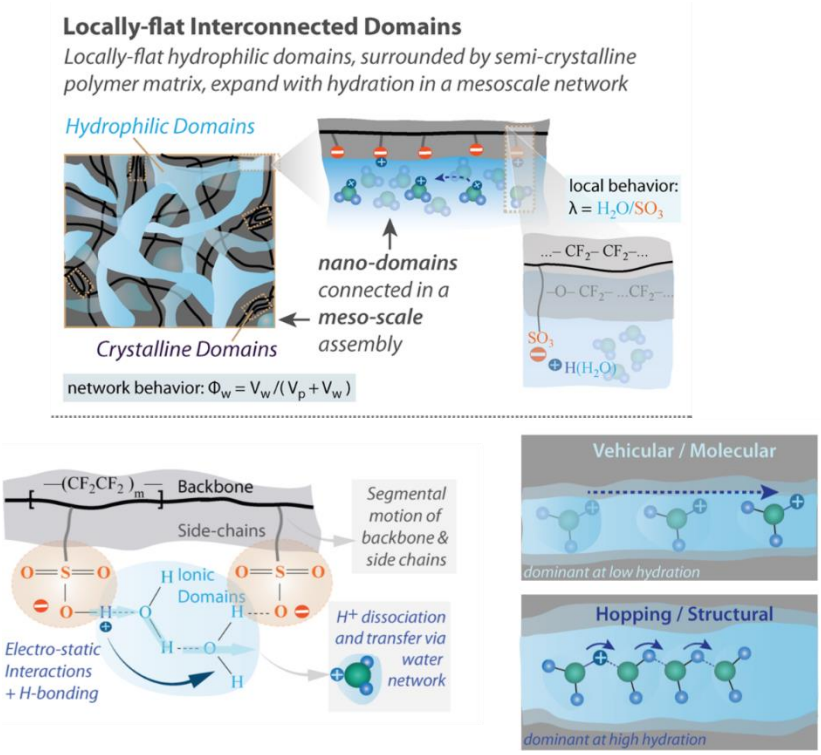


**Fig. 1.5** Nafion microstructure and proton transport mechanism in the ionic domains (image credits: [28])

- Catalyst coated membrane (CCM)

Catalyst coated membrane is fabricated by coating the PEM with catalyst on either side of the membrane. A popular method for the fabrication of CCM is 'Decal transfer'. In this process, a slurry of catalyst particles (Pt/C), ionomer (nafion) and volatile solvents is coated on a teflon substrate by bar coating and is called as decal electrode. A sandwich of two such decal electrodes with the PEM (nafion) in between is then hot-pressed such that catalyst on the decal

electrode gets transferred onto the PEM. A direct coating of catalyst slurry on the membrane using spray coating is now emerging as a popular substitute for the decal process.

- Membrane electrode assembly (MEA)

The CCM fabricated by the process mentioned above is sandwiched between two GDLs and the assembly is typically hot pressed. Thus, five layers namely, cathode GDL, cathode catalyst layer (CCL), PEM, anode catalyst layer (ACL) and anode GDL come in intimate contact during hot pressing and this assembly is popularly known as membrane electrode assembly (MEA). These MEAs are arranged in series with bipolar plates in-between to assemble a fuel cell stack.

A PEMFC works as follows. Hydrogen is convected through the channels on the anode flow field plate and simultaneously diffuses through anode GDL and ACL to reach to the active sites in the ACL. Here, the spontaneous oxidation of $H_2$ produces protons ($H^+$) and electrons ($e^-$). Under a potential gradient, the protons get migrated through the PEM and electrons get migrated through the external circuit to the CCL. On the cathode side, the compressor or blower sets a pressure driven flow of air in the channels of the flow field plate and $O_2$ from air simultaneously diffuses in the GDL and the CCL. This diffused $O_2$, the electrons migrating through the external circuit and proton migrating through the PEM together combine to form water and heat. The migration of electrons through external circuit is the current, and the electrical power obtained from the PEMFC is the product of operating potential and the current drawn. Therefore, electrical power is dictated by various physicochemical rate processes occurring in an operational PEMFC. These are:

- Pressure driven flow of $H_2$ and air in the channels of the flow field plate
- Diffusion of reactant gases in the GDL and CCL
- Dissolution and diffusion of reactant gases in the ionomer phase of CL

- Proton conduction through membrane from the ACL to the CCL
- Conduction of protons in the ionomer phase of CL
- Conduction of electrons in the CL, GDL and bipolar plates
- Consumption of reactant species in the catalyst layer due to reaction

Moreover, these rate processes are dependent on one or more experimentally controllable parameters. We may therefore classify the parametric space in three categories:

- Geometric parameters,
- Operating parameters, and
- MEA parameters

We summarize below all the parameters involved in an operational PEMFC which can influence the electrical power output.

**Geometric parameters**

1 Width of channel

2 Width of rib

3 Depth of channel

4 Number of channels

5 Flow distributor

6 Type of flow field

**Operating parameters**

7 Operating voltage

8 Pressure

9 Temperature

10 Relative humidity

11 Reactants stoichiometry

**MEA parameters**

12 Platinum loading

13 Ionomer to carbon ratio

14 Agglomerate radius

15 Porosity of the CCL

16 Tortuosity for oxygen diffusion across the CCL/in the agglomerate

17 Tortuosity for proton transport in ionomer phase of the CCL

18 Intrinsic cathode exchange current density for the given catalyst

19 Electrochemical active surface area (ECSA)

20 Water content in the CCL

21 Proton conductivity of the membrane

22 Thickness of the membrane

23 Electrical conductivity of the GDL and CCL (through-plane and in-plane)

24 Porosity of the GDL

25 Water content in the GDL

## 1.2) Polarization curve: performance curve of a fuel cell

Figure 1.6 illustrates a typical 'design curve' of a PEMFC. In electrochemistry parlance, this is the polarization curve of PEMFC. It entails a relationship between the operating cell voltage and operating current density. The curve starts at zero current density on the '$x$' axis where the cell voltage on the '$y$' axis is the open circuit voltage (OCV), which is slightly below the equilibrium voltage ($E_o$). The cell voltage decreases as current density is increased i.e., as the cell is taken away from equilibrium. The deviation from OCV is related to different losses involved in an operational PEMFC and will be discussed in detail in this thesis. While the useful electrical power of PEMFC is '$V \times J_{total}$' where '$V$' and '$J_{total}$' respectively are

operating voltage and current density, the losses in voltage leads to heat dissipation ($Q = (E_o - V) \times J_{total}$) and lower energy efficiency. Improving the energy efficiency thus amounts to shifting the polarization curve upwards.

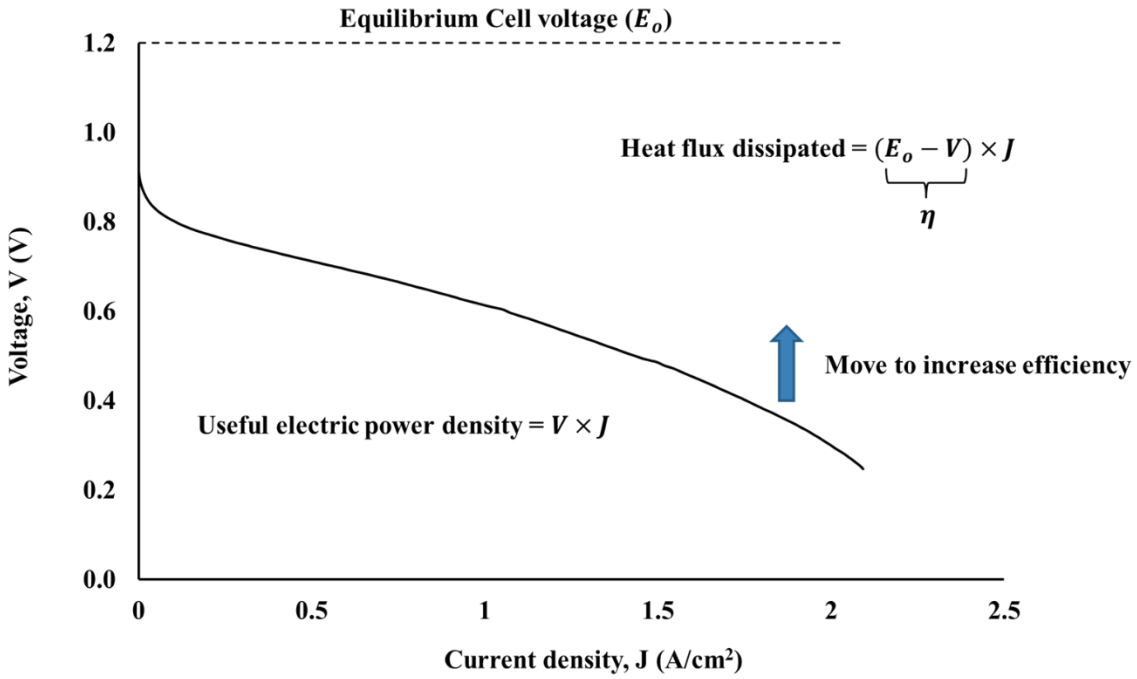


**Fig.1.6** Typical polarization curve of PEMFC

## 1.3) The design equation

We reiterate that the question: 'what innovations are required to be implemented immediately to bring down the capital cost of the PEMFC stack?' can be rigorously answered only if we understand the repercussions of all the physicochemical processes occurring in an operational PEMFC on the electrical power output of the PEMFC. In other words, it becomes necessary to quantify how the 25 parameters listed above influence the polarization curve of the PEMFC and consequently its power density and efficiency.

Therefore, for developing a better understanding of the PEMFC, a physics-based relationship between the physicochemical processes occurring in an operational PEMFC with

the current-potential relationship i.e. the polarization curve of the PEMFC is invaluable. This thesis reports work carried out towards formulation of an analytical equation that describes such a relationship and also its experimental validation.

# Chapter 2

# Review of Analytical Modelling of PEMFC and thesis objectives and outline

The content of this chapter is published in,

"Chemical Engineering Science, volume no. 190, 23rd November 2018, pages: 333–344" [95] and, "Chemical Engineering Science, volume no. 196, 16th March 2019, pages: 166–175" [97].

In this chapter, we present a comprehensive review on the analytical modelling of PEMFCs till-date and describe the historical journey of advances in the understanding of the different physicochemical processes occurring in an operational PEMFC.

Three-dimensional numerical simulations of PEMFC do predict the current-potential relationship. However, given the multi-parametric nature of the problem, there could be many different sets of parameters those may result in similar polarization curve. Thus, numerical simulation does not help in fault diagnosis of PEMFC. On the other hand, deriving analytical solutions to the governing equations of PEMFC can provide invaluable physical insights about the relationship between the physicochemical processes involved in an operational PEMFC with its power output. In fact, as will be discussed in the later chapters that the power output of PEMFC can be captured through seven current density scales corresponding to different rate processes. Therefore, we focus mainly on analytical models.

We first provide a systematic review of the analytical theories of PEMFC developed so far and a brief account of three-dimensional numerical simulations of PEMFC. This is followed

by a summary of unexplored questions in the literature so far. You should have three main sections in this chapter:

2.1: Analytical models

2.2: A brief account on three-dimensional numerical simulation of PEMFC

2.3: Summary of open questions in the literature

2.4: Objectives of the thesis

2.5: Outline of the thesis

## 2.1) Analytical models

The important starting point of all analytical models of PEMFC is the recognition that the HOR on the anode side is $\sim 10^5$ times faster than the ORR [30] on the cathode side. Therefore, even though transport of $H_2$ in the channel, GDL and ACL may modulate the consumption rate of $H_2$, the orders of magnitude faster HOR makes the contribution of anode side on the overall performance of PEMFC immaterial as long as sufficient $H_2$ ($\lambda_{H2} > 1.2$) is available at the inlet of the PEMFC. This allows for simplification of the modelling problem by focusing attention only on the physicochemical processes that occur on the cathode side [31-32]. It must be noted here that certain special cases for which neglecting anode side physicochemical processes may not be realistic, namely a) anode catalyst poisoning because of CO or $NH_3$ which can severely affect the intrinsic kinetics of HOR and b) The case when ACL is completely flooded and transport modulated HOR can start competing with intrinsic ORR kinetics.

Analytical models of ORR start with understanding the phenomena occurring in the CCL. Here, we look at models that are applicable separately in the 'low current density regime' and the 'high current density regime', where the regimes are essentially differentiated based on the

length scale over which oxygen diffusional gradient is set up in the CCL as explained in the sections below.

### 2.1.1) The macro-homogeneous (MH) model of the CCL

Even the simplified problem of focusing on the cathode side of a PEMFC is quite challenging because of the fact that ORR kinetics is coupled with transport of heat, mass and momentum associated with the reactant species and the enthalpy of the reaction. Historically, this complex problem has been reformulated into a relatively simpler one-dimensional problem that focuses only on the reaction and transport processes occurring along the thickness of the CCL inside the MEA. This approach assumes a reasonably high reactant flow in the channel and fast oxygen diffusion in the GDL such that the oxygen concentration at the CCL-GDL boundary is uniform over the entire active area. The criticality of this assumption is discussed in the next section.

In the one-dimensional formulation, [33-34] first proposed and discussed the macro-homogeneous (MH) model of the CCL which essentially visualizes CCL as a homogeneous media wherein the transport properties are volume averaged. Neglecting the fine microstructure of the CCL is equivalent to stating that while the transport gradients for oxygen and protons are tracked across the CCL thickness (length scale is 7-8 microns), these gradients are assumed to be negligible at the microstructure level (length scale corresponding to ionomer phase of the CCL ~ 100 nm). However, this is not valid at high current density and will be explained in the next subsection.

The schematic of the MH model of the CCL is shown in figure 2.1. The CCL can be visualized as a slab of thickness $l_t$ flanked by GDL of thickness $l_{GDL}$ on the one side and a membrane of thickness $l_m$ on the other. Proton flux enters the CCL at membrane-CCL interface and gets consumed in the CCL such that proton flux is zero at CCL-GDL interface since there

is no medium to transport protons beyond this interface. Oxygen flux enters the CCL at CCL-GDL interface and goes to zero at CCL-membrane interface as membrane is impermeable for oxygen. The intrinsic reaction rate of ORR strongly depends on cathodic overpotential ($\eta_{o,CCL}$) and is captured accurately by the empirical Tafel equation.

At steady state, the governing equations are:

$$\frac{dj}{dy} = -i_{o,c}A\left[\exp\left(\frac{\eta}{A_c}\right)\right] \times \frac{C}{C_{in}} \tag{2.1}$$

$$\sigma\frac{d\eta}{dy} = -j \tag{2.2}$$

$$D_{CCL}\frac{dC}{dy} = \frac{J-j}{4F} \tag{2.3}$$

Here, $y$ is the dimension along CCL thickness with $y = 0$ being the CCL-membrane boundary and $y = l_t$ being the CCL-GDL boundary; $j$ is the proton flux, $\eta$ is the overpotential across CCL, $C$ and $C_{in}$ are respectively the oxygen concentrations (mol/m$^3$) at any point $y$ along the thickness of the CCL and at inlet of a PEMFC, $i_{o,c}A$ is the volumetric exchange current density (A/m$^3$), $A_c$ is the Tafel slope, $\sigma$ is the proton conductivity of CCL, $D_{CCL}$ is oxygen diffusion coefficient in the CCL, $F$ is Faraday's constant and $J$ is the proton flux at CCL-membrane interface.

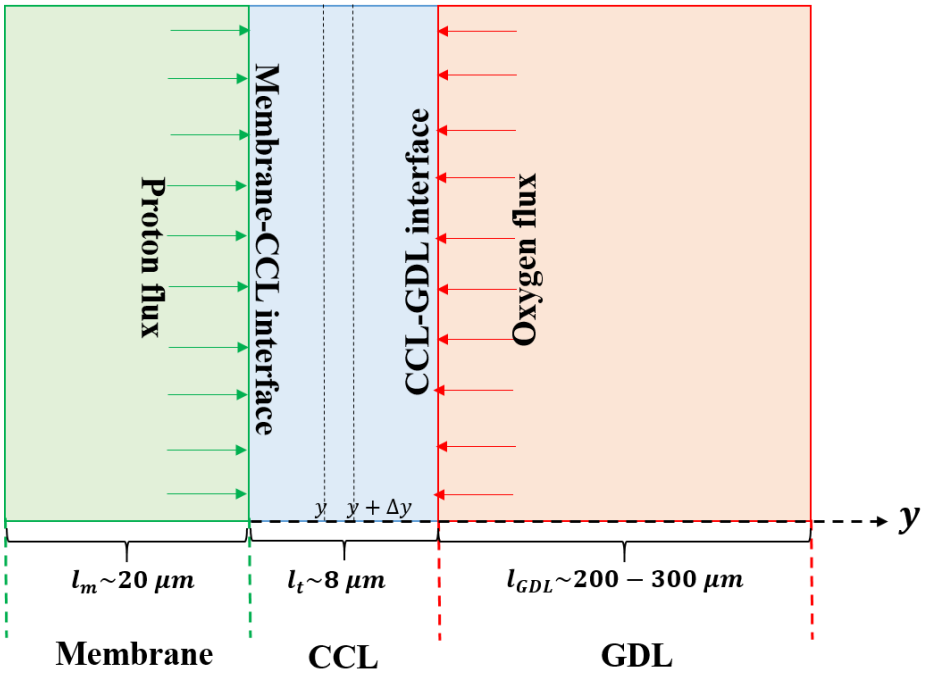


**Fig. 2.1** Macro-homogeneous (MH) model of the cathode catalyst layer

Equation (2.1) denotes the macroscopic charge conservation in the CCL and the right hand side of the equation (2.1) is the consumption rate of the protons and oxygen as described by Tafel kinetics. The proton flux $j$ in equation (2.1) is related to the gradient of overpotential $\eta$ by Ohm's law as described by equation (2.2). Equation (2.3) describes the oxygen conservation law where left hand side of equation (2.3) is concentration gradient driven 'Fickian' diffusion and right hand side of equation is the consumption rate of oxygen.

The boundary conditions are:

$$j = J,\ \eta = \eta_{o,CCL}, \frac{dC}{dz} = 0\ at\ y = 0\ and\ C = C_{CCL-GDL}, j = 0\ at\ y = l_t \tag{2.4}$$

Here, $C_{CCL-GDL}$ is the oxygen concentration at CCL-GDL interface and $\eta_{o,CCL}$ is the resulting cathodic overpotential to sustain the proton flux at CCL-membrane interface, $J$. The equation set (2.1)-(2.4) defines the MH model of the CCL and can be solved either numerically or analytically to get the profiles of '$j$', '$\eta$' and '$C$'. Note that setting $y = 0$ in the expressions of $j$ and $\eta$ gives the current-potential relationship of the PEMFC.

The numerical solution was obtained by [35-36], who showed doubling of the apparent Tafel slope in the cases when the intrinsic ORR kinetics happens to be slower than oxygen transport rate across the CCL or proton transport rate across the CCL. The doubling of Tafel slope is shown experimentally as well [37-40]. As the experimental manifestation of doubling of Tafel slope turns out to be the same for poor transport rates of both reacting species, protons and oxygen, therefore, it is important to understand the physical laws which can distinguish between these two possible regimes. This problem was solved by Kulikovsky [41-42] by deriving analytical solutions to the governing equations of MH model in limiting cases. We now discuss these limiting regimes briefly.

- *Ideal oxygen transport as well as ideal proton transport in the CCL*

It was shown that, in the very low current density regime when $J < \frac{4FD_{CCL}C_{CCL-GDL}}{l_t}$ $and$ $\frac{2\sigma A_c}{l_t}$, intrinsic ORR kinetics as described by 'Tafel kinetics' is slower than oxygen transport across the CCL as well as proton transport across the CCL [42]. Therefore, oxygen concentration and overpotential remains uniform in the CCL i.e. oxygen and protons are available everywhere in the CCL for the reaction. $J - \eta_{o,CCL} - C_{CCL-GDL}$ relation in this particular regime is therefore solely dictated by intrinsic Tafel kinetics of ORR. Hence,

$$J = i_{o,c}Al_t\left[\exp\left(\frac{\eta_{o,CCL}}{A_c}\right)\right]\frac{C_{CCL-GDL}}{C_{in}} \tag{2.5a}$$

or equivalently,

$$\eta_{o,CCL} = A_c ln\left\{\frac{J}{i_{o,c}Al_t(\frac{C_{CCL-GDL}}{C_{in}})}\right\} \tag{2.5b}$$

The $j, \eta$ $and$ $C$ profiles in this particular regime are shown pictorially in figure 2.2.

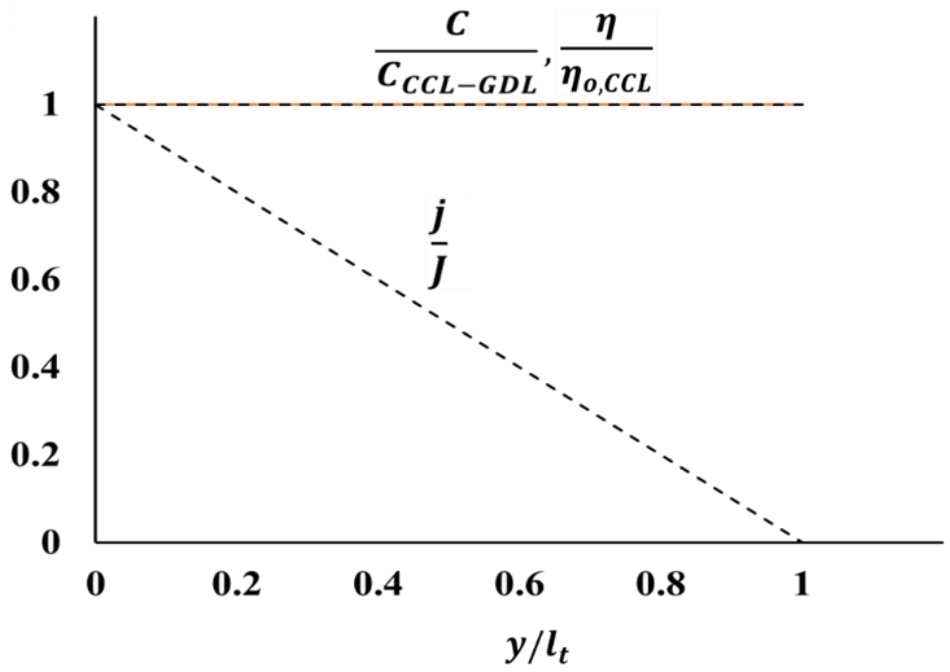


**Fig. 2.2** Profiles of proton flux, overpotential and oxygen concentration along the thickness of the CCL in the regime of ideal oxygen transport as well as ideal proton transport in the CCL

- *Ideal proton transport in the CCL*

At higher current density it is possible that although protons are available in the CCL everywhere i.e., overpotential is uniform everywhere in the CCL, oxygen flux may not be large enough to support the ORR as demanded by intrinsic Tafel kinetics. In this scenario, increasing amount of concentration polarization of oxygen happens in the CCL near the CCL-GDL interface, and the oxygen consumption rate decreases sharply away from the interface. Equations (2.1) and (2.3) can be solved together with an assumption of uniform '$\eta$' in the CCL. [42] showed that the profiles of oxygen concentration and proton flux in this limiting regime are given as,

$$C = \frac{JC_{in}}{\sqrt{\frac{4FD_{CCL}C_{in}}{l_t} i_{o,c} A l_t \left[\exp\left(\frac{\eta_{o,CCL}}{A_c}\right)\right]}} \frac{\cosh(\zeta_o \frac{y}{l_t})}{\sinh(\zeta_o)} \tag{2.6}$$

$$j = J\left(1 - \frac{\sinh(\zeta_o \frac{y}{l_t})}{\sinh(\zeta_o)}\right) \tag{2.7}$$

Here, $\zeta_o = \sqrt{\frac{i_{o,c}Al_t\left[\exp\left(\frac{\eta_{o,CCL}}{A_c}\right)\right]}{\frac{4FD_{CCL}C_{in}}{l_t}}}$.

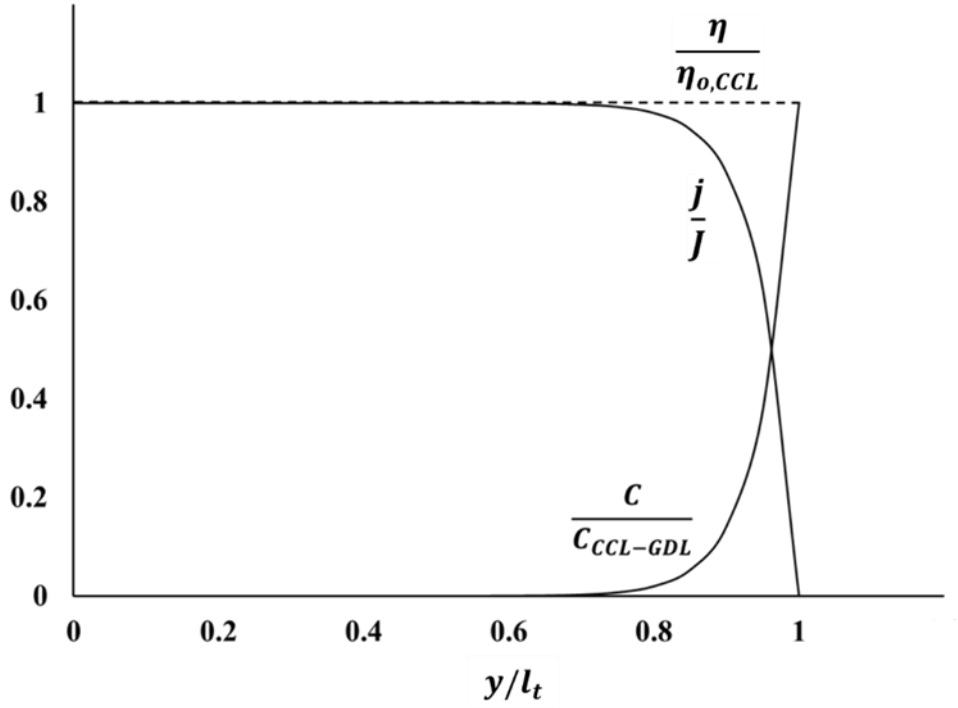


**Fig. 2.3** Profiles of proton flux, overpotential and oxygen concentration along the thickness of the CCL in the regime of ideal proton transport but poor oxygen transport in the CCL ($J > \frac{4FD_{CCL}C_{in}}{l_t}$)

These profiles are illustrated schematically in figure 2.3. Substituting $C = C_{CCL-GDL}\ at\ y = l_t$ in equation (2.6) we get the current-potential relationship in this particular regime as,

$$J = \frac{4FD_{CCL}C_{in}}{l_t} \times \sqrt{\frac{i_{o,c}Al_t\left[\exp\left(\frac{\eta_{o,CCL}}{A_c}\right)\right]}{\frac{4FD_{CCL}C_{in}}{l_t}}}\ \tanh\left\{\sqrt{\frac{i_{o,c}Al_t\left[\exp\left(\frac{\eta_{o,CCL}}{A_c}\right)\right]}{\frac{4FD_{CCL}C_{in}}{l_t}}}\right\}\frac{C_{CCL-GDL}}{C_{in}} \qquad (2.8)$$

It can be noticed that when $i_{o,c}Al_t\left[\exp\left(\frac{\eta_{o,CCL}}{A_c}\right)\right] < \frac{4FD_{CCL}C_{in}}{l_t}$, $\tanh\left\{\sqrt{\frac{i_{o,c}Al_t\left[\exp\left(\frac{\eta_{o,CCL}}{A_c}\right)\right]}{\frac{4FD_{CCL}C_{in}}{l_t}}}\right\} \approx \sqrt{\frac{i_{o,c}Al_t\left[\exp\left(\frac{\eta_{o,CCL}}{A_c}\right)\right]}{\frac{4FD_{CCL}C_{in}}{l_t}}}$ and therefore, equation (2.8) becomes $J \approx i_{o,c}Al_t\left[\exp\left(\frac{\eta_{o,CCL}}{A_c}\right)\right]\frac{C_{CCL-GDL}}{C_{in}}$

which is exactly same as equation (2.5) or intrinsic Tafel kinetics of ORR. However, for $i_{o,c}Al_t\left[\exp\left(\frac{\eta_{o,CCL}}{A_c}\right)\right] \gg \frac{4FD_{CCL}C_{in}}{l_t}$, $\tanh\left\{\sqrt{\frac{i_{o,c}Al_t\left[\exp\left(\frac{\eta_{o,CCL}}{A_c}\right)\right]}{\frac{4FD_{CCL}C_{in}}{l_t}}}\right\} \approx 1$ and therefore, equation (2.8) takes the form,

$$J = \sqrt{\frac{4FD_{CCL}C_{in}}{l_t} i_{o,c}Al_t\left[\exp\left(\frac{\eta_{o,CCL}}{A_c}\right)\right]}\frac{C_{CCL-GDL}}{C_{in}} \tag{2.9a}$$

or equivalently,

$$\eta_{o,CCL} = A_c ln\left\{\frac{J}{i_{o,c}Al_t\left(\frac{C_{CCL-GDL}}{C_{in}}\right)}\right\} + A_c ln\left\{\frac{J}{\frac{4FD_{CCL}C_{in}}{l_t}\left(\frac{C_{CCL-GDL}}{C_{in}}\right)}\right\} \tag{2.9b}$$

The apparent doubling of Tafel slope due to high oxygen transport resistance is evident from equation (2.9) and the critical current density ($J_{crit,(O2)transport}$) above which oxygen transport resistance starts modulating the Tafel kinetics is the point of intersection of the curves given by equations (2.5) and (2.9). It is straightforward to show that,

$$J_{crit,(O2)transport} = \frac{4FD_{CCL}C_{CCL-GDL}}{l_t} \tag{2.10}$$

Therefore, for $J > \frac{4FD_{CCL}C_{CCL-GDL}}{l_t}$, intrinsic ORR kinetics gets modulated by oxygen transport resistance in the CCL and equation (2.9) gives the current-potential relationship whereas for $J < \frac{4FD_{CCL}C_{CCL-GDL}}{l_t}$, intrinsic ORR kinetics i.e. equation (2.5) gives the current-potential relationship.

As a final comment, we would like to point out here that the aforementioned formulation is valid only when '$\eta$' is uniform everywhere in the CCL which essentially implies that the proton transport resistance in the CCL is *infinitesimally* small. This, in fact may not be realistic as proton conductivity in the CCL ($\sigma$) is not infinitely large. Thus, the repercussion of *finite* proton

transport resistance for a case of $J > \frac{4FD_{CCL}C_{CCL-GDL}}{l_t}$ on current-potential relationship is not understood in the literature so far. As will be discussed in the next sub-section, the assumption of uniform overpotential is only valid for $J \ll \frac{2\sigma A_c}{l_t}$. Substituting $\sigma = 2\frac{S}{m}$ [43-45], $A_c = 0.026\ V$ and $l_t = 8\ \mu m$, we get $\frac{2\sigma A_c}{l_t} = 1.3\frac{A}{cm^2}$ and therefore, the aforementioned formulation is inappropriate for $J > 0.2\ \frac{A}{cm^2}$.

- *Ideal oxygen transport in the CCL*

If oxygen concentration is uniform everywhere in the CCL, the ORR kinetics may get modulated depending on whether the rate of proton transport in the CCL is greater or smaller than the intrinsic ORR kinetics. This regime deals with such a situation. For a case when proton transport rate is slower than intrinsic Tafel kinetics of ORR, the reaction rate is the highest at the CCL-membrane interface and it decreases rapidly away from the interface. Equations (2.1) and (2.2) are solved with '$C$' independent of '$y$' and the profiles of current density and overpotential turn out to be [41,42],

$$\frac{j}{\frac{\sigma A_c}{l_t}} = \zeta \tan\left\{\frac{\zeta}{2}(1 - y^*)\right\} \tag{2.11}$$

$$\frac{\eta}{A_c} = \ln\left[\frac{\zeta^2}{2}\frac{C_{in}}{C_{CCL-GDL}}\frac{\sigma A_c/l_t}{i_{o,c}Al_t}\left\{1 + \left(\tan\left(\frac{\zeta}{2}(1 - y^*)\right)\right)^2\right\}\right] \tag{2.12}$$

The schematic representation of these profiles is shown in figure 2.4 for the case when proton transport rate is slower than intrinsic Tafel kinetics.

For $y = 0$ and $J < \frac{\sigma A_c}{l_t}$, equation (2.11) suggests that $J \approx \frac{\sigma A_c}{l_t}\frac{\zeta^2}{2}$ and substituting in equation (2.12), we get current-potential relationship as $J \approx i_{o,c}Al_t\left[\exp\left(\frac{\eta_{o,CCL}}{A_c}\right)\right]\frac{C_{CCL-GDL}}{C_{in}}$, which is in

fact the intrinsic Tafel kinetics as suggested by equation (2.5). For $y = 0$ and $J \gg \frac{\sigma A_c}{l_t}$, $\tan(\frac{\zeta}{2}) > > 1$ and therefore equation (2.12) takes the form,

$$J = \sqrt{\frac{2\sigma A_c}{l_t} i_{o,c} A l_t \left[\exp\left(\frac{\eta_{o,CCL}}{A_c}\right)\right] \frac{C_{CCL-GDL}}{C_{in}}} \tag{2.13a}$$

or equivalently,

$$\eta_{o,CCL} = A_c \ln\left\{\frac{J}{i_{o,c} A l_t (\frac{C_{CCL-GDL}}{C_{in}})}\right\} + A_c ln\left\{\frac{J}{\frac{2\sigma A_c}{l_t}}\right\} \tag{2.13b}$$

Equation (2.13) suggests an apparent doubling of Tafel slope when proton transport across the CCL is significantly limited, and the critical current density ($J_{crit,(H+)transport}$) above which this happens is the point of intersection of curves given by equations (2.5) and (2.13). It is straightforward to show that,

$$J_{crit,(H+)transport} = \frac{2\sigma A_c}{l_t} \tag{2.14}$$

Thus, proton transport resistance is not significant for $J < \frac{2\sigma A_c}{l_t}$ and current-potential relationship is governed by intrinsic ORR rate and given by equation (2.5) whereas it becomes significant for $J > \frac{2\sigma A_c}{l_t}$ and the intrinsic ORR rate gets modulated by proton transport resistance in the CCL. Equation (2.13) gives the corresponding current-potential relationship in this particular regime of operation.

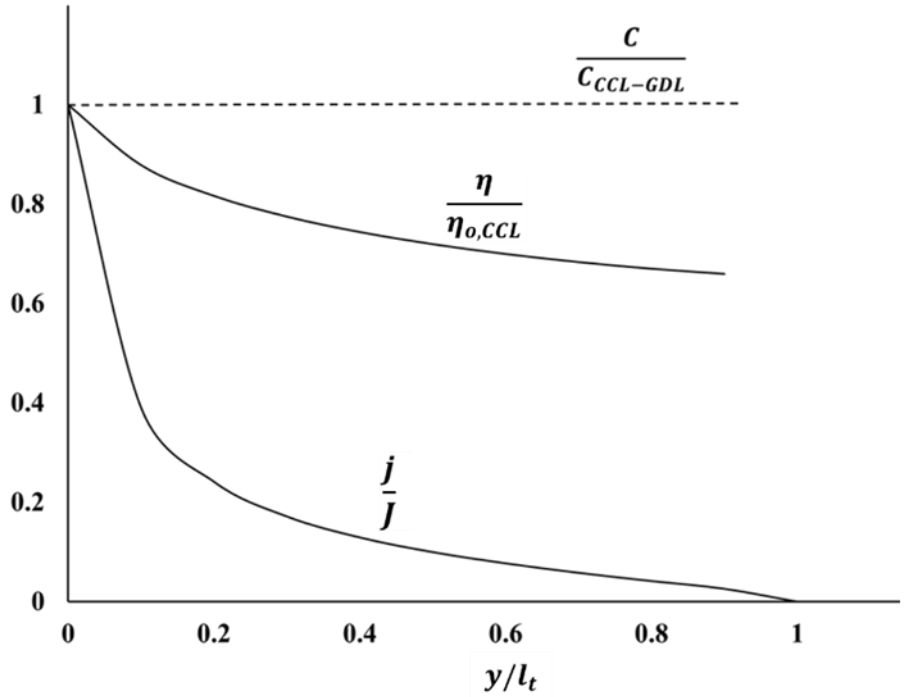


**Fig. 2.4** Profiles of proton flux, overpotential and oxygen concentration along the thickness of the CCL in the regime of ideal oxygen transport but poor proton transport in the CCL ($J > \frac{2\sigma A_c}{l_t}$)

It must be noted here that oxygen concentration is assumed to be uniform in this particular regime which suggests unrealistically high numerical value of oxygen diffusion coefficient in the CCL. Therefore, the impact of finite oxygen transport resistance with a realistic value of oxygen diffusion coefficient in the CCL on the current-potential relationship for the regime of $J > \frac{2\sigma A_c}{l_t}$ is not discussed in the literature so far. As will be discussed in the next sub-section, the assumption of uniform overpotential is only valid for $J \ll \frac{4FD_{CCL}C_{CCL-GDL}}{l_t}$. Substituting $D_{CCL} = 10^{-7}\frac{m^2}{s}$ (assuming oxygen diffusion in voids [46-47]), $C_{CCL-GDL} = 8\ \frac{mol}{m^3}$ and $l_t = 8\ \mu m$, we get $\frac{4FD_{CCL}C_{CCL-GDL}}{l_t} = 3.8\frac{A}{cm^2}$ and therefore, the aforementioned formulation is inappropriate for $J > 0.4\ \frac{A}{cm^2}$.

In summary, we would like to reiterate that the three limiting regimes of ideal oxygen transport as well as ideal proton transport in the CCL, ideal proton transport but poor oxygen

transport in the CCL and ideal oxygen transport but poor proton transport in the CCL have been understood thoroughly in the literature. However, more realistic regimes wherein both oxygen transport and proton transport in the CCL are simultaneously rate limiting are not discussed so far in the literature. The consequence is that there is no analytical solution of polarization curve available for the realistic operational current density range, $J > 0.2 - 0.4\ \frac{A}{cm^2}$ ($J > \frac{2\sigma A_c}{l_t}$ or $J > \frac{4FD_{CCL}C_{CCL-GDL}}{l_t}$).

### 2.1.2) Flooded agglomerate (FA) model of the CCL

The MH model of the CCL as discussed in the previous sub-section glosses over the microstructural details of the CCL and instead describes it using volume average transport properties. However, at any location $y$ along the CCL thickness the catalyst has a microstructure, which is depicted in Figure 2.5 along the lines of the so-called flooded agglomerate (FA) model [48-53]. Locally, the CCL microstructure comprises spherical agglomerates of size $R_{agg}$ that are flooded with electrolyte in which supported catalyst particles are suspended. The electrolyte is typically similar to the ionomer that is used as the proton conducting membrane. It was shown that the diffusional resistance of oxygen in such agglomerates does become important at high current density [55]. This is mainly because the assumption of negligible transport gradients at the microstructure level as invoked in the MH model does not hold true at high current density and the overall consumption rate in fact gets modulated by transport resistances at the microstructure level as well.

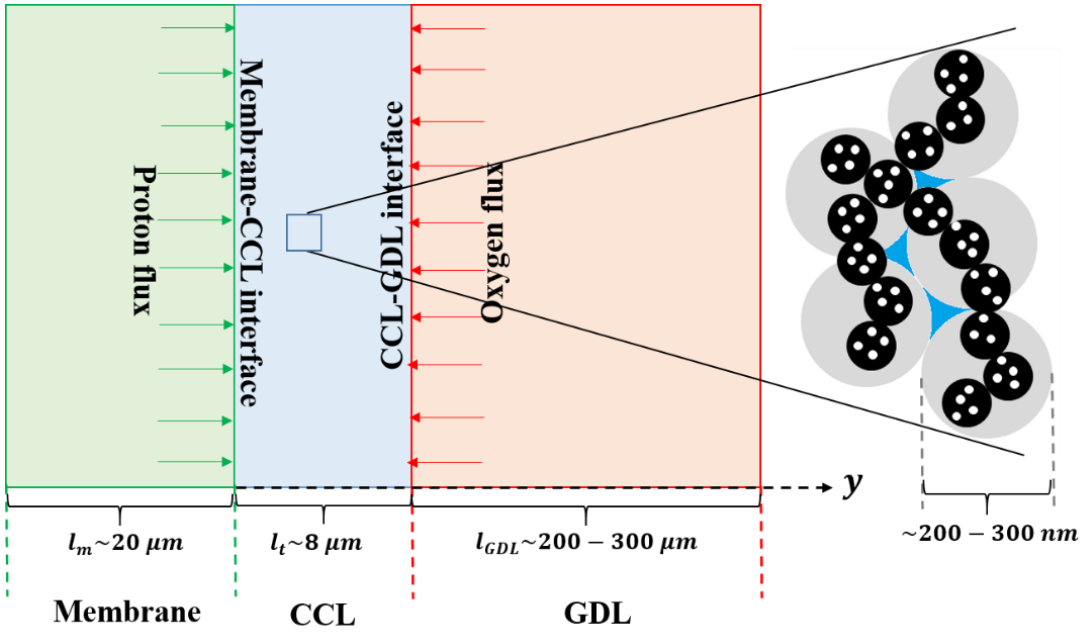


**Fig. 2.5** Microstructure of cathode catalyst layer as idealized in the agglomerate modelling approach. Grey circles indicate ionomer-filled spherical agglomerates. Black circles with white dots indicate respectively carbon support particles decorated with nano-catalyst particles. Interstitial voids between agglomerates can be filled with liquid water denoted in blue.

The proton flux balance along the thickness of the CCL in a FA corrected MH model can be written as [56],

$$\frac{dj}{dy} = -i_{o,c}A\left[\exp\left(\frac{\eta}{A_c}\right)\right] \times E(\eta) \times \frac{C}{C_{in}} \tag{2.15}$$

$E(\eta)$ is the effectiveness factor and is given by,

$$E = \frac{1}{M_T}\left(\frac{1}{\tanh(3M_T)} - \frac{1}{3M_T}\right) \tag{2.16}$$

$$\text{Where, } M_T = \frac{R_{agg}}{3}\sqrt{\frac{i_{o,c}\left[\exp\left(\frac{\eta}{A_c}\right)\right]a}{4FD_{agg}C_{in}}} \tag{2.17}$$

The Thiele modulus $M_T$ compares the intrinsic reaction rate to the diffusion rate of oxygen along the radius of the agglomerate. $D_{agg}$ is the effective diffusion coefficient of oxygen in an agglomerate, $a$ is electrochemical active area of agglomerate per unit volume of the agglomerate. The overpotential gradient inside an agglomerate is neglected since the size of

agglomerate is typically 1-2 orders of magnitude smaller than the CCL thickness and the proton conductivity along the thickness of the CCL and inside the agglomerate is not much different (as the medium for proton conduction is the same i.e. ionomer). However, for oxygen transport, the effective oxygen diffusion coefficient inside the agglomerate ($O_2$ diffusion in ionomer) is order of magnitude lower than effective oxygen diffusion coefficient along the CCL thickness ($O_2$ diffusion in voids filled with water). Therefore, it is realistic to have oxygen concentration gradient inside the agglomerate while overpotential gradient inside the agglomerate is unlikely. It is to be noted that the Henri's constant of dissolution of oxygen in the ionomer is incorporated in the value of the exchange current density. The other two governing equations are identical to that of MH model i.e. Ohm's law for proton migration (2.2) and Fick's law for oxygen transport (2.3) along the thickness of the CCL.

Numerical solutions of governing equations for a FA model of CCL have been presented by several authors [56-62]. An approximate analytical solution for the MH model which incorporates FA description has been recently proposed [55] and showed that the oxygen transport resistance in the electrolyte phase i.e. in the agglomerates becomes increasingly dominant only at higher current densities. Therefore, it is crucial to couple MH model with FA model in the high current density regime. It should be particularly noted that in this regime neither oxygen transport resistance nor proton transport resistance across the CCL can be neglected. There is however no analytical model that rationally accounts for the regime of simultaneous oxygen transport as well as proton transport limited ORR kinetics along with a correction due to non-negligible oxygen transport resistance in the agglomerate.

### 2.1.3) Two dimensional model formulation

The assumption of uniform oxygen concentration over the entire active area at the CCL-GDL boundary as invoked in the earlier one-dimensional models is not realistic under operating

conditions of PEMFC. For typical air stoichiometry between 2 and 4, oxygen depletes along the length of the cathode channel due to consumption in CCL. Thus, a more realistic model should invoke a two-dimensional problem defined by convection of gas along the axis of the flow channel and simultaneous diffusion through GDL in the transverse direction together with consumption in the CCL. Kulikovsky [63-64] derived an analytical solution to this two-dimensional model and derived expression for polarization curve for the case when ORR kinetics is the rate determining step. In a subsequent paper, Kulikovsky [65] also derived analytical expressions of polarization curves for the regimes corresponding to slow proton transport and slow oxygen transport in the CCL.

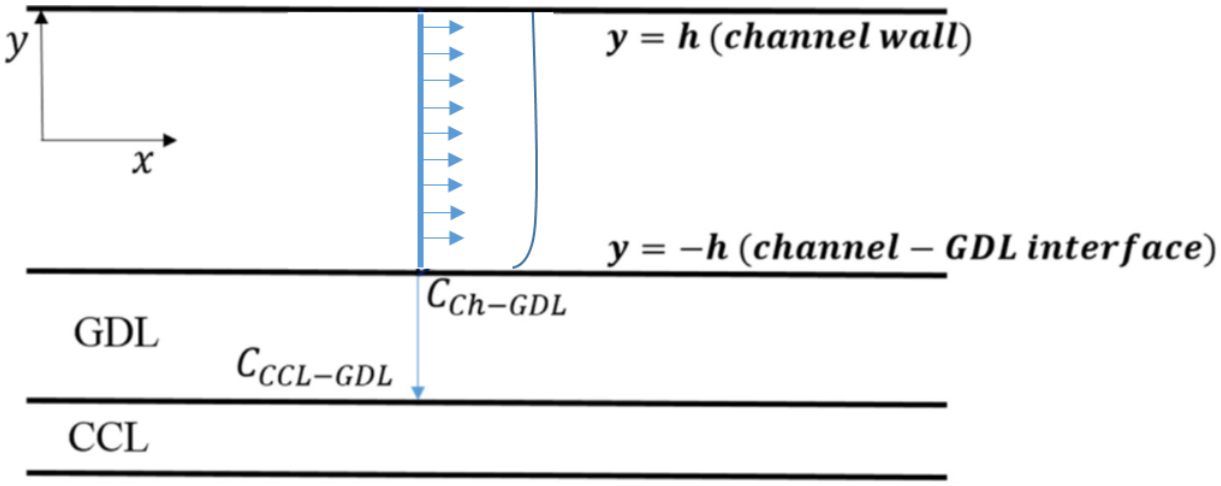


**Fig. 2.6** Two-dimensional domain of a PEMFC with uniform oxygen concentration and velocity in the transverse direction $(-y)$

Figure 2.6 depicts the model geometry as idealized by [63] comprising a channel of length $L$ and depth $2h$ in which reactant gas flows along the axial $(x-)$ direction and has no momentum gradient along the channel depth. The channel wall is located at $y = h$ and the channel-GDL interface at $y = -h$. Oxygen consumption at the channel-GDL interface due to ORR in the CCL sets an oxygen concentration gradient along $x$. The steady state oxygen balance in the channel can be written as,

$$U(2h)\frac{dC}{dx} = -\frac{J}{4F} \tag{2.17}$$

Here, $C$ is the local oxygen concentration in the channel and $U$ is the inlet velocity. $J$ is the local current density at point along '$x$'. For the case of negligible transport losses of reactant species in a macro-homogeneous CCL, $J - \eta_{o,CCL} - C_{CCL-GDL}$ relationship is given by Tafel kinetics i.e. equation (2.5). The relation between $C_{CCL-GDL}$ and oxygen concentration at channel-GDL interface ($C_{Ch-GDL}$) can be obtained by writing oxygen conservation equation across GDL as,

$$\frac{4FD_{GDL}}{l_{GDL}}(C_{Ch-GDL} - C_{CCL-GDL}) = i_{o,c}Al_t\left[\exp\left(\frac{\eta_{o,CCL}}{A_c}\right)\right]\frac{C_{CCL-GDL}}{C_{in}} \quad (2.18)$$

Here, $D_{GDL}$ is the oxygen diffusion coefficient in GDL and $l_{GDL}$ is the GDL thickness. Defining $J_{1-D} = i_{o,c}Al_t\left[\exp\left(\frac{\eta_{o,CCL}}{A_c}\right)\right]$, $J_{GDL} = \frac{4FD_{GDL}C_{in}}{l_{GDL}}$ , $\alpha = \frac{J_{1-D}}{J_{GDL}}$ and combining equations (2.5) and (2.18), we get

$$J = \frac{J_{1-D}}{1+\alpha}\frac{C_{Ch-GDL}}{C_{in}} \quad (2.19)$$

Substituting equation (2.19) in equation (2.17) for $J$ and solving it with boundary condition $C = C_{in}\ at\ x = 0$, we get,

$$C(x) = C_{in}\exp(-\frac{\beta\frac{x}{L}}{1+\alpha}) \quad (2.20)$$

Here, $\beta = \frac{J_{1-D}}{J_{flow}}$ and $J_{flow} = \frac{4FU(2h)C_{in}}{L}$.

This describes the oxygen concentration profile along the axis of the flow channel. Equations (2.17) and (2.20) further gives the current density profile along '$x$' as,

$$J = \frac{J_{1-D}}{1+\alpha}\exp(-\frac{\beta\frac{x}{L}}{1+\alpha}) \quad (2.21)$$

Equation (2.21) is integrated over the channel length to yield current-potential relationship (polarization curve) for the entire active area:-

$$J_{total} = J_{flow}\left\{1 - \exp(-\frac{\beta}{1+\alpha})\right\} \quad (2.22)$$

Equation (2.22) gives a current-potential relationship by considering intrinsic Tafel kinetics to be the consumption rate in the CCL and oxygen transport resistance across the GDL coupled with material balance equation along flow channel.

However, it was assumed that flow in the channel was plug flow and oxygen concentration was allowed to vary only along the channel length but not along the channel depth. Under typical operating conditions of PEMFC, the flow in channels is laminar and therefore the assumption of plug flow is not realistic. Furthermore, as will be seen later, the resistances to oxygen diffusion in the GDL and in the channel are of the same order for a typical fuel cell construction. Hence, the assumption of uniform oxygen concentration along the channel depth is also not realistic. In particular, this assumption can lead to considerable deviations at high current density as will be shown later. Thus, it establishes a need to invoke a more realistic two-dimensional analytical model that relaxes these two key assumptions and to derive current-potential relationship under these conditions. Moreover, the new model should also take into consideration the other regimes of CCL operation in which overall oxygen consumption rate in the CCL is modulated by transport resistances in the CCL.

### 2.1.4) Experimental validation of the analytical model

In order to validate the analytical model with experimental data, it is necessary to first quantify oxygen diffusivities in the different domains of PEMFC namely, flow channel, GDL and CCL. In most of the earlier studies, the so-called limiting current method has been used to estimate oxygen transport resistance in these domains [66-70]. However, there are two limitations of this method:

1. The method assumes that the oxygen concentration is linear in all domains. While this is true in the GDL, the assumption does not hold in the CCL. A rapid non-linear decay of oxygen

concentration in the CCL near the GDL-CCL interface is predicted when the rate of oxygen transport across the CCL is considerably slower compared to intrinsic ORR kinetics (discussed in previous section, 2.2). The experimental manifestation of this rapid decay is that the local slope of polarization curve (i.e., the local apparent Tafel slope) depends strongly on overpotential and eventually leads to apparent doubling of Tafel slope. Therefore, correlating oxygen transport resistance in the CCL to the limiting current density, which is independent of overpotential, is not appropriate.

2. The influence of transverse oxygen diffusion along the channel depth is assumed to be negligible in these studies, which may not be realistic. To determine the effective oxygen diffusion coefficient in GDL, it is imperative to segregate the contribution of oxygen diffusion along the channel depth from the limiting current density.

Therefore, there are at least two issues that must be addressed in the previous studies as far as experimental determination of oxygen diffusivities in the various domains of PEMFC is concerned.

## 2.2) A brief account on three-dimensional numerical simulation of PEMFC

Three-dimensional numerical simulations of PEMFC solve the fundamental conservation equations for mass, momentum, species and charge without invoking any simplification. Some of the earlier work in this area are by [71-80], while a comprehensive review of prior work in this area can be found in [81-85]. While there are numerous studies involving different types of flow fields (refer review papers [86-88]), we focus here on a representative flow field namely, a geometry comprised of a channel and a rib. Such a domain for numerical simulation is shown in figure 2.7. It includes a single flow channel each for $H_2$ and air, GDLs and catalyst layers on the anode and cathode sides, and a central proton exchange membrane. Commercial

simulation packages are available to predict the polarization curve of PEMFC for a given set of input parameters [89].

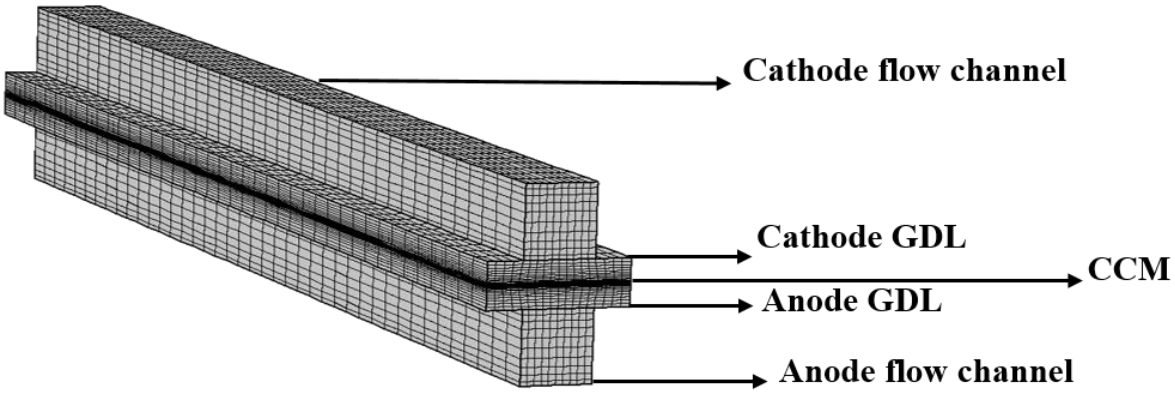


**Fig. 2.7** Three-dimensional computational domain considered for simulation

The key governing equations are:-

- *Conservation of mass*

$$\nabla.(\rho u) = Q \tag{2.23}$$

Where, Q is the source term (kg/m$^3$-s).

$$Q = \sum R_i \tag{2.24}$$

$$R_i = \frac{v_i M_i S}{nF} \tag{2.25}$$

$$S = i_{o,c} A \left[\exp\left(\frac{\eta}{A_c}\right)\right] \frac{C_{CCL}}{C_{in}} E(\eta) \tag{2.26}$$

Here, $v_i$ is stoichiometric coefficient of i$^{th}$ species (2 for $H_2$ and 1 for $O_2$ and 2 for $H_2O$), $n$ is the number of electrons transferred ($n = 4$), $C_{CCL}$ is local oxygen concentration in the CCL and $E(\eta)$ is given by equation (2.16). It must be noted that $Q = 0$ for GDL and flow channels.

- *Conservation of momentum*

For gas flow in the channel, the momentum balance is given by

$$\rho[(u.\nabla)u] = \nabla.\left[-pI + \mu\{(\nabla u) + (\nabla u)^T\} - \frac{2\mu}{3}\{(\nabla.u)I\}\right] \quad (2.27)$$

For porous medium (GDL and catalyst layer),

$$\rho\left[\left(\frac{u}{\varepsilon}.\nabla\right)\frac{u}{\varepsilon}\right] = \nabla.\left[-pI + \frac{\mu}{\varepsilon}\{(\nabla u) + (\nabla u)^T\} - \frac{2\mu}{3}\{(\nabla.u)I\}\right] - \left(\frac{\mu}{k_{br}} + \frac{Q}{\varepsilon^2}\right)u \quad (2.28)$$

where, $u$ is the velocity (m/s), $\rho$ is the density (kg/m$^3$), $p$ is pressure (N/m$^2$), μ is the viscosity (Pa-s) and $I$ is a unit tensor. The $\frac{\mu u}{k_{br}}$ term in the above equation is Darcy's law for flow through porous medium.

- *Conservation of species*

Conservation of species over entire computation domain can be expressed in terms of mass fractions for i$^{th}$ species as follows:-

$$\nabla.j_i + \rho(u.\nabla)w_i = R_i \quad (2.29)$$

where, the flux $j_i$ is given as,

$$j_i = -\left(\rho D_i \nabla w_i + \rho D_i w_i \frac{\nabla_i M_n}{M_n} +\right) \quad (2.30)$$

$$M_n = (\sum_i \frac{w_i}{M_i})^{-1} \quad (2.31)$$

Here $w_i$ is the mass fraction of i$^{th}$ species and $D_i$ is a diffusion coefficient. There is no reaction source term in GDL and thus, $R_i = 0$ for GDL. For catalyst layer, $R_i$is given as equation (2.25).

- *Conservation of charge*

$$\nabla.(-\sigma_s \nabla.\Phi_s) = S_s \quad (2.32)$$

$$\nabla.(-\sigma_m \nabla.\Phi_m) = S_m \quad (2.33)$$

$$\eta = E_{eq} + \Phi_m - \Phi_s \tag{2.34}$$

Here, $m$ is electrolyte phase and $s$ is a solid phase and $-S_s = S_m = S$. $S$ is given by equation (2.26). $E_{eq}$ is equilibrium voltage or open circuit voltage, typically, $E_{eq} \sim 0.92\,V$ . Anode source term is modelled as a linearized Butler-Volmer equation and $(i_o A)$ for anode is $10^7$ times higher than $(i_{o,c} A)$.

These governing equations are solved with following constraints:

- Inlet mass fractions of all species are specified.
- Anode side and cathode side inlet velocities are specified.
- Anode collector is set at 0 V and cathode collector is set at an operating voltage 'V'. Polarization curve is obtained by varying voltage 'V' from ~0.9 V to ~0.3 V.
- All the impermeable walls and surfaces are set to follow no slip and no flux conditions.

In the present thesis, three-dimensional numerical simulations are used to verify the different approximations invoked while deriving comprehensive analytical model of PEMFC. We have used the in-built fuel cell module in COMSOL Multiphysics version 5.3 (a finite element solver) to perform numerical simulations.

### 2.3) Summary of open questions in the literature

As summarized above, substantial efforts have been made in the recent past to derive algebraic relations between all the physicochemical processes involved in an operational PEMFC to its performance. However, there are following important unanswered issues in the work reported so far:-

a) Generalized solution to MH model of the CCL that encompasses all the possible regimes of CCL operation is missing in the literature. In particular, the regimes of

simultaneous oxygen transport and proton transport limited ORR kinetics in the CCL have not been understood.

b) A correction to the generalized solution of MH model invoking the microstructural details of the CCL through FA model can provide a comprehensive current-potential relationship that captures *all* the physicochemical processes occurring in the CCL and relates it with power output of the fuel cell. Such a relationship has not been derived.

c) Two-dimensional framework that incorporates laminar flow in the channel and non-uniform oxygen concentration profile in the transverse direction of the channel and all the regimes of CCL operation can rationalize the repercussions of oxygen transport resistance in GDL and channel (transverse direction) and the depletion in the oxygen concentration along the length of the channel on the polarization curve of a PEMFC. There exists no such framework in the literature.

d) Rigorous experimental validation of the analytical model is missing in the literature.

The work presented in this thesis addresses all these lacunae and presents a comprehensive analytical model that predicts polarization behaviour of a PEMFC over the entire range of current density from zero to limiting values. Also, a methodology for rigorously comparing the model predictions against experimental data is presented.

The specific objective of the thesis are as follows:

## 2.4) Objectives of the thesis

- To derive generalized analytical solutions to the MH model of the CCL in the regimes of simultaneous oxygen and proton transport limited ORR kinetics of the CCL.
- To incorporate the microstructural details of the CCL through FA model of the CCL as a correction to MH model in the regime of simultaneous oxygen and proton transport limited ORR kinetics of the CCL.

- To relax the assumptions of plug flow and uniform oxygen concentration along the depth of the flow channel and derive analytical expressions of the polarization curve of the PEMFC by considering all the possible regimes of CCL operation as dictated by MH model.
- To illustrate a methodology to estimate effective oxygen diffusion coefficients in the different domains of the PEMFC.
- To validate the analytical model with experimental data.

## 2.5) Outline of the thesis

This thesis has been divided into following chapters:

Chapter 1 introduces importance of energy sustainability and the role of fuel cell in this regard. We provide a brief account on the construction and working principle of a PEMFC.

Chapter 2 illustrates the efforts made in the literature towards obtaining analytical solution of polarization curve of a PEMFC. Also, a brief summary of numerical work done in the literature to solve the governing equations of PEMFC is presented. This summarizes the foundations of mathematical modelling of the PEMFC. We then explicitly enlist the objectives of the thesis and the outline of the thesis.

Chapter 3 presents a derivation of analytical solutions to the governing equations of MH model of the CCL in the regime of simultaneous oxygen and proton transport limited reaction kinetics. Oxygen transport resistance in the ionomer phase of the CCL is also captured as a correction described by FA model to the MH model.

Chapter 4 develops two-dimensional isothermal model of a cathode flow channel and its analytical solution under reaction-controlled regime of CCL operation relaxing the assumptions of plug flow and uniform oxygen concentration along the channel depth.

Chapter 5 extends the two-dimensional isothermal model of a cathode flow channel developed in chapter 5 in the transport limited regimes of CCL operation namely, ideal proton transport but poor oxygen transport and ideal oxygen transport but poor proton transport.

Chapter 6 derives '*The PEM fuel cell equation*' i.e., the analytical expression for steady state polarization curve which is valid for the entire range of current density, from zero to limiting current.

Chapter 7 summarizes the key scaling laws relating experimentally measurable current density and inlet oxygen concentration that are suggested by the model. We also elucidate in this chapter, a systematic experimental methodology to estimate the effective diffusion coefficients of oxygen in the CCL, GDL and channel which define a parametric space over which polarization curve described by *The PEM fuel cell equation* and experimental polarization curve are compared.

Chapter 8 summarizes the main contribution of the work and elaborates a path forward in the PEMFC research.

# Chapter 3

# Isothermal one-dimensional model for CCL: Derivation of current-potential relationship over wide range of current density

The content of this chapter is published in,
"Chemical Engineering Science, volume no. 206, 12th October 2019, pages: 96–117" [90].

As described in detail in section 2.2 of chapter 2, the relationship between current density ($J$)- cathodic overpotential ($\eta_{o,CCL}$) and- oxygen concentration at CCL-GDL interface ($C_{CCL-GDL}$) have been derived for three limiting cases viz., (a) ideal proton and ideal oxygen transports in CCL (overall ORR determined by intrinsic kinetics), (b) ideal proton transport in the CCL (ORR kinetics modulated by oxygen transport), and (c) ideal oxygen transport in the CCL (ORR kinetics modulated by proton transport). These limiting cases imply infinitely large values of proton conductivity and/or oxygen diffusivity in the CCL. Real CCLs will however have finite values of these transport coefficients. Thus, under realistic operating conditions of PEM fuel cells and at sufficiently high current density, both oxygen and proton transport resistances can *simultaneously* dictate $J - \eta_{o,CCL} - C_{CCL-GDL}$ relation. Also, as mentioned in section 2.3 of chapter 2, oxygen transport resistance inside local catalyst agglomerates in the CCL can become significant at high current density. To the best of our knowledge, literature lacks an analytical expression for $J - \eta_{o,CCL} - C_{CCL-GDL}$ relation in the regime where oxygen and proton transport resistances in the CCL are simultaneously effective and are *coupled* to the oxygen transport resistance inside local catalyst agglomerates. In this chapter we present the

derivation of such a comprehensive relation using one-dimensional model for CCL wherein it is assumed that oxygen concentration and cathodic overpotential vary only along the CCL thickness but are uniform over the active area. We also assume isothermal conditions throughout the CCL volume.

While the FA-corrected-MH model of the CCL is discussed in detail in chapter 2, we reproduce here the key governing equations of the same:

$$\frac{dj}{dy} = -i_{o,c}A\left[\exp\left(\frac{\eta}{A_c}\right)\right] \times E(\eta) \times \frac{C}{C_{in}} \tag{3.1}$$

$$\sigma \frac{d\eta}{dy} = -j \tag{3.2}$$

$$4FD_{CCL}\frac{dC}{dy} = J - j \tag{3.3}$$

Equation (3.1) describes the proton flux balance along the thickness of the CCL, equation (3.2) is Ohm's law relating proton flux in the CCL to the gradient of overpotential across CCL, and equation (3.3) is the oxygen conservation law in the CCL. We again note the different symbols here: $y$ is the dimension along CCL thickness with $y = 0$ being the CCL-membrane boundary and $y = l_t$ being the CCL-GDL boundary; $j$ is the proton flux, $\eta$ is the overpotential across CCL, $C$ and $C_{in}$ are respectively the oxygen concentrations (mol/m$^3$) at any point $y$ along the thickness of the CCL and at inlet of a PEMFC, $i_{o,c}A$ is the volumetric exchange current density (A/m$^3$), $A_c$ is the Tafel slope, $\sigma$ is the proton conductivity of CCL, $D_{CCL}$ is oxygen diffusion coefficient in the CCL, $F$ is Faraday's constant and $J$ is the proton flux at CCL-membrane interface.$E(\eta)$ is the effectiveness factor given by,

$$E = \frac{1}{M_T}\left(\frac{1}{\tanh(3M_T)} - \frac{1}{3M_T}\right) \tag{3.4}$$

where, $M_T = \frac{R_{agg}}{3}\sqrt{\frac{i_{o,c}\left[\exp\left(\frac{\eta}{A_c}\right)\right]a}{3FD_{agg}C_{in}}}$ (3.5)

We first explore two limiting cases which are dictated by comparative rates of intrinsic kinetics and oxygen diffusion in agglomerates. This is followed by the general case.

### 3.1) Limiting case 1: $M_T \ll 1$

This implies that the rate of diffusion of $O_2$ in agglomerates is much faster than intrinsic ORR rate so that $E(\eta) \approx 1$ and consequently, the FA model simplifies to the MH model. Equations (3.1-3.3) can therefore be recast in non-dimensional form as,

$$\varepsilon^2 C_{in}^* \frac{dj^*}{dy^*} = -C^*[\exp(\eta^*)] \tag{3.6}$$

$$\frac{d\eta^*}{dy^*} = -j^* \tag{3.7}$$

$$D^* \frac{dC^*}{dy^*} = J^* - j^* \tag{3.8}$$

The non-dimensional variables are defined as

$$j^* = \frac{j}{\frac{\sigma A_c}{l_t}}, \quad J^* = \frac{J}{\frac{\sigma A_c}{l_t}}, \quad \eta^* = \frac{\eta}{A_c}, \quad \varepsilon^2 = \frac{\sigma A_c}{i_{o,c} A l_t^2}, \quad C^* = \frac{C}{C_{CCL-GDL}}, \quad C_{in}^* = \frac{C_{in}}{C_{CCL-GDL}} \quad \text{and} \quad D^* = \frac{4FD_{CCL}C_{CCL-GDL}}{\sigma A_c} \tag{3.9}$$

The boundary conditions are given by $j^* = 0$ and $C^* = 1$ at $y^* = 1$, and $j^* = J^*$, $\frac{dC^*}{dy^*} = 0$ and $\eta = \eta_{o,CCL}$ at $y^* = 0$, where $\eta_{o,CCL}$ is the resulting overpotential at the CCL-membrane interface required to sustain current density $J$. We also note that the quantity $D^*$ defined in equation (3.9) is the ratio of $J_{crit,(O2)transport}$ and $J_{crit,(H+)transport}$.

The solution to equations (3.6-3.9) describes the current-overpotential relation (polarization curve) of the PEM fuel cell. $\frac{d\eta^*}{dx^*} \to 0$ and $\frac{dC^*}{dx^*} \to 0$ respectively denote the regimes of ideal proton transport across the CCL and ideal oxygen transport across the CCL for which analytical solutions to equation set (3.6-3.8) have been derived in the literature (refer chapter 2). We now

explore generalized solution to (3.6-3.9) when neither $\frac{d\eta^*}{dx^*} \to 0$ nor $\frac{dC^*}{dx^*} \to 0$ holds true. Thus, both oxygen transport resistance and proton transport resistance will be simultaneously significant which results into two possible sub-regimes of operation namely, $J_{crit,(O2)transport} < J_{crit,(H+)transport}$ i.e., $D^* < 1$ and $J_{crit,(O2)transport} > J_{crit,(H+)transport}$ i.e., $D^* > 1$.

- ***The regime of simultaneous oxygen and proton transport limited reaction kinetics in the CCL for the case of*** $\frac{4FD_{CCL}C_{in}}{l_t} \ll \frac{\sigma A_c}{l_t}$***, i.e.*** $D^* \ll 1$

The solution to MH CCL model (equations 3.6-3.9) in the limiting case of 'ideal proton transport' was presented by Kulikovsky (2010) [42]. In this limiting case the overpotential $\eta$ is spatially uniform in the CCL (equivalent to having nearly infinite proton conductivity), and since $\frac{4FD_{CCL}C_{in}}{l_t} < \frac{\sigma A_c}{l_t}$, therefore oxygen concentration decreases rapidly near CCL-GDL interface and goes to zero (refer section 2.1.1 of chapter 2, ideal proton transport in the CCL). This regime is valid only when $J_{total} \ll \frac{\sigma A_c}{l_t}$. In practical situations such as for humidified low temperature PEM fuel cells, $\frac{\sigma A_c}{l_t} \sim 0.65 - 1 \frac{A}{cm^2}$ and therefore the analytical expression derived by Kulikovsky is valid only till $J_{total} \ll 0.65 \frac{A}{cm^2}$. This establishes a need to explore more realistic expression for polarization curve for higher current densities where both oxygen diffusion resistance and proton transport resistance will simultaneously influence the overall ORR rate. In this regime one can expect the oxygen concentration to again decrease rapidly near the CCL-GDL interface but $\eta$ will no longer remain uniform in the CCL. Indeed an overpotential gradient will be required to drive protons from the CCL-membrane interface to the CCL-GDL interface because of finite resistance to proton conduction. It should also be noted that once oxygen concentration reduces to zero in the CCL (say at $y^* = \delta$), the

consumption rate becomes zero and consequently, $j^*$ becomes independent of $y^*$ (equation 7) while $\eta$ decreases linearly along $y^*$ (equation 8). These expected profiles are schematically shown in figure 3.1.

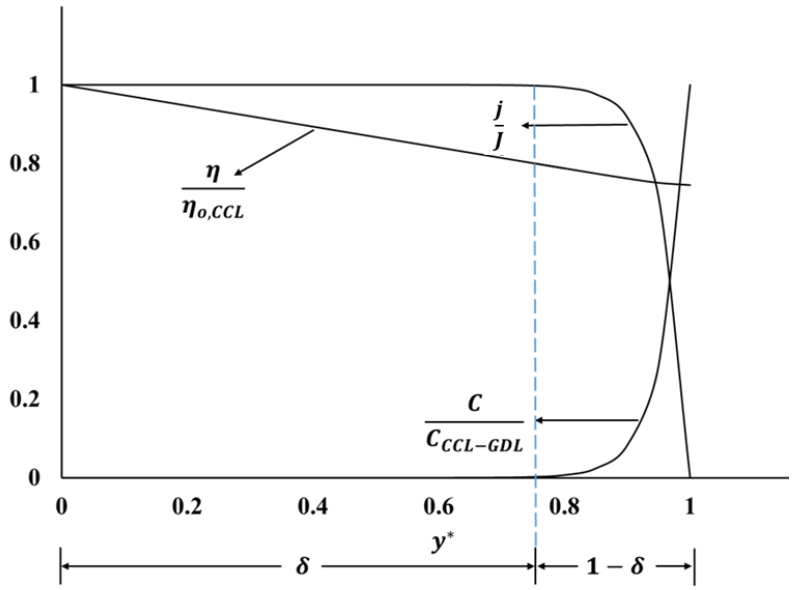


**Fig.3.1** Pictorial representation of profiles of current density, overpotential ($\eta = \eta_{o,CCL}$ at $y^* = 0$) and concentration for $J > \frac{3FD_{CCL}C_{in}}{l_t}$ $and$ $\frac{3FD_{CCL}C_{in}}{l_t} < \frac{\sigma A_c}{l_t}$

Since the boundary condition dictates that $\frac{d\eta^*}{dy^*} = 0$ at $y^* = 1$, therefore it is possible to expand $\exp(\eta^*)$ around $\eta^*_{GDL}$ over the region $\delta \leq y^* \leq 1$ as

$$\exp(\eta^*) = \exp(\eta^*_{GDL})\{1 + \eta^*_{GDL}(\tilde{\eta} - 1)\} \tag{3.10}$$

where, $\tilde{\eta} = \frac{\eta^*}{\eta^*_{GDL}}$ and $\eta^*_{GDL}$ is the overpotential at $y^* = 1$.

The length scale $(1 - \delta)$ in figure A-1 can be estimated from equation (3.8) and equation (3.6) as,

$$(1 - \delta) \sim \frac{D^*}{J^*} \tag{3.11(a))}$$

$$(1 - \delta) \sim \frac{J^*}{p} \tag{3.11(b))}$$

where, $p = \frac{\exp(\eta^*_{GDL})}{\varepsilon^2 C^*_{in}}$. Equating these expressions gives the useful relation,

$$J^{*2} \sim D^* p \tag{3.11(c)}$$

Combining equations (3.7) and (3.8) by eliminating $j^*$ and integrating using the boundary condition, $j^* = 0$ and $C^* = 1$ at $y^* = 1$ gives another useful relation,

$$\eta^*_{GDL}(\tilde{\eta} - 1) = C^* D^* + J^*(1 - y^*) - D^* \tag{3.12}$$

We now seek a power series solution for equations (3.6)-(3.8). From the expected profiles shown in figure A-1, we will need higher order polynomials for $j^*$ and $C^*$. Here we specify a 5th order polynomial for $j^*$. As will be shown later, the final solution is independent of the assumed order of the polynomial as long as it is sufficiently high.

$$j^* = \sum_{i=1}^{5} a_i (1 - y^*)^i \tag{3.13}$$

Substituting for $j^*$ in equation (3.8) and integrating the same gives the concentration profile

$$C^* = 1 - \frac{J^*}{D^*}(1 - y^*) + \frac{1}{D^*}\left(\sum_{i=2}^{6} \frac{a_{i-1}}{i}(1 - y^*)^i\right) \tag{3.14}$$

Substituting for $C^*$ in equation (3.12) gives the overpotential profile

$$\eta^*_{GDL}(\tilde{\eta} - 1) = \sum_{i=2}^{6} \frac{a_{i-1}}{i}(1 - y^*)^i \tag{3.15}$$

We now substitute equations (3.10) and (3.13)-(3.15) in equation (3.6) for the particular case of $D^* \ll 1$, which also implies $p \gg J^{*2}$ from equation (3.11(c)) and hence $(1 - \delta) \ll 1$. This gives,

$$a_1 = p;\ a_2 = -\frac{pJ^*}{2D^*} \text{ and } a_{n+2} \approx \frac{p}{n+2}\left[\frac{a_n}{(n+1)D^*}\right] \text{ (for } n \geq 1) \tag{3.16}$$

Substituting equation (3.16) back into equations (3.13)-(3.15) gives profiles of $j^*$, $C^*$ and $\eta^*_{GDL}(\tilde{\eta} - 1)$ for $\delta \leq y^* \leq 1$ as follows

$$j^* = j_o^* + \sqrt{pD^*}\sinh\left(\sqrt{\frac{p}{D^*}}(1-y^*)\right) - j_o^*\cosh\left(\sqrt{\frac{p}{D^*}}(1-y^*)\right) \quad (3.17)$$

$$C^* = \cosh\left(\sqrt{\frac{p}{D^*}}(1-y^*)\right) - \frac{j_o^*}{\sqrt{pD^*}}\sinh\left(\sqrt{\frac{p}{D^*}}(1-y^*)\right) \quad (3.18)$$

$$\eta^* = \eta_{GDL}^* + D^*\cosh\left(\sqrt{\frac{p}{D^*}}(1-y^*)\right) - \frac{j_o^*}{\sqrt{\frac{p}{D^*}}}\sinh\left(\sqrt{\frac{p}{D^*}}(1-y^*)\right) + j_o^*(1-y^*) - D^* \quad (3.19)$$

Substituting $j^* = J^*$ and $C^* = 0$ at $y^* = \delta$ in equations (3.17) and (3.18) and solving them together gives

$$J^* = \sqrt{pD^*} = \sqrt{\frac{\exp(\eta_{GDL}^*)}{\varepsilon^2 C_{in}^*}D^*} \quad (3.20)$$

Equation (3.12) at $y^* = \delta$ gives

$$(\eta^*)_\delta = \eta_{GDL}^* + J^*(1-\delta) - D^* \quad (3.21)$$

Since $j^* \approx J^*$ is a constant over $0 < y^* \leq \delta$ therefore equation (3.7) (Ohm's law) dictates that $\eta^*$ has to be linear in this domain. Thus,

$$(\eta^*)_{0-\delta} = \eta_{o,CCL}^* - J^* y^* \quad (3.22)$$

where, $\eta^* = \eta_{o,CCL}^*$ at $y^* = 0$ i.e., at membrane-CCL interface. At $y^* = \delta$ the two solutions given by equations (3.21) and (3.22) must match. Equating them and substituting equation (3.20) for $\eta_{GDL}^*$ we get for $D^* \ll 1$,

$$\boldsymbol{\eta_{o,CCL}^* = ln\left\{\frac{\varepsilon^2 C_{in}^* J^{*2}}{D^*}\right\} + J^*} \quad \textbf{(3.23)}$$

For the limiting case when proton transport resistance is negligible i.e. $J^* \ll 1$, equation (3.23) simplifies to

$$\eta_{o,CCL}^* = ln\left\{\frac{\varepsilon^2 C_{in}^* J^{*2}}{D^*}\right\} \quad (3.24)$$

which is in fact the polarization curve for the case of ideal proton transport ($\frac{d\eta^*}{dx^*} \to 0$) but with considerable oxygen transport resistance across the CCL (Kulikovsky 2010, [42]).

It is informative to write Equation (3.23) alternatively in dimensional form as

$$\boldsymbol{\eta_{o,CCL} = A_c ln\left\{\frac{J}{i_{o,c} A l_t (\frac{C_{CCL-GDL}}{C_{in}})}\right\} + A_c ln\left\{\frac{J}{\frac{4FD_{CCL}C_{in}}{l_t}(\frac{C_{CCL-GDL}}{C_{in}})}\right\} + \frac{J}{\sigma/l_t}} \qquad \textbf{(3.25)}$$

The right side of equation (3.25) shows contributions of intrinsic kinetics (first term), mass transfer resistance for oxygen in the CCL (second term) and proton transport resistance in CCL (third term) to the overall cathode overpotential. In fact, the form of equation (3.25) can be intuitively expected. In the region $0 < y^* < \delta$ the proton flux experiences just the 'DC' resistance of ($\frac{\delta}{\sigma} \sim \frac{l_t}{\sigma}$) because in this region the consumption rate of protons is zero due to absence of oxygen. This gives the overpotential contribution due to proton transport as expressed by the third term of equation (3.25). This 'DC' resistance is in series with the resistance of oxygen transport modulated ORR kinetics in the region $\delta < y^* < 1$ where proton transport resistance ($\sim \frac{1-\delta}{\sigma}$) is negligible. Thus, the oxygen transport modulation of ORR is given by equation (3.24), or equivalently, by the first two terms of equation (3.25). Hence the three terms are added to give the total overpotential.

Equations (3.23) or (3.25) represents the iR-free polarization curve when both transport resistances across the CCL namely oxygen transport resistance and proton transport resistance simultaneously modulate the rate of oxygen reduction reaction for the case $D^* \ll 1$. Thus we expect these expressions to be valid for current densities greater than $J_{crit,O2\ transport}$.

We first compare the polarization curves predicted by equations (3.23) and (3.25) with the polarization curve predicted by three-dimensional numerical simulation in figure 3.2. The

details of the numerical simulation are provided in section 2.2 of chapter 2. The numerical values of oxygen diffusion coefficient ($D_{CCL}$) and proton conductivity in the CCL are, $D_{CCL} = 5.06 \times 10^{-9} \frac{m^2}{s}$ ($\frac{4FD_{CCL}C_{in}}{l_t} = 0.2 \frac{A}{cm^2}$) and $\sigma = 2.8 \frac{S}{m}$ ($\frac{\sigma A_c}{l_t} = 0.91 \frac{A}{cm^2}$) ensuring that $D^* = 0.22$ ($< 1$). The intrinsic volumetric exchange current density is taken to be $i_{o,c}A = \sim 0.5 \times 10^7 \frac{A}{m^3}$. The other model parameters were selected to ensure that there exist no limitations on mass transport of oxygen through the GDL and in the channel. Also, the stoichiometry selected was high enough to ensure that oxygen concentration at CCL-GDL interface remains equal to inlet oxygen concentration over entire active area $\left(D_{GDL} = 1.79 \times 10^{-5} \frac{m^2}{s}, U_{in} = 1.3 \frac{m}{s}, D = 4 \times 10^{-5} \frac{m^2}{s}\right)$. The numerical values of proton conductivity of the membrane and electrical conductivity of GDL are assigned to be high enough such that the resulted polarization curve in the three-dimensional numerical simulation is 'iR-free'.

As can be observed from figure 3.2, polarization curve predicted by equation (3.25) gives an excellent match with the polarization curve predicted by three-dimensional numerical simulation over entire range of current densities $J > J_{crit,(O2)\,transport}$, whereas polarization curve predicted by equation (3.24) shows considerable deviation at high current density. Thus, equation (3.25) gives a comprehensive expression of polarization curve of PEMFC when oxygen transport and proton transport resistances are simultaneously modulating overall ORR kinetics with the condition $D^* < 1$.

That the improved predictive ability of equation (3.25) is indeed because of relaxing the assumption of uniform overpotential in the CCL is confirmed by comparing the profiles of $j^*$, $C^*$ and $\eta^*$ along the thickness of the CCL (equations (3.17)-(3.19) and (3.22) respectively), with the profiles predicted by three-dimensional numerical simulation. Figure 3.3 illustrates

this comparison at the operating current density of $J = 0.98 \frac{A}{cm^2}$. As can be noted, analytical predictions show excellent agreement with numerical simulation results.

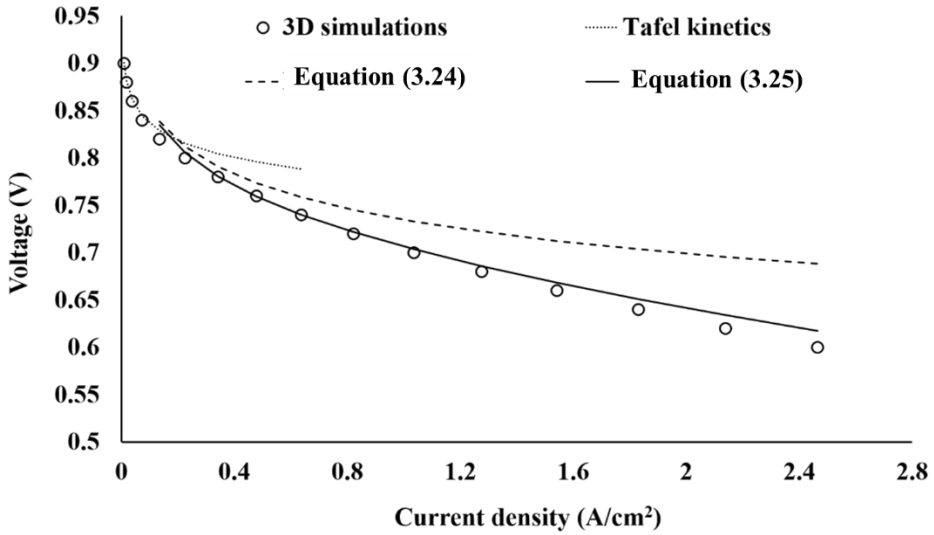


**Fig.3.2** Comparison between the polarization curves predicted by analytical expressions and that obtained from three-dimensional numerical simulation for $D^* \ll 1$ and $M_T \ll 1$

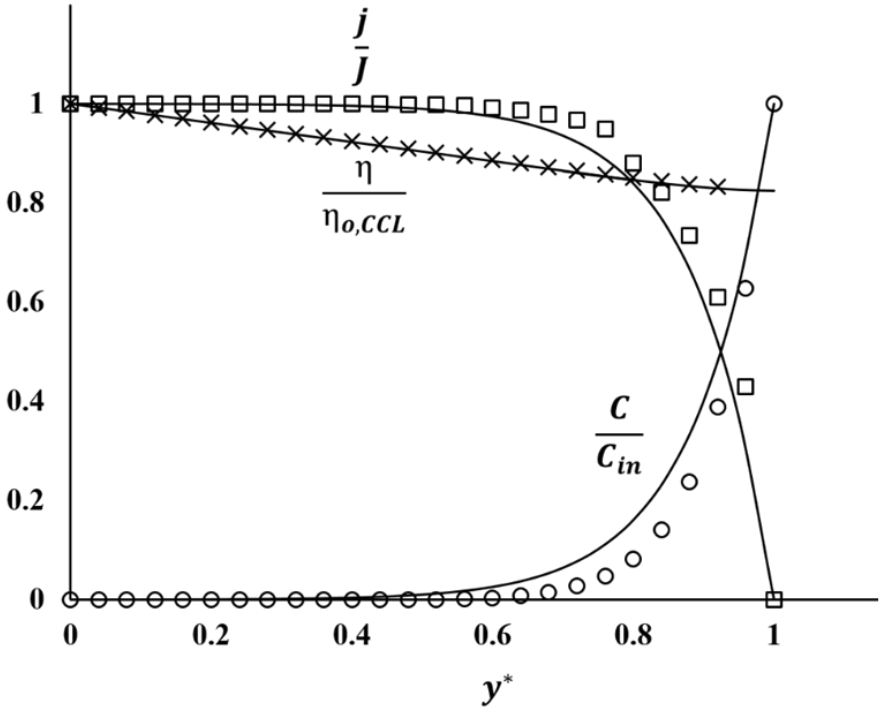


**Fig.3.3** Comparison between the profiles of current density, oxygen concentration and overpotential obtained by analytical expressions (lines) and three-dimensional numerical simulation (circles: oxygen concentration, squares: current density, cross: overpotential) at 1.83 A/cm$^2$ (cell voltage ~0.63 V) for $D^* \ll 1$

- ***The regime of simultaneous oxygen and proton transport limited reaction kinetics in the CCL for the case of*** $\frac{4FD_{CCL}C_{in}}{l_t} \gg \frac{\sigma A_c}{l_t}$ ***i.e.,*** $D^* \gg 1$

Kulikovsky (2010) [42] provided the equation of polarization curve in the regime of ideal oxygen transport wherein oxygen concentration is uniform in the CCL while overall ORR kinetics is modulated by resistance to proton conduction for $J > J_{crit,(H+),transport}$ (refer section 2.1.1 of chapter 2, ideal oxygen transport). In this regime, the proton flux and consequently the reaction rate decays sharply from the CCL-membrane interface. While this regime implies very high values of $D_{CCL}$, in reality the finite value of diffusion coefficient will ensure that both proton conduction and oxygen diffusion resistances in the CCL will simultaneously modulate ORR kinetics. In this regime also, we can expect a thin reaction zone near the CCL-membrane interface. However, the absence of reaction and the non-negligible oxygen diffusion resistance in the region away from the interface will set up a linear gradient of oxygen concentration in the CCL in order to transport the oxygen to the reaction zone. In the reaction zone itself, the boundary condition $\frac{dC^*}{dy^*} = 0$ at $y^* = 0$ requires the oxygen concentration profile to become independent of $y^*$. Therefore, the expected profiles of oxygen concentration, current density and overpotential in the CCL for $J > \frac{\sigma A_c}{l_t}$ $and$ $\frac{\sigma A_c}{l_t} < \frac{4FD_{CCL}C_{in}}{l_t}$ are schematically shown in figure 3.4.

The linear oxygen concentration profile can be determined from equation (3.8) by invoking $j^* = 0$ in $\delta < y^* < 1$. Neglecting the flattening out of oxygen concentration in the reaction zone, the oxygen concentration profile in the CCL can be given by

$$C^* = 1 - \frac{J^*}{D^*}(1 - y^*) \tag{3.26}$$

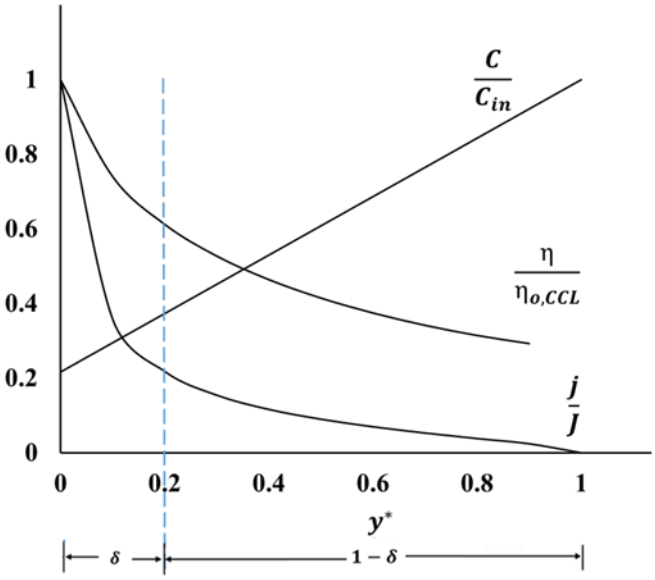


**Fig3.4** Pictorial representation of profiles of current density, overpotential ($\eta = \eta_{o,CCL}$ at $x^* = 0$) and concentration for $J > \frac{\sigma A_c}{l_t}$ $and$ $\frac{\sigma A_c}{l_t} < \frac{4FD_{CCL}C_{in}}{l_t}$. The dotted line is the uniform oxygen concentration as assumed in Kulikovsky (2010)

Equations (3.6), (3.7) and (3.26) then simplify to,

$$\frac{d^2j^*}{dy^{*2}} + \frac{1}{2}\frac{dj^{*2}}{dy^*} = \frac{dj^*}{dy^*}\frac{dln\left\{1-\frac{J^*}{D^*}(1-y^*)\right\}}{dy^*} \tag{3.27}$$

Given that we are exploring the case of $D^* \gg 1$, $ln\left\{1-\frac{J^*}{D^*}(1-y^*)\right\} \approx -\frac{J^*}{D^*}(1-y^*)$, therefore, equation (3.27) takes the form,

$$\frac{d^2j^*}{dy^{*2}} + \frac{1}{2}\frac{dj^{*2}}{dy^*} = \frac{J^*}{D^*}\frac{dj^*}{dy^*} \tag{3.28}$$

Equation (3.28) can be integrated twice to give a profile of current density as,

$$j^* = \zeta \tan\left\{\frac{\zeta}{2}(1-y^*-\frac{2J^*}{\zeta^2 D^*})\right\} \tag{3.29}$$

Equations (3.6), (3.26) and (3.29) then give a profile of overpotential as,

$$\eta^* = \ln\left[\frac{\frac{\zeta^2 C_{in}^* \varepsilon^2}{2}\left\{1+\left(\tan\left(\frac{\zeta}{2}(1-y^*-\frac{2J^*}{\zeta^2 D^*})\right)\right)^2\right\}}{1-\frac{J^*}{D^*}(1-y^*)}\right] \tag{3.30}$$

Here, $\zeta$ is a constant and can be found by substituting $y^* = 0$ and $j^* = J^*$in equation (3.29). For $J \gg J_{crit,(H+),transport}$, we get $\tan\left\{\frac{\zeta}{2}\left(1 - \frac{2J^*}{\zeta^2 D^*}\right)\right\} \gg 1$. Therefore, equation (3.30) gives,

$$\boldsymbol{\eta^*_{o,CCL} = \ln\left[\frac{\frac{J^{*2} C^*_{in} \varepsilon^2}{2}}{1 - \frac{J^*}{D^*}}\right]} \qquad \textbf{(3.31)}$$

Equation (3.31) can be recast in a dimensional form as,

$$\boldsymbol{\eta_{o,CCL} = 2A_c \ln\left\{\frac{J}{\sqrt{\frac{2\sigma A_c}{l_t} i_{o,c} A l_t \left(\frac{C_{CCL-GDL}}{C_{in}}\right)}}\right\} + 2A_c ln\left\{\frac{1}{\sqrt{\left(1 - \frac{J}{\frac{4FD_{CCL}C_{in}}{l_t}\left(\frac{C_{CCL-GDL}}{C_{in}}\right)}\right)}}\right\}} \qquad \textbf{(3.32)}$$

For the limiting case when $J \ll \frac{4FD_{CCL}C_{CCL-GDL}}{l_t}$, equation (3.32) gets transformed to,

$$\eta_{o,CCL} = 2A_c \ln\left\{\frac{J}{\sqrt{\frac{2\sigma A_c}{l_t} i_{o,c} A l_t \left(\frac{C_{CCL-GDL}}{C_{in}}\right)}}\right\} \qquad (3.33)$$

Equation (3.33) is in fact is the same expression derived by Kulikovsky (2010) [42] for the case of ideal oxygen transport. An important difference between equation (3.32) and equation (3.33) is the presence of the second term on the right-hand side of equation (3.32), which arises as a repercussion of finite oxygen transport resistance. An interesting feature of equation (3.32) is that $\eta \to \infty$ when $J \to \frac{4FD_{CCL}C_{CCL-GDL}}{l_t}$ i.e., the polarization curve will tend to show a limiting current. Interestingly, low humidity fuel cell operations do tend to show such limiting current behaviour in polarization curves (Chen et al. 2017, [91]).

Figure 3.5 compares the polarization curve predicted by equation (3.32) and equation (3.33) with the polarization curve predicted by three-dimensional numerical simulation. In this simulation, we have assigned the following values of model parameters: $D_{CCL} = 1 \times 10^{-8} \frac{m^2}{s}$ and $\sigma = 0.026 \frac{S}{m}$, which respectively imply $J_{crit,(O2),transport} = 0.3 \frac{A}{cm^2}$ and $J_{crit,(H+),transport} = 0.0083 \frac{A}{cm^2}$ so that $D^* = 48$. The intrinsic volumetric exchange current density is taken to be $i_{o,c}A = \sim 0.5 \times 10^7 \frac{A}{m^3}$. We reiterate that the numerical values of other model parameters were selected to ensure that there exist no limitations on mass transport of oxygen through the GDL and in the channel. Also, the stoichiometry selected was high enough to ensure that oxygen concentration at CCL-GDL interface remains equal to inlet oxygen concentration over entire active area ($D_{GDL} = 1.79 \times 10^{-5} \frac{m^2}{s}, U_{in} = 1.3 \frac{m}{s}, D = 4 \times 10^{-5} \frac{m^2}{s}$) and the numerical values of proton conductivity of the membrane and electrical conductivity of GDL are assigned to be high enough such that the resulted polarization curve in the three-dimensional numerical simulation is 'iR-free'.

It can be noted from figure 3.5 that the polarization curve predicted by equation (3.32) is in close agreement with the polarization curve predicted by three-dimensional numerical simulation whereas polarization curve predicted by equation (3.33) shows considerable deviation. The feature of limiting current is evident from the polarization curve predicted by numerical simulation and is also captured in polarization curve predicted by equation (3.32). This is clearly absent in the polarization curve predicted by equation (3.33). Figure 3.6 compares local profiles of $C^*$, $j^*$ and $\eta^*$ along the thickness of the CCL predicted by equations (3.26), (3.29) and (3.30) respectively, with those predicted by numerical simulation at the same current density of $J = 0.27 \frac{A}{cm^2}$. It is evident that analytical predictions match reasonably well with the predictions of numerical simulation.

The deviation between the polarization curves predicted by equation (3.32) versus three-dimensional numerical simulation is a consequence of assumption of linear profile of oxygen concentration in the reaction zone, whereas as mentioned earlier, the oxygen concentration should flatten out near CCL-membrane interface. Because of this, the reaction zone actually needs lower flux of oxygen than that assumed by the analytical model and hence the limiting current density predicted analytically is smaller than that predicted by simulations. Nonetheless, the analytical model does capture the limiting current behavior qualitatively whereas the same is clearly absent in the earlier work (Kulikovsky 2010 [42]).

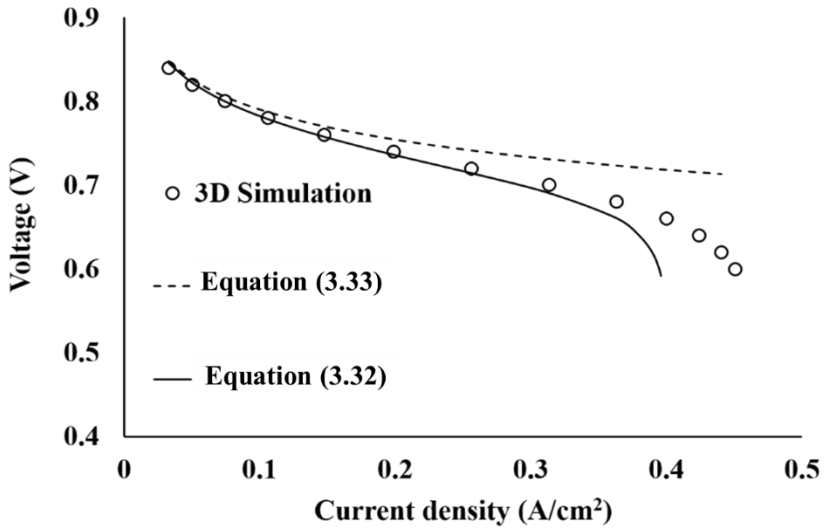


**Fig.3.5** Comparison between the polarization curves obtained by analytical expressions and three-dimensional numerical simulation for $D^* \gg 1$ and $M_T \ll 1$

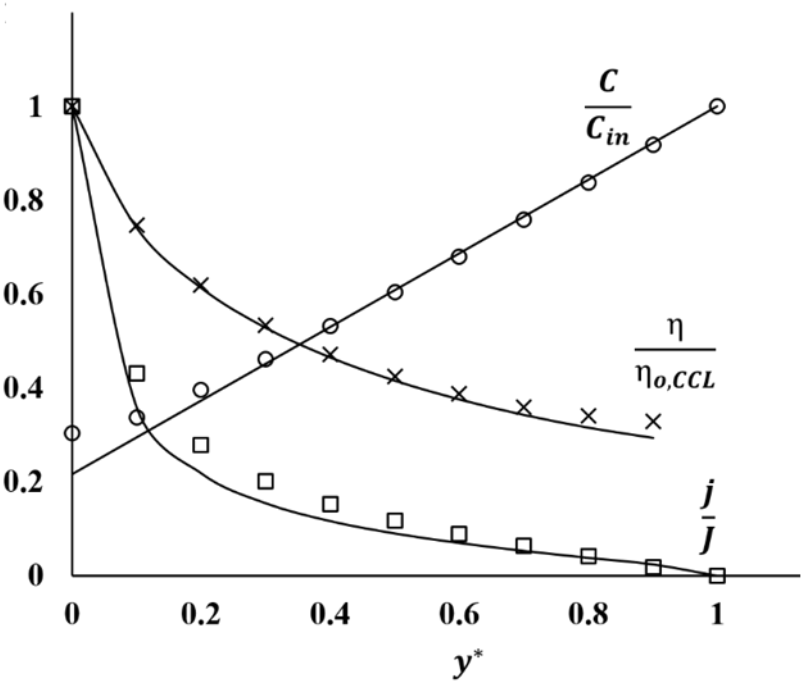


**Fig.3.6** Comparison between the profiles of current density, oxygen concentration and overpotential obtained by analytical expressions (lines) and three-dimensional numerical simulation (circles: oxygen concentration, squares: current density, cross: overpotential) at 0.31 A/cm$^2$ (cell voltage ~ 0.7 V) for $D^* \gg 1$

We will show in 7 that for many realistic cases of PEM fuel cell operation such as a fully humidified low temperature PEM fuel cell, which is also experimentally investigated in this thesis, the sub-regime given by $D^* < 1$ turns out to be more relevant. Thus, we will restrict the scope of the following derivation to the case $D^* < 1$.

In summary, equations (3.25) and (3.32) describe the $J - \eta_{o,CCL} - C_{CCL-GDL}$ relationships in the regime of simultaneous oxygen and proton transport modulated ORR kinetics and when the rate of diffusion of $O_2$ in agglomerates is much faster than intrinsic ORR rate so that $M_T <$ $< 1$ and $E(\eta) \approx 1$.

### 3.2) Limiting case 2: $M_T \gg 1$

This represents the case when rate of diffusion of $O_2$ in agglomerates is considerably slower than the intrinsic ORR rate, and consequently the effectiveness factor can be approximated as $E(\eta) \approx \frac{1}{M_t}$. Therefore, equation (3.1) can be modified as,

$$\frac{dj}{dy} = -\left\{\sqrt{\frac{i_{o,c}A\left[\exp\left(\frac{\eta}{A_c}\right)\right]36FD_{agg}C_{in}}{R_{agg}^2}} \times \frac{A}{a}\right\} \times \frac{C}{C_{in}} \tag{3.34}$$

Note that, $\frac{A}{a} = 1 - \varepsilon_{CCL}$ where, $\varepsilon_{CCL}$ is the porosity of the CCL.

Equation (3.34) can be re-cast in non-dimensional form as,

$$\varepsilon'^2 \theta C_{in}^* \frac{dj'}{dy^*} = -C^*[\exp(\eta')] \tag{3.35}$$

And equations (3.2) and (3.3) can be written in non-dimensional form as,

$$\frac{d\eta'}{dy^*} = -j' \tag{3.36}$$

$$D' \frac{dC^*}{dy^*} = J' - j' \tag{3.37}$$

Here, $j' = \frac{j}{\frac{2\sigma A_c}{l_t}}$ , $J' = \frac{J}{\frac{2\sigma A_c}{l_t}}$, $\eta' = \frac{\eta}{2A_c}$, $\varepsilon'^2 = \frac{2\sigma A_c}{i_{o,c}Al_t^2}$, $D' = \frac{4FD_{CCL}C_{CCL-GDL}}{2\sigma A_c}$ and $\theta = \sqrt{\frac{i_{o,c}A}{36FD_{agg}C_{in}(1-\epsilon_{CCL})/R_{agg}^2}}$ (3.38)

Noting the similarity between the equation sets (3.35-3.37) and (3.6-3.8), it is straightforward to show that the solution to the equations (3.35-3.37) is given by

$$\boldsymbol{\eta'_{o,CCL} = ln\left\{\frac{\varepsilon'^2 C_{in}^* \theta J'^2}{D'}\right\} + J'} \tag{3.39}$$

Which, in dimensional form is given by

$$\boldsymbol{\eta_{o,CCL} = A_c ln\left\{\frac{J}{i_{o,c} A l_t (\frac{C_{CCL-GDL}}{C_{in}})}\right\} + A_c ln\left\{\frac{J}{\frac{4FD_{CCL}C_{in}}{l_t}(\frac{C_{CCL-GDL}}{C_{in}})}\right\} + \frac{J}{\sigma/l_t} + A_c ln\left\{\frac{J^2}{(\frac{4FD_{CCL}C_{in}}{l_t})(\frac{36FD_{agg}C_{in}(1-\epsilon_{CCL})}{R_{agg}} \times \frac{l_t}{R_{agg}})(\frac{C_{CCL-GDL}}{C_{in}})^2}\right\}} \quad \textbf{(3.40)}$$

The first three terms on the right side of equation (3.40) have the same meaning as those in equation (3.25). The additional fourth term is the contribution of oxygen transport resistance in the ionomer phase inside the agglomerate. This contribution will become substantial when $J \gg J_{crit,(O2)\ transport\ in\ CCL\ and\ agglomerate}$, where

$$J_{crit,(O2)\ transport\ in\ CCL\ and\ agglomerate} = \sqrt{(\frac{4FD_{CCL}C_{in}}{l_t})(\frac{36FD_{agg}C_{in}(1-\epsilon_{CCL})}{R_{agg}} \times \frac{l_t}{R_{agg}})} \quad (3.41)$$

It is worth noting here that in equations (3.25) and (3.30), the third term on the right side can be identified as an ohmic contribution of the CCL to the cathode overpotential whereas all other terms contribute to iR-free cathode overpotential. In other words, we can visualize proton transport resistance in the CCL as a DC resistance, which is in series with the oxygen transport resistance in CCL. Hence, we can recast equations (3.25) and (3.40) in the form,

$$\eta_{o,CCL} = \eta_{o,iR-free,CCL} + \frac{J}{\sigma/l_t} \quad (3.42)$$

Note that the first term in equation (3.42) is equivalent to the case where the overpotential across CCL is constant, while the second term entirely accounts for the gradient in overpotential in CCL for finite values of $\sigma$. The iR-free overpotential in equation (3.42) takes the form

$$\eta_{o,iR-free,CCL} = A_c ln\left\{\frac{J}{i_{o,c} A l_t (\frac{C_{CCL-GDL}}{C_{in}})}\right\} + A_c ln\left\{\frac{J}{\frac{4FD_{CCL}C_{in}}{l_t}(\frac{C_{CCL-GDL}}{C_{in}})}\right\} \quad (3.43)$$

or equivalently,

$$J = \sqrt{\frac{4FD_{CCL}C_{in}}{l_t} i_{o,c} A l_t \left[\exp\left(\frac{\eta_{o,iR-free,CCL}}{A_c}\right)\right]} \frac{C_{CCL-GDL}}{C_{in}} \tag{3.44}$$

when $J \ll J_{crit,(O2)\ transport\ in\ CCL\ and\ agglomerate}$.

Alternatively, the iR-free cathode overpotential takes the form

$$\eta_{o,iR-free,CCL} = A_c ln\left\{\frac{J}{i_{o,c} A l_t (\frac{C_{CCL-GDL}}{C_{in}})}\right\} + A_c ln\left\{\frac{J}{\frac{4FD_{CCL}C_{in}}{l_t}(\frac{C_{CCL-GDL}}{C_{in}})}\right\} +$$

$$A_c ln\left\{\frac{J^2}{(\frac{4FD_{CCL}C_{in}}{l_t})(\frac{36FD_{agg}C_{in}(1-\epsilon_{CCL})}{R_{agg}} \times \frac{l_t}{R_{agg}})(\frac{C_{CCL-GDL}}{C_{in}})^2}\right\} \tag{3.45}$$

or equivalently,

$$J = \sqrt{4FD_{CCL}C_{in}\sqrt{\frac{36FD_{agg}C_{in}(1-\epsilon_{CCL})}{R_{agg}} \times \frac{1}{R_{agg}} i_{o,c} A \left[\exp\left(\frac{\eta_{o,iR-free,CCL}}{A_c}\right)\right]}} \frac{C_{CCL-GDL}}{C_{in}} \tag{3.46}$$

when $J \gg J_{crit,(O2)\ transport\ in\ CCL\ and\ agglomerate}$.

### 3.3) General case: $\frac{1}{M_T} < E(\eta) < 1$

We derived the exact analytical solutions to equations (3.1-3.3) in the limiting cases of $M_T \ll 1$ and $M_T \gg 1$. As noted earlier, both asymptotic solutions suggest that it is possible to find the $J - \eta_{o,iR-free,CCL} - C_{CCL-GDL}$ relation by considering $\eta$ in equation (3.1) to be independent of $y$ and then separately adding the proton transport resistance in the CCL as a DC resistance to obtain $J - \eta_{o,CCL} - C_{CCL-GDL}$ relation. We apply the same logic to the transition regime and first find the $J - \eta_{o,iR-free,CCL} - C_{CCL-GDL}$ relation in this transition regime by assuming $\eta$ in equation (3.1) to be independent of $y$. This is identical to the regime of ideal proton transport (refer section 2.1.1 of chapter 2, ideal proton transport) and therefore, in the most general case, equation (2.9) from chapter 2 takes the form

$$J = \frac{4FD_{CCL}C_{in}}{l_t} \times \sqrt{\frac{i_{o,c}Al_t\left[\exp\left(\frac{\eta_{o,iR-free,CCL}}{A_c}\right)\right]\times E\left(\eta_{o,iR-free,CCL}\right)}{\frac{4FD_{CCL}C_{in}}{l_t}}} \tanh\left\{\sqrt{\frac{i_{o,c}Al_t\left[\exp\left(\frac{\eta_{o,iR-free,CCL}}{A_c}\right)\right]\times E\left(\eta_{o,iR-free,CCL}\right)}{\frac{4FD_{CCL}C_{in}}{l_t}}}\right\} \times \frac{C_{CCL-GDL}}{C_{in}} \quad \textbf{(3.47a)}$$

To this $\eta_{o,iR-free,CCL}$, the overpotential contribution due to proton transport resistance in the CCL can be added linearly (see equation 3.42) and thus, $J - \eta_{o,CCL} - C_{CCL-GDL}$ relation in the most generalized case is also,

$$\boldsymbol{\eta_{o,CCL} = \eta_{o,iR-free,CCL} + \frac{J}{\sigma/l_t}} \quad \textbf{(3.47b)}$$

Here, $\eta_{o,iR-free,CCL}$ is given by equation (3.47a).

Figure 3.7 compares the polarization curves predicted by i) equation (3.24), ii) equation (3.25), iii) equation (3.40), iv) equation (3.47) and v) three-dimensional numerical simulation. While $D_{CCL} = 5.06 \times 10^{-9}\frac{m^2}{s}$ $(\frac{4FD_{CCL}C_{in}}{l_t} = 0.2\ \frac{A}{cm^2})$ and $\sigma = 2.8\frac{S}{m}$ $(\frac{\sigma A_c}{l_t} = 0.91\ \frac{A}{cm^2})$ ensuring that $D^* = 0.22\ (< 1)$, the numerical value of oxygen diffusion coefficient in the agglomerate ($D_{agg} \sim 10^{-11}\frac{m^2}{s}$), radius of the agglomerate ($R_{agg} \sim 100\ nm$) and porosity of the CCL ($\varepsilon_{CCL} \sim 0.3$) leads to $\frac{36FD_{agg}C_{in}(1-\epsilon_{CCL})}{R_{agg}} \times \frac{l_t}{R_{agg}} \sim 10\ \frac{A}{cm^2}$ and therefore $J_{crit,(O2)\ transport\ in\ CCL\ and\ agglomerate} \sim 1.5\ \frac{A}{cm^2}$. The diffusion of oxygen in the ionomer phase of agglomerate can be estimated by Bruggeman correlation, $D_{agg} = \varepsilon_{agg}^{1.5}D_{O2-ionomer}$ [92], where $\varepsilon_{agg}$ is the volume fraction of ionomer in the agglomerate (it is straight forward to show that $\varepsilon_{agg} = \frac{\varepsilon_l\ (ionomer\ volume\ fraction\ in\ the\ CCL)}{1-\varepsilon_{CCL}}$)) and $D_{O2-ionomer}$ is the bulk diffusion

coefficient of oxygen in ionomer. When nafion is used as the ionomer, $D_{O2-nafion} \sim 10^{-10}\frac{m^2}{s}$ [93]. Therefore, for $\varepsilon_l \sim 0.2$ and $\varepsilon_{CCL} \sim 0.4$, the value of D_agg obtained from the Bruggeman correlation is $D_{agg} \sim 10^{-11}\ \frac{m^2}{s}$. The value of CCL porosity $\epsilon_{CCL} \sim 0.4$ is representative of random close packing of spherical agglomerates. The value of $R_{agg}$ was chosen to be ~100 nm, which is within the range determined experimentally using nanometer scale x-ray computed tomography, TEM and mercury injection porosimetry techniques [94]. As stated earlier, the numerical values of other model parameters were selected to ensure that there exist no limitations on mass transport of oxygen through the GDL and in the channel. Also, the numerical values of proton conductivity of the membrane and electrical conductivity of GDL are assigned to be high enough such that the resulted polarization curve in the three-dimensional numerical simulation is 'iR-free'.

Figure 3.7 clearly shows that the polarization curve predicted by equation (3.47) gives an excellent match with the polarization curve predicted by three-dimensional numerical simulation. As expected, the polarization curve predicted by equation (3.40) matches with the three-dimensional numerical simulation at only high current density ($J \gg J_{crit,(O2)\ transport\ in\ CCL\ and\ agglomerate}$ ($\sim 1.5\ \frac{A}{cm^2}$)) whereas polarization curve predicted by equation (3.25) which does not incorporate oxygen diffusion resistance in the agglomerates deviates at high current density. It must be noted here that equations (3.25) and (3.40) describe the iR-free polarization curves for the asymptotic cases $M_T \ll 1$ and $M_T \gg 1$ respectively. It is evident from the figure 3.7 that the polarization curve predicted by equation (3.47) (general case: $\frac{1}{M_T} < E(\eta) < 1$) not only agrees with the asymptotic solutions but also connects them in the intermediate region. This suggests that the method of separating potential losses due to oxygen transport and proton transport in the CCL, which was rigorously derived for the asymptotic cases, does work for the general case also.

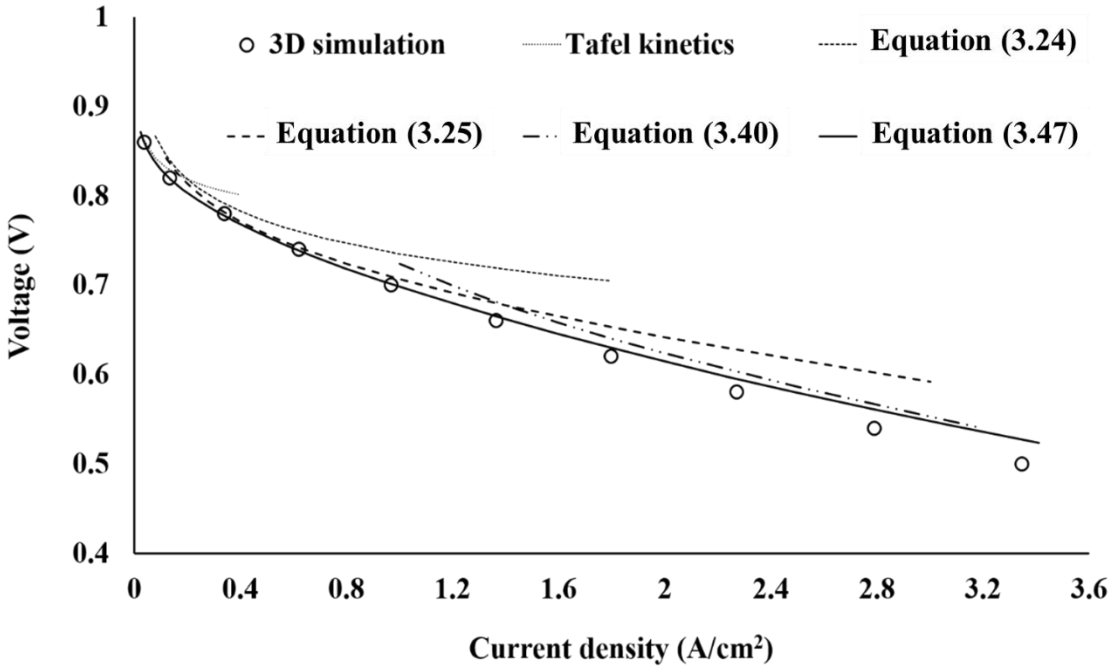


**Fig.3.7** Comparison between the polarization curves obtained by analytical expressions and three-dimensional numerical simulation for $D^* \ll 1$

## 3.4) Conclusion

In conclusion, we have derived $J - \eta_{o,CCL} - C_{CCL-GDL}$ relationships for all possible regimes of CCL operation; and these are summarized in table 3.1. The simplifications invoked while deriving analytical $J - \eta_{o,CCL} - C_{CCL-GDL}$ relationships are validated by comparing the predictions of analytical with the predictions of three-dimensional numerical simulations wherein no such simplifying assumption are made. While the analytical $J - \eta_{o,CCL} - C_{CCL-GDL}$ relationships were known in the limiting regimes of CCL operations (Regime 1-3) which demands unrealistic values of $D_{CCL}$ or $\sigma$, the present work provides $J - \eta_{o,CCL} - C_{CCL-GDL}$ relationships in the regimes of CCL operation which are practically relevant (Regimes 4a, 4b and 5). This work also derives the most generalized $J - \eta_{o,CCL} - C_{CCL-GDL}$ relationship which is valid over entire range of current density that relates the cathodic overpotential $\eta_{o,CCL}$ to the current density $J$ by accounting for simultaneous oxygen and proton transport resistances in the CCL coupled with oxygen transport resistance in the agglomerates.

We further note that the oxygen transport resistances in GDL and flow channel will affect only the iR-free part of the cathode overpotential ($\eta_{o,iR-free,CCL}$) through modulation of $C_{CCL-GDL}$. The repercussions of these resistances on the polarization curve of PEM will be the main focus of the three subsequent chapters: Chapter 4 couples the oxygen transport resistances in GDL and flow channel for the case of reaction controlled regime of CCL operation i.e. Regime 1 (Table 3.1), whereas chapters 5 and 6 focus respectively on Regimes 2,3 and Regimes 4b,5.

**Table 3.1** Regimes of CCL operation and corresponding $J - \eta_o - C_{CCL-GDL}$ relations

| | |
|---|---|
| Regime 1<br>Intrinsic kinetics control case<br>$J < \frac{4FD_{CCL}C_{CCL-GDL}}{l_t}$<br>$and\ J < \frac{2\sigma A_c}{l_t}$ | $J = i_{o,c}Al_t \exp(\frac{\eta_{o,CCL}}{A_c}) \frac{C_{CCL-GDL}}{C_{in}}$ (Kulikovsky 2010, [42]) |
| Regime 2<br>Ideal proton transport case<br>$J > \frac{4FD_{CCL}C_{CCL-GDL}}{l_t}$<br>$and\ \frac{2\sigma A_c}{l_t} \to \infty$ | $J = \sqrt{i_{o,c}Al_t \frac{4FD_{CCL}C_{in}}{l_t}} \exp(\frac{\eta_{o,CCL}}{2A_c}) \frac{C_{CCL-GDL}}{C_{in}}$ (Kulikovsky 2010, [42]) |
| Regime 3<br>Ideal oxygen transport case<br>$J > \frac{2\sigma A_c}{l_t}\ and$<br>$\frac{4FD_{CCL}C_{CCL-GDL}}{l_t} \to \infty$ | $J = \sqrt{i_{o,c}Al_t \frac{2\sigma A_c}{l_t} \frac{C_{CCL-GDL}}{C_{in}}} \exp(\frac{\eta_{o,CCL}}{2A_c})$ (Kulikovsky 2010, [42]) |

| | |
|---|---|
| Regime 4a<br>Simultaneous oxygen and proton transport limited case<br>$J > \frac{2\sigma A_c}{l_t}$ *and* $(D^* > 1)$<br>$(M_T \ll 1)$ | $\frac{J}{\sqrt{\left(1-\frac{J}{\frac{4FD_{CCL}C_{in}C_{CCL-GDL}}{l_t}\frac{}{C_{in}}}\right)}} = \sqrt{i_{o,c}Al_t\frac{2\sigma A_c}{l_t}\frac{C_{CCL-GDL}}{C_{in}}}\exp(\frac{\eta_{o,CCL}}{2A_c})$<br>**(This work)** |
| Regime 4b<br>Simultaneous oxygen and proton transport limited case<br>$J > \frac{4FD_{CCL}C_{CCL-GDL}}{l_t}$<br>*and* $(D^* < 1)$<br>$(M_T \ll 1)$ | $J = \sqrt{i_{o,c}Al_t\frac{4FD_{CCL}C_{in}}{l_t}}\exp(\frac{\eta_{o,iR-free,CCL}}{2A_c})\frac{C_{CCL-GDL}}{C_{in}}$<br>$\eta_{o,CCL} = \eta_{o,iR-free,CCL} + \frac{\mathrm{J}}{\sigma/l_t}$<br>**(This work)** |
| Regime 5<br>Simultaneous oxygen and proton transport limited case with agglomerate resistance<br>$J > \sqrt{\frac{4FD_{CCL}C_{CCL-GDL}}{l_t}} \times \sqrt{\frac{36FD_{agg}C_{in}(1-\epsilon_{CCL})}{R_{agg}^2/l_t}}$<br>*and* $(D^* < 1)$ | $J = \sqrt{\frac{4FD_{CCL}C_{in}}{l_t}\sqrt{i_{o,c}Al_t\frac{36FD_{agg}C_{in}(1-\epsilon_{CCL})}{R_{agg}}\times\frac{l_t}{R_{agg}}}}\exp\left(\frac{\eta_{o,iR-free,CCL}}{3A_c}\right)\frac{C_{CCL-GDL}}{C_{in}}$<br>$\eta_{o,CCL} = \eta_{o,iR-free,CCL} + \frac{\mathrm{J}}{\sigma/l_t}$<br>**(This work)** |
| Most generalized polarization curve:<br>$J = \frac{4FD_{CCL}C_{in}}{l_t}\sqrt{\frac{i_{o,c}Al_t\left[\exp\left(\frac{\eta_{o,iR-free,CCL}}{A_c}\right)\right]E(\eta_{o,iR-free,CCL})}{\frac{4FD_{CCL}C_{in}}{l_t}}}\tanh\left\{\sqrt{\frac{i_{o,c}Al_t\left[\exp\left(\frac{\eta_{o,iR-free,CCL}}{A_c}\right)\right]E(\eta_{o,iR-free,CCL})}{\frac{4FD_{CCL}C_{in}}{l_t}}}\right\}\frac{C_{CCL-GDL}}{C_{in}}$<br>$\eta_{o,CCL} = \eta_{o,iR-free,CCL} + \frac{J}{\sigma/l_t}$<br>**(This work)** | |

# Chapter 4

# Isothermal two-dimensional model of a proton exchange membrane fuel cell: Analytical solution for reaction-controlled regime of CCL operation

The content of this chapter is published in,
"Chemical Engineering Science, volume no. 190, 23rd November 2018, pages: 333–344" [95].

The typical boundary condition of uniform oxygen concentration at CCL–GDL interface in one dimensional modelling of CCL, (as was assumed in chapter 3) is typically not true in practical situations. It is intuitively clear that consumption of oxygen in the ORR would reduce its concentration in the oxidant during its travel in the flow channels of the cathode plates. Therefore, oxygen concentration at the CCL-GDL interface should also reduce from inlet to the outlet. This non-uniformity of oxygen concentration gives rise to a current density profile along the channel. Three-dimensional numerical simulations of PEMFC rigorously account for the non-uniform oxygen concentration at the CCL-GDL interface over the entire active area. Some of the earlier work in this area are by [71-80], while a comprehensive review of prior work in this area can be found in [81-85]. However, analytical treatments of governing equations are sparse even in the limiting cases. The only exception is the work of Kulikovsky et al. (2004) [63] and Kulikovsky (2004) [64] who proposed a two-dimensional isothermal model comprising intrinsic Tafel kinetics in the CCL and oxygen transport resistance across the GDL coupled with material balance equation along flow channel, and provided analytical derivation of the current-potential relationship (refer section 2.1.3 of chapter 2). However, it was assumed that flow in the channel was plug flow and oxygen concentration was allowed to

vary only along the channel length but not along the channel depth. Under typical operating conditions of PEMFC, the flow in channels is laminar and therefore the assumption of plug flow is not realistic. Furthermore, as will be seen later, the resistances to oxygen diffusion in the GDL and in the channel are of the same order for a typical fuel cell construction. Hence, the assumption of uniform oxygen concentration along the channel depth is also not realistic. In particular, this assumption can lead to considerable deviations at high current density as will be shown later. A comparison between three-dimensional numerical simulation of governing equations and the two-dimensional analytical model proposed by Kulikovsky et al (2004) [63] should bring out the criticality of these assumptions and to the best of our knowledge, literature lacks such a comparison.

This chapter relaxes the assumptions of laminar flow and uniform oxygen concentration along the channel depth and presents analytical solutions of the revised two-dimensional model. The effects of relaxing the two assumptions are highlighted by comparing the model predictions with those of Kulikovsky et al. (2004) [63] as well as with the results of full three-dimensional numerical simulation of PEMFC under identical operating conditions.

## 4.1) Mathematical model

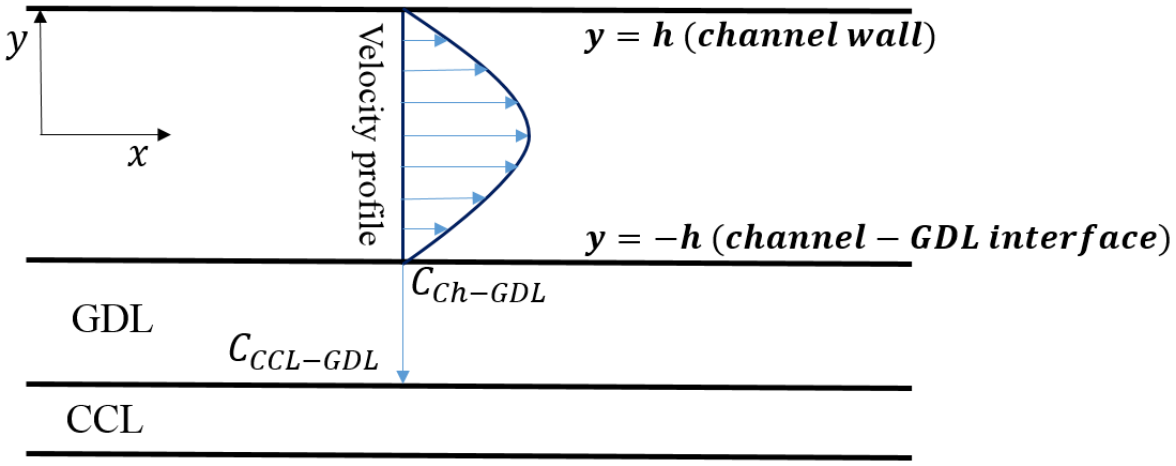


**Fig.4.1** A typical two dimensional domain in PEMFC

Figure 4.1 depicts the two-dimensional domain of the model comprising a channel of length $L$ and depth $2h$ in which laminar flow of the reactant gas occurs along the axial $(x-)$ direction and flow gradient is along the transverse $(y-)$ direction. Channel wall is located at $y = h$ and channel-GDL interface at $y = -h$. No-slip condition is assumed at both boundaries. Because of the reaction in the CCL and the consequent consumption of oxygen, the oxygen concentration in the reactant gas is expected to vary along both $x$ and $y$ directions in the flow channel. Oxygen flux at the channel wall is zero while that at the channel-GDL interface is related to the rate of consumption by ORR in the CCL.

At steady state, transport equation for oxygen in channel can be written as,

$$u\frac{\partial C}{\partial x} = D\left(\frac{\partial^2 C}{\partial x^2} + \frac{\partial^2 C}{\partial y^2}\right) \tag{4.1}$$

where $C(x, y)$ and $u(y)$ are respectively the local oxygen concentration and velocity at any point $(x, y)$ in the channel and $D$ is the oxygen diffusion coefficient in channel. It is assumed here that the volumetric flow rate in the channel does not change along the length. This is a reasonable assumption if the change in number of moles due to ORR is not substantial compared to the inert concentration ($N_2$) in the flow for a given stoichiometry. This assumption is revisited later in this chapter.

For typical commercial fixtures of closed cathode type such as 25 $cm^2$ or 100 $cm^2$ of Fuel Cell Technologies Inc., whose specifications given in Table 4.1, operating at 1 $A/cm^2$ with air stoichiometry of 3 on the cathode side, the Reynolds numbers turn out to be ~ 440 and ~ 780 for 25 $cm^2$ and 100$cm^2$, respectively. This suggests that the flow in the channels is in the laminar regime. Estimation of Reynolds number in flow fields of larger area cathode plates also suggests laminar regime of flow. Further, as will be verified later, it is appropriate to

neglect the term $\frac{\partial^2 C}{\partial x^2}$ when compared with the term $\frac{\partial^2 C}{\partial y^2}$ in equation (4.1). Thus, equation (4.1) can be written as

$$\frac{3}{2} U_{mean} \left[1 - \left(\frac{y}{h}\right)^2\right] \frac{\partial C}{\partial x} = D \frac{\partial^2 C}{\partial y^2} \tag{4.2}$$

where $U_{mean}$ is the average inlet velocity. The boundary conditions are,

$$\text{At } y = h, \quad \frac{\partial C}{\partial y} = 0 \tag{4.3a}$$

$$\text{At } y = -h, \quad 4FD \frac{\partial C}{\partial y} = J \tag{4.3b}$$

$$\text{At } x = 0, \; C = C_{in}(y) \tag{4.3c}$$

Here $J$ is the local current density at any point '$x$' along the channel length and $C_{in}$ is inlet oxygen concentration. The boundary condition (4.3c) essentially neglects the entry effect and suggests that a steady state concentration profile is developed only along the channel depth. The consequences of this assumption are discussed later in the chapter.

**Table 4.1** Specifications of typical commercial fixtures (by Fuel Cell Technologies., inc)

| **Parameter** | **25 cm$^2$** | **100 cm$^2$** |
|---|---|---|
| Flow field type | Serpentine | Serpentine |
| Number of channels | 3 | 4 |
| Width of the channel | 0.8 mm | 0.8 mm |
| Depth of channel | 1 mm | 2 mm |
| Volumetric flow rate of air according to stoichiometry of 3 at 1 A/cm$^2$ | 1.24 lpm | 4.97 lpm |
| Reynolds number | ~ 440 | ~ 780 |

It may be noted here that the governing equation (4.2) is similar to the classical Graetz problem of heat transfer albeit with a different boundary condition (Leal 2007 [96]). The classical Graetz problem has a constant temperature boundary condition (analogously, a constant oxygen concentration at the wall) whereas the boundary condition given by equation (4b) for the

problem of our interest involves a flux that varies in the axial $(-x)$ direction. Therefore, while the solution to Graetz problem is not applicable to our problem directly, nonetheless, we invoke a similar methodology of separation of variables followed by a power series approach to seek a solution to equation (4.2) and equations (4.3a-4.3c).

We look for analytical solutions to equation (4.2) by invoking separation of variables such that $C = C_x(x)C_y(y)$, where $C_x(x)$ has dimensions of concentration and scales with $C_{in}$ while $C_y$ denotes the dimensionless concentration profile along the channel depth. Substituting in equation (4.2) gives

$$\frac{1}{C_x}\frac{dC_x}{dx} = \frac{D}{\frac{3}{2}U_{mean}\left(1-\left(\frac{y}{h}\right)^2\right)}\frac{1}{C_y}\frac{d^2C_y}{dy^2} = -m^2 \tag{4.4}$$

Strictly speaking, there exists a finite length near the inlet over which the concentration profile develops with the flow and after which it becomes self-similar for any '$x$' thereafter. Neglecting this entry length (as reflected in equation (4.3c)), we propose a solution as,

$$C(x,y) = C_{in}\exp(-m^2Lx^*)C_y \tag{4.5}$$

With $x^* = \frac{x}{L}$, $C_y^* = C_y$, $y^* = \frac{y}{h}$ and $k^2 = \frac{3}{2}\frac{U_{mean}h^2m^2}{D}$, equation (4.4) yields,

$$\frac{d^2C_y^*}{dy^{*2}} = -k^2(1-y^{*2})C_y^* \tag{4.6}$$

We expect to have a monotonic decrease in oxygen concentration along the depth of the channel from a maximum value near channel wall equal to $C_{in}\exp(-m^2Lx^*)$ to some minimum value at the channel-GDL interface. We, therefore explore a power series solution for $C_y^*$ as follows

$$C_y^* = \sum_{n=0} a_n(1-y^*)^n \tag{4.7}$$

Substituting equation (4.7) in equation (4.6) and simplifying we get,

$a_2 = 0$, $a_3 = -\frac{a_0 k^2}{3}$ and $a_{n+2} = \frac{k^2(a_{n-2} - a_{n-1})}{(n+2)(n+1)}$.

The condition of maximum concentration near the channel wall suggests that $C_y^* = 1$ at $y^* = 1$ and the boundary condition (4a) yield $a_0 = 1$ and $a_1 = 0$. Furthermore, the recursive formula for $a_{n+2}$ gives $a_4 = \frac{k^2}{12}$, $a_4 = 0$, $a_6, a_7, a_8 \sim O(k^4)$ and so on. Restricting power series to $O(k^2)$, we get the approximate solution

$$C_y^* = 1 - \frac{k^2}{3}(1 - y^*)^3 + \frac{k^2}{12}(1 - y^*)^4 \tag{4.8}$$

Thus, oxygen concentration profile in the channel is,

$$C = C_{in}\exp(-m^2 L x^*)\left\{1 - \frac{k^2}{3}(1 - y^*)^3 + \frac{k^2}{12}(1 - y^*)^4\right\} \tag{4.9}$$

The unknown $k^2$ and therefore $m^2$ can be estimated using the boundary condition (4.3b).

In the reaction kinetics-controlled regime, the overall consumption of oxygen is governed by the intrinsic ORR kinetics while the oxygen concentration remains constant along the thickness of CCL. The current-overpotential-concentration relationship is then given by the Tafel equation as

$$J = i_{o,c} A l_t \left[\exp\left(\frac{\eta_{o,CCL}}{A_c}\right)\right] \frac{C_{CCL-GDL}}{C_{in}} \tag{4.10}$$

Where, $i_{o,c}A$ is volumetric exchange current density (A/m$^3$), $l_t$ is CCL thickness (m), $\eta_{o,CCL}$ is cathodic overpotential which is assumed to be uniform along the length of the channel (V), $A_c$ is Tafel slope (V) and $C_{CCL-GDL}$ is oxygen concentration at the CCL-GDL interface (mol/m$^3$). Here, local $J - \eta_{o,CCL} - C_{CCL-GDL}$ relation at any point '$x$' along the length of the channel is assumed to be get dictated by one-dimensional MH model of the CCL (in reaction controlled regime of CCL operation) i.e. the gradients in '$x$' and '$z$' directions in the CCL are assumed to be negligible. This assumption is verified later in the sixth chapter. The relation between

$C_{CCL-GDL}$ and oxygen concentration at channel-GDL interface ($C_{Ch-GDL} = C|_{x;y=-h} = C_x C_y|_{y=-h}$) can be obtained by writing oxygen conservation equation across GDL as,

$$\frac{4FD_{GDL}}{l_{GDL}}(C_{Ch-GDL} - C_{CCL-GDL}) = i_{o,c} A l_t \left[\exp\left(\frac{\eta_{o,CCL}}{A_c}\right)\right]\frac{C_{CCL-GDL}}{C_{in}} \quad (4.11)$$

Here, $D_{GDL}$ is the diffusion coefficient for oxygen in the GDL and $l_{GDL}$ is the GDL thickness. Defining $J_{1-D} = i_{o,c} A l_t \left[\exp\left(\frac{\eta_{o,CCL}}{A_c}\right)\right]$, $J_{GDL} = \frac{4FD_{GDL}C_{in}}{l_{GDL}}$ , $\alpha = \frac{J_{1-D}}{J_{GDL}}$ and combining equations (4.10) and (4.11), we get,

$$J = \frac{J_{1-D}}{1+\alpha}\frac{C_x C_y|_{y=-h}}{C_{in}} \quad (4.12)$$

Note that $J_{GDL}$ is the limiting current density corresponding to the maximum flux of oxygen diffusion through the GDL. Substituting equation (4.12) in the boundary condition (4.3b), we get,

$$\frac{dC_y}{dy^*} = \frac{\xi}{1+\alpha} C_y \text{ at } y^* = -1 \quad (4.13)$$

Here, $\xi = \frac{J_{1-D}}{J_{diff,ch}}$ and $J_{diff,ch} = \frac{4FDC_{in}}{h}$. Note that $J_{diff,ch}$ is the limiting current density corresponding to the maximum flux of oxygen diffusing towards the channel-GDL interface in the channel.

Now, equation (4.9) must satisfy equation (4.13) at $y^* = -1$ and therefore,

$$k^2 = \frac{3}{4}\frac{\xi}{1+\alpha+\xi} \quad (4.14)$$

Since $\alpha, \xi$ are positive numbers, it is clear from equation (4.14) that $k^2 < 1$ thus confirming that the series solution equation (4.7) converges. Recalling that $k^2 = \frac{3}{2}\frac{U_{mean}h^2m^2}{D}$ gives,

$$m^2 L = \frac{\beta}{1+\alpha+\xi} \quad (4.15)$$

Here $\beta = \frac{J_{1-D}}{J_{flow}}$ and $J_{flow} = \frac{8FU_{mean}hC_{in}}{L}$. Note that $J_{flow}$ signifies the current density corresponding to the molar flux of oxygen that is convected in the channel. $J_{flow}$ is proportional to the stoichiometry of oxidant.

Now, combining equations (4.9), (4.14) and (4.15), we get,

$$C(x,y) = C_{in}\exp(-\frac{\beta x^*}{1+\alpha+\xi})\left\{1 - \frac{\xi}{4(1+\alpha+\xi)}(1-y^*)^3 + \frac{\xi}{16(1+\alpha+\xi)}(1-y^*)^4\right\} \quad (4.16)$$

Equation (4.16) defines the local oxygen concentration at any given point $(x, y)$. Correspondingly, the local current density at any point '$x$' along the channel is,

$$J = \frac{4FDC_x}{h}\left\{\frac{\partial C_y^*}{\partial y^*}|_{y^*=-1}\right\} = \frac{J_{1-D}}{1+\alpha+\xi}\exp(-\frac{\beta x^*}{1+\alpha+\xi}) \quad (4.17)$$

Equation (4.17) can be integrated over the channel length to yield the current-potential relationship (polarization curve) for the entire active area. Thus, we get,

$$J_{total} = J_{flow}\left\{1 - \exp(-\frac{\beta}{1+\alpha+\xi})\right\} \quad (4.18)$$

Note that,

$$\alpha = \frac{J_{1-D}}{J_{GDL}} \quad (4.19)$$

$$\beta = \frac{J_{1-D}}{J_{flow}} \quad (4.20)$$

$$\xi = \frac{J_{1-D}}{J_{diff,ch}} \quad (4.21)$$

Where, $J_{1-D} = i_{o,c}Al_t\left[\exp\left(\frac{\eta_{o,CCL}}{A_c}\right)\right]$, $J_{GDL} = \frac{4FD_{GDL}C_{in}}{l_{GDL}}$, $J_{flow} = \frac{8FU_{mean}hC_{in}}{L}$ and $J_{diff,ch} = \frac{4FDC_{in}}{h}$.

Equation (4.18) gives an analytical expression for the polarization curve in a single straight-channel flow field for the case of reaction-controlled CCL regime. In deriving equation (4.18)

we have relaxed the assumptions of plug flow and uniform oxygen concentration along the channel depth, which were invoked in the earlier efforts of analytical modelling (Kulikovsky et al (2004) [63]). Before comparing the predictions of equation (4.18) with earlier work, we will briefly discuss the limiting cases of equation (4.18).

***Limiting cases***

**a)** $\boldsymbol{J_{1-D} << J_{flow}, J_{diff,ch}, J_{GDL}}$ **or** $\boldsymbol{\alpha, \xi, \beta << 1.}$

This physically means that the consumption rate of oxygen by intrinsic ORR kinetics is the rate controlling step i.e., it is slower than the rates of oxygen transport across GDL, oxygen diffusion in channel and inlet oxygen molar flow rate. This typically happens at lower overpotentials. For $\alpha, \xi, \beta << 1$, $\exp\left(-\frac{\beta}{1+\alpha+\xi}\right) \approx 1 - \frac{\beta}{1+\alpha+\xi}$. Also, neglecting $\alpha$ and $\xi$ relative to 1, equation (4.18) gives $J_{total} = J_{1-D}$. Therefore, the power density is solely dictated by intrinsic ORR kinetics in the CCL, while the gradients of oxygen in the channel and in the GDL are negligible.

**b)** $\boldsymbol{J_{GDL} << J_{1-D}, J_{diff,ch}, J_{flow}}$ **or** $\boldsymbol{\alpha >> 1}$ **and** $\boldsymbol{\alpha >> \xi, \beta}$ **.**

This regime implies that oxygen transport across GDL is the rate limiting step i.e., it is slower than intrinsic ORR kinetics, inlet oxygen molar flow rate and oxygen diffusion in channel. This possibility can become a reality at high current density if the GDL is over-compressed or flooded, causing substantial loss of porosity. For $\alpha >> 1$ and $\alpha >> \xi, \beta$, , $\exp\left(-\frac{\beta}{1+\alpha+\xi}\right) \approx 1 - \frac{\beta}{\alpha}$ and therefore equation (4.18) simplifies to $J_{total} = J_{GDL}$. The power density is then limited by oxygen transport rate across the GDL.

c) $\boldsymbol{J_{diff,ch} << J_{1-D}, j_{GDL}, J_{flow}}$ **or** $\boldsymbol{\xi >> 1}$ **and** $\boldsymbol{\xi >> \alpha, \beta}$ **.**

When the diffusion resistance for oxygen in channel is higher than diffusion resistance in the GDL, and when the diffusive flux of oxygen in the channel is less than the rate of consumption of oxygen by intrinsic ORR kinetics and molar flux of inlet oxygen, then equation (4.18) yields $J_{total} = J_{diff,ch}$. This could be possible at higher current densities when the flow channels are deep and when the GDL is highly porous.

d) $\boldsymbol{J_{flow} << J_{1-D}, J_{GDL}, J_{diff,ch}}$ **or** $\boldsymbol{\beta >> 1}$ **and** $\boldsymbol{\beta >> \alpha, \xi}$ **.**

When the stoichiometry of the oxidant is limiting i.e., when inlet oxygen molar flux is lower than the rate of oxygen consumption in the CCL, the oxygen flux across GDL and the diffusive flux rate in the channel, then $\exp\left(-\frac{\beta}{1+\alpha+\xi}\right)$ may be neglected relative to 1 in equation (4.18), and consequently we get $J_{total} = J_{flow}$.

The final limiting case is that of fast oxygen diffusion in the channel relative to diffusion through the GDL. In this case, $\xi << \alpha$ and so equation (4.18) simplifies to

$$J_{total} = J_{flow}\left\{1 - \exp(-\frac{\beta}{1+\alpha})\right\} \tag{4.22}$$

Equation (4.22) is in fact the expression derived by Kulikovsky et al. (2004) [63] (refer section 2.4 of chapter 2). It is instructive to compare $\xi$ with $\alpha$. For a given $J_{1-D}$, $\frac{\alpha}{\xi} = \frac{D}{D_{GDL}}\frac{l_{GDL}}{h}$. For typical values of $D \sim 3 \times 10^{-5}\ m^2/s$, $D_{GDL} \sim 6.67 \times 10^{-6}\ m^2/s$ (Pharoah et al. 2006 [92]), $l_{GDL} \sim 3 \times 10^{-4}\ m$, and $h \sim 1 \times 10^{-3}\ m$, we get $\frac{\alpha}{\xi} \sim O(1)$. Thus, the diffusional resistances in the GDL and in the channel are of the same order of magnitude and consequently, the contribution of concentration gradient in the channel on the polarization curve cannot be neglected in a practical scenario. Thus, the polarization curve derived here (equation (4.18)) is an important correction to equation (4.22).

In the following section we will first compare the predictions of equation (4.18) and equation (4.22) with full three-dimensional simulations of governing equations for the same flow geometry and operating conditions. Next, the differences between these three predictions will be assessed based on the effects of entrance length. This will be followed by a discussion on the non-monotonic nature of local polarization curves predicted by equations (4.18) and (4.22). We then assess the effect of velocity profiles and concentration gradient in the channel on the polarization curve predicted by analytical models. We will also critically assess the validity of assumptions made while deriving equation 4.18 viz., 1) constant volumetric flow rate along the length of the channel and 2) neglecting $\frac{\partial^2 C}{\partial x^2}$ over $\frac{\partial^2 C}{\partial y^2}$ in equation 4.1.

## 4.2) Results and Discussions

*Comparison between two-dimensional analytical solution and three-dimensional numerical simulation*

Figure 4.2 describes a single channel flow geometry invoked for simulation study. It includes single flow channels on the anode and cathode sides, GDLs and catalyst layers on the anode and cathode sides, and a membrane in between. Details about the numerical simulation are provided in section 2.6 of chapter 2. The numerical values of different parameters used in the simulation are listed in table 4.2. Identical values are used for predictions of the analytical model. It must be noted that the two-dimensional description assumes an infinitely small rib-width. However, the three-dimensional simulation requires a finite rib-width since it is the path for electron transport. Therefore, in order to compare the analytical model predictions with the three-dimensional simulations, we purposefully invoked a geometry in the numerical simulations such that $w_{channel} >> w_{rib}$, where $w$ denotes width. The effect of realistic rib width is discussed in the subsequent chapter.

**Table 4.2** Numerical values of different parameters

| | |
|---|---|
| $A_c$ | 0.026 V |
| $C_{in}$ | 8.2 $mol/m^3$ |
| $D$ | $3 \times 10^{-5}\ m^2/s$ |
| $D_{GDL}$ | $6.7 \times 10^{-6}\ m^2/s$ |
| $D_{CCL}$ | $1 \times 10^{-5}\ m^2/s$ |
| $F$ | 96500 $C/mol$ |
| $2h$ | 0.001 $m$ |
| $i_{o,c}A$ | 1000 $A/m^3$ |
| $L$ | 0.02 $(m)$ |
| $l_{GDL}$ | 300 $\mu m$ |
| $l_t$ | 8 $\mu m$ |
| $U_{mean}$ | 0.195 $m/s$ |
| $w_{channel}$ | 0.001 $m$ |
| $w_{rib}$ | 0.00002 $m$ |
| $J_{GDL}$ | $6.9\frac{A}{cm^2}$ |
| $J_{flow}$ | $3\frac{A}{cm^2}$ |
| $J_{diff,ch}$ | $18.4\frac{A}{cm^2}$ |

The numerical values of parameters shown in table 4.2 are purposely selected to ensure that oxygen consumption rate in CCL is governed by intrinsic ORR kinetics. This can be checked as follows. It was shown by Kulikovsky (2010) [42] that oxygen consumption rate in the CCL gets modulated due to oxygen transport resistance across CCL when $\frac{4FD_{CCL}C_{in}}{l_t} < J_{1-D}$. Here the value of gas phase diffusion coefficient of oxygen in the CCL is assigned as $D_{CCL}$~$10^{-5}\ m^2/s$, which yields $\frac{4FD_{CCL}C_{in}}{l_t} \sim 400\frac{A}{cm^2}$. The maximum $J_{1-D}$ considered in our calculations is $J_{1-D,max} = 38\frac{A}{cm^2}$ at $\eta_{o,CCL} = 0.46\,V$. Thus, $J_{1-D} \ll \frac{4FD_{CCL}C_{in}}{l_t}$. Similarly, Kulikovski (2002, 2010) [41,42] has shown than the consumption rate in CCL gets modulated due to proton transport resistance across the CCL only when $\frac{2\sigma A_c}{l_t} < J$. Here, $\sigma$ is the proton conductivity of membrane and it's value is taken as 20 S/cm. Thus, the numerical value of $\frac{2\sigma A_c}{l_t}$ is $\sim 1300\ \frac{A}{cm^2}$. Therefore, the aforementioned choice of parameter values ensures that the consumption rate in the CCL is dominated by intrinsic kinetics. Also, it is assumed in the

simulations that anode side exchange current density ($i_{o,a}Al_t$) is $10^7$ times higher than the cathode side exchange current density and $J_{GDL} \approx 400\frac{A}{cm^2}$, $J_{flow} \approx 30\frac{A}{cm^2}$ on the anode side. These values ensure that the anode is not starved of fuel. The proton conductivity of membrane is assumed to be 10000 S/m and the electrical conductivity is assumed to be 100000 S/m. This therefore ensures that the polarization curve from the simulations is an iR corrected polarization curve (as overpotential caused due to ohmic resistance will be negligible).

It is worth reiterating here that in this study the consumption rate in the CCL is assumed to be equal to the intrinsic Tafel's kinetics, which essentially suggests a reaction controlled regime. The other regimes namely, regime of poor oxygen transport in the CCL and poor proto transport in the CCL will be dealt in the next chapter.

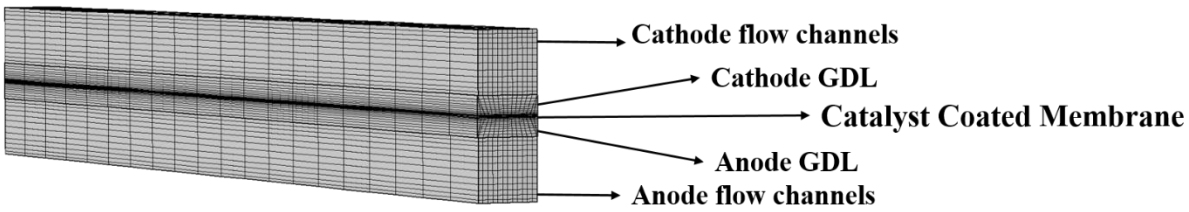


**Fig.4.2** Three dimensional computational domain considered for simulation

Figure 4.3 shows comparison between polarization curves obtained from analytical theories equation (4.18), equation (4.22) and the three-dimensional simulation. It is evident that for overpotentials above 0.35 V the analytical model described by Kulikovsky et al (2004) [63], which assumes plug flow and uniform oxygen concentration along the channel depth, overpredicts the current density relative to the three-dimensional simulation. On the other hand, predictions of the analytical model developed in this work (equation (4.18)), in which these assumptions were relaxed, are in quantitative agreement with the simulated three-dimensional polarization curve. This underlines the importance of diffusional resistance along the depth of the channel, specifically at higher current densities.

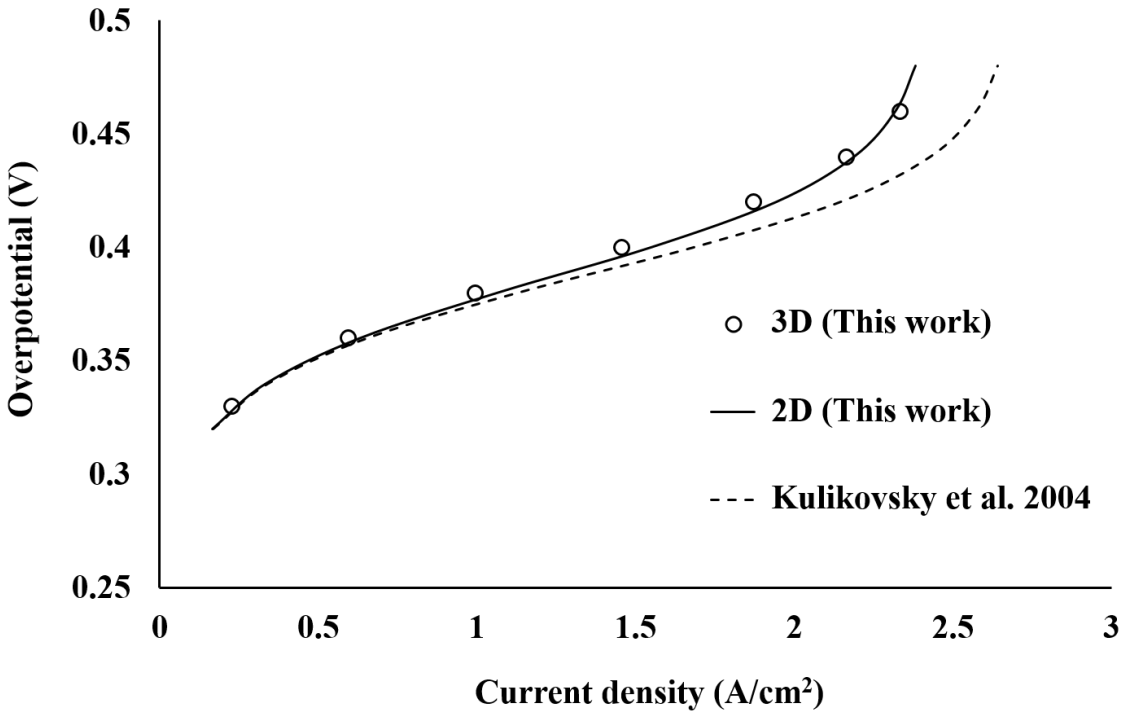


**Fig.4.3** Comparison between the polarization curves obtained by analytical theories versus a three-dimensional numerical simulation

While the oxidant (air) flow rate used in the above calculations corresponds to the stoichiometry of 3 for the current density of $1\frac{A}{cm^2}$ , the same trends can be seen for higher stoichiometries as long as the flow is in the laminar regime.

The accuracy of the predicted local current density along channel length [equation (4.17)] and concentration profile along the channel depth [equation (4.8) and equation (4.14)], which were obtained from the approximate power series solution, was tested by comparing against numerical solution to the governing equation (4.2) obtained using COMSOL's in-built PDE solver. For simplicity, we will call the analytical solution as $2D_{analytical}$ and numerical solution as $2D_{numerical}$ henceforth in the paper.

Figure 4.4 illustrates the local current density profiles along the axial $(x-)$ direction obtained by $2D_{analytical}$, $2D_{numerical}$ and the full three-dimensional simulation at $\eta = 0.46\,V$. The current density profile from the three-dimensional simulation is taken at the mid-plane of

membrane thickness and at middle of the channel width. It can be observed that except in the initial region along the axial ($x-$) direction of the flow channel, the $2D_{analytical}$ current density profile matches well with the $2D_{numerical}$ as well as with the current density profile predicted by three-dimensional simulation. The discrepancy in the initial region is related to the entrance length effect, and is discussed in the next sub-section. Figure 4.5 shows the comparison between concentration profiles along the transverse (y-) direction obtained by $2D_{analytical}$, $2D_{numerical}$ and three dimensional simulation at $x^* = 0.5L$ and $\eta_{o,CCL} = 0.46\,V$. The concentration profile predicted by the $2D_{analytical}$ approach is similar to that predicted by the three-dimensional simulation. The comparisons shown in figure 4.4 and figure 4.5 validate the accuracy of the approximate analytical power series solution.

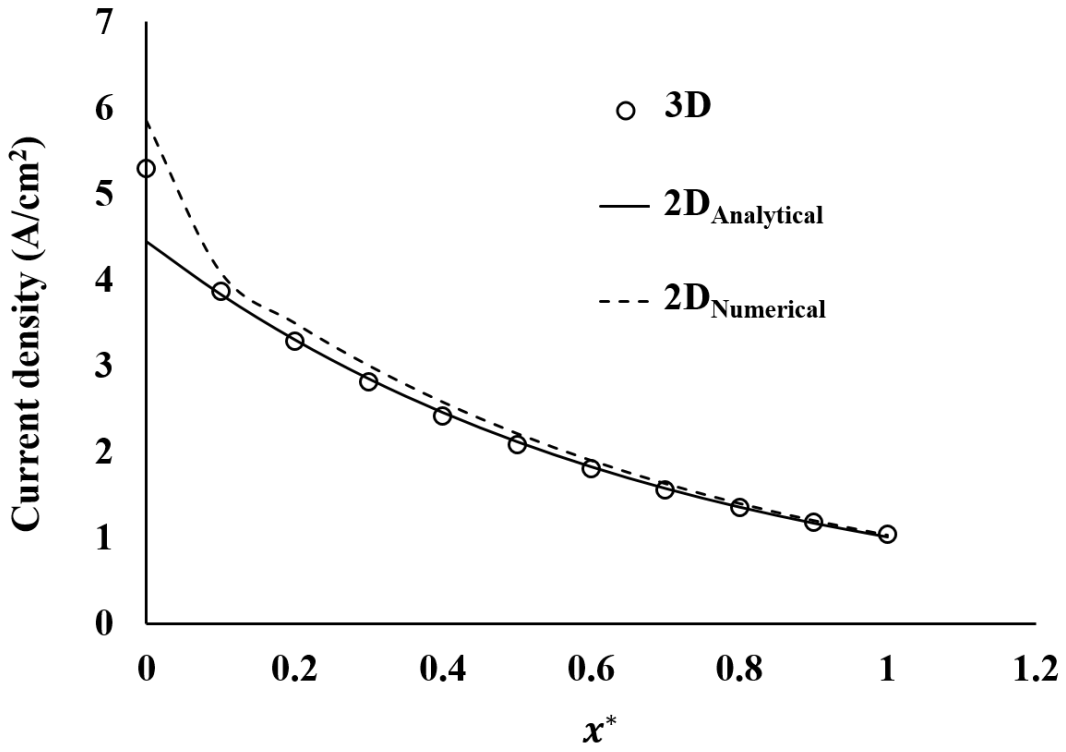


**Fig.4.4** Comparison between the local current density profiles along the axial ($x-$) direction obtained by two dimensional analytical as well as numerical solution versus a three-dimensional numerical simulation at $\eta_{o,CCL} = 0.46\,V$

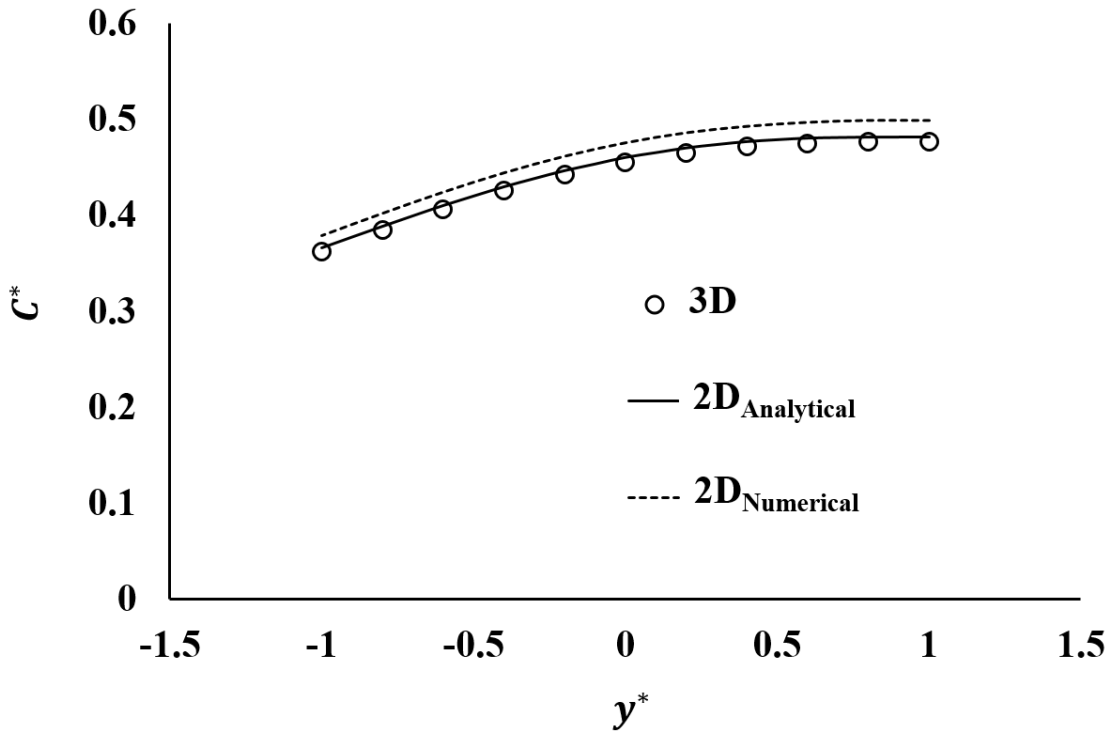


**Fig.4.5** Comparison between the oxygen concentration profiles along the transverse $(y-)$ direction obtained by two dimensional analytical as well as numerical solution versus a three-dimensional numerical simulation at , $x^* = 0.5L$ and $\eta_{o,CCL} = 0.46\,V$

*Effect of finite 'entrance length'*

As explained in Section 4.1 (equation (4.3c)), we have assumed that concentration profile along the transverse $(y-)$ direction develops within an infinitesimal axial length. The three-dimensional numerical simulation and the $2D_{numerical}$ solution do not assume fully developed concentration profile at the inlet. The inlet boundary condition is taken as $C = C_{in}$ for all $y^*$, and the concentration profile is allowed to develop over a finite entry length. The higher oxygen concentration near the GDL over the entry length relative to the fully developed concentration profile results in prediction of higher current density in the entry length by the $2D_{numerical}$ and three dimensional simulation compared to the $2D_{analytical}$ prediction. This was seen in figure 4.4. The development of oxygen concentration profile along the transverse $(y-)$ direction for different $x^*$ as computed using the three-dimensional numerical simulation is elucidated in figure 4.6. It can be observed that after $x^* = 0.04$, oxygen concentration profile becomes self-

similar in $x$. Thus the entry length required for achieving fully developed oxygen concentration profile is only 4% of the total length or equivalently, it is $L_{entry} = 0.8(2h)$ i.e., about one channel depth. The effect of this small entry length does not have significant influence on polarization curve for the entire active area.

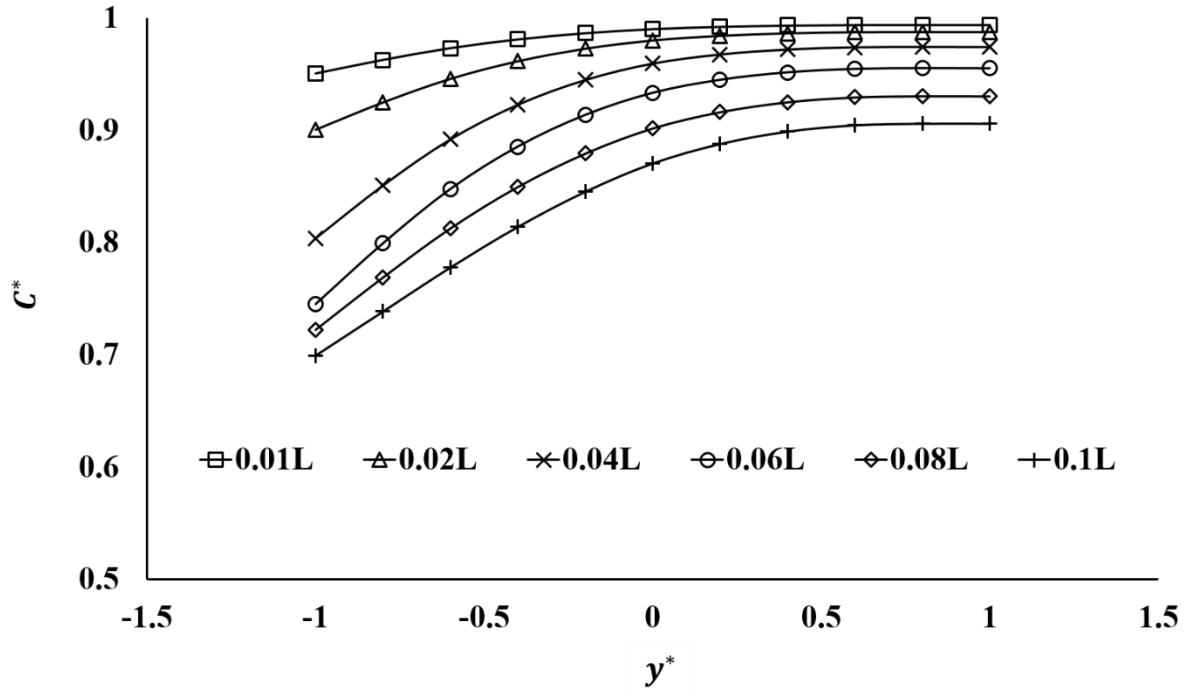


Figure 4.6:- Development of oxygen concentration profile along the transverse $(y-)$ direction in a three dimensional simulation

*Locally non-monotonic nature of polarization curve*

Kulikovsky et al (2004) [63] showed that if the oxidant stoichiometry is low then depletion in oxygen concentration along the channel can cause a turning point in the local polarization curve making it non-monotonic. However, the total polarization curve was shown to be monotonic. The authors showed that $\alpha \geq \beta$ is a sufficient condition to avoid the local non-monotonicity in current-potential relationship. The expression for local current density (equation (4.17)) suggests that there exists a critical $(x^*)_{crit}$ at which $\frac{\partial j}{\partial \eta} = 0$. Here, we explore

the effects of relaxing the assumptions of plug flow and uniform oxygen concentration along the channel depth on the local non-monotonicity in polarization curve. Figure 4.7 compares the local polarization curves at $x^* = 0.8$ and $\eta_{o,CCL} = 0.46\,V$ obtained from: (i) equation (4.17), (ii) three-dimensional simulations, and (iii) the Kulikovsky (2004) model [63]. From equation (4.17), it can be shown that at the turning point, $\frac{dj}{d\eta_{o,CCL}} = 0$ gives the condition $\frac{1}{J_{1-D}} = \frac{0.8}{J_{flow}} - (\frac{1}{J_{GDL}} + \frac{1}{J_{diff,ch}})$, which predicts a critical overpotential $\eta_{crit}$ for incipient non-monotonicity. For the numerical values enlisted in table 4.2, we get $\eta_{crit} = 0.434\,V$. Note that for the Kulikovsky (2004) model [63], $J_{diff,ch} \to \infty$ gives $\frac{1}{J_{1-D}} = \frac{0.8}{J_{flow}} - \frac{1}{J_{GDL}}$ and correspondingly $\eta_{crit} = 0.42\,V$. As can be seen from figure 4.7, the polarization curve predicted by the $2D_{analytical}$ solution agrees well with the three-dimensional simulation in terms of its shape and value of $\eta_{crit}$. The Kulikovsky model underpredicts the maximum current density and the critical overpotential.

Also, the condition to avoid local non-monotonicity can be derived by equating $J_{max}$ and $J_\infty$ where $J_{max}$ is the current density corresponding to $\frac{dj}{d\eta_{o,CCL}} = 0$ and $J_\infty$ is the current density when $\eta_{o,CCL} \to \infty$. Setting $\frac{dj}{d\eta} = 0$ gives $(x^*)_{crit} = \frac{1+\alpha+\xi}{\beta}$ and correspondingly $J_{max} = \frac{J_{1-D}}{\beta(x^*)_{crit}}\exp(-1)$. Substituting $\eta_{o,CCL} \to \infty$ in equation (4.17) gives $J_\infty = \frac{J_{1-D}}{\alpha+\xi}\exp(-\frac{\beta x^*}{\alpha+\xi})$. Note here that $\alpha, \xi >> 1$ for $\eta_{o,CCL} \to \infty$. Thus $J_{max} = J_\infty$ leads to $\frac{\beta(x^*)_{crit}}{\alpha+\xi} = 1$. Hence, relaxing the assumptions of plug flow and uniform oxygen concentration along the channel depth yields $\alpha + \xi \geq \beta$ (or, $\frac{1}{J_{GDL}} + \frac{1}{J_{diff,ch}} > \frac{1}{J_{flow}}$) to be a sufficient condition to avoid local non-monotonic nature of polarization curves. It can be observed that for a given overpotential and $J_{flow}$, Kulikovsky's formulation underpredicts $(x^*)_{crit}$.

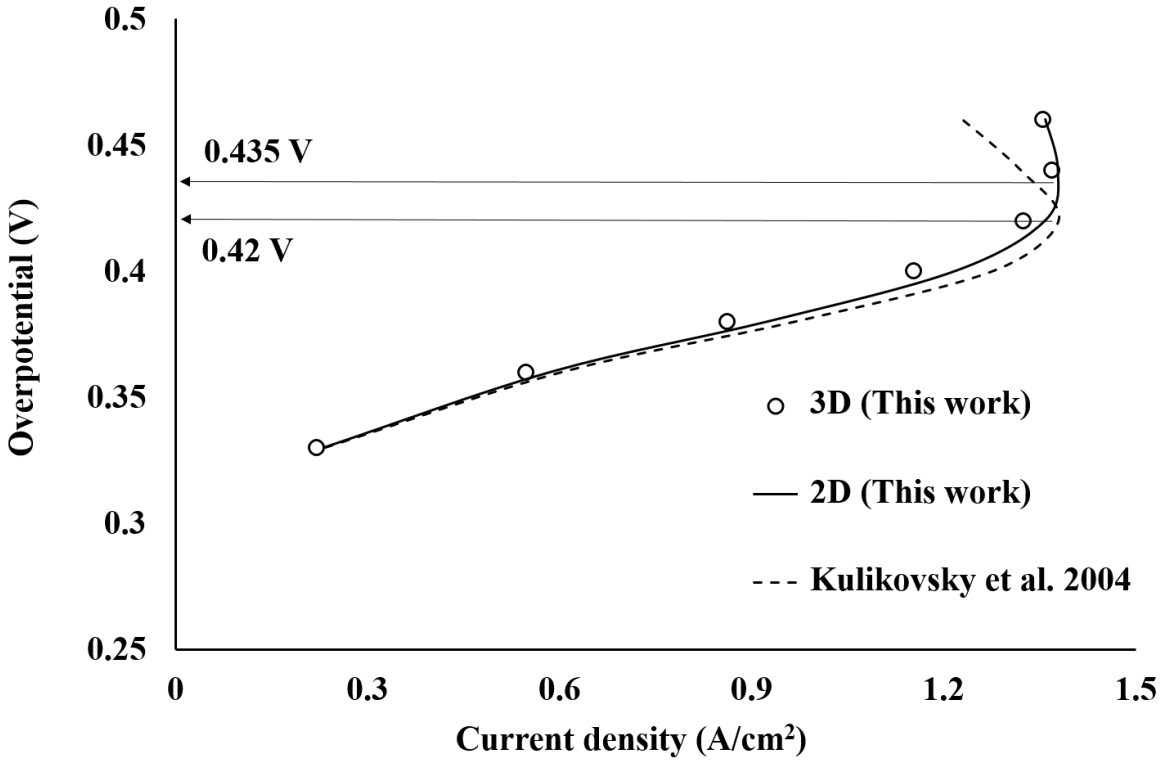


**Fig.4.7** Comparison between local polarization curves at $x^* = 0.8$ and corresponding $\eta_{crit}$

*Plug flow versus Laminar flow*

In order to understand the effects of velocity profile and oxygen concentration gradient in the channel independently, we explore the case of plug flow while still retaining oxygen concentration gradient along the depth of channel. The polarization curve predicted for this case can then be compared with equation (4.18) to understand the effect of velocity profile, and with equation (4.22) to understand the effect of concentration gradient.

When flow in the channel is plug flow, equation (4.2) transforms to,

$$U_{mean}\frac{\partial C}{\partial x} = D\frac{\partial^2 C}{\partial y^2} \tag{4.23}$$

Equation (4.23) along with the boundary conditions given by equations (4.3a-4.3c) can be solved in a straightforward manner using separation of variables to give

$$C(x,y) = \sum_{i=0}^{i=\infty} C_{in} \exp\left(-\frac{2k_i^2 \beta x^*}{\xi}\right) \cos k_i (1 - y^*) \quad (4.24)$$

where, $k_i^2 = \frac{U_{mean} h^2 m_i^2}{D}$ are the eigen values. The local current density is then given by

$$J = \frac{4FDC_x}{h} \left\{ \frac{\partial C_y^*}{\partial y^*} |_{y^*=-1} \right\} = \frac{J_{1-D}}{\xi} \sum_{i=0}^{i=\infty} \exp\left(-\frac{2{k_i}^2 \beta x^*}{\xi}\right) k_i \sin 2k_i \quad (4.25)$$

The boundary condition (4.3b) provides the eigen values

$$k_i \tan 2k_i = \frac{\xi}{1+\alpha} \quad (4.26)$$

Numerical solution of equation (4.26) shows that $k_0 >> k_1 >>> k_2$ and so on. Therefore, the first term in the series is sufficient to give the current density. Integration of the current density profile over the channel length leads to the polarization curve given by

$$J = J_{flow} \frac{\sin 2k_0}{2k_0} \left(1 - \exp\left(-\frac{\beta}{1+\alpha} \frac{2k_0}{\tan 2k_0}\right)\right) \quad (4.27)$$

Figure 4.8 shows comparison between polarization curves given by equation (4.18), equation (4.22) and equation (4.27). The numerical values of different parameters are listed in table 4.2. Comparison between equations (4.18) and (4.27) shows the effect of velocity profile in the channel (note that oxygen concentration gradient in the channel is allowed in both cases). It can be observed that current density at a given overpotential is higher in case of laminar flow compared to plug flow. This is a consequence of dispersion due to laminar flow that helps in reducing the concentration gradient along the depth of channel and therefore improves transverse $(y-)$ direction oxygen transport. Similarly, comparison between equations (4.22) and (4.23) shows the effect of concentration profile in the channel (note that in both cases the velocity profile in the channel is assumed to be plug flow). It can be seen that concentration profile along the depth of the channel has a large effect on the polarization curve. The presence of concentration gradient reduces the current density for a given overpotential, as may be

expected. The polarization curve predicted by equation (4.22) would better represent the case of turbulent flow of oxidant in flow channels wherein turbulence removes gradients of velocity and concentration along the channel depth. The polarization curve predicted by equation (4.18) on the other hand, better represents the case of laminar flow of oxidant in flow channels wherein the gradient of velocity couples with the concentration gradient and improves current density.

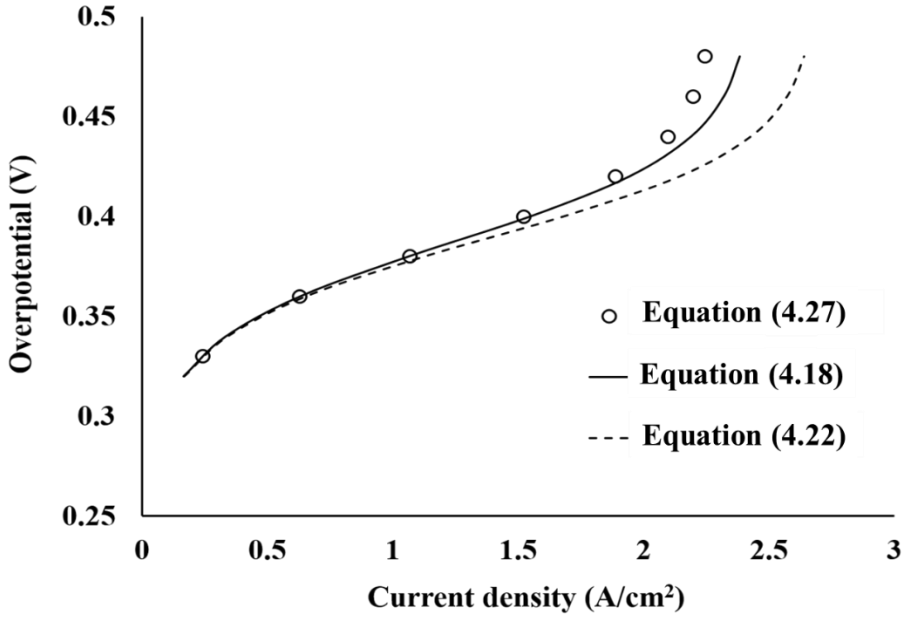


**Fig.4.8** Comparison between polarization curves for the cases when the flow is laminar versus plug type

*Verifying the constant flow rate assumption*

Figure 4.9 shows variation of velocity at the center of the channel ($U_{max}$) along axial length predicted by three-dimensional numerical simulations for two different overpotentials $\eta_{o,CCL} = 0.33\,V$ and $\eta_{o,CCL} = 0.46\,V$. The velocity was found to increase only by 11% (for $\eta_{o,CCL} = 0.46\,V$) and 1% (for $\eta_{o,CCL} = 0.33\,V$) over $0 < x^* < 1$. Thus, the assumption of a nearly constant axial velocity is a reasonable approximation.

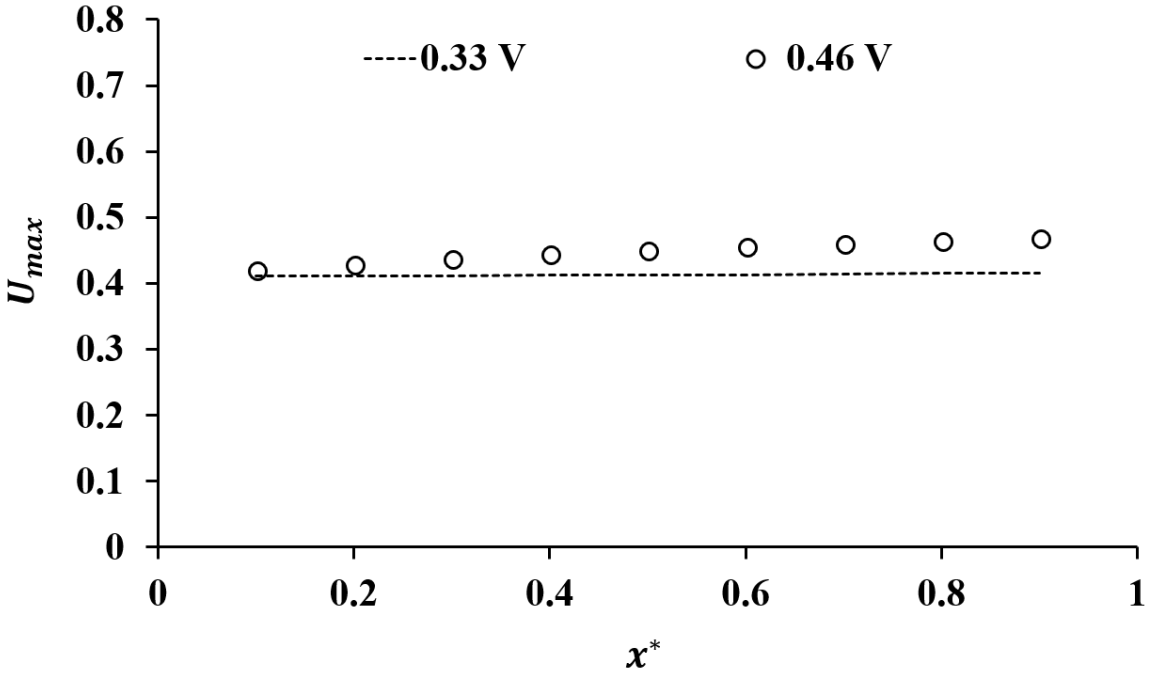


**Fig.4.9** $U_{max}$ obtained numerically from the three-dimensional simulation at two different overpotentials

*Justification for neglecting $\frac{\partial^2 C}{\partial x^2}$ over $\frac{\partial^2 C}{\partial y^2}$ in equation (4.1) and validation of this assumption*

Following the treatment of the standard Graetz problem in heat transfer, equation (4.1) can be written in non-dimensionalized form as

$$Pe\ \varepsilon\ (1 - y^{*2})\ \frac{\partial C^*}{\partial x^*} = \varepsilon^2\ \frac{\partial^2 C^*}{\partial x^{*2}} + \frac{\partial^2 C^*}{\partial y^{*2}} \tag{4.28}$$

Where, $Pe = \frac{3}{2}\frac{U_{mean}h}{D}$ is the Peclet number, $C^* = \frac{C}{C_{in}}$ and $\varepsilon = \frac{h}{l^*}$. Here, $l^*$ is a characteristic length scale along axial direction, which can be estimated following the standard method suggested by (Leal 2007, [96]). The molar flux of oxygen consumption in a section of length $\Delta x$ along the channel is $w_{channel} \times \int_x^{x+\Delta x} \frac{J}{4F} dx$. Substituting for $J$ from equation (4.17), we get consumption in the $\Delta x$ section $= w_{channel}\ \frac{j_{1-D}}{4F(1+\alpha+\xi)} \int_x^{x+\Delta x} \exp(-\frac{\beta x}{(1+\alpha+\xi)L})\ dx$.

Now, the difference between the molar flux entering and leaving the section $\Delta x$ is, $\frac{3}{2}U_{mean}w_{channel}\int_{-h}^{h}(C|_x - C|_{x+\Delta x})(1-y^{*2})\,dy$. At steady state, these two fluxes must balance out. Therefore,

$$w_{channel}\,\frac{j_{1-D}}{4F(1+\alpha+\xi)}\int_x^{x+\Delta x}\exp\left(-\frac{\beta x}{(1+\alpha+\xi)L}\right)dx = \frac{3}{2}U_{mean}w_{channel}\int_{-h}^{h}\Delta C(1-y^{*2})\,dy \qquad (4.29)$$

Evaluating the integral on the LHS, equation (4.29) can be further simplified as,

$$\frac{j_{1-D}}{4F}\exp\left(-\frac{\beta x}{(1+\alpha+\xi)L}\right)\frac{\Delta x}{(1+\alpha+\xi)} = \frac{3}{2}U_{mean}hC_{in}\int_{-1}^{1}\Delta C^{*}(1-y^{*2})\,dy^{*} \qquad (4.30)$$

Noting that $\xi = \frac{j_{1-D}}{(4FDC_{in}/h)}$ and $k^2 = \frac{3}{4}\frac{\xi}{1+\alpha+\xi}$, we get

$$\Delta x = \frac{h\,Pe}{\frac{4}{3}k^2}\exp\left(\frac{\beta x}{(1+\alpha+\xi)L}\right)\int_{-1}^{1}\Delta C^{*}(1-y^{*2})\,dy^{*} \qquad (4.31)$$

Thus, a change in scaled concentration by an amount of order one occurs over an axial length that is proportional to the right side of equation (4.31). This suggests that the characteristic axial length scale will be $l^{*}\sim h\frac{Pe}{k^2}\exp\left(\frac{\beta x}{(1+\alpha+\xi)L}\right)$. Note that for typical numerical values of parameters considered in the manuscript ($U_{mean} = 0.194\frac{m}{s}$, $D = 3\times10^{-5}\frac{m^2}{s}$ and $2h = 0.001\,m$) we have $Pe > 1$. Also, $k^2 < 1$ as noted earlier. Further, the exponential term in equation (4.31) is due to the non-uniform consumption flux (1st order in concentration) at the boundary and its effect is to stretch $l^{*}$ more and more as the fluid travels downstream in the channel. It is therefore evident that $\varepsilon^2 = \frac{h^2}{l^{*2}} \ll 1$ and hence the first term on RHS of equation (4.28) can be neglected. In other words, neglecting $\frac{\partial^2 C}{\partial x^2}$ over $\frac{\partial^2 C}{\partial y^2}$ is reasonable.

This assumption is further validated by comparing the magnitudes of the two derivatives obtained from 3d-numerical simulations in which no such assumption was made. Figure 4.10 below shows the comparison for the following typical case: $\eta_{o,CCL} = 0.67\,V$, $y^{*} = -0.6$.

As can be seen, the magnitude of $\frac{\partial^2 C}{\partial x^2}$ is at least two orders magnitude smaller than $\frac{\partial^2 C}{\partial y^2}$.

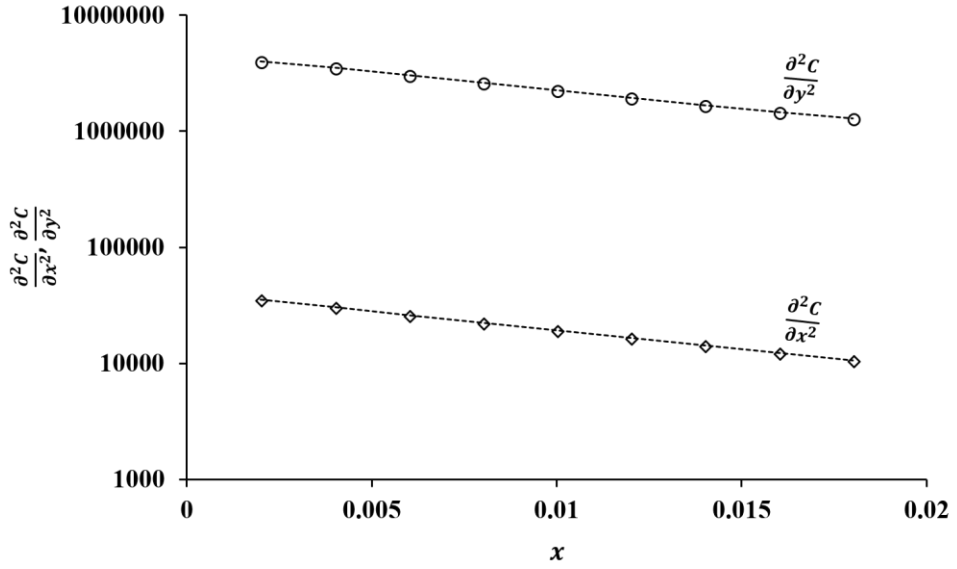


**Fig.4.10** Spatial double derivatives of oxygen concentrations obtained numerically from the three-dimensional simulation at $y^* = -0.6$ and $\eta = 0.67\ V$.

## 4.3) Conclusion

Analytical solutions of two-dimensional isothermal model for coupled reaction and transport phenomenon in a single cathode-side channel of PEMFC were derived by relaxing the assumptions of plug flow and uniform oxygen concentration along the channel depth. The analytical solutions derived here present a more comprehensive description of polarization curve and oxygen concentration profiles in the channel. Comparison of analytical solutions with three-dimensional numerical simulation highlights the importance of oxygen diffusion resistance and velocity profile along the channel depth. The local oxygen concentration profiles, total polarization curve and non-monotonic nature of local current density for low oxidant stoichiometry predicted by the two-dimensional analytical model show excellent match with three-dimensional simulation for similar geometry namely, one consisting of a channel and a narrow rib.

# Chapter 5

# Isothermal two-dimensional model of a proton exchange membrane fuel cell: Analytical solutions for transport limited regimes of CCL

The content of this chapter is published in,
"Chemical Engineering Science, volume no. 196, 16th March 2019, pages: 166–175" [97].

Our work presented in chapter 4 on developing a two-dimensional model for PEMFC under reaction-controlled regime of operation (regime 1 mentioned in table 3.1 of chapter 3) in which the two assumptions of plug flow and uniform oxygen concentration in the channel depth were specifically relaxed, showed better comparison between model predictions and the predictions of full three-dimensional simulations over the entire range of current density thereby suggesting the importance of diffusional resistance in the channel in the presence of a non-uniform velocity field.

In this chapter, we extend our two-dimensional model to other regimes of CCL operation in which overall oxygen consumption rate in the CCL is modulated by transport resistances. We begin by briefly summarizing the governing equations of the model for the case of reaction controlled regime as presented in chapter 4. Next, we present analytical expressions of polarization curve in the two transport limited regimes of CCL operation: (1) Ideal proton transport case $J > \frac{4FD_{CCL}C_{in}}{l_t}\ and\ \frac{2\sigma A_c}{l_t} \to \infty$ (regime 2 mentioned in table 3.1 of chapter 3), (2) Ideal oxygen transport case $J > \frac{2\sigma A_c}{l_t}\ and\ \frac{4FD_{CCL}C_{in}}{l_t} \to \infty$ (regime 3 mentioned in table 3.1 of

chapter 3). The polarization curves predicted by analytical expressions derived in this work for both these regimes are compared with predictions of full three-dimensional numerical simulations carried out for identical geometric, operating and material parameters.

The two-dimensional domain of PEMFC (see figure 4.1). and boundary conditions as presented in chapter 4 are:

$$\frac{3}{2}U_{mean}\left[1-\left(\frac{y}{h}\right)^2\right]\frac{\partial C}{\partial x}=D\frac{\partial^2 C}{\partial y^2} \tag{5.1}$$

where $U_{mean}$ is the average inlet velocity, $C$ is local oxygen concentration in channel and $D$ is the oxygen diffusion coefficient in channel. The boundary conditions are,

$$\text{At } y=h, \quad \frac{\partial C}{\partial y}=0 \tag{5.2a}$$

$$\text{At } y=-h, \quad 4FD\frac{\partial C}{\partial y}=J \tag{5.2b}$$

$$\text{At } x=0, \; C=C_{in}(y) \tag{5.2c}$$

In equation (5.2b), $J$ is the local current density at any point '$x$' along the channel length and is related to the overall rate of consumption of the reactants at that point.

For the case of negligible transport losses of reactant species in a macrohomogeneous CCL, $J$ is given by Tafel kinetics as

$$J=i_{o,c}Al_t\left[\exp\left(\frac{\eta_{o,CCL}}{A_c}\right)\right]\frac{C_{CCL-GDL}}{C_{in}} \tag{5.3}$$

Where, $i_{o,c}A$ is volumetric exchange current density (A/m$^3$), $l_t$ is CCL thickness (m), $\eta_{o,CCL}$ is cathodic overpotential which is assumed to be uniform along the length of the channel (V), $A_c$ is Tafel slope (V) and $C_{CCL-GDL}$ and $C_{in}$ are respectively, the oxygen concentration at the CCL-GDL interface and at the inlet (mol/m$^3$). The relation between $C_{CCL-GDL}$ and oxygen

concentration at channel-GDL interface ($C_{Ch-GDL} = C|_{x;y=-h} = C_x C_y|_{y=-h}$) can be obtained by writing oxygen conservation equation across GDL as,

$$\frac{4FD_{GDL}}{l_{GDL}}(C_{Ch-GDL} - C_{CCL-GDL}) = i_{o,c} A l_t \left[\exp\left(\frac{\eta_{o,CCL}}{A_c}\right)\right]\frac{C_{CCL-GDL}}{C_{in}} \tag{5.4}$$

Here, $D_{GDL}$ is the oxygen diffusion coefficient in GDL and $l_{GDL}$ is the GDL thickness. Defining $J_{1-D} = i_{o,c} A l_t \left[\exp\left(\frac{\eta_{o,CCL}}{A_c}\right)\right]$, $J_{GDL} = \frac{4FD_{GDL}C_{in}}{l_{GDL}}$ , $\alpha = \frac{J_{1-D}}{J_{GDL}}$ and combining equations (5.3) and (5.4), we get

$$J = \frac{J_{1-D}}{1+\alpha}\frac{C_{ch-GDL}}{C_{in}} \tag{5.5}$$

The solution to equations (5.1), (5.2) and (5.5) provided local oxygen concentration profile, local current density profile and total current density:

$$C(x,y) = C_{in}\exp(-\frac{\beta x^*}{1+\alpha+\xi})\left\{1 - \frac{\xi}{4(1+\alpha+\xi)}(1-y^*)^3 + \frac{\xi}{15(1+\alpha+\xi)}(1-y^*)^4\right\} \tag{5.6a}$$

$$J = \frac{4FDC_x}{h}\left\{\frac{\partial C_y^*}{\partial y^*}|_{y^*=-1}\right\} = \frac{J_{1-D}}{1+\alpha+\xi}\exp(-\frac{\beta x^*}{1+\alpha+\xi}) \tag{5.6b}$$

$$J_{total} = J_{flow}\left\{1 - \exp(-\frac{\beta}{1+\alpha+\xi})\right\} \tag{5.6c}$$

Here, $x^* = \frac{x}{L}$, $y^* = \frac{y}{h}$, $\beta = \frac{J_{1-D}}{J_{flow}}$, $J_{flow} = \frac{8FU_{mean}hC_{in}}{L}$, $\xi = \frac{J_{1-D}}{J_{diff,ch}}$ and $J_{diff,ch} = \frac{4FDC_{in}}{h}$

$J_{GDL}$ is the limiting current density corresponding to the maximum molar flux of oxygen diffusion through the GDL, $J_{flow}$ signifies the current density corresponding to the molar flux of oxygen that is convected in the channel and $J_{diff,ch}$ is the limiting current density corresponding to the maximum flux of oxygen diffusing towards the channel-GDL interface in the channel.

The different limiting cases of equation (5.6c) were discussed in chapter 5. In particular, for the limiting case of fast diffusion rate in the channel relative to the diffusion through GDL, and correspondingly $\xi \ll \alpha$, equation (5.6c) simplifies to

$$J_{total} = J_{flow}\left\{1 - \exp(-\frac{\beta}{1+\alpha})\right\} \tag{5.7}$$

Equation (5.7) is in fact the current-potential relationship derived by Kulikovsky et al (2004) [63] by assuming uniform oxygen concentration and uniform velocity (plug flow) across the channel. Thus, it may be noted that replacing $\alpha$ in equation (5.7) by $(\alpha + \xi)$ gives equation (5.6c). This is intuitively expected since the diffusional resistances in the GDL and channel are in series.

The current-potential relationship as given by equation (5.6c) is only valid when the transport losses of reacting species across the CCL are negligible. As indicated earlier, this may not always be true. Therefore, we now seek analytical expressions for polarization curves in the different regimes of CCL operation where overall oxygen consumption rate gets modulated due to transport resistances. We will also compare the predictions of the analytical model with three-dimensional numerical simulations in which no simplifying approximations are made. Details about the numerical simulation are provided in section 2.2 of chapter 2 and the details of model geometry is discussed in section 4.2 of chapter 4. It should be noted that the width of the ribs adjacent to the channel is purposefully kept small ($w_{channel} >> w_{rib}$) so as to mimic the geometry solved in the analytical model.

### 5.1) Ideal proton transport case $J > \frac{4FD_{CCL}C_{in}}{l_t}$ *and* $\frac{2\sigma A_c}{l_t} \to \infty$ (regime 2 mentioned in table 3.1 of chapter 3)

As discussed earlier (see section 2.1.1 of chapter 2), $J < \frac{4FD_{CCL}C_{CCL-GDL}}{l_t}$ describes the regime where oxygen transport resistance is negligible. In this regime, intrinsic Tafel kinetics defines

the current-overpotential relationship and oxygen concentration remains uniform across the CCL thickness. As the current density increases beyond this limit, increasing amount of concentration polarization of oxygen happens in the CCL near the CCL-GDL interface, and the oxygen consumption rate decreases sharply away from the interface. The current-overpotential relationship for this case was derived by Kulikosky (2010) [42] and is given by,

$$J = \sqrt{\frac{4FD_{CCL}C_{in}}{l_t} i_{o,c} A l_t \left[\exp\left(\frac{\eta_{o,CCL}}{A_c}\right)\right]} \frac{C_{CCL-GDL}}{C_{in}} \tag{5.8}$$

This is the same as the equation for Regime 2 given in table 3.1 of chapter 3. The doubling of apparent Tafel slope, which is also observed experimentally, is evident from equation (5.8). The conservation equation for oxygen across the GDL can now be written as

$$\frac{4FD_{GDL}}{l_{GDL}}(C_{ch-GDL} - C_{CCL-GDL}) = \sqrt{\frac{4FD_{CCL}C_{in}}{l_t} i_{o,c} A l_t \left[\exp\left(\frac{\eta_{o,CCL}}{A_c}\right)\right]} \frac{C_{CCL-GDL}}{C_{in}} \tag{5.9}$$

Equations (5.8) and (5.9) can be combined to give

$$J = \frac{J_{1-D}}{1+\alpha} \frac{C_{ch-GDL}}{C_{in}} \tag{5.10}$$

Here,

$$J_{1-D} = \sqrt{\frac{4FD_{CCL}C_{in}}{l_t} i_{o,c} A l_t \left[\exp\left(\frac{\eta_{o,CCL}}{A_c}\right)\right]},\ J_{GDL} = \frac{4FD_{GDL}C_{in}}{l_{GDL}}, \text{ and } \alpha = \frac{J_{1-D}}{J_{GDL}} \tag{5.11}$$

Equation (5.11) is exactly the same as equation (5.5) except for the definition of $J_{1-D}$. This implies that the polarization curve in this regime remains

$$J_{total} = J_{flow}\left\{1 - \exp\left(-\frac{\beta}{1+\alpha+\xi}\right)\right\} \tag{5.12}$$

Except that, $\alpha$, $\beta$ and $\xi$ are defined based on $J_{1-D}$ given by equation (5.11).

In the limiting case when diffusion of oxygen in the channel is faster relative to diffusion in the GDL $(i.e.,\ \xi \ll \alpha)$, equation (5.12) simplifies to

$$J_{total} = J_{flow}\left\{1 - \exp(-\frac{\beta}{1+\alpha})\right\} \quad (5.13)$$

We now compare the predictions of equations (5.12) and (5.13) with numerical simulations for the case when oxygen transport resistance in the CCL modulates ORR kinetics and proton transport is not rate limiting. Calculations were done using parametric values given in Table 5.1. These values were chosen purposefully to ensure that the operational regime in CCL is that corresponding to slow oxygen transport. Thus, the diffusion coefficient of oxygen in CCL was chosen to be $D_{CCL} = 2.52 \times 10^{-9} m^2/s$, which gives $J_{crit,(O2)transport} = \frac{4FD_{CCL}C_{in}}{l_t} \sim 0.1 \frac{A}{cm^2}$. Similarly, a high (admittedly unrealistic) value of proton conductivity of $\sigma = 20\ S/cm$ was chosen to ensure rapid proton transport (i.e., the critical current density at which proton transport limitation can be expected will be $\frac{2\sigma A_c}{l_t} \sim 1300\ \frac{A}{cm^2}$). In short, we expect the polarization curve to be determined by intrinsic kinetics for $J < 0.1 \frac{A}{cm^2}$ and by oxygen transport in CCL for $J > 0.1 \frac{A}{cm^2}$.

**Table 5.1** Numerical values of model parameters

| | |
|---|---|
| $A_c$ | 0.025 V |
| $C_{in}$ | 8.2 $mol/m^3$ |
| $D$ | $3 \times 10^{-5}\ m^2/s$ |
| $D_{GDL}$ | $6.7 \times 10^{-6}\ m^2/s$ |
| $F$ | 95500 $C/mol$ |
| $2h$ | 0.001 $m$ |
| $i_{o,c}A$ | 1000 $A/m^3$ |
| $L$ | 0.02 $(m)$ |
| $l_{GDL}$ | 300 $\mu m$ |
| $l_t$ | 8 $\mu m$ |
| $U_{mean}$ | 0.195 $m/s$ |
| $w_{channel}$ | 0.001 $m$ |
| $w_{rib}$ | 0.00002 $m$ |
| $j_{lim}$ | $6.9 \frac{A}{cm^2}$ |
| $j_{flow}$ | $3 \frac{A}{cm^2}$ |
| $j_{diff,ch}$ | $18.5 \frac{A}{cm^2}$ |

Figure 5.1 shows comparison between polarization curves predicted by equations (5.12) and (5.13) and the three-dimensional numerical simulations, which were performed for the same values of model parameters as listed in Table 5.1. It can be seen that the polarization curve predicted by equation (5.12) matches better with the simulated result compared to that predicted by equation (5.13) over the entire range of current density. The improved predictive ability of equation (5.12) is a consequence of oxygen concentration gradient along the transverse direction $(-y)$ in the flow channel. This is demonstrated in figure 5.2 where oxygen concentration profiles along the transverse direction $(-y)$ in the flow channel predicted by analytical theories and simulation are compared at $x^* = 0.5$ and $\eta_{o,CCL} = 0.58\,V$. The simulated oxygen concentration profile (open circles in figure 4) matches well with that predicted by equation (5.6a) (with $J_{1-D}$ given by equation (5.11)) of the present work (solid line in figure 5.2). The earlier model (Kulikovsky 2011) [65] assumes uniform oxygen concentration across the channel depth (dashed lined in figure 5.2). Figure 5.3 illustrates the current density profiles along the channel length $(-x)$ at the mid-section of the membrane predicted by analytical model (equation (5.6b) with $J_{1-D}$ given by equation (5.11)) and by the three-dimensional simulation at $\eta_{o,CCL} = 0.58\,V$. The simulated current density profile is in good agreement with the analytical model. The discrepancy at lower $x^*$ is a result of entry length effect and has already been discussed in detail in chapter 5.

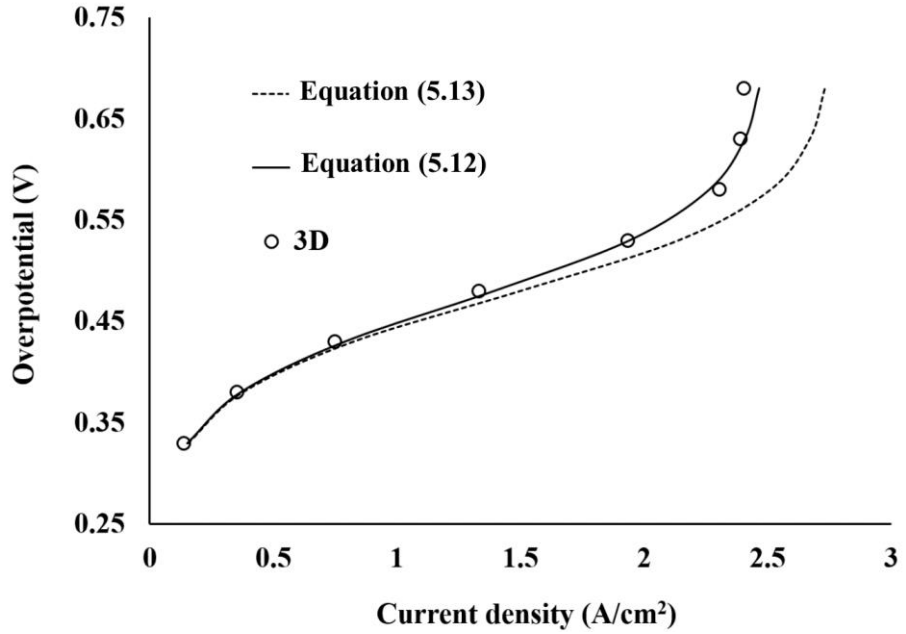


**Fig.5.1** Comparison between the polarization curves obtained by analytical theories versus a three-dimensional numerical simulation in the regime of poor oxygen transport across the CCL

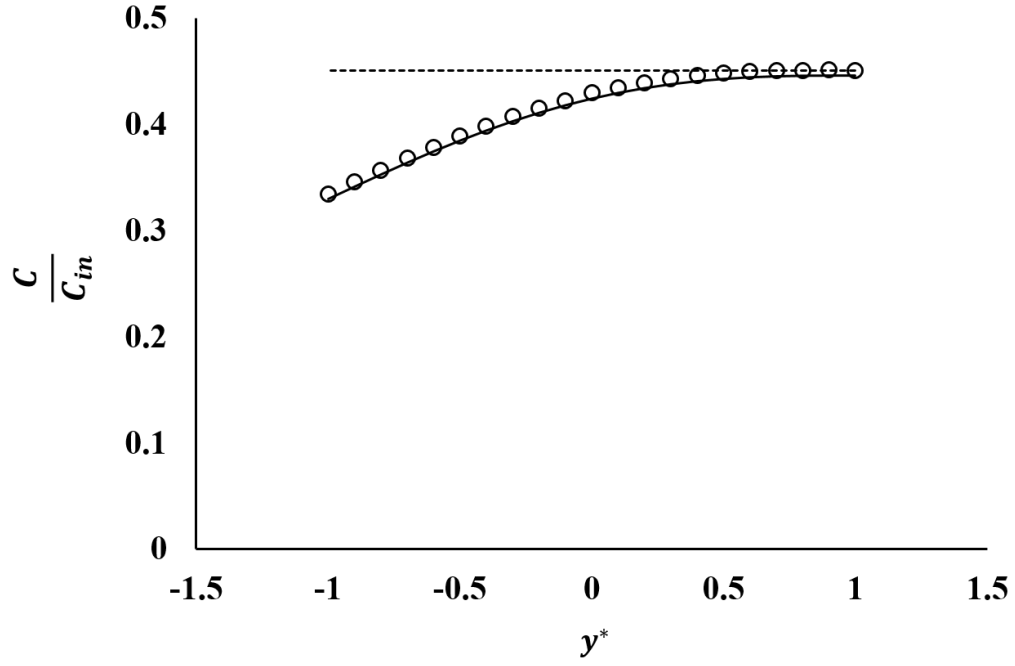


**Fig.5.2** Comparison between the oxygen concentration profiles along the transverse ($y-$) direction in the flow channel (dotted line:- Assumption of uniform oxygen concentration along the channel depth, solid line:- with this assumption relaxed, circles:- three-dimensional numerical simulation) in the regime of poor oxygen transport across the CCL

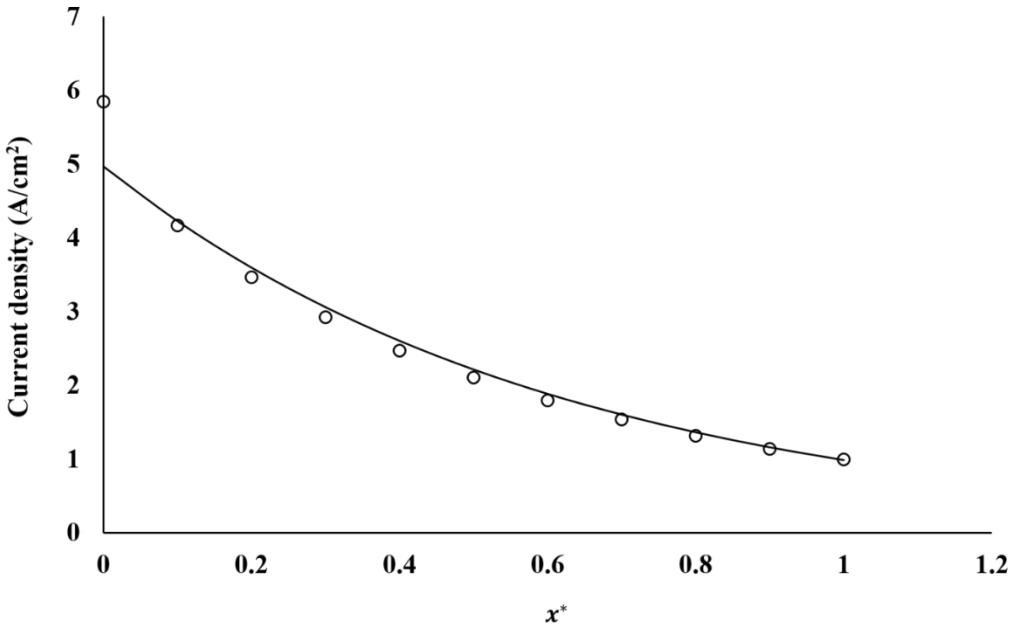


**Fig.5.3** Comparison between the current density profiles along the channel length ($x-$) at the mid-of the membrane (solid line:- equation (5.6b), circles:- three-dimensional numerical simulation) in the regime of poor oxygen transport across the CCL

## 5.2) Ideal oxygen transport case $J > \frac{2\sigma A_c}{l_t}$ $and$ $\frac{4FD_{CCL}C_{in}}{l_t} \to \infty$ (regime 3 mentioned in table 3.1 of chapter 3)

Kulikovsky (2002, 2010) [41, 42] showed that proton transport resistance across the CCL can become significant for $J > \frac{2\sigma A_c}{l_t}$. Under these conditions, oxygen consumption rate is the highest at the CCL-membrane interface and it decreases rapidly away from the interface. This gives rise to doubling of the apparent Tafel slope, and the current-overpotential relationship in the CCL is given by (see section 2.1.1 of chapter 2 and regime 3 in table 3.1)

$$J = \sqrt{\frac{2\sigma A_c}{l_t} i_{o,c} A l_t \frac{C_{CCL-GDL}}{C_{in}} \left[\exp\left(\frac{\eta_{o,CCL}}{A_c}\right)\right]} \tag{5.14}$$

The oxygen conservation equation across GDL is given by,

$$\frac{4FD_{GDL}}{l_{GDL}}(C_{ch-GDL} - C_{CCL-GDL}) = \sqrt{\frac{2\sigma A_c}{l_t} i_{o,c} A l_t \frac{C_{CCL-GDL}}{C_{in}} \left[\exp\left(\frac{\eta_{o,CCL}}{A_c}\right)\right]} \tag{5.15}$$

The main difference between equation (5.14) and equations (5.3) and (5.8) is the non-linear (square root) dependence of $J$ on oxygen concentration at the CCL-GDL interface.

Equations (5.14) and (5.15) can be solved together to give

$$J = \frac{J_{1-D}}{2}(p - \alpha) \tag{5.16}$$

Here,

$$p = \sqrt{4\frac{C_{ch-GDL}}{C_{in}} + \alpha^2}, J_{1-D} = \sqrt{\frac{2\sigma A_c}{l_t} i_{o,c} A l_t \frac{C_{CCL-GDL}}{C_{in}} \left[\exp\left(\frac{\eta_{o,CCL}}{A_c}\right)\right]}, \quad J_{GDL} = \frac{4FD_{GDL}C_{in}}{l_{GDL}}, \quad \alpha = \frac{J_{1-D}}{J_{GDL}} \tag{5.17}$$

Equation (5.16) together with equation (5.17) is required to be substituted in equation (5.2b) in order to solve equation (5.1). The non-linear concentration dependence prevents derivation of analytical solution to equation (5.1). However, we will look for asymptotic solutions for the cases of low and high overpotentials followed by an approximate solution.

- ***Limiting case of low overpotential***

At low overpotentials within the proton transport limited regime, the consumption of oxygen in the CCL is low and hence $C_{CCL-GDL} \approx C_{in}$. Consequently, we can linearize the concentration term under the square root as $\sqrt{\frac{C_{CCL-GDL}}{C_{in}}} = \frac{1}{2}(1 + \frac{C_{CCL-GDL}}{C_{in}})$, which allows for seeking solution to equation (5.2) by separation of variables. Substituting for $\sqrt{\frac{C_{CCL-GDL}}{C_{in}}}$ in equation (5.14), the current-potential relationship at the CCL is transformed t

$$J = \frac{1}{2}\sqrt{\frac{2\sigma A_c}{l_t} i_{o,c} A l_t \left[\exp\left(\frac{\eta_{o,CCL}}{A_c}\right)\right]}(1 + \frac{C_{CCL-GDL}}{C_{in}}) \tag{5.18}$$

Oxygen conservation across GDL gives,

$$\frac{4FD_{GDL}}{l_{GDL}}(C_{ch-GDL} - C_{CCL-GDL}) = \frac{1}{2}\sqrt{\frac{2\sigma A_c}{l_t} i_{o,c} A l_t \left[\exp\left(\frac{\eta_{o,CCL}}{A_c}\right)\right]}\,(1 + \frac{C_{CCL-GDL}}{C_{in}}) \quad (5.19)$$

Defining $J_{1-D} = \sqrt{\frac{2\sigma A_c}{l_t} i_{o,c} A l_t \left[\exp\left(\frac{\eta_{o,CCL}}{A_c}\right)\right]}$, $J_{GDL} = \frac{4FD_{GDL}C_{in}}{l_{GDL}}$, $\alpha = \frac{J_{1-D}}{J_{GDL}}$ and combining equations (5.18) and (5.19), we get,

$$J = \frac{J_{1-D}}{2}\left(\frac{1+C^*_{ch-GDL}}{1+\frac{\alpha}{2}}\right) \quad (5.20)$$

where, $C^*_{ch-GDL} = \frac{C_{ch-GDL}}{C_{in}}$. Note that $C^*_{ch-GDL}$ denotes the concentration $C^* = \frac{C}{C_{in}}$ at $y = -h$.

Defining $\chi = 1 + C^*$, equation (5.1) can be recast as,

$$\frac{3}{2} U_{mean}\left[1 - \left(\frac{y}{h}\right)^2\right]\frac{\partial \chi}{\partial x} = D\frac{\partial^2 \chi}{\partial y^2} \quad (5.21)$$

Equation (5.21) can be solved by the method of separation of variables wherein $\chi(x, y) = \chi_x \chi_y$. The solution yields

$$\chi(x, y) = 2\exp(-m^2 L x^*)\chi_y$$

Defining $\chi^*_y = \chi_y$, $y^* = \frac{y}{h}$ and $k^2 = \frac{3}{2}\frac{U_{mean}h^2m^2}{D}$, we get,

$$\frac{d^2\chi^*_y}{dy^{*2}} = -k^2(1 - y^{*2})\chi^*_y \quad (5.22)$$

Equation (5.22) can be solved using power series method (Chapter 5) and the solution is given by

$$\chi^*_y = 1 - \frac{k^2}{3}(1 - y^*)^3 + \frac{k^2}{12}(1 - y^*)^4 \quad (5.23)$$

Now, the boundary condition equation (5.2b) can be transformed in terms of $\varphi$ as

$$\frac{d\chi^*_y}{dy^*} = \frac{\frac{\xi}{2}}{1+(\frac{\alpha}{2})}\chi^*_y \text{ at } y^* = -1 \quad (5.24)$$

Equation (5.24) yields $k^2 = \frac{3}{4}\frac{\xi}{2+\alpha+\xi}$ and therefore $m^2 L = \frac{\beta}{2+\alpha+\xi}$.

Hence, the local current density at any point '$x$' along the channel can be written as

$$J = \frac{4FDC_{in}}{h}(2\exp(-\lambda^2 Lx^*))\left\{\frac{\partial \chi_y^*}{\partial y^*}|_{y^*=-1}\right\} = \frac{2J_{1-D}}{2+\alpha+\xi}\exp(-\frac{\beta x^*}{2+\alpha+\xi}) \quad (5.25)$$

Correspondingly, the area averaged current density-potential relationship is given as,

$$J_{total} = \int_0^1 J dx^* = 2J_{flow}\left\{1 - \exp(-\frac{\beta}{2+\alpha+\xi})\right\} \approx J_{1-D} \quad (5.26)$$

For the regime of poor proton transport across the CCL, equation (5.26) describes the polarization curve when $\alpha, \beta, \xi \ll 1$ ($J > \frac{2\sigma A_c}{l_t}$ and $J_{1-D} < J_{GDL}, J_{flow}, J_{diff,ch}$).

where $\alpha$, $\beta$ and $\xi$ are defined based on $J_{1-D}$ given by equation (5.17).

- ***Limiting case of high overpotential***

At higher overpotentials in the proton transport limited regime when $J_{1-D} >> J_{GDL}$, or specifically when $\alpha > 2$, then $p$ in equation (5.17) can be linearized as,

$$p \approx \alpha(1 + \frac{2}{\alpha^2}\frac{C_{ch-GDL}}{C_{in}}) \quad (5.27)$$

Combining equations (5.15) and (5.27), we get,

$$J = \frac{J_{1-D}}{\alpha}(\frac{C_{ch-GDL}}{C_{in}}) \quad (5.28)$$

Equation (5.28) is similar to equation (5.5) except that $\frac{J_{1-D}}{1+\alpha}$ is replaced by $\frac{J_{1-D}}{\alpha}$ and $J_{1-D}$ is defined by equation (5.17). Therefore, the polarization curve becomes,

$$J_{total} = J_{flow}\left\{1 - \exp(-\frac{\beta}{\alpha+\xi})\right\} \quad (5.29)$$

Equation (5.29) shows that $J_{total}$ is independent of $\eta_{o,CCL}$ and therefore this asymptotic solution corresponds to a vertical line in the polarization curve. Equation (5.25) and equation (5.29)

describe the polarization curve in the regime of poor proton transport across the CCL at low and high overpotentials, respectively.

- ***Approximate solution***

We now explore an approximate solution which matches the two limiting cases discussed above. We begin by considering the simpler case of plug flow in the flow channel and uniform oxygen concentration across the channel depth. Under this condition, equation (5.1) takes the simpler form

$$4FU_{mean}(2h)\frac{\partial C_{ch-GDL}}{\partial x} = -J \tag{5.30}$$

Substituting for $J$ from equation (5.16) into equation (5.30) and solving using the boundary condition $C_{ch-GDL} = C_{in}$ at $x = 0$, it is straightforward to derive the local current density profile at any axial position $x^*$ as

$$\frac{2J}{J_{1-D}} + \alpha \ln\left(\frac{2J}{J_{1-D}}\right) = (\sqrt{4+\alpha^2} - \alpha) + \alpha ln\left(\sqrt{4+\alpha^2} - \alpha\right) - \beta x^* \tag{5.31}$$

The total current density can be obtained numerically from the integration $\int_0^1 J dx^*$.

We now follow the same argument that can be used to derive equation (5.7) from equation (5.6c). Since diffusional resistances for oxygen in the channel and in the GDL are in series, therefore replacing $\alpha$ in equation (5.31) by $(\alpha + \xi)$ should yield the expression for polarization curve when the two assumptions of uniform oxygen concentration along channel depth and plug flow velocity profile are relaxed. Hence, we will examine the following approximate expression for local current density in the proton transport limited regime of operation:

$$\frac{2J}{J_{1-D}} + (\alpha+\xi) \ln\left(\frac{2J}{J_{1-D}}\right) = \left(\sqrt{4+(\alpha+\xi)^2} - (\alpha+\xi)\right) + (\alpha+\xi) ln\left(\sqrt{4+(\alpha+\xi)^2} - (\alpha+\xi)\right) - \beta x^* \tag{5.32}$$

And consequently, $\int_0^1 Jdx^*$ gives the total current density.

We now test the limiting cases discussed earlier. For the case $\alpha, \beta, \xi < 1$, equation (5.32) simplifies to $\frac{2J}{J_{1-D}} \approx 2 - \beta x^* \approx 2$, or equivalently, $J_{total} \approx J_{1-D}$. Note that equation (5.26) also simplifies to the same result.

In the other limiting case of $\alpha \gg 2$, equation (5.32) simplifies to,

$$(\alpha + \xi)\ln(J) = (\alpha + \xi) ln\left((\sqrt{4 + (\alpha + \xi)^2} - (\alpha + \xi))\frac{J_{1-D}}{2}\right) - \beta x^* \quad (5.33)$$

It can be shown that $ln\left((\sqrt{4 + (\alpha + \xi)^2} - (\alpha + \xi))\frac{J_{1-D}}{2}\right) = ln\left(\frac{4}{(\sqrt{4+(\alpha+\xi)^2}+(\alpha+\xi))}\frac{J_{1-D}}{2}\right) \approx ln(\frac{J_{1-D}}{\alpha+\xi})$ for $\alpha \gg 2$ and therefore, equation (5.32) transforms to

$$J = \frac{J_{1-D}}{\alpha+\xi}\exp(-\frac{\beta x^*}{\alpha+\xi}) \quad (5.34)$$

Correspondingly, total current density is,

$$J_{total} = J_{flow}\left\{1 - \exp(-\frac{\beta}{\alpha+\xi})\right\} \quad (5.35)$$

Equation (5.35) is identical to equation (5.29). Thus, the approximate local current density given by equation (5.32) satisfies the two limiting cases of low and high overpotentials. We now test its predictions against numerical simulations.

Figure 5.4 shows comparison between polarization curves obtained from the two limiting cases (equation (5.25) and equation (5.29)), numerical integration of the approximate analytical solution given by equation (5.32) and the full three-dimensional simulation. To ensure that we are in the proton transport limited operating regime in CCL, we have purposefully assigned the values $\sigma = 0.0015\frac{S}{cm}$ and $D_{CCL} = 1 \times 10^{-5}\frac{m^2}{s}$ so that $\frac{2\sigma A_c}{l_t} \sim 0.1\ \frac{A}{cm^2}$ << $\frac{4FD_{CCL}C_{in}}{l_t} \sim 400\frac{A}{cm^2}$ thereby ensuring that there is no limitation from oxygen diffusion

resistance in the CCL. The numerical values of other parameters are mentioned in Table 5.1. It can be observed in figure 5.4 that the polarization curve obtained by the approximate solution is in close agreement with the asymptotic solutions and with the polarization curve obtained from three-dimensional simulations. In comparison, the polarization curve obtained by numerically integrating equation (5.31), which assumes plug flow and uniform oxygen concentration along the depth of the channel, shows deviation at higher current densities. The cause of deviation lies in the comparison of oxygen concentration profiles along the transverse direction ($y-$) of the flow channel. In figure 5.5, we compare oxygen concentration profiles of the analytical theories with numerical simulation results at $x^* = 0.5$ and $\eta_{o,CCL} = 0.68\,V$. The earlier model corresponds to uniform oxygen concentration profile (dashed line in figure 5.5), which is in disagreement with numerical simulations. The predicted oxygen concentration profile shown by the solid line in figure 5.5 gives an excellent match with three-dimensional simulations. Figure 5.6 compares the simulated current density profile (circles) with the analytical model prediction (solid line) along the channel length at the mid-of the membrane. As can be observed from figure 5.6, the analytical model prediction and simulated result are in excellent agreement. In the present model, oxygen concentration profile and current density profile for the limiting case of high overpotential are respectively given by equation (5.6a) and equation (5.6b) with $(\alpha + \xi)$ replacing $(1 + \alpha + \xi)$ and $J_{1-D}$ is given by equation (5.17).

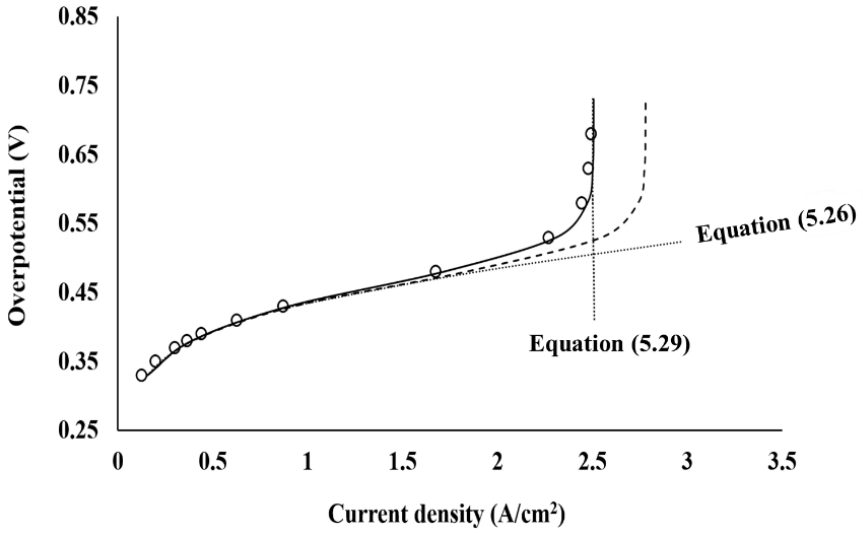


**Fig.5.4** Comparison between the polarization curves obtained by analytical theories (dotted line:- obtained using equation (5.31), solid line:- obtained using equation (5.32)) versus a three-dimensional numerical simulation (circles) in the regime of poor proton transport across the CCL

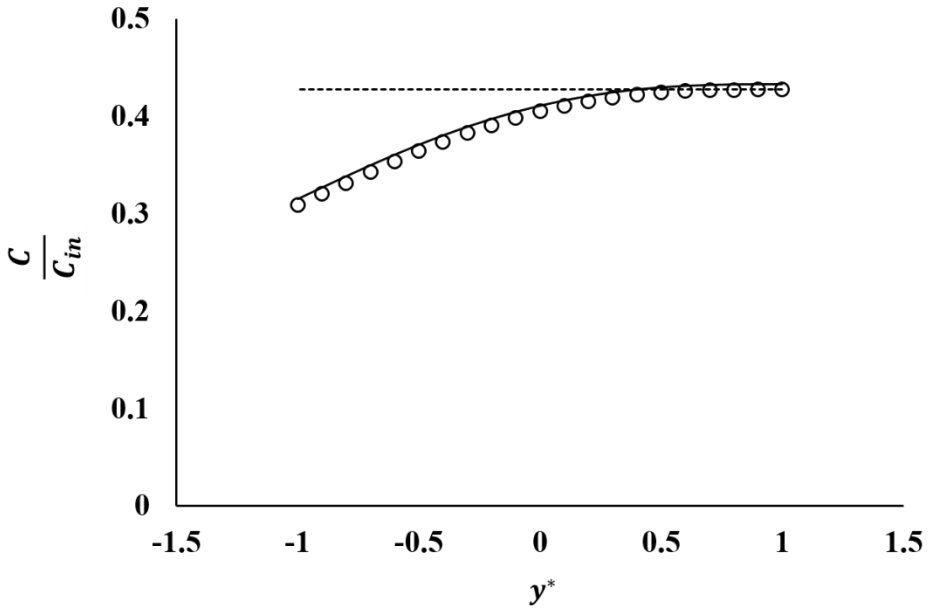


**Fig.5.5** Comparison between the oxygen concentration profiles along the transverse ($y-$) direction in the flow channel (dotted line:- Assumption of uniform oxygen concentration along the channel depth, solid line:- with this assumption relaxed, circles:- three-dimensional numerical simulation) in the regime of poor proton transport across the CCL

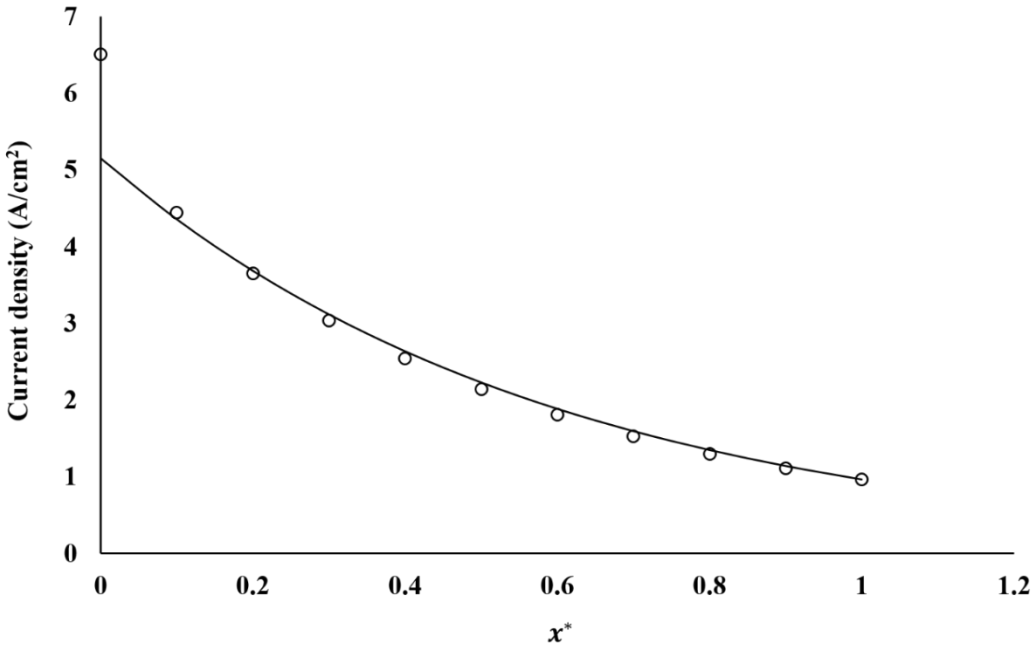


**Fig.5.6** Comparison between the current density profiles along the channel length ($x$ −) at the mid-of the membrane (solid line:- equation (5.6b) with (α+ξ) replacing (1+α+ξ), circles:- three-dimensional numerical simulation) in the regime of poor proton transport across the CCL

Figure 5.7 compares polarization curves obtained from the approximate analytical solution with the results of three-dimensional simulations for various values of $J_{GDL}$,$J_{flow}$,$J_{diff,ch}$ and $J_{1-D}$. The excellent matching of the results in all cases confirms that equation (5.32) describes the local current density profile in proton transport limited operating regime of the CCL over the entire range of current density above $\frac{2\sigma A_c}{l_t}$.

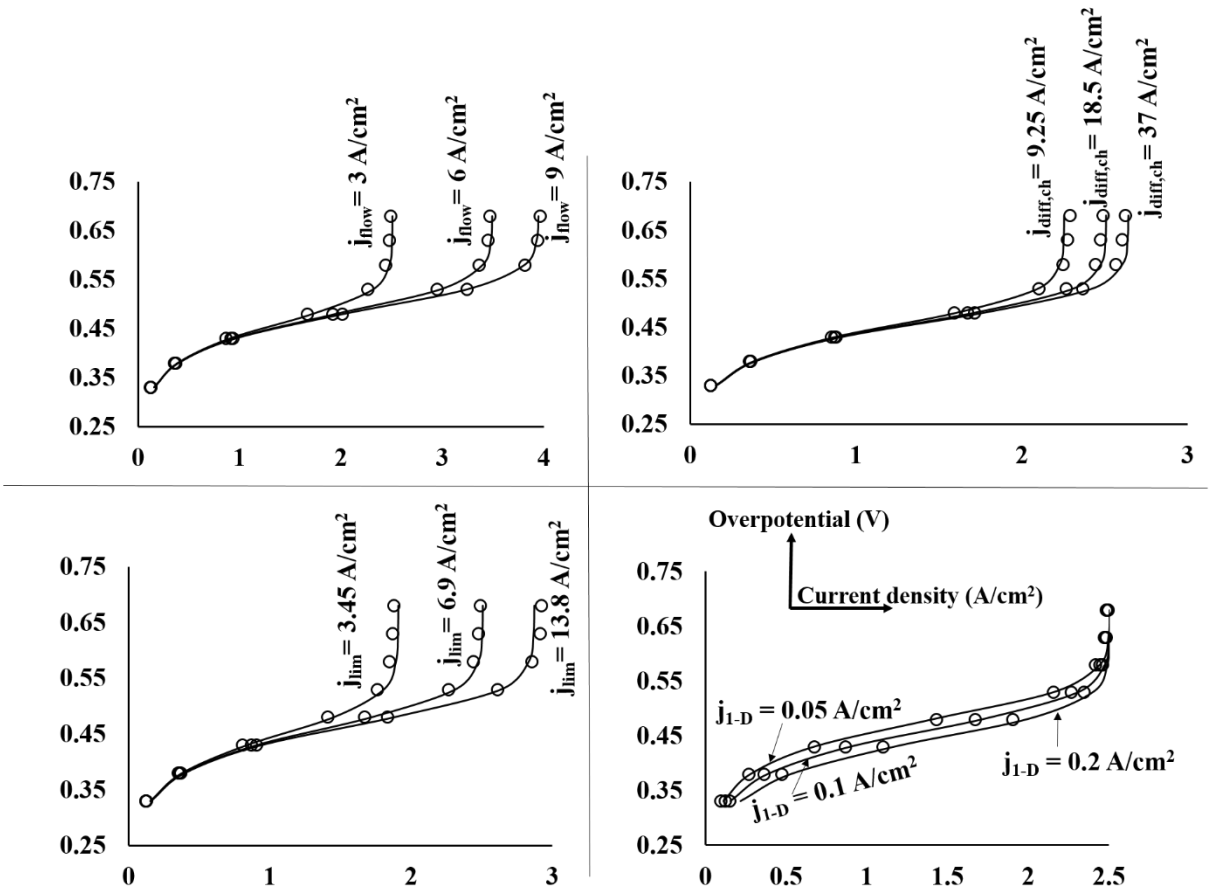


**Fig.5.7** Comparison between the polarization curves (overpotential in V on the y-axis and current density in A/cm$^2$ on the x-axis) obtained by using equation (5.32) (solid lines) versus three-dimensional numerical simulations (circle) in the regime of poor proton transport across the CCL for different values of $J_{GDL}$,$J_{flow}$,$J_{diff,ch}$ and $J_{1-D}$ varied one at a time.

## 5.3) Discussion

We summarize below analytical expressions of polarization curve derived for the various regimes of CCL operation. For $J_{lim} = \frac{4FD_{GDL}C_{in}}{l_{GDL}}$, $J_{flow} = \frac{8FU_{mean}hC_{in}}{L}$, $J_{diff,ch} = \frac{4FDC_{in}}{h}$, $\alpha = \frac{J_{1-D}}{J_{lim}}$, $\beta = \frac{J_{1-D}}{J_{flow}}$ and $\xi = \frac{J_{1-D}}{J_{diff,ch}}$, the polarization curves are given by

A. Regime in which overall oxygen consumption rate is determined by intrinsic ORR kinetics:

$$J_{total} = J_{flow}\left\{1 - \exp(-\frac{\beta}{1+\alpha+\xi})\right\} \text{ where } J_{1-D} = i_{o,c}Al_t\left[\exp\left(\frac{\eta}{A_c}\right)\right] \quad \text{(S1)}$$

B. Regime in which overall oxygen consumption rate is determined by slow oxygen transport modulated kinetics:

$$J_{total} = J_{flow}\left\{1 - \exp(-\frac{\beta}{1+\alpha+\xi})\right\} \text{ where } J_{1-D} = \sqrt{4FDC_{in}i_{o,c}A\left[\exp\left(\frac{\eta}{A_c}\right)\right]} \quad \text{(S2)}$$

C. Regime in which overall oxygen consumption rate is determined by slow proton transport modulated kinetics:

$$\frac{2J}{J_{1-D}} + (\alpha+\xi)\ln\left(\frac{2J}{J_{1-D}}\right) = \left(\sqrt{4+(\alpha+\xi)^2} - (\alpha+\xi)\right) + (\alpha+\xi)ln\left(\sqrt{4+(\alpha+\xi)^2} - (\alpha+\xi)\right) - \beta x^* \text{ and } J_{total} = \int_0^1 J dx^* \text{ where } J_{1-D} = \sqrt{2i_{o,c}A\sigma A_c\left[\exp\left(\frac{\eta}{A_c}\right)\right]} \quad \text{(S3)}$$

Equation (S2) can be rearranged as shown below in equation (S4) to give overpotential explicitly in terms of current density. The contribution of ohmic cell resistance (second term) is purposely added on the right side of equation (S4).

$$\eta = A_c ln\left(\frac{J_{total}}{i_{o,c}Al_t}\right) + J_{total}R + A_c ln\left(\frac{J_{total}}{\frac{4FD_{CCL}C_{in}}{l_t}}\right) + 2A_c ln\left(\frac{\ln\left(\frac{1}{1-\frac{J_{total}}{J_{flow}}}\right)}{\frac{J_{total}}{J_{flow}} + \ln\left(1-\frac{J_{total}}{J_{flow}}\right)\left\{\frac{J_{total}}{J_{GDL}} + \frac{J_{total}}{J_{diff,ch}}\right\}}\right) \quad \text{(S4)}$$

Equation (S4) is equivalent to the popularly used empirical form of polarization equation (Larminie and Dicks, 2003 [98])

$$\eta = A_c ln\left(\frac{J_{total}}{i_{o,c}Al_t}\right) + J_{total}R + m\,exp(n \times J_{total}) \quad \text{(S5)}$$

where, $m$ and $n$ are empirical constants.

The first and second terms on the right side of equation (S4) are respectively, the contribution of intrinsic ORR kinetics and cell resistance, and are identical to the first two terms on the right side of equation (S5). The third and fourth terms on the right side of equation (S4) give explicitly the contributions of the internal mass transfer resistance of the CCL and the external

mass transfer resistance arising from GDL and channel. Thus, the empirical description of mass transfer contribution in equation (S5) can now be calculated exactly.

In Section 5.2 when comparing model predictions with simulations, we assumed some unrealistic values of material parameters in order to ensure that the operating regime of CCL was either only oxygen transport limited or only proton transport limited. As a final comment, we will consider here the case of a real representative MEA in a low-temperature PEM fuel cell operated at high air (oxidant) stoichiometry, and check if there exists clearly defined current density range for each of the different operating regimes. Table 5.2 summarizes numerical values of different parameters that constitute such a MEA. Table 2 also lists the important current density scales, from which it can be inferred that intrinsic ORR kinetics will determine the overall oxygen consumption rate for $J < 0.1\ \frac{A}{cm^2}$, oxygen transport modulated ORR kinetics will determine the overall oxygen consumption rate for $0.1\frac{A}{cm^2} < j < 0.3 - 0.4\ \frac{A}{cm^2}$. Above $0.5\ \frac{A}{cm^2}$ one may expect a regime where poor oxygen transport as well as poor proton transport across the CCL can simultaneously modulate the ORR kinetics. The analysis of this regime will be dealt in next chapter. Eventually at higher current densities, the power output of PEMFC may be severely limited by diffusional resistances in the GDL and channel. We will revisit these values in chapter 6 and 7. In fact, we will provide a systematic experimental methodology to estimate oxygen diffusion coefficient in CCL, GDL and channel.

**Table 5.2** Numerical values of MEA parameters of a typical low temperature PEM fuel cell

| Parameter | Numerical Value | Remarks |
|---|---|---|
| $D_{CCL}$ | $O\ (10^{-9}\frac{m^2}{s})$ | $D_{CCL} = D_{O2-H2O}(\varepsilon_{CCL})^{1.5}$ for a completely flooded CCL and $D_{O2-H2O} \sim 5 \times 10^{-9}\ \frac{m^2}{s}$ [99], $\varepsilon_{CCL}$ is catalyst layer porosity. For 40% porous CCL, $D_{CCL} \sim 1.25 \times 10^{-9}\ \frac{m^2}{s}$. |
| $D$ | $3 \times 10^{-5}\ m^2/s$ | Oxygen diffusion coefficient in air [100] |
| $D_{GDL}$ | $6.7 \times 10^{-6}\ m^2/s$ | $D_{GDL} = D(\varepsilon_{GDL})^{1.5}$. $\varepsilon_{GDL}$ is GDL porosity. For 35% porous GDL [101], $D_{GDL} \sim 6 \times 10^{-6}\ \frac{m^2}{s}$. This is for a GDL having no pore flooded with water. |
| $\sigma$ | $2\ S/m$ | [43-45] |

| | | |
|---|---|---|
| $2h$ | 0.001 $m$ | Channel depth |
| $l_{GDL}$ | 300 $\mu m$ | GDL thickness |
| $l_t$ | 8 $\mu m$ | CCL thickness |
| $J_{GDL}$ | $7\frac{A}{cm^2}$ | Current density corresponding to maximum possible diffusive flux across the GDL ($\frac{4FD_{GDL}C_{in}}{l_{GDL}}$) |
| $J_{diff,ch}$ | $18\frac{A}{cm^2}$ | Current density corresponding to maximum possible diffusive flux along the channel depth ($\frac{4FDC_{in}}{h}$) |
| $J_{crit,(O2)\ transport}$ | $\sim 0.1 - 0.2\frac{A}{cm^2}$ | Current density scale above which oxygen transport in the CCL modulates the intrinsic ORR rate ($\frac{4FD_{CCL}C_{CCL-GDL}}{l_t}$) |
| $J_{crit,(H+)\ transport}$ | $\sim 1 - 1.5\frac{A}{cm^2}$ | Current density scale above which proton transport in the CCL modulates the intrinsic ORR rate ($\frac{2\sigma A_c}{l_t}$) |
| $J_{flow}$ | - | Function of stoichiometry |

## 5.4) Conclusion

An analytical isothermal two-dimensional model of a cathode flow channel in a PEM fuel cell is developed to capture coupled transport processes in CCL, GDL and flow channel along with reaction in CCL. The oxidant velocity profile in the flow channel is assumed to be parabolic and oxygen concentration is allowed to vary along the depth of the channel. Analytical current-potential relationships are derived from the model for transport limited operating regimes of CCL namely, restricted oxygen transport and restricted proton transport across a macrohomogenous CCL. Polarization curves predicted by the model in these operating regimes are found to be in excellent agreement with results of three-dimensional simulations. The polarization curves were also re-cast into a form that corresponds to the widely used empirical equation of polarization curve. This allows for estimation of internal and external mass transfer resistances for the CCL.

# Chapter 6

# The PEM fuel cell equation

The content of this chapter is published in,
"Chemical Engineering Science, volume no. 206, 12th October 2019, pages: 96–117" [90].

In chapters 4 and 5, we developed an isothermal two-dimensional model for a straight single cathode channel, which accounts for oxygen concentration gradient in the flow direction along the channel as well as transverse oxygen concentration gradients in the GDL and channel, while also accounting for non-uniform velocity profile inside the channel. We showed how this two-dimensional model can be combined with the MH-CCL model for three limiting operating regimes viz., intrinsic kinetic controlled regime, ideal proton transport regime and ideal oxygen transport regime. In this chapter, we significantly extend our earlier work by combining the two-dimensional model of a single cathode flow channel with the comprehensive MH-CCL model described in chapter 3 that accounts for simultaneous oxygen diffusion and proton conduction resistances as well as the local resistance offered by oxygen diffusion inside catalyst agglomerates. Finally, we incorporate the ohmic cell resistance namely, the electrical resistance and protonic resistance of the PEMFC components. This leads us to the *PEM fuel cell equation*, which is an analytical expression for steady state polarization curve valid over the entire range of current density, from zero to limiting current. Such a comprehensive analytical expression of polarization curve has not been derived before. We show that the limiting cases of the PEM fuel cell equation have the same mathematical form as the well-known empirical polarization equation (Larminie and Dicks, 2003 [98]); however, unlike the fitting parameters of the

empirical equation, the model parameters of the PEM fuel cell equation have definite physical meaning and are experimentally determinable.

The governing equations are exactly identical to (5.1) and (5.2) and '$J$' in equation (5.2b) can be obtained by solving the MH-CCL model locally at any $x$. The limiting cases considered in the earlier chapters imply infinitely large values of proton conductivity and/or oxygen diffusivity in the CCL. Real CCLs will however have finite values of these transport coefficients. Thus, under realistic operating conditions of PEM fuel cells and at sufficiently high current density, both oxygen and proton transport resistances can *simultaneously* dictate $J - \eta_{o,CCL} - C_{CCL-GDL}$ relation. Also, oxygen transport resistance inside local catalyst agglomerates in the CCL can become significant at high current density (see section 2.1.2 of chapter 2). Thus, depending on the comparative rates of oxygen diffusion and oxygen consumption in the agglomerate as captured by Thiele modulus ($M_T$) and effectiveness factor [$E(\eta)$], three cases namely, (1) $M_T \ll 1$ and $E(\eta) \approx 1$, (2) $M_T \gg 1$ and $E(\eta) \approx \frac{1}{M_T}$ and (3) the general case $\frac{1}{M_T} \leq E(\eta) \leq 1$ are possible and are discussed below:

### 6.1) $M_T \ll 1$ and $E(\eta) \approx 1$

As discussed in chapter 3, there could be two possible sub-regimes of operation namely, $J_{crit,(O2)transport} < J_{crit,(H+)transport}$ i.e., $D^* < 1$ and $J_{crit,(O2)transport} > J_{crit,(H+)transport}$ i.e., $D^* > 1$. However, as will be discussed in chapter 7, for the operation of a fully humidified low temperature PEM fuel cell, which is also experimentally investigated in the present work, the sub-regime given by $D^* < 1$ turns out to be more relevant. Thus, we will restrict the scope of the following sub-sections to the case $D^* < 1$.

While the detailed derivation is provided in chapter 4, we reproduce here $J - \eta_{o,CCL} - C_{CCL-GDL}$ relationship (see Regime 4b in table 3.1):

$$J = \sqrt{\frac{4FD_{CCL}C_{in}}{l_t} i_{o,c} A l_t \left[\exp\left(\frac{\eta_{o,iR-free,CCL}}{A_c}\right)\right]} \frac{C_{CCL-GDL}}{C_{in}} \quad (6.1a)$$

$$\eta_{o,CCL} = \eta_{o,iR-free,CCL} + \frac{J}{\sigma/l_t} \quad (6.1b)$$

It is to be noted from equations (5.2b) and (5.4) from chapter 5 that the oxygen transport resistances in GDL and flow channel will modulate $C_{CCL-GDL}$, which will affect only the iR-free part of the CCL overpotential ($\eta_{o,iR-free,CCL}$). Thus the equation set (5.1) and (5.2) can be solved to derive oxygen concentration profile and current density profile along the length of the channel for a given $\eta_{o,iR-free,CCL}$. Upon integration over the domain area, the equation for iR-free polarization curve $(J_{total} - \eta_{o,iR-free,CCL})$ relation can be derived. We can then add separately overpotential due to proton transport resistance in the CCL to the iR-free CCL overpotential, which leads to the total current – cathodic overpotential relationship, $(J_{total} - \eta_{CCL})$.

Following the work presented in earlier chapters, we now solve for the regime of *Simultaneous non-ideal oxygen transport and proton transport and* $M_T \ll 1$ and $E(\eta) \approx 1$. The conservation equation for oxygen across the GDL can now be written as,

$$\frac{4FD_{GDL}}{l_{GDL}}(C_{ch-GDL} - C_{CCL-GDL}) = J \quad (6.2)$$

Thus eliminating $C_{CCL-GDL}$ from equations (6.1a) and (6.2), we get,

$$J = \frac{J_{1-D}}{1+\alpha} \frac{C_{ch-GDL}}{C_{in}} \quad (6.3a)$$

Here,

$$J_{1-D} = \sqrt{\frac{4FD_{CCL}C_{in}}{l_t} i_{o,c} A l_t \left[\exp\left(\frac{\eta_{o,iR-free,CCL}}{A_c}\right)\right]}, \alpha = \frac{J_{1-D}}{J_{GDL}}, J_{GDL} = \frac{4FD_{GDL}C_{in}}{l_{GDL}} \quad (6.3b)$$

Substituting equation (6.3) in equation (5.2b) and solving equation set (5.1) and (5.2) lead to profiles of local oxygen concentration and local current density along '$x$' as,

$$C(x,y) = C_{in}\exp(-\frac{\beta x^*}{1+\alpha+\xi})\left\{1 - \frac{\xi}{4(1+\alpha+\xi)}(1-y^*)^3 + \frac{\xi}{16(1+\alpha+\xi)}(1-y^*)^4\right\} \quad (6.4a)$$

$$J = \frac{4FDC_x}{h}\left\{\frac{\partial C_y^*}{\partial y^*}|_{y^*=-1}\right\} = \frac{J_{1-D}}{1+\alpha+\xi}\exp(-\frac{\beta x^*}{1+\alpha+\xi}) \quad (6.4b)$$

Integrating equation (6.4b) gives the total current density across the channel active area as

$$J_{total} = J_{flow}\left\{1 - \exp(-\frac{\beta}{1+\alpha+\xi})\right\} \quad (6.4c)$$

where, $J_{flow} = \frac{8FU_{mean}hC_{in}}{L}, J_{diff,ch} = \frac{4FDC_{in}}{h}, \beta = \frac{J_{1-D}}{J_{flow}}$ $and$ $\xi = \frac{J_{1-D}}{J_{diff,ch}}$

Equation (6.4c) can be rearranged as

$$\eta_{o,iR-free,CCL} = A_c ln\left(\frac{J_{total}}{i_{o,c}Al_t}\right) + A_c ln\left(\frac{J_{total}}{\frac{4FD_{CCL}C_{in}}{l_t}}\right) + 2A_c ln\left(\frac{\ln(\frac{1}{1-\frac{J_{total}}{J_{flow}}})}{\frac{J_{total}}{J_{flow}}+\ln(1-\frac{J_{total}}{J_{flow}})\left\{\frac{J_{total}}{J_{GDL}}+\frac{J_{total}}{J_{diff,ch}}\right\}}\right) \quad (6.4d)$$

The total current-cathodic overpotential is (note equation (6.1b)),

$$\eta_{o,CCL} = A_c ln\left(\frac{J_{total}}{i_{o,c}Al_t}\right) + A_c ln\left(\frac{J_{total}}{\frac{4FD_{CCL}C_{in}}{l_t}}\right) + 2A_c ln\left(\frac{\ln(\frac{1}{1-\frac{J_{total}}{J_{flow}}})}{\frac{J_{total}}{J_{flow}}+\ln(1-\frac{J_{total}}{J_{flow}})\left\{\frac{J_{total}}{J_{GDL}}+\frac{J_{total}}{J_{diff,ch}}\right\}}\right) + \frac{J_{total}}{\sigma/l_t} \quad (6.4e)$$

Equation (6.4e), being valid for $M_T \ll 1$ provides a total current – cathodic overpotential relationship for the current density range, $\frac{4FD_{CCL}C_{in}}{l_t} < J_{total} < \sqrt{(\frac{4FD_{CCL}C_{in}}{l_t})(\frac{36FD_{agg}C_{in}(1-\epsilon_{CCL})}{R_{agg}}\frac{l_t}{R_{agg}})}$.

### 6.2) $M_T \gg 1$ and $E(\eta) \approx \frac{1}{M_T}$

The same solution procedure as outlined above can be used to find equations for iR-free polarization curves for $J_{total} > \sqrt{(\frac{4FD_{CCL}C_{in}}{l_t})(\frac{36FD_{agg}C_{in}(1-\epsilon_{CCL})}{R_{agg}}\frac{l_t}{R_{agg}})}$. $J - \eta_{o,CCL} - C_{CCL-GDL}$ relationship for this case is derived to be (see Regime 5 in table 3.1):

$$J = \sqrt{4FD_{CCL}C_{in}\sqrt{\frac{36FD_{agg}C_{in}(1-\epsilon_{CCL})}{R_{agg}} \times \frac{1}{R_{agg}} i_{o,c}A\left[\exp\left(\frac{\eta_{o,iR-free,CCL}}{A_c}\right)\right]}\frac{C_{CCL-GDL}}{C_{in}}} \quad (6.5a)$$

$$\eta_{o,CCL} = \eta_{o,iR-free,CCL} + \frac{J}{\sigma/l_t} \quad (6.5b)$$

And the oxygen conservation law across the GDL can now be written as,

$$\frac{4FD_{GDL}}{l_{GDL}}(C_{ch-GDL} - C_{CCL-GDL}) = J \quad (6.6)$$

Similarity between equations (6.1) and (6.5) allows to follow a similar logic as stated above that that the oxygen transport resistances in GDL and flow channel will modulate $C_{CCL-GDL}$, which will affect only the iR-free part of the CCL overpotential ($\eta_{o,iR-free,CCL}$). Thus, we will first derive $(J_{total} - \eta_{o,iR-free,CCL})$ relationship followed by addition of overpotential due to proton transport resistance in the CCL to the iR-free CCL overpotential, which leads to the total current – cathodic overpotential relationship, $(J_{total} - \eta_{CCL})$.

Following similar process of eliminating $C_{CCL-GDL}$ from equation (6.5a) and (6.6), we get,

$$J = \frac{J_{1-D}}{1+\alpha}\frac{C_{ch-GDL}}{C_{in}} \quad (6.7a)$$

Here,

$J_{1-D} = \sqrt{4FD_{CCL}C_{in}\sqrt{\frac{36FD_{agg}C_{in}(1-\epsilon_{CCL})}{R_{agg}} \times \frac{1}{R_{agg}} i_{o,c}A\left[\exp\left(\frac{\eta_{o,iR-free,CCL}}{A_c}\right)\right]}}$, $J_{GDL} = \frac{4FD_{GDL}C_{in}}{l_{GDL}}$ and

$$\alpha = \frac{J_{1-D}}{j_{GDL}} \tag{6.7b}$$

Equation (6.7a) is exactly the same as equation (6.3a) except for the definition of $J_{1-D}$ given in equations (6.7b) and (6.3b). Therefore, the total current–iR-free cathodic overpotential relationship in this regime is also given by

$$J_{total} = J_{flow}\left\{1 - \exp(-\frac{\beta}{1+\alpha+\xi})\right\} \tag{6.8a}$$

However, here $\alpha$, $\beta$ and $\xi$ are defined based on $J_{1-D}$ given by equation (6.7b).

Equation (6.8a) can also be recast as

$$\eta_{o,iR-free,CCL} = A_c ln\left(\frac{J_{total}}{i_{o,c}Al_t}\right) + A_c ln\left(\frac{J_{total}}{\frac{4FD_{CCL}C_{in}}{l_t}}\right) + A_c ln\left\{\frac{J_{total}^2}{(\frac{4FD_{CCL}C_{in}}{l_t})(\frac{36FD_{agg}C_{in}(1-\epsilon_{CCL})}{R_{agg}} \times \frac{l_t}{R_{agg}})}\right\} +$$

$$4A_c ln\left(\frac{\ln(\frac{1}{1-\frac{J_{total}}{J_{flow}}})}{\frac{J_{total}}{J_{flow}} + \ln(1-\frac{J_{total}}{J_{flow}})\left\{\frac{J_{total}}{J_{GDL}} + \frac{J_{total}}{J_{diff,ch}}\right\}}\right) \tag{6.8b}$$

The total current-cathodic overpotential is (note equation (6.5b)),

$$\eta_{o,CCL} = A_c ln\left(\frac{J_{total}}{i_{o,c}Al_t}\right) + A_c ln\left(\frac{J_{total}}{\frac{4FD_{CCL}C_{in}}{l_t}}\right) + A_c ln\left\{\frac{J_{total}^2}{(\frac{4FD_{CCL}C_{in}}{l_t})(\frac{36FD_{agg}C_{in}(1-\epsilon_{CCL})}{R_{agg}} \times \frac{l_t}{R_{agg}})}\right\} +$$

$$4A_c ln\left(\frac{\ln(\frac{1}{1-\frac{J_{total}}{J_{flow}}})}{\frac{J_{total}}{J_{flow}} + \ln(1-\frac{J_{total}}{J_{flow}})\left\{\frac{J_{total}}{J_{GDL}} + \frac{J_{total}}{J_{diff,ch}}\right\}}\right) + \frac{J_{total}}{\sigma/l_t} \tag{6.8c}$$

Equation (6.8c), being valid for $M_T \gg 1$ provides a total current – cathodic overpotential relationship for the current density range, $J_{total} > \sqrt{(\frac{4FD_{CCL}C_{in}}{l_t})(\frac{36FD_{agg}C_{in}(1-\epsilon_{CCL})}{R_{agg}}\frac{l_t}{R_{agg}})}$.

### 6.3) General case $\frac{1}{M_T} \leq E(\eta) \leq 1$

$J - \eta_{o,CCL} - C_{CCL-GDL}$ relationship for this case is derived to be (see final equation in table 3.1):

$$J = \frac{4FD_{CCL}C_{in}}{l_t} \times \sqrt{\frac{i_{o,c}Al_t\left[\exp\left(\frac{\eta_{o,iR-free,CCL}}{A_c}\right)\right]\times E(\eta_{o,iR-free,CCL})}{\frac{4FD_{CCL}C_{in}}{l_t}}} \tanh\left\{\sqrt{\frac{i_{o,c}Al_t\left[\exp\left(\frac{\eta_{o,iR-free,CCL}}{A_c}\right)\right]\times E(\eta_{o,iR-free,CCL})}{\frac{4FD_{CCL}C_{in}}{l_t}}}\right\} \times \frac{C_{CCL-GDL}}{C_{in}} \quad (6.9a)$$

$$\eta_{o,CCL} = \eta_{o,iR-free,CCL} + \frac{J}{\sigma/l_t} \quad (6.9b)$$

It is straightforward to show that by following a similar mathematical analysis as explained above, the current-potential relationship in this general case of $\frac{1}{M_T} \leq E(\eta) \leq 1$ can be given as,

$$J_{total} = J_{flow}\left\{1 - \exp(-\frac{\beta}{1+\alpha+\xi})\right\} \quad (6.10a)$$

Here,

$$\alpha = \frac{J_{1-D}}{J_{GDL,eff}}, \beta = \frac{J_{1-D}}{J_{flow}}, \xi = \frac{J_{1-D}}{J_{diff,ch}}, J_{GDL,eff} = \frac{4FD_{GDL}C_{in}}{l_{eff,GDL}}, J_{flow} = \frac{8FU_{mean}hC_{in}}{L}, J_{diff,ch} = \frac{4FDC_{in}}{h} \; and$$

$$J_{1-D} = \frac{4FD_{CCL}C_{in}}{l_t} \times \sqrt{\frac{i_{o,c}Al_t\left[\exp\left(\frac{\eta_{o,iR-free,CCL}}{A_c}\right)\right]\times E(\eta_{o,iR-free,CCL})}{\frac{4FD_{CCL}C_{in}}{l_t}}} \tanh\left\{\sqrt{\frac{i_{o,c}Al_t\left[\exp\left(\frac{\eta_{o,iR-free,CCL}}{A_c}\right)\right]\times E(\eta_{o,iR-free,CCL})}{\frac{4FD_{CCL}C_{in}}{l_t}}}\right\} \quad (6.10b)$$

Thus, equation (6.9b) and (6.10b) provide the most general total current – cathodic overpotential relationship which is valid over entire range of current density. Here, $l_{eff,GDL}$ is

the effective length scale for oxygen diffusion in the GDL and will be discussed in the section 6.5.

### 6.4) Overpotential contribution from net ohmic resistance

In order to get total current – cell voltage relationship, we must now quantify the overpotential contribution of net ohmic resistance. As noted earlier, the net ohmic resistance will first have a contribution of proton resistance in the CCL. Next, we also add the overpotential contributions due to ohmic resistances in the other domains comprising: (a) protonic DC resistance in the membrane and (b) total electrical DC resistance (comprising that of GDL, flow field plate). Thus, the overpotential loss due to total ohmic resistance can be written as

$$\eta_{ohmic} = J_{total}\left\{\frac{l_t}{\sigma} + \frac{l_{membrane}}{\sigma_{membrane}} + 2 \times \left[(1-\varphi)\frac{l_{GDL}}{\sigma_{GDL,tp}} + \varphi\left(\frac{\frac{w_{channel}}{2}}{\sigma_{GDL,ip}} + \frac{l_{GDL}}{\sigma_{GDL,tp}}\right)\right]\right\} \quad (6.10c)$$

Here, $l_{membrane}$ is the thickness of the membrane, $\sigma_{membrane}$ is the proton conductivity of the membrane, $\sigma_{GDL,tp}$ and $\sigma_{GDL,ip}$ are respectively, electrical conductivities of the GDL in the through-plane and in-plane directions and $\varphi = \frac{w_{channel}}{w_{channel}+w_{rib}}$ is the ratio of flow area to the total area. The term in the curly bracket in equation (6.10c) is net ohmic resistance, $R_{ohmic}$.

Thus, the operating cell voltage ($V$) of the PEM fuel cell is given by,

$$V = E_{eq} - \eta_{o,iR-free,CCL} - \eta_{ohmic} \quad (6.10d)$$

Equations (6.10a-6.10d) give the final polarization curve, and we call this '***The PEM fuel cell equation***'. It relates the cell potential $V$ to the total current $J_{total}$ by accounting for simultaneous oxygen and proton transport resistances in the CCL coupled with oxygen transport resistance in the agglomerates. Additionally, the equation accounts for axial convection in the flow channel, transverse transport resistances for oxygen in the channel and GDL and the ohmic resistances of the cell. The procedure for calculating the polarization curve

is straight forward: $J_{total}$ is first calculated from equations (6.10a) and (6.10b) for a given $\eta_{o,iR-free,CCL}$. This is then used to calculate $\eta_{ohmic}$ from equation (6.10c) followed by calculating the cell voltage using equation (6.10d).

We would like to point out that an intrinsic assumption made in writing equation (6.10c) is that the cathode overpotential across the entire active area is uniform. This allows us to multiply the $R_{ohmic}$ with $J_{total}$ in order to calculate the ohmic contribution of overpotential. However, in reality, the profile of current density from inlet to the outlet leads to non-uniformity in the overpotential. Accounting for non-uniformity in overpotential over the active area results in significant coupling of governing equations, the solutions for which are beyond the scope of the present study. We therefore invoke here the simplified approach of using area-averaged current density ($J_{total}$) to correct for the ohmic contribution of overpotential. We believe that this approximation is in fact not unreasonable because the change in overpotential along the length of the channel is much smaller compared to the change in current density itself except for the cases when the current density is close to limiting values. We will validate this assumption later in this chapter.

### 6.5) Effect of rib-width

It must also be noted that the domain of the analytical model as depicted in figure 4.1 (chapter 4) does not incorporate a 'rib'. In reality, flow field will include channels and ribs. The consequence of having a finite rib width is that oxygen from the channel has to diffuse across the rib width, which leads to non-uniform oxygen concentration across rib and hence non-uniform current density in '$x-z$' plane. In our 1-D model for CCL, we have neglected gradients in this plane. In other words, we consider only average concentration and current density along '$x-z$' plane. In the averaged sense, we can however account for the additional

resistance to oxygen transport under the rib using an effective length scale for oxygen diffusion in GDL. We propose that this effective length, $l_{eff,GDL}$, can be estimated as

$$l_{eff,GDL} = \varphi l_{GDL} + (1-\varphi)\left(\frac{w_{rib}}{2} + l_{GDL}\right) \quad (6.11)$$

Thus, we replace $J_{GDL}$ in the earlier expressions with $J_{GDL,eff} = \frac{4FD_{GDL}C_{in}}{l_{GDL,eff}}$. All the model calculations illustrated in the subsequent sections are based on $J_{GDL,eff}$. That this approximation is indeed reasonable is shown later in the chapter.

In summary, we provide below in Table 6.1 a set of analytical expressions that represent polarization curves spanning the entire range of current density. We note that the equations in Table 6.1 have the same mathematical form as the well-known empirical equation of polarization curve (Larminie and Dicks, 2003 [98]). However, there are no empirical or fit parameters in the equations listed in Table 6.1.

Finally, we summarize below the assumptions made at various stages in deriving the *PEM fuel cell equation*:

1) Local $J - \eta_{o,CCL} - C_{CCL-GDL}$ relation at any point '$x$' along the length of the channel is assumed to be get dictated by one-dimensional FA-corrected MH model of the CCL i.e. the gradients in '$x$' and '$z$' directions in the CCL are assumed to be negligible (the quasi two-dimensional approach).
2) The contribution of net ohmic resistance (protonic + electrical) in the total potential loss is assumed to be quantified based on area averaged current density ($J_{total}$).
3) Oxygen transport resistance below the rib is incorporated by introducing effective length scale for oxygen diffusion in the GDL, which simply allowed to replace $l_{GDL}$ by $l_{GDL,eff}$ (equation 38) in all the equations.

In the following section, we will take a closer look at these approximations and check their validity.

**Table 6.1** Expressions of polarization curve spanning the entire range of current density

| Sr.no | Regime of CCL operation | $J_{total} - \eta_o$ |
|---|---|---|
| 1 | $J_{total} < \frac{4FD_{CCL}C_{in}}{l_t}$ | $\eta_o = A_c ln\left(\frac{J_{total}}{i_{o,c}Al_t}\right)$ |
| 2 | $\frac{4FD_{CCL}C_{in}}{l_t} < J_{total} < \sqrt{\left(\frac{4FD_{CCL}C_{in}}{l_t}\right)\left(\frac{36FD_{agg}C_{in}(1-\epsilon_{CCL})}{R_{agg}}\frac{l_t}{R_{agg}}\right)}$ | $\eta_o = \eta_{o,iR-free,CCL} + \eta_{ohmic}$<br>$\eta_{o,iR-free,CCL} = A_c ln\left(\frac{J_{total}}{i_{o,c}Al_t}\right) + A_c ln\left(\frac{J_{total}}{\frac{4FD_{CCL}C_{in}}{l_t}}\right) + 2A_c ln\left(\frac{\ln\left(\frac{1}{1-\frac{J_{total}}{J_{flow}}}\right)}{\frac{J_{total}}{J_{flow}}+\ln\left(1-\frac{J_{total}}{J_{flow}}\right)\left\{\frac{J_{total}}{J_{GDL,eff}}+\frac{J_{total}}{J_{diff,ch}}\right\}}\right)$<br>$\eta_{ohmic} = J_{total}\left\{\frac{l_t}{\sigma}+\frac{l_{membrane}}{\sigma_{membrane}}+2\times\left[(1-\varphi)\frac{l_{GDL}}{\sigma_{GDL,tp}}+\varphi\left(\frac{\frac{w_{channel}}{2}}{\sigma_{GDL,ip}}+\frac{l_{GDL}}{\sigma_{GDL,tp}}\right)\right]\right\}$ |

| | | |
|---|---|---|
| 3 | $J_{total} > \sqrt{\left(\frac{4FD_{CCL}C_{in}}{l_t}\right)\left(\frac{36FD_{agg}C_{in}(1-\epsilon_{CCL})}{R_{agg}}\frac{l_t}{R_{agg}}\right)}$ | $\eta_o = \eta_{o,iR-free,CCL} + \eta_{ohmic}$<br>$\eta_{o,iR-free,CCL} = A_c ln\left(\frac{J_{total}}{i_{o,c}Al_t}\right) + A_c ln\left(\frac{\frac{J_{total}}{4FD_{CCL}C_{in}}}{l_t}\right) + A_c ln\left\{\frac{\frac{J_{total}^2}{\left(\frac{4FD_{CCL}C_{in}}{l_t}\right)\left(\frac{36FDaggC_{in}(1-\epsilon_{CCL})}{Ragg}\times\frac{l_t}{Ragg}\right)}}{4A_c ln\left(\frac{\frac{1}{1-\frac{J_{total}}{J_{flow}}}}{\frac{J_{total}}{J_{flow}}+\ln(1-\frac{J_{total}}{J_{flow}})\left\{\frac{J_{total}}{J_{GDL,eff}}+\frac{J_{total}}{J_{diff,ch}}\right\}}\right)}\right\}+$<br>$\eta_{ohmic} = J_{total}\left\{\left(\frac{l_t}{\sigma}+\frac{l_{membrane}}{\sigma_{membrane}}+2\times\left[(1-\varphi)\frac{l_{GDL}}{\sigma_{GDL,tp}}+\varphi\left(\frac{\frac{w_{channel}}{2}}{\sigma_{GDL,ip}}+\frac{l_{GDL}}{\sigma_{GDL,tp}}\right)\right]\right)\right\}$ |

## 6.6) Results and Discussions

In this section we compare predictions of analytical model with three-dimensional numerical simulations in which none of the simplifying assumptions made during the derivation of the *PEM fuel cell equation* were made. This provides an independent way to assess the validity of the assumptions. The details about three-dimensional numerical simulations are provided in the section, 2.2 of chapter 2. Identical values of geometric, material and operating parameters were used in the simulations as those used in the calculations of analytical model. The geometry invoked for simulations included a single flow channel each

for $H_2$ and air, GDLs and catalyst layers on the anode and cathode sides, and a central proton exchange membrane (see Figure 6.1). As can be noted from figure 4.2 of chapter 4 and figure 6.1 below, we have also relaxed the assumptions of $W_{channel} \gg W_{rib}$. The mesh density was the finest in the catalyst layer and decreased from catalyst layer to channel. Mesh independence studies were performed leading to the choice of optimized mesh. All the results reported here are for fully converged and mesh independent simulations.

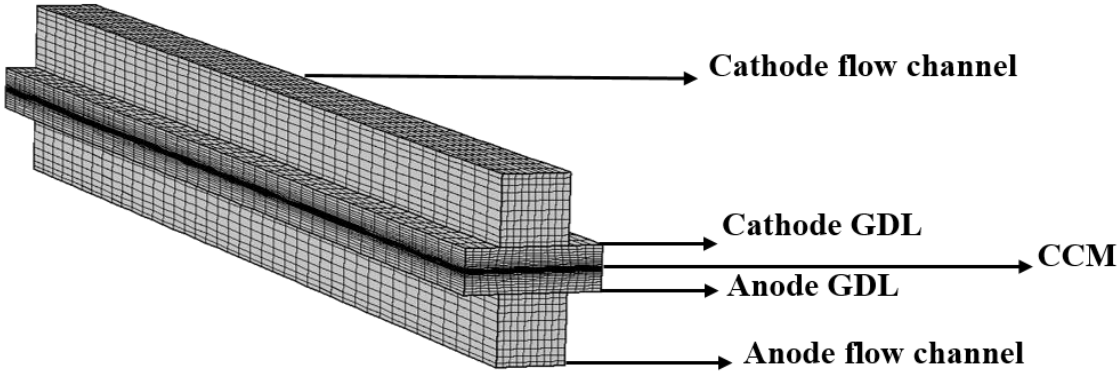


**Fig. 6.1** Three dimensional computational domain considered for simulation

The numerical values of model parameters are listed in Table 6.2. As will be discussed in the next chapter, $R_{ohmic}$ was determined from impedance spectroscopy to be $75\ m\Omega - cm^2$. The model parameter values in Table 6.2 give $\left\{\frac{l_t}{\sigma} + \frac{l_{membrane}}{\sigma_{membrane}} + 2 \times \left[(1-\varphi)\frac{l_{GDL}}{\sigma_{GDL,tp}} + \varphi\left(\frac{\frac{w_{channel}}{2}}{\sigma_{GDL,ip}} + \frac{l_{GDL}}{\sigma_{GDL,tp}}\right)\right]\right\} = 75\ m\Omega - cm^2$. The numerical values of oxygen diffusion coefficients in the different domains (CCL, GDL and channel) are experimentally determined and will be discussed in detail in chapter 8. While all other values of numerical parameters are discussed in table 6.2, the values of two parameters related to the catalyst microstructure as implied in the flooded agglomerate model namely, oxygen diffusion coefficient in an agglomerate $D_{agg}$, and porosity of CCL $\epsilon_{CCL}$, are also provided in Table 6.2. The diffusivity of oxygen in the ionomer phase of agglomerate can be estimated by the Bruggeman correlation, $D_{agg} = \varepsilon_{agg}^{1.5} D_{O2-ionomer}$ [56], where $\varepsilon_{agg}$ is the volume fraction of ionomer in the

agglomerate ($\varepsilon_{agg} = \frac{\varepsilon_l}{1-\varepsilon_{CCL}}$; $\epsilon_l$ being ionomer volume fraction in the CCL) and $D_{O2-ionomer}$ is the bulk diffusion coefficient of oxygen in ionomer. For $O_2$-nafion system, $D_{O2-nafion} \sim 10^{-10}\,\frac{m^2}{s}$ [93]. For $\varepsilon_l \sim 0.2$ and $\varepsilon_{CCL} \sim 0.4$, $D_{agg} \sim 10^{-11}\ \frac{m^2}{s}$. The value of CCL porosity $\epsilon_{CCL} \sim 0.4$ is representative of random close packing of spherical agglomerates. The value of $R_{agg}$ was chosen to be ~100 nm, which is within the range determined experimentally using nanometer scale x-ray computed tomography, TEM and mercury injection porosimetry techniques [94].

**Table 6.2** Numerical values of model parameters

| Parameter | Value | Remarks |
|---|---|---|
| $A_c$ | 0.026 V | Tafel slope |
| $F$ | 96500 $C/mol$ | Faraday constant |
| $2h$ | 0.001 $m$ | Depth of the channel |
| $i_{o,c}A$ | $\sim 0.5 \times 10^6\,\frac{A}{m^3}$ | This is calculated using $i_{o,c} \sim 1 \times 10^{-4}\ A/cm^2_{Pt}$ [38], electrochemical surface area of 60 $m^2_{Pt}/g_{Pt}$, catalyst loading of 0.25 $mg_{Pt}/cm^2$ and CCL thickness of 8 $\mu m$ |
| $L$ | 0.02 $m$ | Length of the channel |
| $l_{GDL}$ | 300 $\mu m$ | GDL thickness |
| $l_t$ | 8 $\mu m$ | Typical CCL thickness of a decal electrode |
| $w_{channel}$ | 0.001 $m$ | Width of the channel |
| $w_{rib}$ | 0.001 $m$ | Rib Width |
| $2h$ | 0.001 $m$ | Depth of the channel |
| $l_{membrane}$ | 25 $\mu m$ | Membrane thickness |
| $\sigma_{membrane}$ | 10 $S/m$ | Membrane proton conductivity [102] |
| $\sigma$ | 2.8 $S/m$ | CCL proton conductivity [43-45] |
| $\sigma_{GDL,ip}$ | 10000 $S/m$ | GDL In-plane electrical conductivity [101] |
| $\sigma_{GDL,tp}$ | 300 $S/m$ | GDL through-plane electrical conductivity [101] |
| $E_{eq}$ | 0.922 V | Open circuit voltage |
| $R_{agg}$ | 120 $nm$ | Discussed in the text |
| $D_{agg}$ | $\sim 10^{-11}\ m^2/s$ | Discussed in the text |
| $C_{in}$ | $\sim 8\ mol/m^3$ | Inlet oxygen concentration |
| $\varepsilon_{CCL}$ | 0.4 | Discussed in the text |
| $D_{CCL}$ | $\sim 5 \times 10^{-9}\ m^2/s$ | Chapter 7 |
| $D_{GDL}$ | $\sim 6 \times 10^{-6}\ m^2/s$ | Chapter 7 |
| $D$ | $\sim 3 \times 10^{-5}\ m^2/s$ | Chapter 7 |
| $J_{crit,(O2)transport}$ | $\sim 0.2\ A/cm^2$ | Equation (7.4) from chapter 7 |
| $J_{crit,(O2)\ transport\ in\ CCL\ and\ agglomerate}$ | $\sim 1.4\ A/cm^2$ | Equation (3.41) from chapter 3 |
| $J_{GDL,eff}$ | $\sim 3.2\ A/cm^2$ | Equation (6.10b) and (6.11) |
| $J_{flow}$ | $5.5 \times J_{expt}\ A/cm^2$ | Experimentally set value |
| $J_{diff,ch}$ | $\sim 18\ A/cm^2$ | Equation (6.10b) |
| $R_{ohmic}$ | $75\ m\Omega - cm^2$ | Equation (6.10c) |

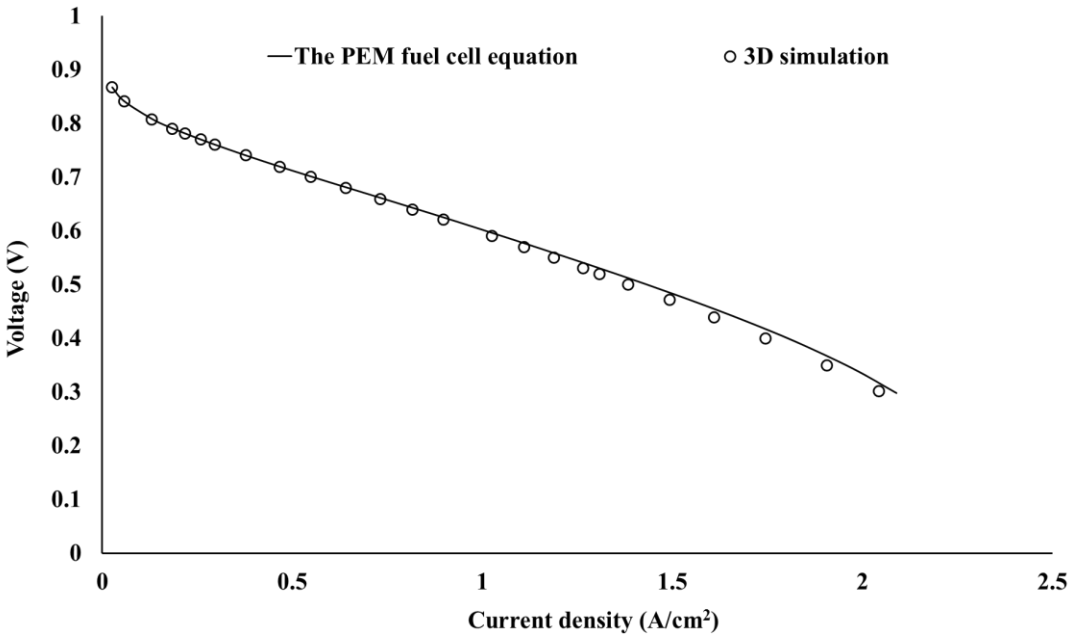


**Fig. 6.2** Comparison of polarization curves predicted by analytical theory and full three-dimensional numerical simulation

Figure 6.2 shows comparison between polarization curves predicted by the *PEM fuel cell equation* (equation (6.10)) and the three-dimensional numerical simulations. An excellent match between analytical model and the simulation was observed over the entire range of current density, which gives the first confirmation that the analytical model adequately captures the coupled reaction-diffusion-convection phenomena in an operational PEMFC and relates all material, geometrical and operating parameters to its performance. This is further supported by a comparison of the profiles of variables $C, j$ and $\eta$ in the three physical domains: flow channel, GDL and CCL, as predicted by the analytical theory and by the three-dimensional numerical simulations. Figure 6.3 shows comparison of analytical model predictions and results of three-dimensional numerical simulations at three representative axial positions ($x^* = 0.2, 0.5$ and 0.8) and at one representative operating cell voltage of 0.44 V ($\eta_{o,iR-free,CCL} = 0.36\,V$). The simulation results are reported for centre of channel width. The profiles are calculated from the analytical model as follows. The oxygen concentration profile at any $x^*$ in the channel depth

including at the channel-GDL interface is given by equation (6.4a) with $\alpha$, $\beta$ and $\xi$ being defined based on $J_{1-D}$ given by equation (6.10b). The oxygen concentration at the CCL-GDL interface is calculated from equations (6.2) and (6.9a), and the profile in the GDL thickness linearly varies between $C_{ch-GDL}$ and $C_{CCL-GDL}$. Equations (3.16)-(3.19) (from chapter 3) respectively, give the profiles of current density, oxygen concentration and overpotential in the CCL for the case of $M_T \ll 1$. However, as discussed in chapter 3, the mathematical similarity between the equation sets (3.6)-(3.8) (from chapter 3) corresponding to the case of $M_T \ll 1$ and equations (3.35)-(3.37) (from chapter 3) corresponding to the case of $M_T \gg 1$ suggests that the same equations (3.16)-(3.19) will also provide the profiles for the case of $M_T \gg 1$ with the only difference that $j^*, \eta^*, J^* \; and \; \varepsilon^2$ (defined in equation (3.9)) must be replaced by $j', \eta', J' \; and \; \varepsilon'^2\theta$ (defined in equation (3.38)). This procedure gives the required profiles of the variables $C, J$ and $\eta$ in the channel, GDL and CCL. As can be observed in figure 6.3, the profiles predicted by analytical model match reasonably well with the 3-D simulation results at all $x^*$s in all three domains. Furthermore, figure 6.4 compares the local current density profile along the channel length obtained from equation (6.4b) (where $\alpha$, $\beta$ and $\xi$ are defined based on $J_{1-D}$ given by equation (6.10b)) at the operating cell voltage of 0.44 V ($\eta_{o,iR-free,CCL} = 0.36\,V$) with that obtained from 3-D simulations (at the mid-plane of the membrane) at the same cell voltage. The simulations in fact give a profile of current density in '$x-z$' plane (see figure 6.5). Since the analytical model only considers average values of variables in the '$x-z$' plane, therefore the current density profile in the 3-D simulations was averaged out in '$z$' direction for a given '$x^*$', and the average values are compared with analytical results in figure 6.4. It can be observed that analytical model predictions and three-dimensional numerical simulation predictions are in close agreement. Thus, figures 6.3 and 6.4 justify the adequacy of using the quasi two-dimensional approach to describe the local $J - \eta_{o,CCL} - C_{CCL-GDL}$ relation as well as the axial oxygen concentration (and hence also current density).

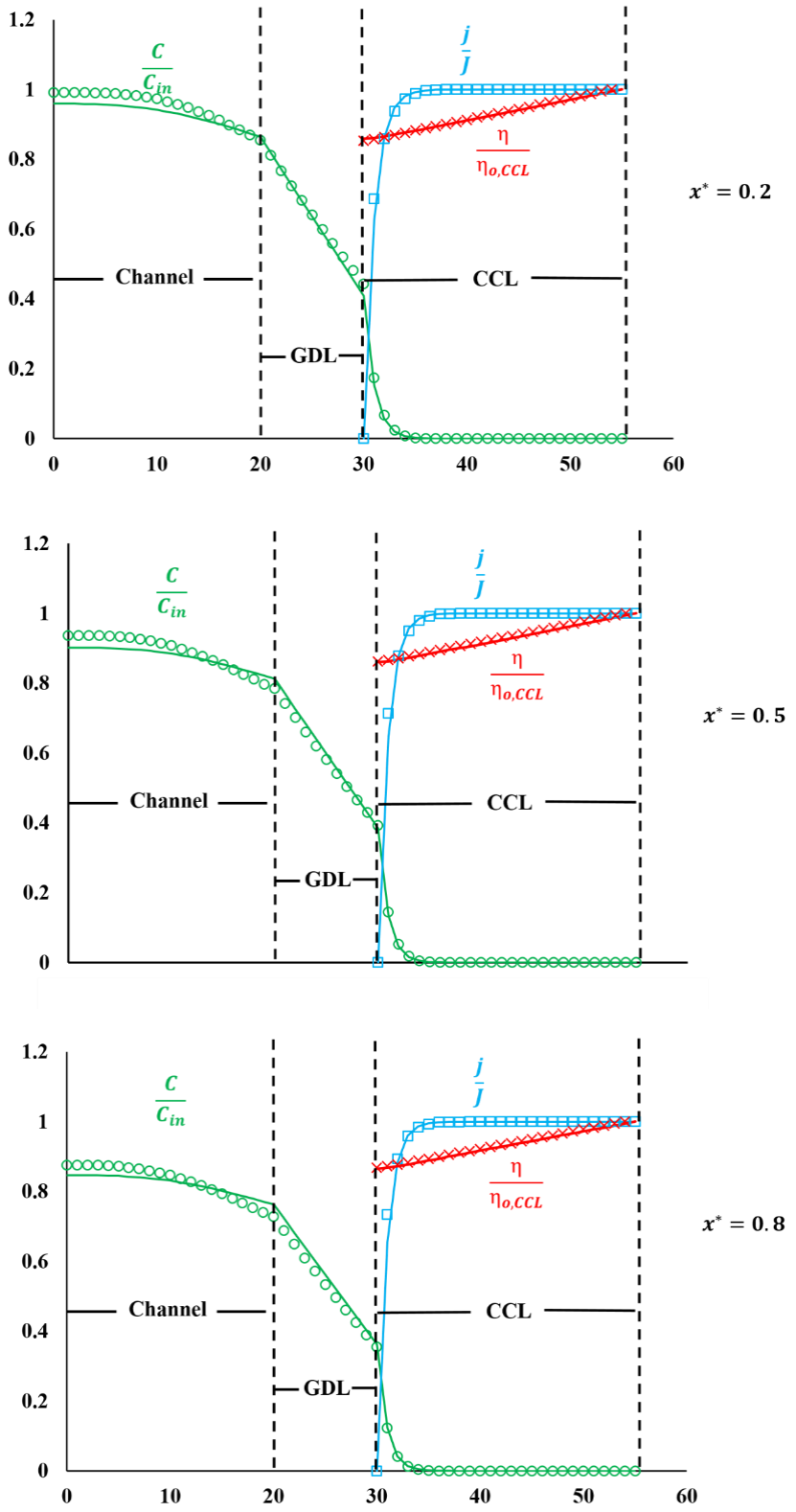


**Fig. 6.3** Transverse ($-y$) profiles of current density, overpotential ($\eta = \eta_{o,CCL}$ at membrane-CCL interface) and oxygen concentration in the different domains of the PEMFC for three different $x^*$ at the mid-of the channel width and operating cell voltage of 0.439 V ($\eta_{o,iR-free,CCL} = 0.363\ V$). Lines represent analytical model predictions while the numerical simulation results are given by symbols

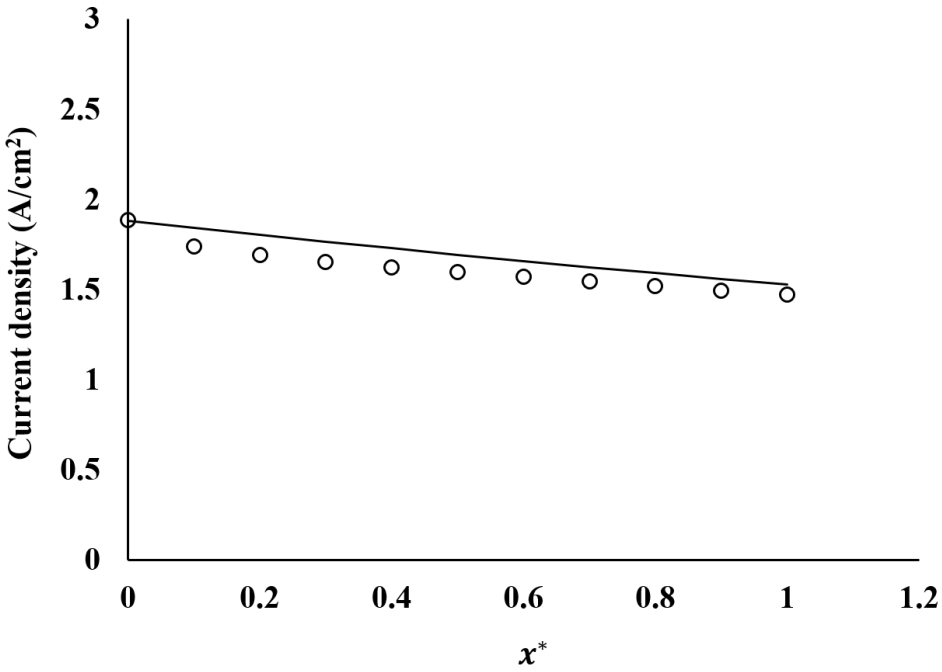


**Fig. 6.4** Comparison between the local current density profiles along the axial $(-x)$ direction obtained from analytical model (line) versus $z$- averaged numerical simulation results (symbol) at operating cell voltage of 0.439 V ($\eta_{o,iR-free,CCL} = 0.363\ V$).

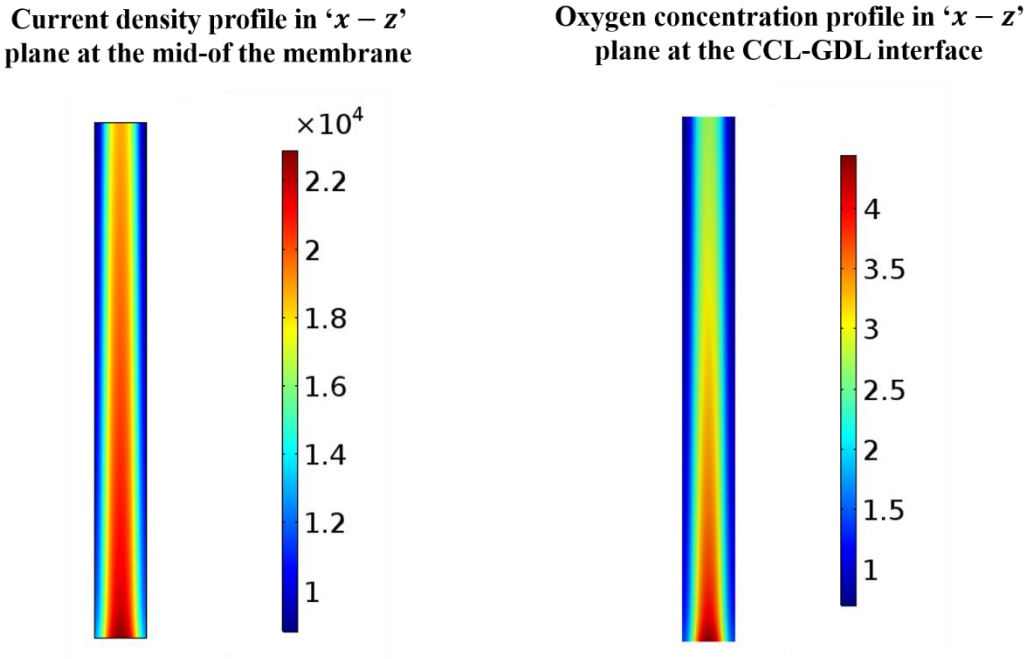


**Fig. 6.5** Simulated '$x-z$' plane current density (mid-of the membrane) and oxygen concentration (at CCL-GDL interface) profiles at operating cell voltage of 0.439 V ($\eta_{o,iR-free,CCL} = 0.363\ V$).

We now check whether the approximation of effective length (equation 6.11) is adequate to capture average variable values in the '$x-z$' direction especially for different rib widths. For this, we systematically varied rib-widths (1 mm, 1.2 mm and 1.4 mm) in the simulation and estimated the corresponding effective lengths (555 μm, 660 μm and 790 μm) using equation (6.11). The channel width was adjusted for each rib width to maintain the same total active area so that the air flow rate at the inlet of the channel remained identical for all three cases. All the other model parameters are listed in table 6.2. A reasonable agreement between polarization curves predicted by the PEM fuel cell equation and the simulated polarization curves (symbols) for all the three rib-widths can be seen in figure 6.6, which suggests that $l_{eff,GDL}$ can effectively capture average values of current density and oxygen concentration along '$x-z$' plane.

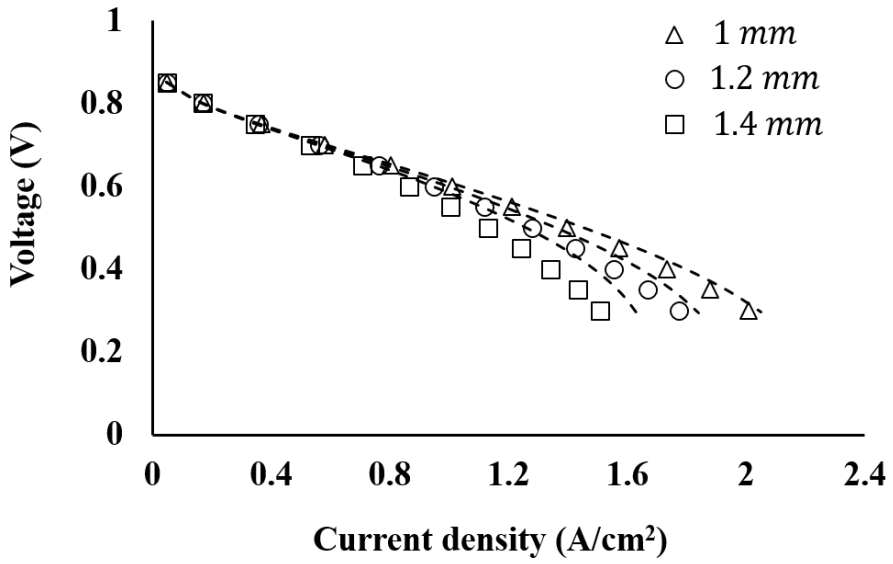


**Fig. 6.6** Comparison between the polarization curve obtained by analytical model (dotted lines) versus there-dimensional numerical simulation for different rib-widths.

We now check the assumption of using area-average current density $J_{total}$ (which is the same as assuming constant overpotential $\eta_o$ across active area) to calculate the ohmic overpotential loss in the analytical model by comparing it's predictions with numerical simulations, which rigorously determine the ohmic loss by calculating gradient of overpotential

across the active area. Figure 6.7 compares the polarization curves predicted by analytical model and 3-D simulations for three different ohmic resistances, 75, 100 and 150 $m\Omega - cm^2$, achieved by varying the proton conductivity of the membrane (10 S/m, 5 S/m and 2.5 S/m). The polarization curves predicted by analytical model agree reasonably well with the simulated polarization curves, which confirms the reasonability of the assumption.

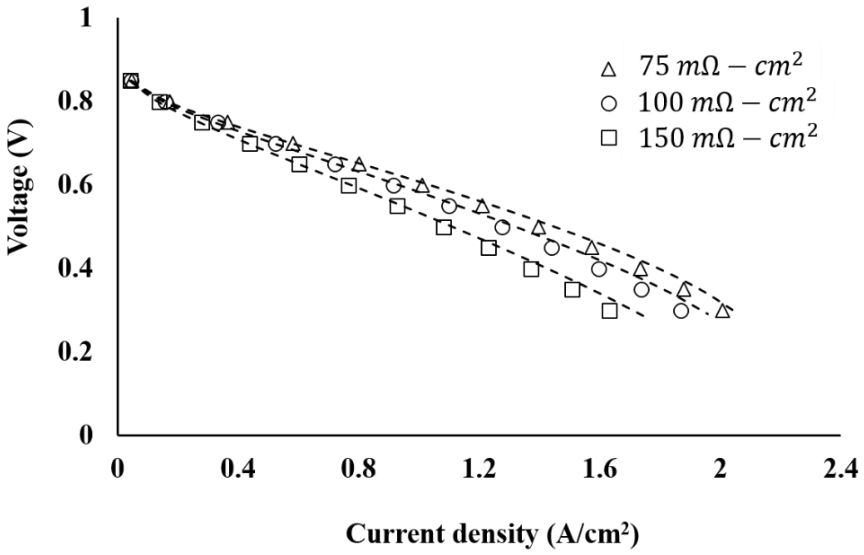


**Fig. 6.7** Comparison between the polarization curves obtained by analytical model (dotted lines) versus there-dimensional numerical simulation for different ohmic resistances.

In the end, it is worth noting that in the PEM fuel cell equation the various geometrical, operational and material parameters which control the performance of PEM fuel cell get combined into seven physically meaningful and experimentally measurable current density scales and one ohmic resistance. These are summarized in table 6.3. The current density scales are: one exchange current density, which corresponds to the intrinsic ORR kinetics, three critical current densities, $J_{crit,(H+)transport}$, $J_{crit,(O2)transport}$ and $J_{crit,(O2)\ transport\ in\ CCL\ and\ agglomerate}$, which denote the current densities above which these respective transport processes start modulating the intrinsic ORR kinetics, and three limiting

current density scales, which respectively denote the maximum allowable diffusive flux of oxygen in the GDL($J_{GDL,eff}$), channel ($J_{diff,ch}$) and the input stoichiometry of oxygen ($J_{flow}$).

**Table 6.3** Important current density scales in the PEM fuel cell equation

| **Sr. no** | **Current density scale** | **Expression** |
|---|---|---|
| 1 | Intrinsic exchange current density | $i_{o,c}$ |
| 2 | $J_{crit,(H+)transport}$ | $\frac{2\sigma A_c}{l_t}$ |
| 3 | $J_{crit,(O2)transport}$ | $\frac{4FD_{CCL}C_{in}}{l_t}$ |
| 4 | $J_{crit,(O2)\ transport\ in\ CCL\ and\ agglomerate}$ | $\sqrt{(\frac{4FD_{CCL}C_{in}}{l_t})(\frac{36FD_{agg}C_{in}(1-\epsilon_{CCL})}{R_{agg}} \times \frac{l_t}{R_{agg}})}$ |
| 5 | $J_{GDL,eff}$ | $\frac{4FD_{GDL}C_{in}}{l_{eff,GDL}}$ |
| 6 | $J_{flow}$ | $\lambda \times J_{expt}$ |
| 7 | $J_{diff,ch}$ | $\frac{4FDC_{in}}{h}$ |
| 8 | $R_{ohmic}$ | $\sim\left\{\frac{l_t}{\sigma} + \frac{l_{membrane}}{\sigma_{membrane}} + 2 \times \left[(1-\varphi)\frac{l_{GDL}}{\sigma_{GDL,tp}} + \varphi\left(\frac{\frac{w_{channel}}{2}}{\sigma_{GDL,ip}} + \frac{l_{GDL}}{\sigma_{GDL,tp}}\right)\right]\right\}$ |

## 6.7) Conclusion

This chapter provides an account for all coupled reaction-diffusion-convection processes occurring inside the various components of the PEM fuel cell resulting finally into the *'PEM fuel cell equation*' that relates the effects of all material, geometric and operating parameters of a PEM fuel cell to its performance in a compact manner. The various assumptions made during the derivation of the PEM fuel cell equation were validated by comparing model predictions with the results of full three-dimensional numerical simulations in which no simplifying approximations were made. The polarization curves predicted by the PEM fuel cell

equation, profiles of oxygen concentration, current density and overpotential showed quantitative match with the three-dimensional numerical simulations over a wide range of current density.

The analytical model presented here has elaborated more on the specific case wherein the resistance to oxygen diffusion in CCL affected the ORR kinetics at lower current density than proton transport resistance in CCL ($D^* < 1$). This is because of its relevance to the experimental conditions used in this work. In the future, the analytical model can be extended to the case of $D^* > 1$, which might be relevant to other types of fuel cells such as an open cathode design wherein low humidity conditions could cause higher resistance to proton conduction in the CCL. The analytical model can also be extended in the future to account for detailed two-phase water balance in the MEA.

# Chapter 7

# The PEM fuel cell equation: experimental validation

The content of this chapter is published in,
"Chemical Engineering Science, volume no. 206, 12th October 2019, pages: 96–117" [90].

As mentioned in earlier chapter, PEM fuel cell equation is valid for the case wherein oxygen transport resistance in the cathode catalyst layer (CCL) is encountered at lower current density than proton transport resistance in the CCL i.e., the first deviation from intrinsic Tafel kinetics on the polarization curve is a consequence of oxygen transport resistance across the CCL. This essentially suggests that $D^* < 1$, where $D^*$ is the ratio of $J_{crit,(O2)transport} = \frac{4FD_{CCL}C_{in}}{l_t}$ and $J_{crit,(H+)transport} = \frac{2\sigma A_c}{l_t}$ (see table 6.3). To the best of our knowledge, no experimental methodology is available in the literature to decipher the regime of CCL operation. It should also be noted that while predicting the polarization curve using PEM fuel cell equation, we assumed certain numerical values of oxygen diffusion coefficients in the channel, GDL and CCL (see table 6.2). Thus, it is crucial to first experimentally estimate oxygen diffusivities in the different domains of PEMFC namely, flow channel, GDL and CCL. In most of the earlier studies, the so-called limiting current method has been used to estimate oxygen transport resistance in these domains [66-70]. However, there are two assumptions in this method. We have discussed these assumptions in detail in chapter 2. Here, we briefly summarize them:

1. The method assumes that the oxygen concentration is linear in all domains. This especially does not hold in the CCL. A rapid non-linear decay of oxygen concentration in the

CCL near the GDL-CCL interface is predicted when the rate of oxygen transport across the CCL is considerably slower compared to intrinsic ORR kinetics (see chapter 2) which results in the strong dependence of local apparent Tafel slope on overpotential. Therefore, correlating oxygen transport resistance in the CCL to the limiting current density, which is independent of overpotential, is not appropriate.

2. The influence of oxygen diffusion along the channel depth is assumed to be negligible in these studies, which may not be realistic. The isothermal two-dimensional model of PEMFC (chapter 4-6) clearly shows that the limiting current for high stoichiometric reactant flow rates is a function of oxygen diffusion in the GDL as well as oxygen diffusion along the channel depth. Therefore, to determine the effective oxygen diffusion coefficient in GDL it is imperative to segregate the contribution of oxygen diffusion along the channel depth from the limiting current density.

Thus, there are at least two unrealistic assumptions made in the previous studies insofar as experimental determination of oxygen diffusivities in the various domains of PEMFC is concerned. By using the limiting cases of our PEM fuel cell equation, we elucidate here a systematic experimental methodology to estimate the effective diffusion coefficients of oxygen in the CCL, GDL and channel. Finally, we show that when the experimentally determined diffusion coefficients are used in the PEM fuel cell equation the predicted polarization curve shows excellent match with experimentally measured polarization curve.

We begin by summarizing the key limiting cases of PEM fuel cell equation and the theoretical scaling laws that come out of the model. This is followed by the experimental details and an account of data analysis methods. We then discuss the salient results comparing analytical model with experimental data in the final subsection.

## 7.1) Limiting cases of PEM fuel cell equation

We first reproduce here the PEM fuel cell equation:

$$J_{total} = J_{flow}\left\{1 - \exp(-\frac{\beta}{1+\alpha+\xi})\right\} \tag{7.1a}$$

Here,

$$\alpha = \frac{J_{1-D}}{J_{GDL,eff}}, \beta = \frac{J_{1-D}}{J_{flow}}, \xi = \frac{J_{1-D}}{J_{diff,ch}}, J_{GDL,eff} = \frac{4FD_{GDL}C_{in}}{l_{eff,GDL}}, J_{flow} = \frac{7FU_{mean}hC_{in}}{L}, J_{diff,ch} = \frac{4FDC_{in}}{h} and$$

$$J_{1-D} = \frac{4FD_{CCL}C_{in}}{l_t} \times \sqrt{\frac{i_{o,c}Al_t\left[\exp\left(\frac{\eta_{o,iR-free,CCL}}{A_c}\right)\right]\times E(\eta_{o,iR-free,CCL})}{\frac{4FD_{CCL}C_{in}}{l_t}}} \tanh\left\{\sqrt{\frac{i_{o,c}Al_t\left[\exp\left(\frac{\eta_{o,iR-free,CCL}}{A_c}\right)\right]\times E(\eta_{o,iR-free,CCL})}{\frac{4FD_{CCL}C_{in}}{l_t}}}\right\} \tag{7.1b}$$

$$\eta_{ohmic} = J_{total}\left\{\frac{l_t}{\sigma} + \frac{l_{membrane}}{\sigma_{membrane}} + 2\times\left[(1-\varphi)\frac{l_{GDL}}{\sigma_{GDL,tp}} + \varphi\left(\frac{\frac{w_{channel}}{2}}{\sigma_{GDL,ip}} + \frac{l_{GDL}}{\sigma_{GDL,tp}}\right)\right]\right\} \tag{7.1c}$$

$$V = E_{eq} - \eta_{o,iR-free,CCL} - \eta_{ohmic} \tag{7.1d}$$

We now discuss two important experimentally achievable limiting cases of equation (7.1a) and (7.1b).

### a) $J_{1-D} << J_{GDL}, J_{flow}, J_{diff,ch}$ $(\alpha, \beta, \xi << 1)$

This is experimentally achievable at low overpotential (i.e. high operating cell voltage) and high oxidant stoichiometry. For $\alpha, \beta, \xi << 1$, it can be shown that $\left\{1 - \exp(-\frac{\beta}{1+\alpha+\xi})\right\} \approx \beta$ and therefore, $J_{total} \approx J_{1-D}$. This limiting case physically means that the mass transfer resistance for oxygen is negligible in the GDL and flow channel. Also, oxygen concentration at the CCL-GDL interface is the same as the inlet oxygen concentration $C_{CCL-GDL} \approx C_{in}$ because of high stoichiometry. Hence the current-potential relationship is dictated by the

physicochemical processes occurring *only* in the CCL. We can further sub-divide this limiting regime in the following sub-cases:

- $J_{total} \ll \frac{4FD_{CCL}C_{in}}{l_t}, \sqrt{(\frac{4FD_{CCL}C_{in}}{l_t})(\frac{36FD_{agg}C_{in}(1-\epsilon_{CCL})}{R_{agg}} \times \frac{l_t}{R_{agg}})}$

In this regime, $E(\eta_{iR-free}) \approx 1$, therefore equation (7.1b) transforms to

$\frac{J_{total}}{\frac{4FD_{CCL}C_{in}}{l_t}} = \sqrt{\frac{i_{o,c}Al_t\left[\exp\left(\frac{\eta_{o,iR-free,CCL}}{A_c}\right)\right]}{\frac{4FD_{CCL}C_{in}}{l_t}}} \tanh\left\{\sqrt{\frac{i_{o,c}Al_t\left[\exp\left(\frac{\eta_{o,iR-free,CCL}}{A_c}\right)\right]}{\frac{4FD_{CCL}C_{in}}{l_t}}}\right\} \ll 1$, which suggests

$\tanh\left\{\sqrt{\frac{i_{o,c}Al_t\left[\exp\left(\frac{\eta_{o,iR-free,CCL}}{A_c}\right)\right]}{\frac{4FD_{CCL}C_{in}}{l_t}}}\right\} \approx \sqrt{\frac{i_{o,c}Al_t\left[\exp\left(\frac{\eta_{o,iR-free,CCL}}{A_c}\right)\right]}{\frac{4FD_{CCL}C_{in}}{l_t}}}$.

Therefore, equation (7.1b) gives,

$$J_{total} = J_{1-D} = i_{o,c}Al_t\left[\exp\left(\frac{\eta_{o,iR-free,CCL}}{A_c}\right)\right] \tag{7.2}$$

Equation (7.2) is essentially intrinsic Tafel kinetics of ORR.

- $\frac{4FD_{CCL}C_{in}}{l_t} \ll J_{total} \ll \sqrt{(\frac{4FD_{CCL}C_{in}}{l_t})(\frac{36FD_{agg}C_{in}(1-\epsilon_{CCL})}{R_{agg}} \times \frac{l_t}{R_{agg}})}$

Here again $E(\eta_{iR-free}) \approx 1$. However, equation (7.1b) implies

$\frac{j_{total}}{\frac{4FD_{CCL}C_{in}}{l_t}} = \sqrt{\frac{i_{o,c}Al_t\left[\exp\left(\frac{\eta_{o,iR-free,CCL}}{A_c}\right)\right]}{\frac{4FD_{CCL}C_{in}}{l_t}}} \tanh\left\{\sqrt{\frac{i_{o,c}Al_t\left[\exp\left(\frac{\eta_{o,iR-free,CCL}}{A_c}\right)\right]}{\frac{4FD_{CCL}C_{in}}{l_t}}}\right\} \gg 1$, which suggests

$\tanh\left\{\sqrt{\frac{i_{o,c}Al_t\left[\exp\left(\frac{\eta_{iR-free,CCL}}{A_c}\right)\right]}{\frac{4FD_{CCL}C_{in}}{l_t}}}\right\} \approx 1$.

Therefore, equation (7.1b) reduces to

$$J_{total} = \sqrt{\frac{4FD_{CCL}C_{in}}{l_t} i_{o,c}Al_t\left[\exp\left(\frac{\eta_{o,iR-free,CCL}}{A_c}\right)\right]} \tag{7.3}$$

Equation (7.3) is the current-potential relationship wherein oxygen transport resistance across the CCL modulates the intrinsic Tafel kinetics of ORR. Note that the critical current density above which the rate of oxygen transport process across CCL becomes comparable with intrinsic ORR kinetics i.e., the transition of current-potential relationship from equation (7.2) to equation (7.3) is,

$$J_{crit,(O2)transport} = \frac{4FD_{CCL}C_{in}}{l_t} \tag{7.4}$$

***b) $J_{GDL}, J_{diff,ch} \ll J_{1-D}, J_{flow}$ ($\alpha, \xi \gg 1$)***

This limiting case is realizable at high overpotentials and at high stoichiometries. For $\alpha, \xi \gg 1$, it can be shown that $\left\{1 - \exp(-\frac{\beta}{1+\alpha+\xi})\right\} \approx \frac{\beta}{\alpha+\xi}$ and hence, equation (7.1a) gives

$$\frac{1}{J_{total}} = \frac{1}{J_{GDL}} + \frac{1}{J_{diff,ch}} = \frac{1}{\frac{4FD_{GDL}C_{in}}{l_{eff,GDL}}} + \frac{1}{\frac{4FDC_{in}}{h}} \tag{7.5}$$

The total current density in equation (7.5) is independent of overpotential. Thus, this is a limiting current density value. The two cases (a) and (b) discussed above will be used in the following sections to pull out important scaling laws.

## 7.2) Theoretical scaling laws

In any experimental study that seeks to understand the factors governing fuel cell polarization, it is critical to first decipher which of the two important transport resistances viz., oxygen transport or proton transport resistances, are responsible for modulating the overall consumption rate of oxygen in CCL. We propose that this can be done by experimentally determining scaling laws between measured current density and inlet oxygen concentration under carefully chosen operating conditions, and comparing the same with theoretically predicted scaling laws. To do so, we first extract scaling laws relating measurable current

density $J_{total}$ and inlet oxygen concentration $C_{in}$ from the PEM fuel cell equation (7.1) under two experimentally achievable limiting cases:

- ***Ideal proton transport across the CCL***

The limiting cases of equation (7.1) i.e. equations (7.2), (7.3) and (7.5) suggest the following scaling laws relating $J_{total} - C_{in}$ at a given overpotential,

$$J_{total} \sim (C_{in})^0 \text{ for } J_{total} < \frac{4FD_{CCL}C_{in}}{l_t} \text{ and } \alpha, \beta, \xi \ll 1 \quad (7.6a)$$

$$J_{total} \sim (C_{in})^{0.5} \text{ for } \frac{4FD_{CCL}C_{in}}{l_t} < J_{total} \text{ and } \alpha, \beta, \xi \ll 1 \quad (7.6b)$$

$$J_{total} \sim (C_{in})^1 \text{ for } \frac{4FD_{CCL}C_{in}}{l_t} < J_{total} \text{ and } \alpha \text{ and/or } \xi \gg 1 \quad (7.6c)$$

As noted earlier and also from equations (7.2) and (7.3), with increasing $J_{total}$ the apparent Tafel slope changes from intrinsic Tafel slope of ~26 mV (equivalent to 60 mV when expressed in $\log_{10}$) to ~52 mV (equivalent to 120 mV when expressed in $\log_{10}$) and keeps increasing further until at limiting conditions the current density becomes independent of overpotential (equation 7.5; infinite apparent Tafel slope)). Further, equation (7.4) gives the scaling law relating $J_{crit}$ to inlet oxygen concentration as,

$$J_{crit,(02)transport} \sim (C_{in})^1 \quad (7.7)$$

- ***Ideal oxygen transport across the CCL***

At low current density given by $J_{total} \ll \frac{4FD_{CCL}C_{in}}{l_t}, \frac{2\sigma A_c}{l_t}, J_{GDL}, J_{diff,ch}, J_{flow}$, the current-potential relationship is given by equation (7.2). At intermediate current density, if $\frac{4FD_{CCL}C_{in}}{l_t} \gg J_{total} > \frac{2\sigma A_c}{l_t}$, then proton transport resistance across the CCL becomes significant. The local current-potential relationship for this regime was given by (see chapter 5)

$$\frac{2J}{j_{1-D}} + (\alpha+\xi)\ln\left(\frac{2J}{j_{1-D}}\right) = \left(\sqrt{4+(\alpha+\xi)^2} - (\alpha+\xi)\right) + (\alpha+\xi)ln\left(\sqrt{4+(\alpha+\xi)^2} - (\alpha+\xi)\right) - \beta x^* \quad (7.8)$$

Here, $\alpha$, $\beta$ and $\xi$ are defined based on $J_{1-D} = \sqrt{\frac{2\sigma A_c}{l_t} i_{o,c} A l_t \left[\exp\left(\frac{\eta_{o,CCL}}{A_c}\right)\right]}$. The total current density can be obtained by integrating equation (7.8). It was shown (Thosar and Lele 2017) that for $\alpha, \beta, \xi \ll 1$,

$$J_{total} = \sqrt{\frac{2\sigma A_c}{l_t} i_{o,c} A l_t \left[\exp\left(\frac{\eta_{o,CCL}}{A_c}\right)\right]} \quad (7.9)$$

It was also shown that at high stoichiometry and high overpotential when $J_{1-D} > J_{GDL}, J_{diff,ch}$, then equation (7.8) simplifies to (Thosar and Lele 2017)

$$\frac{1}{J_{total}} = \frac{1}{J_{GDL}} + \frac{1}{J_{diff,ch}} = \frac{1}{\frac{4FD_{GDL}C_{in}}{l_{eff,GDL}}} + \frac{1}{\frac{4FDC_{in}}{h}} \quad (7.10)$$

Note that equation (7.10) is identical to equation (7.5). This physically means that irrespective of the regime of operation in the CCL, the overall limiting current density is dictated by oxygen diffusion rate in the channel and GDL.

Equations (7.2), (7.9) and (7.10) suggest following scaling laws relating $J_{total} - C_{in}$ at a given overpotential,

$$J_{total} \sim (C_{in})^0 \text{ for } J_{total} < \frac{2\sigma A_c}{l_t} \quad (7.11a)$$

$$J_{total} \sim (C_{in})^0 \text{ for } \frac{2\sigma A_c}{l_t} < J_{total} \text{ and } \alpha, \beta, \xi \ll 1 \quad (7.11b)$$

$$J_{total} \sim (C_{in})^1 \text{ for } \frac{2\sigma A_c}{l_t} < J_{total} \text{ and } \alpha \text{ and/or } \xi \gg 1 \quad (7.11c)$$

Also, the scaling law relating $J_{crit,(H+)transport}$ to inlet oxygen concentration is given by

$$J_{crit,(H+)transport} \sim (C_{in})^0 \quad (7.12)$$

In the following sections we will use the limiting cases and the scaling laws extracted from the PEM fuel cell equation to analyse our experimental data. Specifically, we demonstrate three new methods to analyse the data: (1) a graphical method to determine $J_{crit}$, (2) a method to determine the operating regime of CCL using theoretical scaling laws, and (3) a method to determine diffusion coefficients in channel, GDL and CCL. Using this information, we will then compare the experimentally determined polarization curve with predictions of the PEM fuel cell equation.

### 7.3) Experimental details

Nafion-XL grade membrane (27 µm thick) was hot-pressed between two 25 $cm^2$ decal electrodes. The electrodes were fabricated by coating PTFE films with an aqueous slurry of 40 wt% Pt/C catalyst and 5 wt% ionomer solution followed by drying the film. Decal transfer resulted in 7-7 micron thick catalyst layer on both anode and cathode sides covering the active area (25 $cm^2$). Catalyst loading was approximately 0.3 $mg/cm^2$ on anode as well as cathode. Gas diffusion layers (SGL 39 BC) of 25 $cm^2$ area, ~300 micron thickness and having open porosity of 0.5 were used to prepare the membrane electrode assemblies (MEA). The membrane was extrapolated beyond the active area so that no sub-gaskets were required for MEA assembly. MEAs were prepared by hot compression; the compression strain being limited to within 12-15%, which resulted in an estimated porosity of GDL of ~ 0.35. Fiber reinforced teflon (FRT) flat sheets were used as gaskets to avoid peripheral leaks and cross-flow. The MEAs were sandwiched between two graphite monopolar plates each containing 3-channel serpentine flow field. The channels and ribs were both ~1 mm wide and the channels were 1 mm deep unless otherwise stated. The before and after assembly of the test-cell used in the experiments is shown below in figure 7.1. Figure 7.2 illustrates the above mentioned three-channel serpentine flow field used in the experiments.

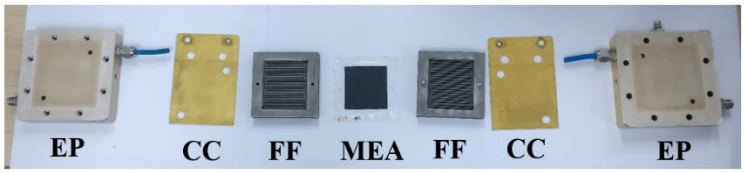


**EP : End Plate** **FF: Flow Field Plate**
**CC: Current Collector Plate** **MEA: Membrane Electrode Assembly**

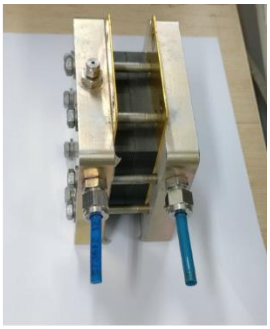

**(a)** **(b)**

**Fig. 7.1** Test-cell set-up (a) before assembly and (b) after assembly

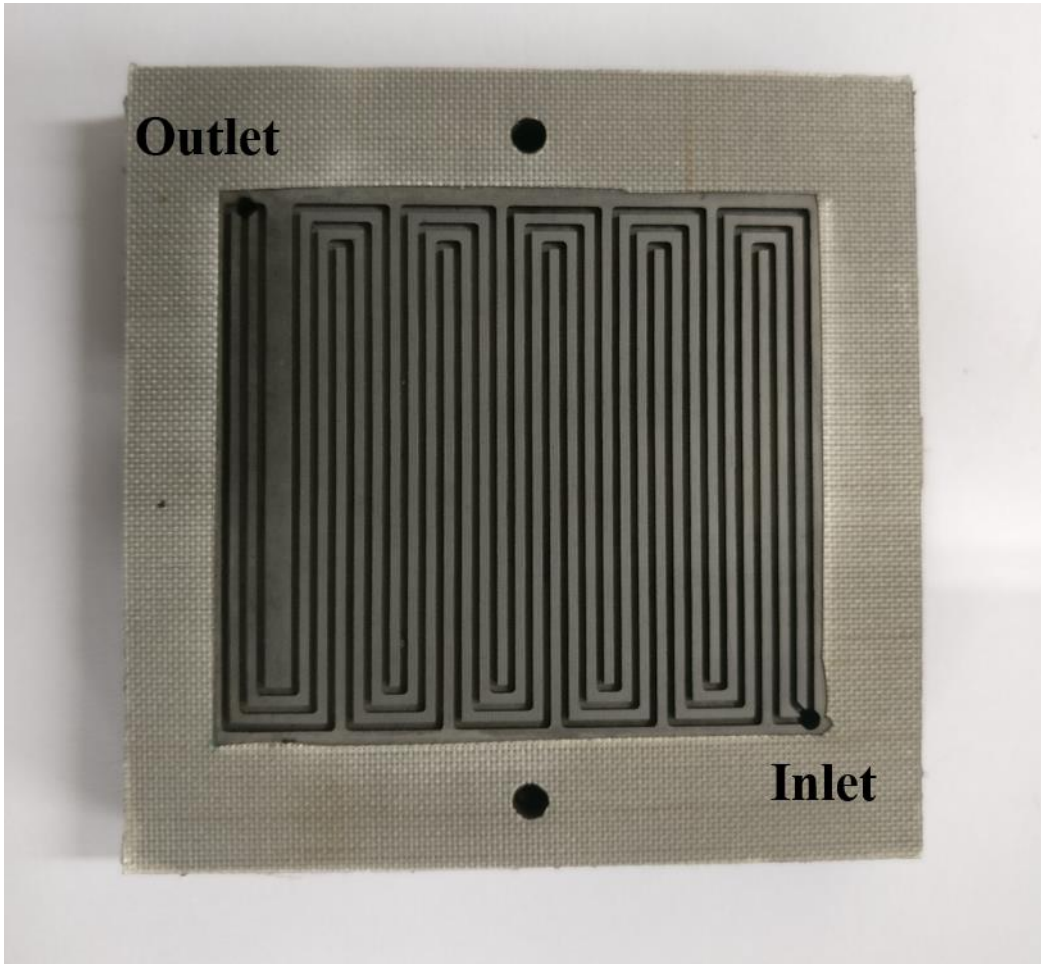


**Fig. 7.2** Three-channel serpentine flow field (used in the experiments)

The cell temperature was maintained at 60° C using external heaters. The temperatures of humidifiers were maintained constant at 60°C and 54 °C for anode and cathode respectively, in order to achieve 100% and 80-85% humidification on anode and cathode sides respectively.

The MEAs were conditioned and tested using a fuel cell test station (Fuel Cell Technologies Inc., Model SFC-TS, USA). The key experimental conditions are described in table 7.1.

**Table 7.1** Experimental conditions and MEA details

| **Parameters** | **Values** |
|---|---|
| Operating temperature ($^{O}$C) | 60 (maintained using external heaters) |
| Relative Humidity | 80% at C and 100% at A |
| Operating pressure (atm, absolute) | 1 |
| Anode Stoichiometry ($H_2$) | 5 (controlled using mass flow controller, MKS instruments) |
| Cathode Stoichiometry | 5.5 (controlled using mass flow controller, MKS instruments) |
| Active Area | 25 $cm^2$ |
| Membrane | Nafion XL Membrane |
| Sealing Gasket | FRT Flat gasket |

Two different sets of experiments were planned to determine the controlling transport resistance in CCL and to quantify the effective diffusion coefficients of oxygen in CCL and GDL:

1) Varying inlet oxygen concentration

Calibrated gas cylinders of oxygen-nitrogen mixtures containing oxygen concentrations of 4%, 6%, 8%, 10% and 21% (air) were used. Pre-conditioned MEAs were further conditioned using each of the calibrated $O_2$-$N_2$ mixtures at constant voltage of 0.6 V for 1 hour to ensure that steady-state current density was reached and then subjected to polarization curve. Pure $H_2$ was used as fuel.

2) Varying channel depth

The cathode side flow field plate was customized to have different channel depths of 1 mm, 2 mm, 3 mm and 4 mm. The channel depth on anode plate was always 1 mm. For each plate, a pre-conditioned MEA was re-conditioned at a constant voltage of 0.6 V for 1 hour so that

steady-state was confirmed and then subjected to polarization curve using 4% $O_2$ as oxidant and pure $H_2$ as fuel.

All polarization experiments were performed at sufficiently high stoichiometries of 5 and 5.5 respectively, for hydrogen and air in flow tracking mode. This ensures uniform hydrogen and oxygen concentration over the flow field at all current densities. For each MEA, its ohmic resistance was independently determined using electrochemical impedance spectroscopy. In particular, the high frequency resistance (HFR) of MEA was determined from Nyquist plot and was used as the value of ohmic resistance. HFR value of ~75 mΩ-cm$^2$ ($\pm$ 2-5 mΩ-cm$^2$) was measured consistently for all MEAs. iR-free polarization data was obtained by adding the voltage loss due to ohmic resistance to the measured cell potential.

## 7.4) Data analysis methods

- ***Graphical method to determine $J_{crit}$ from experimental polarization curve***

Figure 7.3 shows a typical iR-corrected experimental polarization curve on a semi-log scale. Plotted this way, the polarization curve is linear in the very low current density region with a slope equal to the intrinsic Tafel slope ($A_c = RT/F$) for ORR, and it deviates from this line as the current density is increased. At some intermediate current density, the local slope of the polarization curve doubles i.e., it asymptotically merges with a line having slope equal to doubled Tafel slope ($2RT/F$). Figure 7.3 also shows the lines corresponding to local slopes equal to the Tafel slope and double-Tafel slope. The x-coordinate of the intersection point of these asymptotic lines is the critical current density ($J_{crit}$), (refer chapter 2), therefore this graphical method is used in the present work to determine $J_{crit}$ for different oxidant concentrations. It should be noted that the transport resistance, which causes deviation and

eventual doubling of Tafel slope, starts influencing the polarization curve at a current density much lower than $J_{crit}$. This is evident from figure 7.3.

- ***Using scaling laws to discern the operating regime of CCL***

iR-free polarization curves were obtained for different oxidant concentrations under conditions of $J_{crit} \ll J_{GDL}, J_{diff,ch}, J_{flow}$. Current densities at a given overpotential were measured for each oxygen concentration from the respective iR-free polarization curves and plotted against oxygen concentration to give the experimentally measured scaling law. Similarly, the scaling law of $J_{crit}$ versus oxygen concentration was determined. Comparison of these scaling laws with equation sets (7.6), (7.7) and (7.11), (7.12) is used to discern which of the two main transport resistances, oxygen transport or proton transport in CCL, is influencing the overall ORR.

- ***Estimating effective oxygen diffusion coefficient in the CCL, GDL and channel***

If scaling law analysis suggests that oxygen transport in CCL governs the overall rate of ORR, then equation (7.4) suggests that the slope of experimentally determined $J_{crit}$ versus oxygen concentration should yield the effective oxygen diffusion coefficient in the CCL. Note that the other parameters in equation (7.4) are known ($F = 96500 \frac{C}{mol}$ and $l_t = 8\ \mu m$).

Equations (7.5) and (7.10) both suggest that if the channel depth ($2h$) is varied systematically then a plot of reciprocal of limiting current density) versus channel depth should be a line whose slope will allow for estimation of the oxygen diffusion coefficient in air, and whose intercept on the $\frac{1}{J_{total}}$ axis will enable the estimation of effective oxygen diffusion coefficient in the GDL. These experiments were performed using low oxygen concentration and with high stoichiometric reactant gas flow rates to ensure that the limiting current density is because of oxygen diffusional resistances in the channel and GDL. Since the oxygen

diffusion coefficient in air is well known, this value can be used to validate the utility of the methodology. In the experiments, we were not able to reach high enough overpotential to reach limiting current density values because of limitation on the maximum current that could be drawn from the load box. Hence, we have taken the value of current density at highest measured overpotential as the limiting current value. The intrinsic assumption here is that the measured current density has the same dependence on $C_{in}$ as the limiting current density.

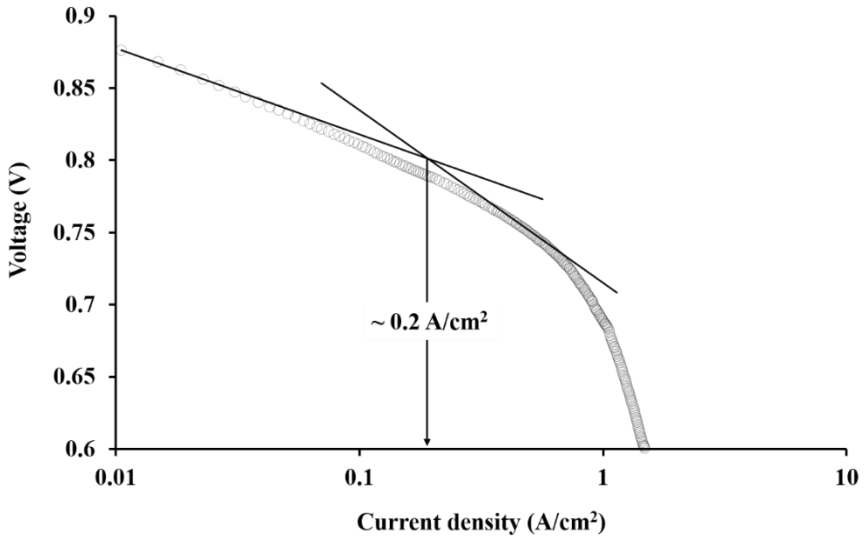


**Fig. 7.3** iR-corrected polarization curve in semi-log scale with $H_2$ as a fuel and air as an oxidant at $T = 60°C$, $H_2$ stoichiometry = 5, air stoichiometry = 5.5, outlet pressure=ambient pressure, anode side RH $= 100\%$ and cathode side RH $= 70\%$. The lines have intrinsic Tafel slope and doubled Tafel slope. Their point of intersection is the critical current density.

## 7.5) Results and discussions

- ***Regime of CCL operation***

We begin by deciphering, for our MEAs, which of the two transport resistances, oxygen diffusion or proton conduction, will start modulating the Tafel kinetics first as the current density is increased. Figure 7.4 shows the polarization curves for different oxygen concentrations namely 4%, 6%, 8%, 10% and 21% (air). The critical current density ($J_{crit}$) was determined for each polarization curve using the aforementioned graphical method (see figure

7.5). A double logarithmic plot of $J_{crit}$ versus $C_{in}$ is shown in figure 7.6a. The slope of the graph gives the scaling exponent of 0.84, which is close to 1 and therefore is suggestive of the scaling $J_{crit} \sim (C_{in})^1$.

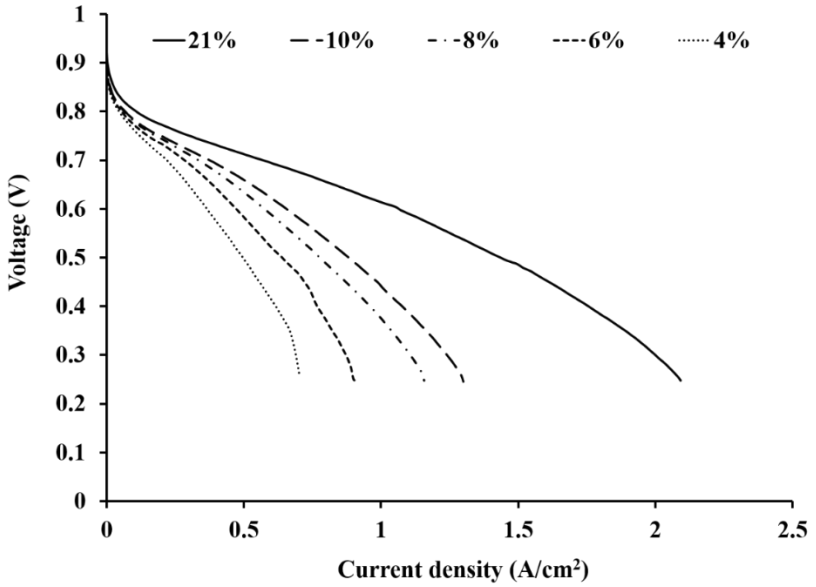


**Fig. 7.4** Polarization curves for different inlet oxygen concentrations with $H_2$ as a fuel at $T = 60°C$, $H2\ stoichiometry = 5$, $oxidant\ stoichiometry = 5.5$, $outlet\ pressure = ambient$, $anode\ side\ RH = 100\%$ and $cathode\ side\ RH = 70\%$

Figure 7.8 shows double logarithmic plot of measured current density versus $C_{in}$ at three different overpotentials. The lower overpotential of 0.069 V corresponds to the regime of Tafel slope on the polarization curve, whereas the higher overpotential of 0.135 V corresponds to a regime of nearly doubled Tafel slope on the polarization curve for all the oxygen concentrations. The overpotential of 0.56 V corresponds to a high current density regime on the polarization curve where oxygen diffusion in GDL or channel is expected to be slower than oxygen consumption rate in the CCL i.e., $\alpha$ and/or $\xi \gg 1$. From figure 7.8 it can be inferred that the experimentally observed scaling laws relating measured current density to inlet oxygen concentration for the three overpotentials are approximately, $J_{total} \sim (C_{in})^0 @\ 0.069\ V \rightarrow J_{total} \sim (C_{in})^{0.5} @\ 0.135\ V \rightarrow J_{total} \sim (C_{in})^1\ @\ 0.56\ V$. Thus, we see a reasonable agreement between theoretical scaling laws (equations (7.6) and (7.7)) and experimentally established

scaling laws, and this suggests that the first deviation from intrinsic Tafel kinetics on the polarization curve is a consequence of oxygen transport resistance across the CCL. In other words, $J_{crit,(O2)transport} < J_{crit,(H+)transport}$.

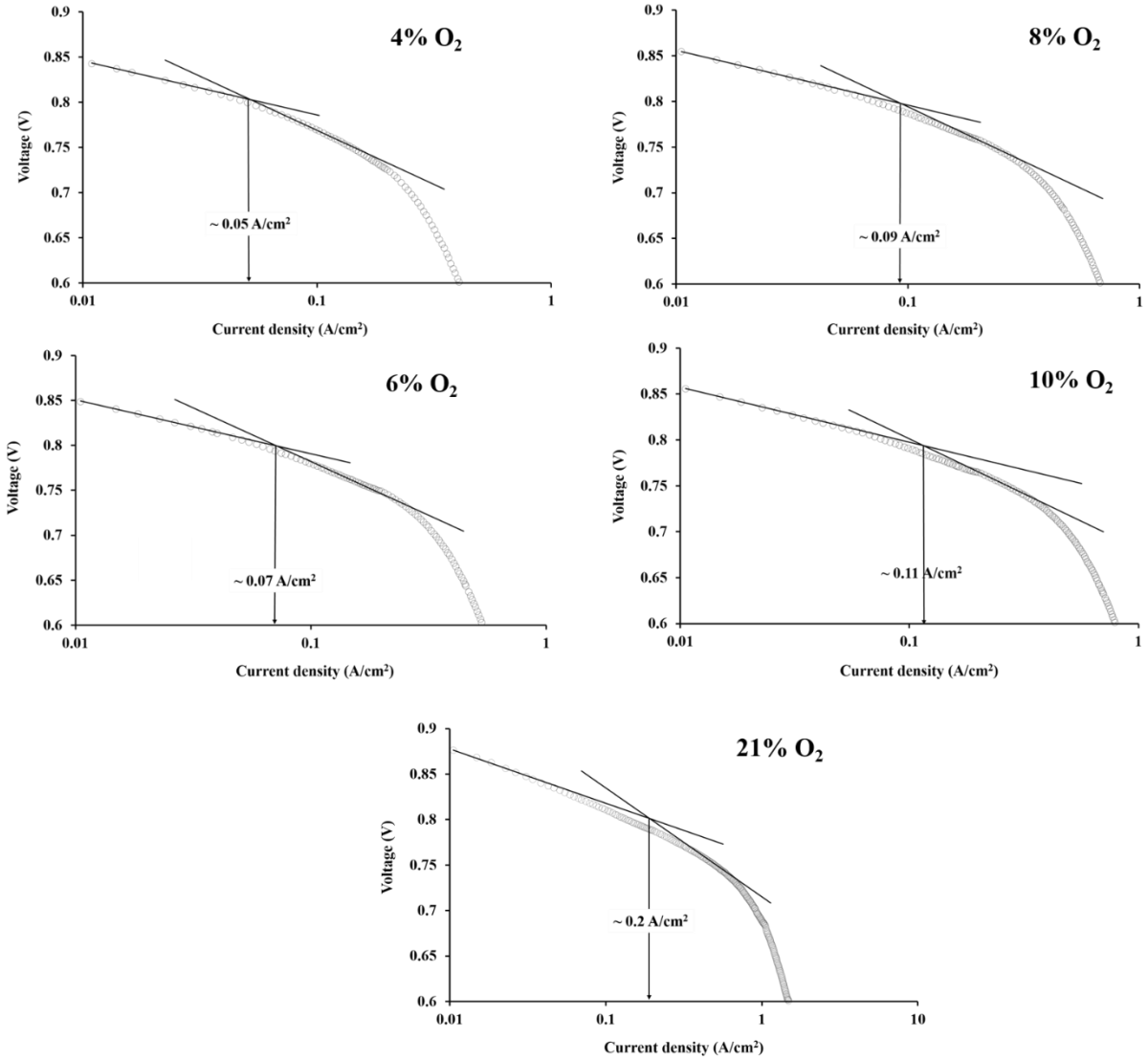


**Fig. 7.5** iR-corrected polarization curves with asymptotic lines having intrinsic Tafel slope and doubled the intrinsic Tafel slope for different inlet oxygen concentrations

The experimentally observed scaling law $J_{total} \sim (C_{in})^{0.7}$ at high overpotential in figure 7.8 shows deviation from the expected scaling of $J_{total} \sim (C_{in})^{1}$. There could be two probable causes for the deviation:

a) The theoretical scaling law $J_{total} \sim (C_{in})^1$ is strictly valid for limiting current density. However, it can be observed from figure 7.4 that except for 4% $O_2$ and 6% $O_2$ cases, we did not see limiting current density in our experimental data.

b) The rate of water generation at higher overpotential increases for increasing $C_{in}$ due to higher current. This might result in varying water content in the GDL, which in turn would affect the effective oxygen diffusion coefficient in GDL. Thus, the assumption of the same $D_{GDL}$ for all $C_{in}$ may not be strictly valid. Capturing the variation in $D_{GDL}$ due to variation in water content in the GDL is possible only in a non-isothermal, multiphase model of PEM fuel cell. This is out of scope of the present study.

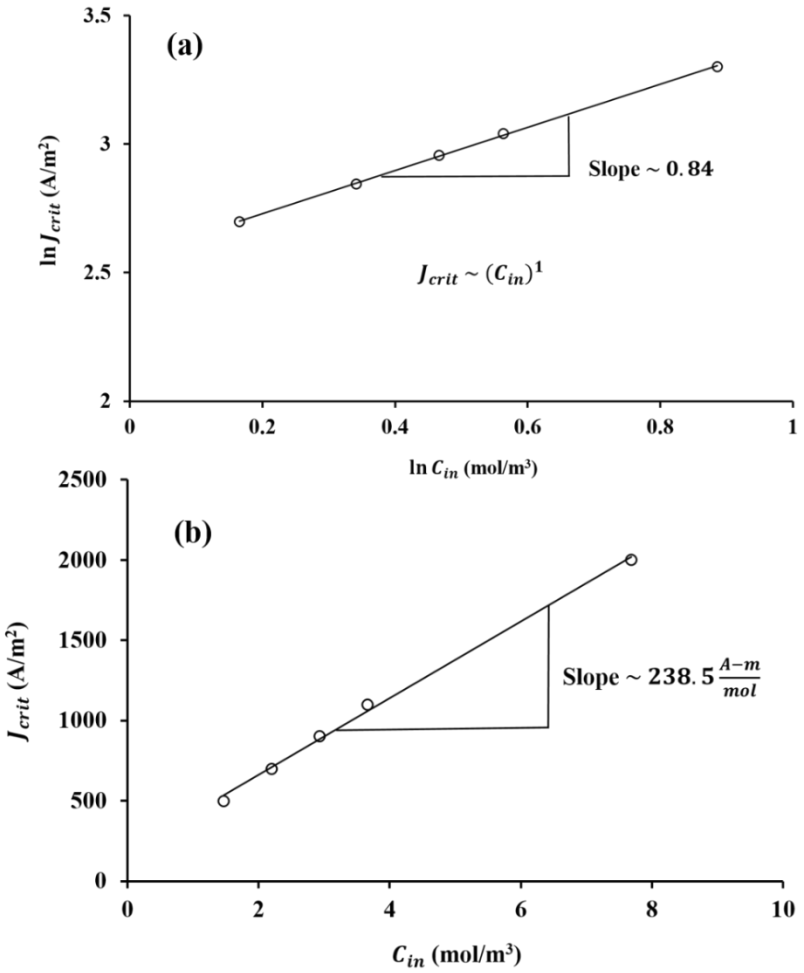


**Fig. 7.6** a) Double logarithmic plot of critical current density ($J_{crit}$) versus inlet oxygen concentration, b) critical current density ($J_{crit}$) versus inlet oxygen concentration

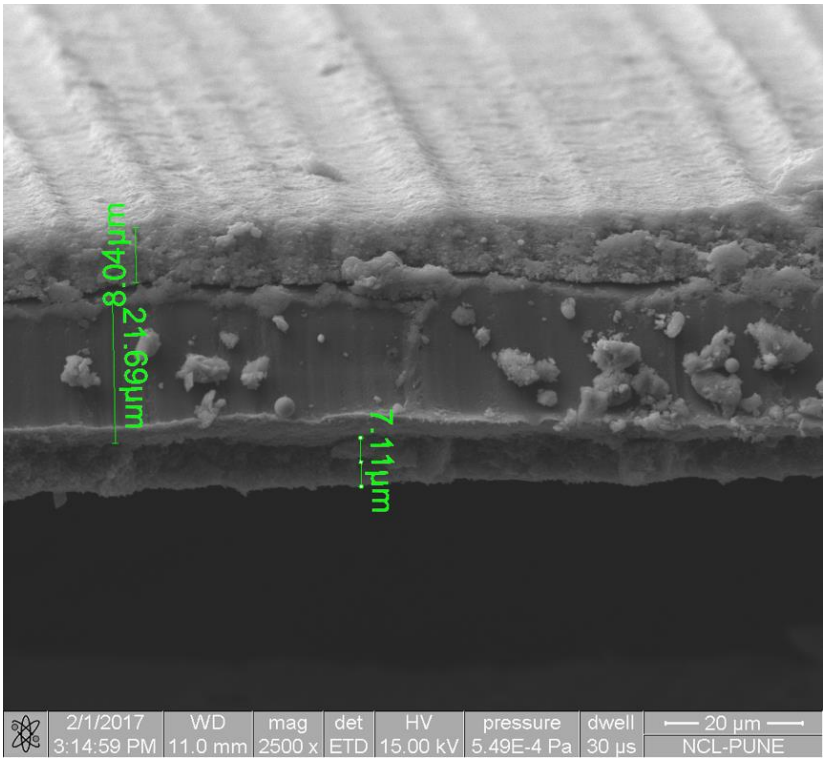


**Fig. 7.7** SEM image of the catalyst coated membrane (CCM)

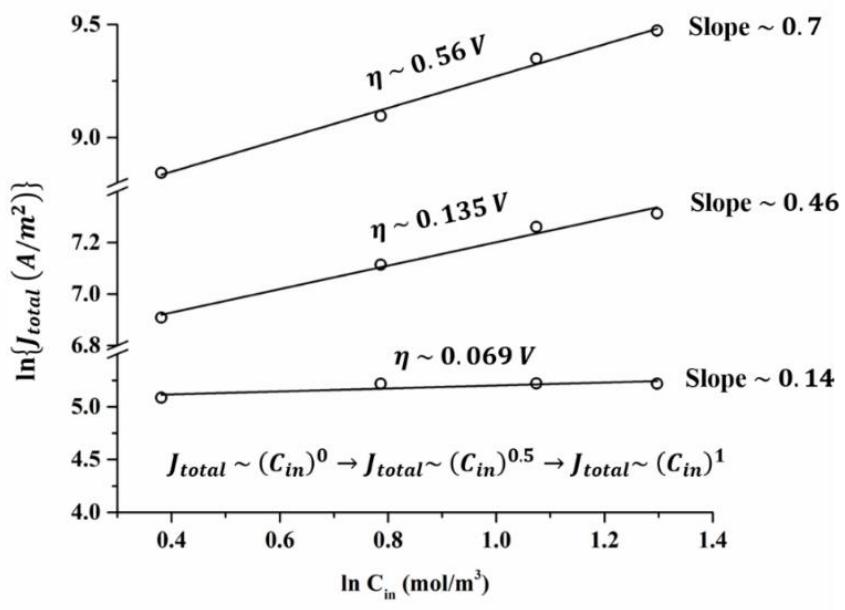


**Fig. 7.8** Double logarithmic plot of total current density ($J_{total}$) versus inlet oxygen concentration ($C_{in}$) at different overpotentials

For the CCLs used in this work, our experimental polarization data for $H_2$/air shows that $J_{crit,(O2)transport} \sim 0.2 - 0.4\ \frac{A}{cm^2}$ over typical operating oxidant back-pressure range. In comparison, since the effective proton conductivity of such a CCL is estimated to be around $\sim 2 - 3\ S/m$ [43-45], we find that $J_{crit,(H+)transport} = \frac{2\sigma A_c}{l_t} \sim 1.2 - 2\ \frac{A}{cm^2}$. However, as discussed earlier, the current density at which *both* oxygen and proton transport resistances will *simultaneously* start influencing the polarization curve will be lower than $J_{crit,(H+)transport}$. Therefore, for the MEAs similar to those used in this work and under humidified operating conditions, the operating regime of CCL is likely to shift from intrinsic Tafel kinetics at low current density to oxygen diffusion modulated ORR kinetics at intermediate current densities to simultaneous oxygen-proton transport resistance modulated ORR at higher current density and further to a regime in which agglomerate diffusion resistance coupled with oxygen-proton transport resistance will modulate ORR at even higher current density. At extreme values of current density one or more of the three limiting factors viz., stoichiometry, GDL diffusion or channel diffusion will determine a limiting current.

- ***Determination of oxygen diffusion coefficients in CCL, GDL and channel***

We now determine the effective oxygen diffusion coefficient in the CCL. As can be seen in figure 7.6b, which shows the same data of figure 7.6a on a linear-linear scale, the slope of $J_{crit}$ versus $C_{in}$ turns out to be about $\sim 237.5\ \frac{A-m}{mol}$. From this and using equation (7.4), the effective oxygen diffusion coefficient in the CCL can be estimated to be $\sim 4.9 \times 10^{-9}\ \frac{m^2}{s}$. That the thickness of the CCL is indeed ~ 8-10 μm is confirmed by the SEM image, as shown in figure 7.7. Since the oxygen diffusion coefficient in water is known to be about $\sim 5 \times 10^{-9}\ \frac{m^2}{s}$ [99], it implies that the CCL is flooded with liquid water. This is likely due to low operating temperature and high humidity conditions (70-75% RH on cathode side and 100% RH on anode

side) coupled with water generation due to reaction. It seems possible then that for the MEAs tested here, flooding of secondary pores in the CCL with water gives rise to oxygen diffusion resistance in the CCL.

As mentioned in the Introduction, earlier attempts to estimate oxygen diffusion coefficient in the CCL by the so-called limiting current method assumed linear oxygen concentration profile in the CCL, which may not be always correct. In the methodology outlined in this work, no assumption whatsoever on the oxygen concentration profile in the CCL was invoked.

We now use the methodology proposed in the section 7.4 to estimate the oxygen diffusion coefficients in GDL and channel. Figure 7.9 shows the polarization curves for different channel depths (1 mm, 2 mm, 3 mm and 4 mm) obtained with $H_2$ as a fuel and 4% $O_2$ as oxidant. The reciprocal of current densities at low operating cell voltage (0.3 V) are plotted as a function of half channel depth in figure 7.10. The slope of the line $\frac{1}{J_{total\ (@\ 0.3V)}}$ versus $h$ obtained from this plot is about $\sim 0.05\ \frac{1}{A/m}$ and from this, the oxygen diffusion coefficient in the channel ($D$) can be estimated using equation (7.5) to be about $\sim 3.5 \times 10^{-5}\ \frac{m^2}{s}$, which is in agreement with the known numerical value of oxygen diffusion coefficient in air at 60°C ($\sim 3 \times 10^{-5}\ \frac{m^2}{s}$) [100]. Further, the intercept of $\frac{1}{J_{total\ (@\ 0.3V)}}$ versus $h$ line is $\sim 0.00014\ \frac{1}{A/m^2}$ from which, as explained in earlier section, the value of $D_{GDL}$ can be estimated from equation (7.5) and by using estimated value of the effective length scale for oxygen diffusion in GDL, $l_{eff,GDL} = \varphi l_{GDL} + (1 - \varphi)\left(\frac{w_{rib}}{2} + l_{GDL}\right)$ (see equation 6.11). Here, $\varphi = \frac{w_{channel}}{w_{channel}+w_{rib}}$ (ratio of flow area to the total area). For the material parameters of our GDL (see experimental section) and for the rib width used in our flow field plate ($w_{rib} = 1mm$), we estimated $l_{eff,GDL} \sim 550$ micron. Using this value, the effective oxygen diffusion coefficient in the GDL ($D_{GDL}$) was found to be $\sim 7 \times 10^{-6}\ \frac{m^2}{s}$.

We may compare this value with an independent estimate of $D_{GDL}$ using the popular Bruggeman correlation ($D_{GDL} \sim \varepsilon_{GDL}^{1.5} D$), where $\varepsilon_{GDL}$ is the porosity of GDL, the exponent 1.5 refers to the tortuosity factor and $D$ is the bulk diffusion coefficient of oxygen in air. Substituting these known values gives $D_{GDL} \sim 6.2 \times 10^{-6} \frac{m^2}{s}$, which is in close agreement with the experimentally estimated value and is be used in model calculations.

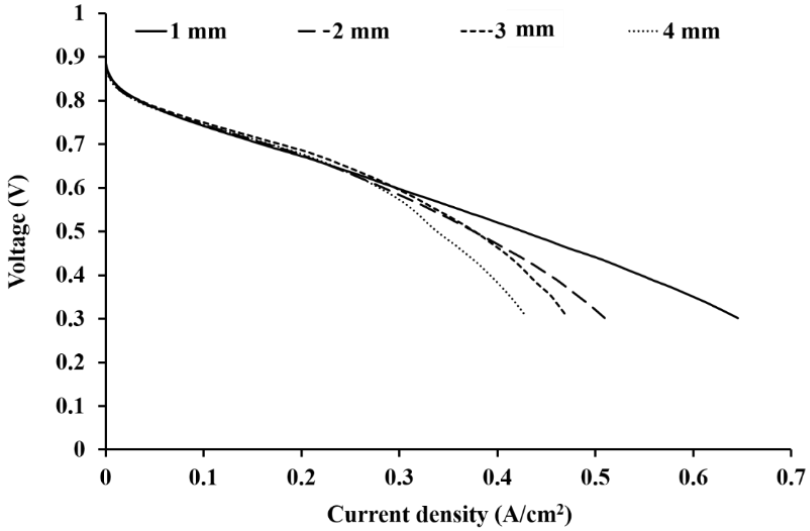


**Fig. 7.9** Polarization curves for different channel depths with $H_2$ as a fuel and 4% $O_2$ as oxidant at $T = 60°C$, $H2\ stoichiometry = 5$, $oxidant\ stoichiometry = 5.5$, $outlet\ pressure = ambient$, $anode\ side\ RH = 100\%$ and $cathode\ side\ RH = 70\%$

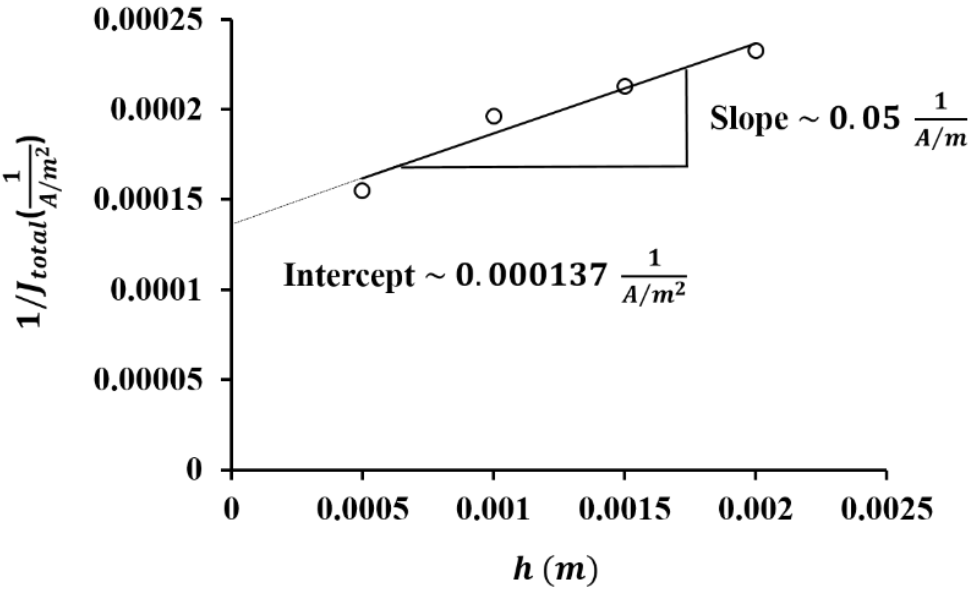


**Fig. 7.10** Plot of $\frac{1}{J_{total}}$ versus different channel depths at voltage of 0.3 V

Thus, we have demonstrated that the experimental methodology proposed in this chapter clarifies the operating regime of the CCL and also gives excellent estimates of the oxygen diffusion coefficients in the channel, GDL and CCL. We summarize the three oxygen diffusion coefficients obtained experimentally in table 7.2.

**Table 7.2** Numerical values of model parameters obtained from experiments

| Parameter | Value |
|---|---|
| $D_{CCL}$ | $\sim 4.9 \times 10^{-9} \frac{m^2}{s}$ |
| $D_{GDL}$ | $\sim 7 \times 10^{-6} \frac{m^2}{s}$ |
| $D$ | $\sim 3.5 \times 10^{-5} \frac{m^2}{s}$ |

- ***Comparison of analytical model, numerical simulations and experiments***

In this section we compare predictions of analytical model with experimental data as well as with three-dimensional numerical simulation. Table 7.2 provided the numerical values of model parameters. While all other values of numerical parameters were discussed earlier in chapter 7, the values of oxygen diffusivities in CCL, GDL and channel were also provided in the table 7.2. In fact, as discussed in the aforementioned sections, those values are experimental estimates.

Figure 7.11 shows comparison between experimentally determined polarization curve, predictions of the *PEM fuel cell equation* given by equations (7.1) and predictions of the three-dimensional numerical simulations. An excellent match between analytical model, simulations and experimental results was observed over the entire range of current density. Note that the various assumptions made during the derivation of the PEM fuel cell equation were already validated in chapter 6 by comparing model predictions with the results of full three-dimensional numerical simulations in which no simplifying approximations were made. Also, model

predictions match the experimental polarization curve without any 'fitting parameter'. Therefore, this validates the ability of PEM fuel cell equation to capture the coupled reaction-diffusion-convection phenomena in an operational PEMFC and to relate all material, geometrical and operating parameters to its performance.

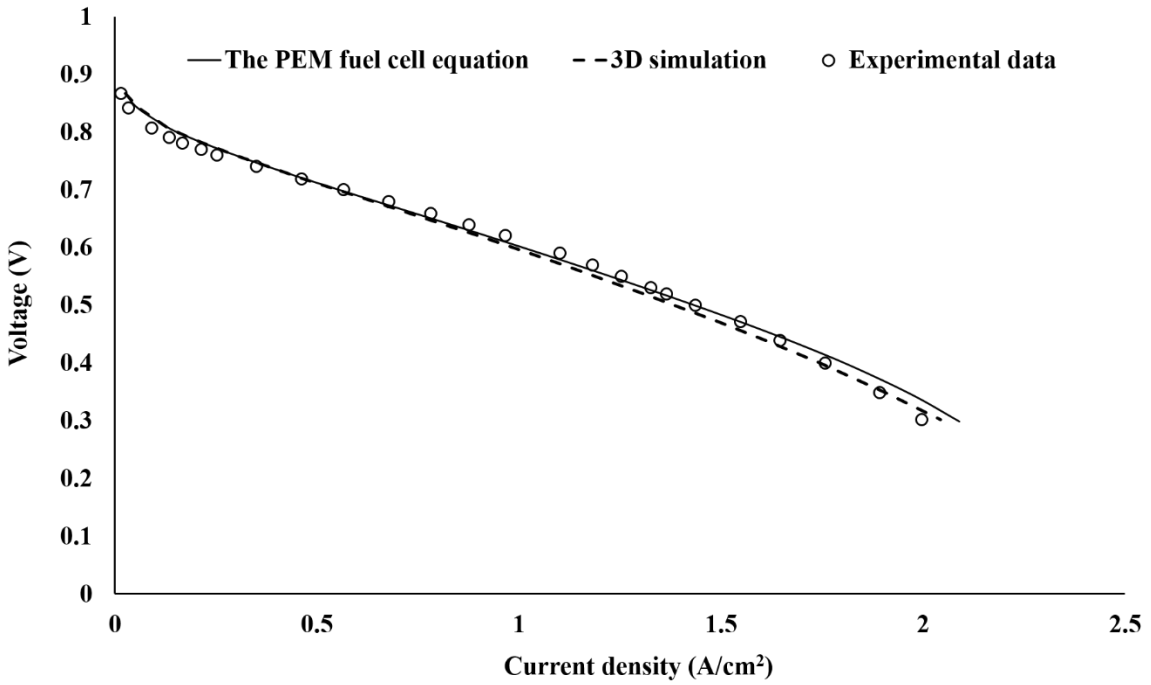


**Fig. 7.11** Comparison of polarization curves predicted by analytical theory, full three-dimensional numerical simulation and an experiment

## 7.6) Conclusions

An experimental approach to quantify mass transport resistance in an operational PEMFC based on the developed analytical theory is presented. This chapter elucidates an approach of comparing theoretical scaling laws with the experimental scaling laws to assess whether the deviation in the polarization curve from intrinsic Tafel kinetics of ORR is because of oxygen transport resistance across the CCL. It allows to quantify effective oxygen diffusion coefficient in the CCL without invoking any restrictions on the oxygen concentration profile in the CCL. Furthermore, a method of segregating oxygen diffusional resistances in the channel and GDL

by varying channel depths is discussed and effective oxygen diffusion coefficient in the GDL is quantified.

Given that a high current density PEMFC operation is common in automotive applications, it is imperative to understand the effect of oxygen transport resistance in the different domains of PEMFC. A simple experimental methodology to quantify oxygen transport resistance in all the domains of an operational PEMFC discussed in this study is an important step forward in this regard.

Finally, we show that the polarization curve predicted by *The PEM fuel cell equation* and typical experimental polarization curve give an excellent match over the entire range of current density.

# Chapter 8

# Conclusions and future scope

This thesis has presented a comprehensive analytical model of PEM fuel cell and its validation using detailed numerical simulations as well as experimental analysis. The work presented in this thesis has led to the following new contributions over existing literature:

## 8.1) Salient findings

The effects of simultaneously active oxygen and proton transport resistances across the CCL thickness as well as oxygen transport resistance in the catalyst agglomerates is captured through one-dimensional FA-corrected-MH model of the CCL. The most generalized analytical solutions relating current density with CCL overpotential are obtained spanning all the possible regimes of CCL operation.

Two-dimensional model capturing the non-uniformity of velocity and oxygen concentration along the depth of the flow channel along with oxygen transport resistance in the GDL is coupled with local FA-corrected-MH model of the CCL such that the consumption flux at the CCL-GDL boundary is dictated by the regime of CCL operation. Analytical solution to this two-dimensional problem resulted in '*The PEM fuel cell equation*', a compact, closed-form algebraic expression that correlates all the geometric, operating and material parameters involved in an operational PEMFC with its power output. Different approximations invoked while deriving analytical solutions to the one-dimensional and two-dimensional models are validated by comparing analytical model predictions with three-dimensional numerical simulation results wherein no simplifying approximations are made.

While almost all the parameters in the analytical model are independently measurable, the determination of two important oxygen transport parameters namely, effective oxygen diffusion coefficient in the GDL and CCL, was non-trivial. A physics-based experimental methodology to determine these parameters is elucidated and therefore all model parameters can now be estimated independently. Finally, we show that the polarization curve predicted by *The PEM fuel cell equation* provides an excellent match with the experimentally determined polarization curve of an externally humidified low temperature PEM fuel cell over the entire range of current density.

The PEM fuel cell equation captures the simultaneous convection-diffusion-reaction phenomena in PEM fuel cell through 7 different current density scales and the net ohmic resistance. Each current density scale is experimentally measurable and has definite physical meaning. Therefore, the PEM fuel cell equation provides deep physical insight into the physicochemical processes occurring in an operational PEM fuel cell and their repercussions on the power output. We believe that PEM fuel cell equation is extremely valuable because it can be used for diagnostic purposes as also for improving the performance of a fuel cell without the need for using expensive numerical simulations. Indeed, the simplicity of the PEM fuel cell equation can be gauged from the fact that it can be programmed in a simple Excel spreadsheet. Here, we provide a snapshot of this excel file (figure 8.1).

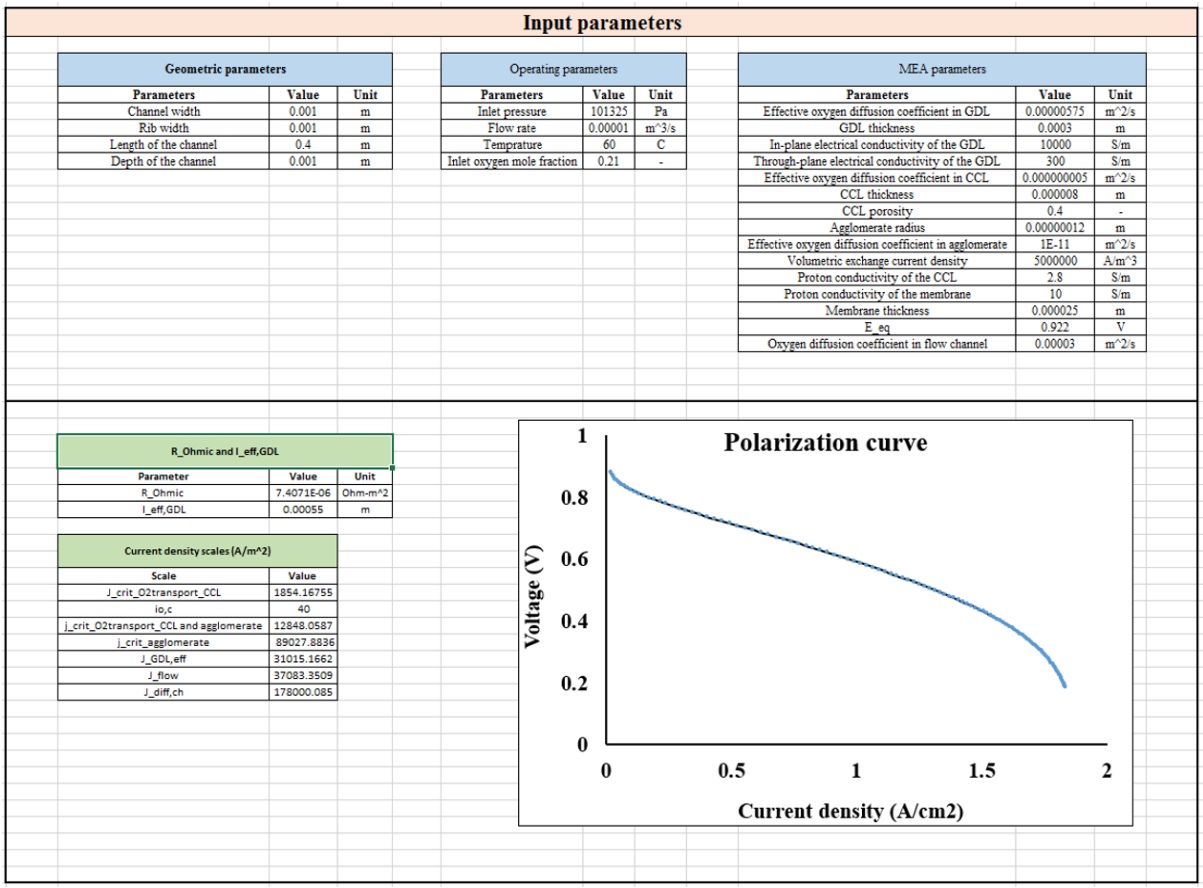


**Fig.8.1** Snapshot of Polarization Calculator illustrating different input parameters and an output plot, 'polarization curve'

## 8.2) Future scope

The work presented in this thesis leads to different opportunities for further investigations in the area of PEMFC technology:

a) Incorporation of water-evaporation and condensation kinetics

The mathematical model of PEMFC discussed in this thesis does not incorporate the physical processes on the cathode and anode sides which dictate the water balance in the cell. At best, the effective oxygen diffusion coefficients in the porous CCL and GDL may be thought to depend on a dimensionless quantity, $s$, which is the ratio of volume occupied by water to the open pore volume in the corresponding domain. While '$s$' would be an input parameter for the PEM fuel cell equation, however, in principle, it is a result of competition between following

rate processes: a) rate of water generation at cathode, b) rate of water condensation at anode and cathode, 3) rate of water evaporation at anode and cathode, 4) rate of water back-diffusion (from cathode-to-anode), 5) water flux due to electro-osmotic drag from anode-to-cathode.

An improved model should incorporate the above five rate processes coupled with other transport processes to predict '$s$', which can then be used to estimate the effective oxygen diffusion coefficients in the CCL and GDL. Such an insight can allow us to design efficient water management protocol to maximize the power output of PEMFC.

b) Engineering CCL microstructure to enhance oxygen diffusion in the CCL

This thesis proves that for the realistic case of a fully humidified low temperature PEM fuel cell, the operating regime of CCL is likely to shift from intrinsic Tafel kinetics to oxygen diffusion modulated ORR kinetics under typical operating conditions. Thus, maximizing the current density scale $\frac{4FD_{CCL}C_{in}}{l_t}$ can maximize the power output of PEMFC. Thus, increasing oxygen diffusion coefficient in the CCL and reducing the thickness of the CCL for the same catalyst loading can improve the PEMFC dramatically.

The enhancement in the oxygen diffusion coefficient can be achieved by either lowering the tortuosity of the CCL (better pore connectivity) and/or by increasing the porosity of the CCL. The preliminary work by Kim et al. 2013 [103] discussed a novel method to fabricate highly porous and less tortuous CCL and demonstrated a great promise in achieving path-breaking power output. Li et al. 2019 [104] recently demonstrated a novel methodology to fabricate low tortuosity battery electrodes. The methodology can be replicated for CCL fabrication which may result in higher power output. This thesis has established a methodology to estimate oxygen diffusion coefficient in the CCL and therefore, we can characterize the fabricated CCLs in terms of $D_{CCL}$.

Lowering the thickness has been pursued in a fuel cell component development program by 3M company which resulted in Nanostructured thin film (NSTF) catalyst layer with a thickness of less than a micron [105]. The analysis suggested that such a CCL follows intrinsic Tafel kinetics for a very large range of current density (up to ~ 1.2 A/cm$^2$). Another report by Lee et al. 2015 [106], shows 30% increment in the power output of PEMFC when the thickness of the CCL is reduced to 2 microns from 7-8 microns.

Therefore, an experimental program can be designed with an aim to develop thin, low tortuous and highly porous CCL by combining the ideas discussed in these reports which may result in impactful increment in the power output of the PEMFC.

# References

[1] Chu S. and Majumdar A., Opportunities and challenges for a sustainable energy future, Nature 488 (2012) 294-303

[2] Denholm P., Ela E., Kirby B. and Milligan M., The Role of Energy Storage with Renewable Electricity Generation, Technical Report NREL/TP-6A2-47187 (2010), available at: https://www.nrel.gov/docs/fy10osti/47187.pdf

[3] Solar tariffs once again hit all-time low of Rs 2.44 a unit at SECI auction, Kaavya Chandrasekaran, The Economic Times, 3rd July, 2018.

[4] Wind power prices crash to ₹2.43/unit in Gujarat auction, M. Ramesh, The Hindu, 21st December 2017.

[5] https://nelhydrogen.com/products/

[6] Rao C. N. R. and Dey S., Solar thermochemical splitting of water to generate hydrogen, PNAS 114 (2017) 13385–13393.

[7] Jia J., Seitz L.C., Benck J.D., Huo Y., Chen Y., Desmond Ng J.W., Bilir T., Harris J.S. and Jaramillo T.F., Solar water splitting by photovoltaic-electrolysis with a solar-to-hydrogen efficiency over 30%, Nature Communications 7 (2016) 1-6.

[8] Intelligent Energy, "The True Cost of Providing Energy to Telecom Towers in India," January 2012. (https://www.gsma.com/membership/wp-content/uploads/2013/01/true-cost-providing-energy-telecom-towers-india.pdf )

[9] https://main.trai.gov.in/sites/default/files/Consultation_Paper_16_jan_2017_0.pdf

[10] Glenk G. and Reichelstein S., Economics of converting renewable power to hydrogen, Nature Energy 4 (2019) 216–222.

[11] http://ballard.com/about-ballard/newsroom/news-releases/2015/04/29/ballard-receives-initial-100-unit-order-from-reliance-jio-infocomm-for-backup-power-systems-in-india

[12] http://ballard.com/about-ballard/newsroom/news-releases/2015/09/30/ballard-announces-sale-of-telecom-backup-power-systems-to-aditya-birla-in-india

[13] https://www.toyota.ca/toyota/en/connect/2954/project-portal-a-more-environmentally-friendly-transport-truck

[14] https://nikolamotor.com/one#motor-features

[15] https://www.hyundai.news/eu/technology/hyundai-motor-presents-first-look-at-new-truck-with-a-fuel-cell-powertrain-ahead-of-iaa-commercial-vehicles-2018-announcement/

[16] https://qz.com/1044347/hydrogen-powered-vehicles-are-finally-taking-off-inside-amazon-amzn-and-walmart-wmt-warehouses/

[17] https://www.gmdefensellc.com/

[18] https://commons.wikimedia.org/wiki/File:SEM_micrograph_of_an_MEA_cross_section.jpg

[19] http://www.graphitestore.com/fuel-cells

[20] https://www.fuelcellstore.com/blog-section/fuel-cell-stack-temperature-in-mid-to-high-temperature-fuel-cells

[21] Kahraman H. and Orhan M.F., Flow field bipolar plates in a proton exchange membrane fuel cell: Analysis & modelling, Energy Conversion and Management 133 (2017) 363-384.

[22] Tawfik H., Hung Y. and Mahajan D., Metal bipolar plates for PEM fuel cell - A review, Journal of Power Sources 163 (2007) 755–767.

[23] Cindrella L., Kannana A.M., Lin J.F., Saminathan K., Ho Y., Lin C.W. and Wertz J., Gas diffusion layer for proton exchange membrane fuel cells - A review, Journal of Power Sources 194 (2009) 146–160.

[24] https://www.m-chemical.co.jp/en/products/departments/mcc/composite-products/product/1201231_7508.html

[25] Schulze M., Schneider A. and Gulzow E., Alteration of the distribution of the platinum catalyst in membrane-electrode assemblies during PEFC operation, Journal of Power Sources 127 (2004) 213–221.

[26] https://www.sigmaaldrich.com/materials-science/renewable-alternative-energy/pem-fuel-cells.html

[27] Kreuer K. D., On the development of proton conducting materials for technological applications, Solid State Ionics 97 (1997) 1-15.

[28] Kusoglu A. and Weber A.Z., New Insights into Perfluorinated Sulfonic-Acid Ionomers, Chemical Reviews 117 (2017) 987−1104.

[29] Kusoglu A., Savagatrup S., Clark K.T. and Weber A.Z., Role of Mechanical Factors in Controlling the Structure−Function Relationship of PFSA Ionomers, Macromolecules 45 (2012) 7467−7476.

[30] Neyerlin K.C., Gasteiger H.A., Mittelsteadt C.K., Jorne J., Gu W., Effect of Relative Humidity on Oxygen Reduction Kinetics in a PEMFC, J. Electrochem. Soc. 152 (6) (2005) A1073-A1080.

[31] Weber A,Z., Newman J., Modeling Transport in Polymer-Electrolyte Fuel Cells, Chem. Rev. 2004, 104, 4679-4726.

[32] Cheddie D., Munroe N., Review and comparison of approaches to proton exchange membrane fuel cell modelling, Journal of Power Sources 147 (2005) 72–84.

[33] Bernardi D.M., Verbrugge M.W., Mathematical Model of a Gas Diffusion Electrode Bonded to a Polymer Electrolyte, AIChE J. 37 (1991) 1151–1163.

[34] Springer T.E., Wilson M.S., Gottesfeld S., Modeling and Experimental Diagnostics in Polymer Electrolyte Fuel Cells, J. Electrochem. Soc. 140 (12) (1993) 3513-3526.

[35] Eikerling M., Kornyshev A.A., Modelling the performance of the cathode catalyst layer of polymer electrolyte fuel cells, J. Electroanal. Chem. 453 (1998) 89–106.

[36] Perry M.L., Newman J., Cairns E.J., Mass Transport in Gas-Diffusion Electrodes: A Diagnostic Tool for Fuel-Cell Cathodes, J. Electrochem. Soc. 145 (1) (1998) 5-15.

[37] Srinivasan S., Ticianelli E.A., Derouin C.R., Redondo A., Advances in Solid Polymer Electrolyte Fuel Cell Technology with Low-Platinum-Loading Electrodes, J. Power Sources, 22 (1988) 359-375.

[38] Neyerlin K.C., Gu W., Jorne J., Gasteiger H.A., Determination of Catalyst Unique Parameters for the Oxygen Reduction Reaction in a PEMFC, J. Electrochem. Soc. 153 (10) (2006) A1955-A1963.

[39] Sambandam S., Ramani V., Influence of binder properties on kinetic and transport processes in polymer electrolyte fuel cell electrodes, Phys. Chem. Chem. Phys. 12 (2010) 6140–6149.

[40] Yu H., Bonville L., Maric R., Analysis of $H_2$/Air Polarization Curves: The Influence of Low Pt Loading and Fabrication Process, J. Electrochem. Soc. 165 (5) (2018) F272-F284.

[41] Kulikovsky A.A., Performance of catalyst layers of polymer electrolyte fuel cells: exact solutions, Electrochemistry Communications 4 (2002) 318–323.

[42] Kulikovsky A.A., The regimes of catalyst layer operation in a fuel cell, Electrochimica Acta 55 (2010) 6391–6401.

[43] Cimenti M., Bessarabov D., Tam M., Stumper J., Investigation of Proton Transport in the Catalyst Layer of PEM Fuel Cells by Electrochemical Impedance Spectroscopy, ECS Transactions, 28 (23) (2010) 147-157.

[44] Liu Y., Murphy M.W., Baker D.R., Gu W., Ji C., Jorne J., Gasteiger H. A., Proton Conduction and Oxygen Reduction Kinetics in PEM Fuel Cell Cathodes: Effects of Ionomer-to-Carbon Ratio and Relative Humidity, J. Electrochem. Soc. 156 (8) (2009) B970-B980.

[45] Makharia R., Mathias M.F., Baker D.R., Measurement of Catalyst Layer Electrolyte Resistance in PEFCs Using Electrochemical Impedance Spectroscopy, J. Electrochem. Soc., 152 (5) A970-A977 (2005).

[46] Inoue G., Yokoyama K., Ooyama J., Terao T., Tokunaga T., Kubo N., Kawase M., Theoretical examination of effective oxygen diffusion coefficient and electrical conductivity of PEFC porous components, Journal of Power Sources 327 (2016) 610-621.

[47] Inoue G. and Kawase M., Effect of porous structure of catalyst layer on effective oxygen diffusion coefficient in polymer electrolyte fuel cell, Journal of Power Sources 327 (2016) 1-10.

[48] L. G. Austin, Tafel Slopes for Flooded Diffusion Electrodes, Trans. Faraday Soc. 60 (1964) 1319-1324.

[49] Giner J. and Hunter C., The Mechanism of Operation of the Teflon-Bonded Gas Diffusion Electrode: A Mathematical Model, J. Electrochem. Soc. 116 (8) (1969) 1124-1130.

[50] Iczkowski R.P. and Cutlip M.B., Voltage Losses in Fuel Cell Cathodes, J. Electrochem. Soc. 127 (7) (1980) 1433-1440.

[51] Striebel K.A., McLarnon F.R., and Cairns E.J., Steady-State Model for an Oxygen Fuel Cell Electrode with an Aqueous Carbonate Electrolyte, Ind. Eng. Chem. Res. 34 (1996) 3632-3639.

[52] Broka K. and Ekdunge P., Modelling the PEM fuel cell cathode, J. Appl. Electrochem. 27 (1997) 281-289.

[53] S.J. Lee, S. Mukerjee, J. McBreen, Y.W. Rho, Y.T. Kho, and T.H. Lee, Effects of Nafion impregnation on performances of PEMFC electrodes, Electrochimica Acta, 43 (1998) 3693-3701.

[54] Siegel N.P., Ellis M.W., Nelson D.J., and von Spakovsky M.R., Single domain PEMFC model based on agglomerate catalyst geometry, Journal of Power Sources, 115 (2003) 81-89.

[55] Kulikovsky A.A., How important is oxygen transport in agglomerates in a PEM fuel cellcatalyst layer, Electrochimica Acta 130 (2014) 826–829.

[56] Khajeh-Hosseini-Dalasm N., Fesanghary M., Fushinobu K., Okazaki K., A study of the agglomerate catalyst layer for the cathode side of a proton exchange membrane fuel cell: Modeling and optimization, Electrochimica Acta 60 (2012) 55– 65.

[57] Jaouen F., Lindbergh G. and Sundholm G., Investigation of Mass-Transport Limitations in the Solid Polymer Fuel Cell Cathode I. Mathematical Model, J. Electrochem. Soc. 149 (4) (2002) A437-A447.

[58] Ihonen J., Jaouen F., Lindbergh G., Lundblad A., and Sundholm G., Investigation of Mass-Transport Limitations in the Solid Polymer Fuel Cell Cathode II. Experimental, J. Electrochem. Soc. 149 (4) (2002) A448-A454.

[59] Sun W., Peppley B.A., Karan K., An improved two-dimensional agglomerate cathode model to study the influence of catalyst layer structural parameters, Electrochimica Acta, 50 (2005) 3359-3374.

[60] Harvey D., Pharoah J.G., Karan K., A comparison of different approaches to modelling the PEMFC catalyst layer, Journal of Power Sources 179 (2008) 209–219.

[61] Marquis J., Coppens M.O., Achieving ultra-high platinum utilization via optimization of PEM fuel cell cathode catalyst layer microstructure, Chem. Eng. Sci 102 (2013) 151–162.

[62] Cetinbas F.C., Advani S.G., Prasad A.K., A modified agglomerate model with discrete catalyst particles for the PEM fuel cell catalyst layer, J. Electrochem. Soc., 160 (2013) F750-F756.

[63] Kulikovsky A.A., Scharmann H., Wippermann K., On the origin of voltage oscillations of a polymer electrolyte fuel cell in galvanostatic regime, Electrochemistry Communications 6 (2004) 729–736.

[64] Kulikovsky A.A., The effect of stoichiometric ratio λ on the performance of a polymer electrolyte fuel cell, Electrochimica Acta 49 (2004) 617–625.

[65] Kulikovsky A.A., Polarization curve of a PEM fuel cell with poor oxygen or proton transport in the cathode catalyst layer, Electrochemistry Communications 13 (2011) 1395–1399.

[66] Baker D.R., Caulk D.A., Neyerlin K.C., Murphy M.W., Measurement of Oxygen Transport Resistance in PEM Fuel Cells by Limiting Current Methods, J. Electrochem. Soc. 156 (9) (2009) B991-B1003.

[67] Beuscher U., Experimental Method to Determine the Mass Transport Resistance of a Polymer Electrolyte Fuel Cell, J. Electrochem. Soc. 153 (9) (2006) A1788-A1793.

[68] Mashio T., Ohma A., Yamamoto S., Shinohara K., Analysis of Reactant Gas Transport in a Catalyst Layer, ECS Transactions, 11 (1) (2007) 529-540.

[69] Nonoyama N., Okazaki S., Weber A.Z., Ikogi Y., Yoshida T., Analysis of Oxygen-Transport Diffusion Resistance in Proton-Exchange-Membrane Fuel Cells, J. Electrochem. Soc. 158 (4) (2011) B416-B423.

[70] Tatyana V. Reshetenko, Jean St-Pierre, Separation Method for Oxygen Mass Transport Coefficient in Gas and Ionomer Phases in PEMFC GDE, J. Electrochem. Soc. 161 (10) (2014) F1089-F1100.

[71] Berning T., Lu D.M., Djilali N., Three-dimesnional computational analysis of transport phenomena in a PEM fuel cell, Journal of Power Sources 106 (2002) 284-294.

[72] Berning T., Djilali N., A 3D, Multiphase, Multicomponent Model of the Cathode and Anode of a PEM Fuel Cell, Journal of The Electrochemical Society, 150 (12) (2003) A1589-A1598.

[73] Dutta S., Shimpalee S., Van Zee J.W., Three-dimensional numerical simulation of straight channel PEM fuel cells, Journal of Applied Electrochemistry 30 (2000) 135–146.

[74] Dutta S., Shimpalee S., Van Zee J.W., Numerical prediction of mass-exchange between cathode and anode channels in a PEM fuel cell, International Journal of Heat and Mass Transfer 44 (2001) 2029-2042.

[75] Ju H., Meng H., Wang Chao-Yang., A single-phase, non-isothermal model for PEM fuel cells, International Journal of Heat and Mass Transfer 48 (2005) 1303–1315.

[76] Mazumder S., Cole J.V., Rigorous 3-D Mathematical Modeling of PEM Fuel Cells II. Model Predictions with Liquid Water Transport, 150 (11) (2003) A1510-A1517.

[77] Um S., Wang C.Y., Three-dimensional analysis of transport and electrochemical reactions in polymer electrolyte fuel cells, Journal of Power Sources 125 (2004) 40–51.

[78] Hu G., Fan J., Chen S., Liu Y. and Cen K., Three-dimensional numerical analysis of proton exchange membrane fuel cells (PEMFCs) with conventional and interdigitated flow fields, Journal of Power Sources 136 (2004) 1–9.

[79] Ubong E.U., Shi Z., Wang X., Three-dimensional modelling and experimental study of a high temperature PBI-based PEM fuel cell, J. Electrochem. Soc. 156 (2009) B1276-B1282.

[80] Hu M., Gu A., Wang M., Zhu X. and Yu L., Three dimensional, two phase flow mathematical model for PEM fuel cell: Part I. Model development, Energy Conversion and Management 45 (2004) 1861–1882.

[81] Djilali N., Computational modelling of polymer electrolyte membrane (PEM) fuel cells: Challenges and opportunities, Energy 32 (2007) 269–280.

[82] Wang Y., Chen K. S., Mishler J., Cho S.C., Adroher X.C., A review of polymer electrolyte membrane fuel cells: Technology, applications, and needs on fundamental research, Applied Energy 88 (2011) 981–1007.

[83] Weber A.Z., Borup R.L., Darling R.M., Das P.K., Dursch T.J., Gu W., Harvey D., Kusoglu A., Litster S., Mench M.M., Mukundan R., Owejan J.P., Pharoah J.G., Secanell M., Zenyuka Iryna V., A Critical Review of Modeling Transport Phenomena in Polymer-Electrolyte Fuel Cells, J. Electrochem. Soc. 161 (12) (2014) F1254-F1299.

[84] Siegel C., Review of computational heat and mass transfer modelling in polymer-electrolyte-membrane (PEM) fuel cells, Energy 33 (2008) 1331– 1352.

[85] Wu H., A review of recent development: Transport and performance modelling of PEM fuel cells, Applied Energy 165 (2016) 81–106.

[86] Manso A.P., Marzo F.F., Barranco J., Garikano X. and Mujika M.G., Influence of geometric parameters of the flow fields on the performance of a PEM fuel cell. A review, international journal of hydrogen energy 37 (2012) 15256–15287.

[87] Aiyejina A. and Sastry M. K. S., PEMFC Flow Channel Geometry Optimization: A Review, Journal of Fuel Cell Science and Technology, 9 (2012) 011011-1–011011-24.

[88] Li X. and Sabir I., Review of bipolar plates in PEM fuel cells: Flow-field designs, International Journal of Hydrogen Energy 30 (2005) 359 – 371.

[89] COMSOL Multiphysics, Batteries & Fuel Cells Module, application library manual, COMSOL Multiphysics 5.3, 2017

(https://www.comsol.com/model/download/458471/models.bfc.ht_pem.pdf).

[90] Thosar A.U., Agarwal H., Govarthan S. and Lele A.K., Comprehensive analytical model for polarization curve of a PEM fuel cell and experimental validation, Chemical Engineering Science 206 (2019) 96–117.

[91] Chen G.Y, Wang C., Lei Y.J., Zhang J., Mao Z., Mao Z.Q., Guo J.W., Li J., Ouyang M., Gradient design of Pt/C ratio and Nafion content incathode catalyst layer of PEMFCs, Int. J. Hydrog. Energy 42 (2017) 29960-29965.

[92] Pharoah J.G., Karan K., Sun W., On effective transport coefficients in PEM fuel cell electrodes: Anisotropy of the porous transport layers, Journal of Power Sources 161 (2006) 214–224.

[93] Buchi F.N., Wakizoe M., Srinivasan S., Microelectrocle Investigation of Oxygen Permeation in Perfluorinated Proton Exchange Membranes with Different Equivalent Weights, J. Electrochem. Soc. 143 (3) (1996) 927–932.

[94] Epting W. K., Gelb J., Litster S., Resolving the Three-Dimensional Microstructure of Polymer Electrolyte Fuel Cell Electrodes using Nanometer-Scale X-ray Computed Tomography. Adv. Funct. Mater 22 (2012) 555-560.

[95] Thosar A.U., Lele A.K., Analytical solutions of an isothermal two-dimensional model of a cathode flow channel in a proton exchange membrane fuel cell, Chemical Engineering Science 190 (2018) 333–344.

[96] Leal G., Advanced Transport Phenomena, Fluid Mechanics and Convective Transport Processes, Cambridge series in Chemical Engineering, Cambridge University Press (2007).

[97] Thosar A.U., Lele A.K., Analytical solutions of an isothermal two-dimensional model of a cathode flow channel in transport limited operational regimes of a proton exchange membrane fuel cell, Chemical Engineering Science 196 (2019) 166–175.

[98] Larminie J., Dicks A., Fuel Cell Systems Explained, 2nd edition, John Wiley & Sons Ltd.

[99] Ferrel R.T., Himmelblau D.M., Diffusion Coeffkients of Nitrogen and Oxygen in Water, J. Chem. Eng. Data, 12 (1) (1967) 111-115.

[100] Cussler E. L., Diffusion: Mass Transfer in Fluid Systems, 3rd edition, Cambridge University Press.

[101] SGL-GDL data sheet (http://www.sglgroup.com/cms/_common/downloads/products/product-groups/su/fuel-cell-components/White-Paper-SIGRACET-GDL-for-Fuel-Cells.pdf)

[102] Kreuer K.D., On the development of proton conducting polymer membranes for hydrogen and methanol fuel cells, J. Membr. Sci. 185 (2001) 29–39.

[103] Kim O.H., Cho Y.H., Kang S.H., Park H.Y., Kim M., Lim J.W., Chung D.Y., Lee M.J., Choe H. and Sung Y.E., Nature Communications 4 (2013) 1-9.

[104] Li L., Erb R.M., Wang J., Wang J., and Chiang Y.M., Fabrication of Low-Tortuosity Ultrahigh-Area-Capacity Battery Electrodes through Magnetic Alignment of Emulsion-Based Slurries, Advanced Energy Materials 9 (2) (2019) 1802472:1-7.

[105] Debe M.K., Tutorial on the Fundamental Characteristics and Practical Properties of Nanostructured Thin Film (NSTF) Catalysts, Journal of The Electrochemical Society, 160 (6) (2013) F522-F534.

[106] Lee J., Yoo J.M., Ye Y., Mun Y., Lee S., Kim O.H., Rhee H.W., Lee H.I., Sung Y.E., and Lee J., Development of Highly Stable and Mass Transfer-Enhanced Cathode Catalysts: Support-Free Electrospun Intermetallic FePt Nanotubes for Polymer Electrolyte Membrane Fuel Cells, Advanced Energy Materials 5 (11) (2015) 1402093:1-9.

# List of Publications

1) **Aniket. U. Thosar** and Ashish. K. Lele, Analytical solutions of an isothermal two-dimensional model of a cathode flow channel in a proton exchange membrane fuel cell, Chemical Engineering Science 190 (2018) 333–344.
2) **Aniket. U. Thosar** and Ashish. K. Lele, Analytical solutions of an isothermal two-dimensional model of a cathode flow channel in transport limited operational regimes of a proton exchange membrane fuel cell, Chemical Engineering Science 196 (2019) 166–175.
3) **Aniket. U. Thosar**, H. Agarwal, Govarthan S. and Ashish. K. Lele, Comprehensive analytical model for polarization curve of a PEM fuel cell and experimental validation, Chemical Engineering Science 206 (2019) 96–117 (Editor's Choice Article).